Chemical Routes to Improved Nanomaterial Suspensions for Electrophoretic Deposition

A thesis submitted for the degree of

Doctor of Philosophy in Material Science



John Alexander Ballentine

St. Cross College, University of Oxford

Hilary Term, 2023

For Rosalind Owen and Christopher Ballentine,

I promise to get a real job one day.

DECLARATION

I confirm that the work presented in this thesis is my own work. No part of this thesis has been accepted or is currently being submitted for any degree, diploma, certificate or other qualification in this University or elsewhere. This thesis is my own work, except where indicated.

ABSTRACT

This thesis develops our understanding of the experimental variables, and viability, for the film production of primarily hexagonal boron nitride (hBN). This is initially achieved by a successful investigation of the dispersibility and deposition of hBN analogous carbon nanotubes (CNT) to create films by the novel combination of CNT reduction and electrophoretic deposition (EPD). This process is then successfully, and for the first time, applied to boron nitride nanotubes (BNNT) and 2D boron nitride platelets (BNP). The reduced dispersion for EPD process bypasses the traditional need to oxidise the starting nanomaterial which can damage the materials' nanostructure. However, any comparative study for the oxidation of hBN materials is problematic as these processes are an underdeveloped field of research. The latter sections of this thesis therefore show that traditional acid oxidation methods used for carbon nanomaterials are ineffective at functionalising, dispersing and depositing the more inert hBN materials.

The novel and improved method for neat CNT film production is first developed by the combination of two established techniques: the electrochemical reduction and suspension of single walled carbon nanotubes (SWCNT) by sodium naphthalide (NaNap), and the charged particle coagulation of EPD. This 'reduced dispersion for EPD method' creates SWCNT films of controllable thicknesses (0-14 μm), in short amounts of time (5-120 s) and requires low field strengths (1-5 V cm^{-1}) to do so. The final nanomaterial products are conductive, mechanically strong, and thermally stable SWCNT films which crucially retain the nanostructure of their initial starting material without the need for additional chemical modification, additives or binders. Free-standing examples of these materials are compared to samples made using the traditional oxidation-based methodology and are found to be mechanically weaker (8.4 vs 14.9 MPa Youngs modulus) and poorer electrical conductors (229 S cm^{-1} vs 694 ±18 S cm^{-1}). This is due to the thicker films containing void spaces caused by the removal of sodium crystals during the post-EPD washing of the samples and thereby increasing the porosity and reducing the density of the material.

This thesis then shows the first reductive dispersion and first EPD of BNNT. It is found that the charge ratio on BNNT is significantly lower (<41_{BN}:1_{Na}) than for CNT (5_C:1_{Na}) and subsequently EPD deposition rates are slower (2.03 μg cm^{-2} min^{-1}). It is hypothesised that this causes the resultant BNNT films to be thicker than CNT (up to 35 μm). The nanotubes within films are proved to have near identical nanostructures to their starting materials showing that the dispersion and EPD processes were none-damaging. However, the similar film density of these materials to CNT equivalents (0.31 g cm^{-3}) and poor mechanical performance imply similar issues with film porosity.

Finally, various solution-based acid etching techniques and methodologies described across literature for carbon nanomaterials are applied to BNP which are shown to be inert to these conditions. Dispersion of these materials is still achieved by bath sonication which is shown to the most effective benchtop method for doing so (concentrations up to 0.232 mg_{BN} mL_{IPA}^{-1}). EPD of the resulting suspensions was slow and produced negligible hBN films leading to the conclusion that this is not an efficient method of film production, especially when compared to the reduced dispersion for EPD method developed previously in this work.

ACKNOWLEDGEMENTS

No large piece of work can be completed in isolation, and I have numerous people to thank for the help and kindness they have shown me on this academic journey over the last four years.

Firstly, I must acknowledge the NbD leadership of Dr Barbara Maciejewska, Sam Pearce, and Greg Cook. You have given me sound advice, kept me focused and on track, as well as providing me the resources and knowledge without which this thesis could not have come to be.

Churchill once said, “Give us the tools, and we will finish the job,” and in this regard, the OMCS team of Colin Johnston, Phil Holdway, Nicola Flanagan and Chris Salter as well as the DCCEM’s Jennifer Holter have become my own “arsenal of democracy”. Their training on, and careful maintenance of, the characterisation equipment made my work infinitely smoother.

I also wish to thank my friends, colleagues and fellow Begbroke inmates who have made this journey bearable. The dry wit of Shiling, hero worship of Justin, gossip from Kailing and Bianca as well as the further help from George, Ryan, Tongshan, Maya, Tara and Ping-Yuan has been first-rate, and I wish you all good luck in your own DPhils to come!

Similarly, to those that came before me: Ceren, Pierre, Pablo, Albert, Ruth, Koen and Toppy. Thank you for the guidance and help you showed to a new and naïve research student who now hopes he has, at least, passed some of your wisdom onto the next generation.

To my housemates Andrew, Andrew, Peter, Rand, Marius, Margie and Kathi. Thank you for tolerating my weird cooking habits, kitchen hammer and shower chicken. You were the best possible people to be in lockdown with and I was lucky to have found such wonderful people.

For my partners in crime; Eoin O’Sullivan and Dillon McGurty. You have endured this entire journey together with me from week one, supporting and caring for me as if I were family. I would not be here, finishing this DPhil, without your friendship and comradery and I shall not allow you to become strangers in the future.

Thank you also to my family: Mum, Dad and Michael (Parental Units 1&2 and Junior Unit 2). Your intelligence, resourcefulness and determination have made me the man I am today, and I hope that I have and will continue to make you proud.

Finally, for Stephanie Mellor. Thank you for your love and support while I’ve been away in Oxford. You have the patience of a saint, the intelligence of a true scientist and my admiration for life.

CONTENTS

Declaration i
Abstract ii
Acknowledgements iv
Contents v
List of Symbols and Abbreviations ix
List of Figures x
List of Tables xiii
List of Equations xiv

1 Introduction

1.1 Background to Research 1
1.2 Aims of Work 6
1.3 Structure of Thesis 6

2 Literature Review

2.1 Dispersion of Nanomaterials 9
2.1.1 Kinetic Separation 9
2.1.2 Adsorbed Solubilising Agents 10
2.1.3 Surface Functionalisation 11
2.1.4 Reductive Dissolution 12
2.2 Nanomaterial Functionalisation 13
2.2.1 Oxidation 13
2.2.1.1 Air Oxidation 13
2.2.1.2 Radical Hydroxylation 14
2.2.1.3 Acid Etching 15
2.2.2 Radical Reactions 16
2.3 Nanomaterial Films 19
2.3.1 Filter Deposition 20
2.3.2 Casting 20
2.3.3 Synthesis in Place 21
2.3.4 Electrophoretic Deposition (EPD) 22

3 Characterisation

3.1 Abstract 26
3.2 Scanning Electron Microscopy 27
3.3 Energy Dispersive X-Ray Spectroscopy 29

3.4 Raman Spectroscopy 30
3.5 Thermal Conductivity Measurements 32
3.6 X-Ray Photoelectron Spectroscopy 33
3.7 Thermogravimetric Analysis 37
3.8 Mechanical Tensile testing 38
3.9 Infrared Spectroscopy 39
3.10 Profilometry 40
3.10.1 Optical Profilometry 40
3.10.2 Mechanical Profilometry 41
3.11 X-Ray Diffraction 42
3.12 Ultraviolet-Visible Light Spectroscopy 44
3.13 Brunauer-Emmett-Teller Measurements 47
4 Reduced SWCNT for EPD
4.1 Abstract 48
4.2 Introduction 49
4.3 Experimental 51
4.3.1 Materials 51
4.3.2 Methods 51
4.4 Results and Discussion 55
4.4.1 Novel Method of Deposition 55
4.4.1.1 Washing Procedure 58
4.4.2 Free Standing Film Macro Properties 61
4.4.2.1 Mechanical Strength 61
4.4.2.2 Electrical Conductivity of Films 64
4.4.2.3 Sub-optimal Macro Property Explanation 66
4.4.3 Film Nano-Structure 69
4.4.3.1 Raman Analysis 70
4.4.3.2 XPS Analysis 71
4.4.3.3 TGA Analysis 73
4.4.4 Mechanism of Deposition 73
4.4.4.1 Deposition Rate 74
4.4.4.2 Concentration of CNT Solution 75
4.4.4.3 Field Strength Variation 77
4.4.4.4 Explanation of Current-Time Result 79
4.4.4.5 Error Check: Solvent and Reducing Agent 80
4.5 Summary and Conclusions 81

5 Reduced BNNT for EPD

5.1 Abstract 82
5.2 Introduction 83
5.3 Experimental 85
5.3.1 Chemicals 85
5.3.2 Methods 85
5.4 Results and Discussion 87
5.4.1 Starting materials 87
5.4.2 Charging of BNNT 89
5.4.2.1 UV-Vis Spectroscopy Analysis 89
5.4.2.2 Bromide Substitution 91
5.4.3 BNNT Film 95
5.4.4 Nanostructure retention 97
5.4.4.1 Raman 97
5.4.4.2 XPS 98
5.4.4.3 Thermogravimetric Analysis 102
5.4.5 Mechanism 103
5.4.5.1 Time vs Deposition 104
5.4.5.2 CNT Concentration vs Deposition Rate 105
5.4.5.3 Current/Time Graphs 107
5.5 Summary and Conclusions 109

6 Acid Oxidation of BNP

6.1 Abstract 110
6.2 Introduction 111
6.3 Experimental 113
6.3.1 Chemicals 113
6.3.2 Methods 113
6.4 Results and Discussion 116
6.4.1 Chemical Etching of BNP Experimental Theory 116
6.4.1.1 IR Analysis 117
6.4.1.2 Raman Analysis 121
6.4.1.3 XPS Analysis 123
6.4.1.4 EDS Analysis of Oxygen Distribution 125
6.4.1.5 SEM Analysis of BNP Size Distribution 127
6.4.2 Kinetic Cleavage Assisted Etching 128

6.4.2.1 FTIR Analysis 130
6.4.2.2 Raman Analysis of Nanostructure 132
6.4.2.3 XPS Analysis 132
6.4.2.4 SEM Analysis 134
6.4.2.5 Surface Area Analysis 138
6.4.2.6 XRD Confirmation of Crystallite Purity 139
6.5 Summary and Conclusions 141
7 Exfoliation and Dispersion of BNP
7.1 Abstract 142
7.2 Introduction 143
7.3 Experimental 145
7.3.1 Chemicals 145
7.3.2 Methods 146
7.4 Results and Discussion 148
7.4.1 Exfoliation of BNP 148
7.4.1.1 Acid Etching of Exfoliated Material 153
7.4.2 Solvation of BNP Samples 155
7.4.2.1 EPD of Solvated BNP Samples 157
7.4.2.2 Issues 161
7.4.2.3 EPD of electrochemically reduced BNP 163
7.5 Summary and Conclusions 169
8 Summary and Conclusions
8.1 Reductive Dispersion of CNT can be applied successfully to EPD 171
8.2 Reductive dispersion for EPD can be applied to BNNT 172
8.3 BNP are inert to acid oxidation 172
8.4 Dispersions of BNP are applicable to EPD 173
9 Future Work
9.1 Reductive Dispersions for EPD of Doped Nanotubes 175
9.2 Impure hBN as Sources for Oxidation Reactivity: BNF 178
10 Bibliography 182
11 Appendix 196

List of Symbols and Abbreviations

Common Abbreviations in Work:

hBN	Hexagonal Boron Nitride
CNT	Carbon Nanotubes
O-CNT	Oxidised CNT
SWCNT	Single walled CNT
EPD	Electrophoretic Deposition
BNNT	Boron Nitride Nanotubes
BNP	Boron Nitride Platelets
BNF	Boron Nitride Fibers
O-BNP	Oxidised BNP
NaNap	Sodium Naphthalide
GO	Graphene Oxide
IPA	Iso-Propenyl Alcohol
EtOH	Ethanol
MeOH	Methanol
DMAc	Di-Methyl Acetamide
H_2SO_4	Sulphuric Acid
HNO_3	Nitric Acid
HCl	Hydrochloric Acid
COOH	Carboxyl Group functionality
OH	Hydroxyl Group functionality
PTFE	Polytetrafluoroethylene
SEM	Scanning Electron Microscopy
EDS	Energy Dispersive X-Rat Spectroscopy
XPS	X-Ray Photoelectron Spectroscopy
TGA	Thermogravimetric Analysis
IR	Infra-Red spectroscopy
FTIR	Fourier-Transform Infra-Red Spectroscopy
UV-Vis	Ultra-Violet/Visible light Spectroscopy
BET	Brunauer-Emmett-Teller surface area measurements
Neat	Consisting of one material

Units

s	Seconds
m	Meters
V	Volts
eV	Electron Volts
A	Ampere
S	Siemens
g	Grams
Pa	Pascals
L	Litres
Å	Angstrom
C	Coulombs
°C	Degrees Celsius
h	Hours
min	Minutes
Hz	Hertz

Unit Prefixes

n	nano-	10^{-9}
µ	micro-	10^{-6}
m	milli-	10^{-3}
c	centi-	10^{-2}
k	kilo	10^{3}
M	mega-	10^{6}
G	Giga-	10^{9}
T	Tera-	10^{12}

LIST OF FIGURES

Figure	Figure Description	Page
1.1.	Visual representation of flattened CNT.	2
1.2.	hBN atomic structure diagram.	3
2.1.	An illustrative potential window diagram for common solvents.	12
2.2.	Reported two step hydroxylation of the hBN surface.	14
2.3.	Proposed reaction scheme of nitric acid with hBN.	15
2.4.	Schematic showing the breadth of potential carbon nanotubide reactions.	17
2.5.	Proposed mechanism by which a charged nanotubide reacts with an R-X reagent.	18
2.6.	Scheme illustrating the reaction of Br-Hex with reduced BNNT.	19
2.7.	Diagram of a generalised spin coating technique.	21
2.8.	Simplified EPD diagram.	22
2.9.	Interaction energy of charged nanoparticles at varying interparticle distances.	24
3.1.	Diagrams of an electron microscope.	27
3.2.	SEM Images showing the damage inflicted upon an M.2B precursor fiber.	28
3.3.	Example platelet diameter analysis.	29
3.4.	Jablonski diagram of the Raman process.	31
3.5.	Characterisation by XPS graphs.	35
3.6.	Example optical profilometry analysis.	41
3.7.	Examples of mechanical profilometry analysis.	42
3.8.	Example XRD analysis of BNF.	44
3.9.	UV-Vis Data Processing Graphs.	46
4.1.	SEM of SWCNT Tubal™ starting material.	55
4.2.	A flow diagram illustrating the novel process by which CNT films are created.	56
4.3.	Image taken of four different anode materials successfully used to deposit CNT films.	57
4.4.	SEM images of the surface of the CNT film taken before [A] and after [B] the washing procedure was carried out.	59
4.5.	The profilometry results taken from a thin film before and after washing procedure.	60
4.6.	Images showing an example free-standing CNT film produced.	60
4.7.	Image showing a demonstration of the flexibility of produced free standing films.	61
4.8.	SEM images of CNT film fracture surfaces.	63
4.9.	Chart showing the sheet conductivities for CNT films.	64
4.10.	SEM of CNT film cross sections demonstrating differences in macro-structure.	66
4.11.	Microscopy of unwashed CNT film cross section.	67

4.12.	Microscopy of washed CNT film cross section.	68
4.13.	Raman results comparing the CNT starting material, reduced film and oxidised film.	70
4.14.	XPS analysis showing CNT retention of nanostructure after film production compared to traditional oxidation methods.	72
4.15.	Thermogravimetric analysis of CNT samples.	73
4.16.	The thickness of films produced both before and after washing is plotted against the time taken for EPD.	74
4.17.	The thickness of films produced in different concentrations.	76
4.18.	The relationship of varying potential difference between the electrodes during a 120 second EPD on 1 mgCNT mL-1 solution and the final film thickness.	77
4.19.	Total charge transfer for a deposition is calculated and shown to be directly proportional to the final film thickness.	78
4.20.	The theoretical chronology of deposition is explained through the analysis of a typical current/time curve recorded during EPD.	79
4.21.	Current/Time graph of electrodes held at 10 V immersed CNT dispersions.	80
5.1.	Images of BNNT starting materials.	87
5.2.	Image showing the dispersion/charging samples lined up in increasing NaNap concentration as indicated by increasing green colouration.	89
5.3.	Results of UV-Vis analysis of the variously charged BNNT.	90
5.4.	Schematic of proposed BNNT/BrHex reaction.	91
5.5.	XPS and TGA analysis of Br-Hex reaction with ‘charged’ BNNT.	93
5.6.	Normalised IR spectra of BNNT immersed in DMAc and reduced BNNT reacted with 1-bromo-hexane (BNNT-Hex).	94
5.7.	Images of BNNT films.	95
5.8.	SEM of BNNT film cross section.	96
5.9.	Raman spectra of BNNT starting material compared to BNNT films created during the concentration and time variance experiments.	98
5.10.	B1s XPS analysis of BNNT films produced by reduced dispersion method.	99
5.11.	C1s XPS analysis of BNNT films produced by reduced dispersion method.	100
5.12.	Summary of BNNT film sample atomic breakdowns as measured by XPS.	102
5.13.	Thermo-gravimetric data comparing the BNNT starting material and films produced using the reduced dispersion EPD method.	103
5.14.	Results of varying the time of EPD.	104
5.15.	Results of varying the BNNT concentration of EPD dispersion.	106
5.16.	Current/Time curve measurements taken during the EPD of differently timed film production and varying BNNT concentrations.	107
6.1.	Schematic diagram of acid-BNP reaction overlaid onto a table showing an overview of the scope of this experimentation.	116
6.2.	Example IR analysis of hBN.	118
6.3.	Relevant IR spectra of BNP samples taken using KBr plating method.	119
6.4.	Collated Raman spectra focussing on the B-N indicating peak at 1364 cm^{-1}.	121

6.5.	Secondary analysis of the BN E2g Raman peak around 1364 cm^{-1}.	122
6.6.	Results from the XPS analysis of acid etched BNP samples.	124
6.7.	EDS elemental maps of BNP samples chemically etched by the nitrating solution.	126
6.8.	Example SEM images of BNP samples.	128
6.9.	Schematic Diagram showing the proposed method of action for the cleavage and subsequent etching of the BNP.	129
6.10.	IR spectra comparing the blank BNP samples to those sonicated in nitrating solution (H2SO4/HNO3) for 18 and 28 hours.	131
6.11.	The hBN E2g peak from the Raman spectra of the 28h sonicated samples are compared to the sonicated blank samples.	132
6.12.	Results summaries for XPS characterisation of sonicated BNP samples.	133
6.13.	Example SEM images from a selection taken of each of the 003 BNP samples drop cast onto Si.	135
6.14.	Example EDS images of the 003 18 hour acid sonication sample.	136
6.15.	Example EDS images of the 015 18 hour acid sonication sample.	137
6.16.	Surface area measurements from BET analysis of BNP samples.	138
6.17.	XRD graphs of sonication cleaved BNP samples.	139
7.1.	Schematic showing the proposed steps of hBN exfoliation and oxidation.	148
7.2.	Example UV-Vis absorbance spectra for the supernatant (1/8 diluted) of the IPA suspended 003 BNP that has been exfoliated by three different methods.	149
7.3.	SEM images showing the BNP starting material compared to platelets exfoliated in this work.	150
7.4.	Example EDS map of bath sonication exfoliated BNP.	152
7.5.	Comparison of IR spectra for the exfoliated and acid etched exfoliated materials.	153
7.6.	XPS of acid etched exfoliated samples.	154
7.7.	Summary of BNP sample dispersion experiments.	156
7.8.	Electrophoretic deposition (EPD) of DMAc dispersed ‘oxidised BNP’ samples.	158
7.9.	EDS of deposited BNP samples.	160
7.10.	Issues with the EPD of DMAc dispersed BNP.	162
7.11.	Schematic diagram for the reduced BNP EPD process.	163
7.12.	Optical profilometry of reduced dispersion BNP EPD depositing electrodes.	165
7.13.	SEM with overlaid EDS atomic map [A] of the Na crystal found on the clear surface of the depositing electrode from reduced BNP dispersion EPD.	166
7.14.	XPS of reduced dispersion BNP EPD 1200s sample compared to starting material.	167
9.1.	Analysis of B-doped CNT reductive dispersion EPD.	177
9.2.	Summary of production of BN Fibers (BNF).	179
9.3.	Summary of investigations into BNF.	180

LIST OF TABLES

Table	Table Description	Page
1.1.	Table of a selection of nanomaterial properties	4
3.1.	Table of common elemental X-Ray photon emission energies from principal electron shells (in eV)	29
4.1.	Materials used in chapter 4. as well as the supplier product numbers	51
4.2.	Table of mechanical properties of free-standing films	62
5.1.	Materials used in chapter 5 as well as the supplier product numbers	85
6.1.	Materials used in chapter 6 as well as the supplier product numbers	113
7.1.	Materials used in chapter 7 as well as the supplier product numbers	142
7.2.	Table of Hansen Solubility Parameters (HSP) for solvents used for the dispersion of BNP samples	156

LIST OF EQUATIONS

Designation	Equation	Page
Eq. 2.1.	$m = \mu \times C_s \times S \times E \times t$	23
Eq. 3.1.	$\Delta\omega\ (cm^{-1}) = \left(\frac{1}{\lambda_0(nm)} - \frac{1}{\lambda_1(nm)}\right) \times \frac{10^7(nm)}{(cm)}$	31
Eq. 3.2.	$Electron\ Binding\ Energy = hf - E_k$	33
Eq. 3.3.	$\sigma_e = \frac{F}{CSA_0}$	38
Eq. 3.4.	$\varepsilon_e = \frac{\delta}{L_0}$	38
Eq. 3.5.	$2\ d\ sin\ \theta = n$	42
Eq. 3.6.	$D = \frac{\kappa\ \lambda}{\beta\ cos\ \theta}$	43
Eq. 3.7.	$\sigma_D = \frac{\kappa\ \lambda}{\beta\ cos(\theta)} \sqrt{\frac{{\sigma_\beta}^2}{\beta^2} + \frac{sin^2(\theta)\ {\sigma_\theta}^2}{cos^2(\theta)}}$	44
Eq. 3.8.	$c = \frac{A}{\varepsilon\ l}$	45
Eq. 6.1.	$\langle E_{Peeling} \rangle = a \times \langle E_{Tearing} \rangle$	129
Eq. 6.2.	$\gamma_{min} = \frac{[\sqrt{E_{S,G}} - \sqrt{E_{S,L}}]^2}{\eta L}$	135
Eq. 7.1.	$Rate\ of\ Sedimentation \propto \frac{r^4\ \Delta\rho\ g}{k_B\ T}$	148

1 INTRODUCTION

1.1 BACKGROUND TO RESEARCH

The nanomaterial graphene[1] is comprised of a single 2D layer of hexagonally bonded, sp^2 hybridised, carbon atoms which stack on top of each other in an ABA Bernal stacking to form graphite.[2] The sp^2 hybridised carbon atoms in graphitic materials all contain a delocalised electron in their pi orbitals which are free to move across the entirety of the materials plane thereby making them electrically conductive.[3] Officially assigned in 1991[4] as 'helical micotubles' of graphitic carbon, carbon nanotubes (CNTs) have the structure of a rolled-up graphene sheet, seamlessly connected along the axis of a long tube capped at both ends by fullerene hemispheres of equal radii to the cylindrical tube. The angle at which this hypothetical graphene sheet is wrapped to create a seamless cylinder is designated by the terms (n,m) which describe zig-zag (n,0), armchair (n, m=n) and chiral (all other values) CNT structures (Figure 1.1)[5], the latter have been found to form tubes of lower thermal[6] and electrical[7] conductance.

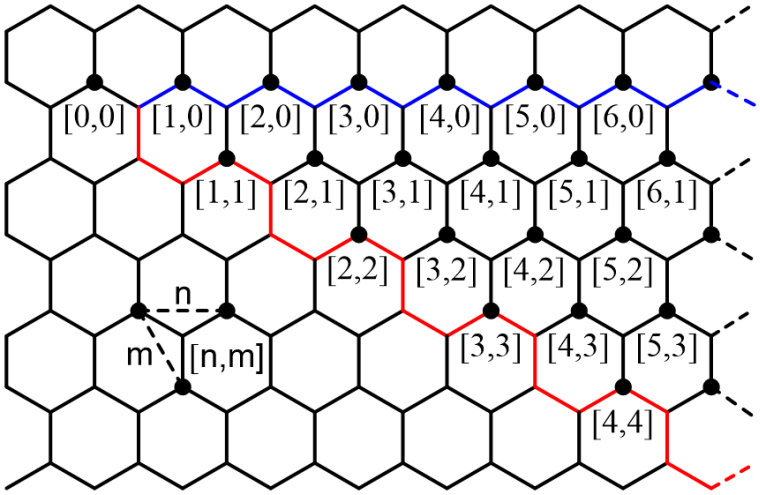


Figure 1.1 Visual representation of flattened CNT. Chirality is designated by which point on the sheet when rolled meets with the point [0,0] so that the vector between them makes the circumference of the formed tube. Chair (red) and Zig-zag (blue) chirality's are highlighted.

Image credit: J Ballentine *et al.*[5]

Boron and nitrogen atoms when bonded exclusively to the other element have the same valence structure as pure carbon and so share many of the structures and properties of these carbon allotropes, but, due to the partially ionic nature of the B-N bond, are electrically insulating.[8] Boron nitride can be found in four distinct forms: amorphous (aBN), wurtzite (wBN), cubic (cBN) and hexagonal (hBN). As its name suggests, amorphous BN lacks any long-distance atomic structure or organisation, but has been proposed for use in electronic applications[9] due to its reportedly high breakdown voltage.[10] Wurtzite BN has a distorted tetrahedron structure and is the only form of boron nitride found naturally, while cubic BN (also designated β-BN) is analogous in structure to diamond in which each constituent atom is held by four covalent bonds. Due to its similarity in structure and properties,[11] cBN is used in similar roles as diamond industrially[12] and, like its carbon twin, is less thermodynamically stable than its hexagonal form.

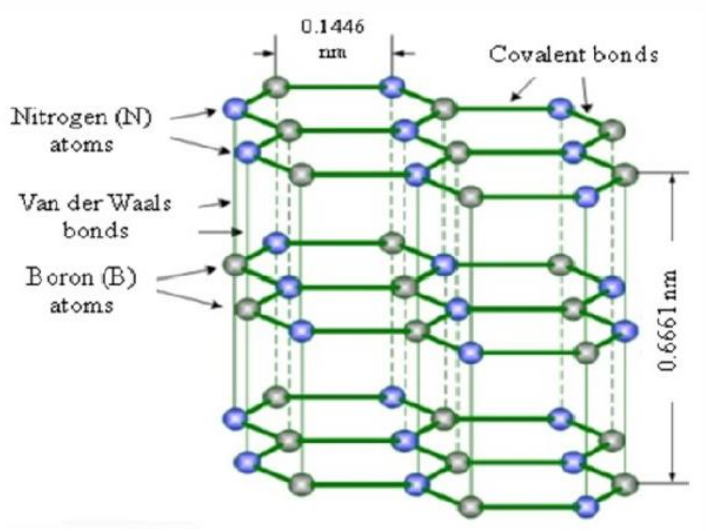


Figure 1.2 hBN atomic structure diagram showing three layers of hexagonally bonded BN stacked on top of each other with alternate atoms eclipsing each other. This alternate stacking causes the stabilisation of individual atoms and increases the energy of delamination.

Image credit: R. Dahal *et al.*[13]

Hexagonal boron nitride (hBN) consists of layers of planar, tri-bonded 2D BN sheets held together by van der Waals forces and is often compared to graphite (even being referred to by some as 'white graphite'). However, it differs from the carbon allotrope as the atoms of different hBN layers fully eclipse one another with nitrogen atoms directly above and below boron constituents of adjacent sheets and vice-versa (Figure 1.2).[13] This eclipsed stacking stabilises individual atoms within the material and increases the energy required to exfoliate individual layers from the bulk material. Theorised after the discovery of CNT[14] and proven practically soon after,[15] hBN can also take the form of nanotubes (BNNT) which again have the same nanostructure as their carbon-based CNT equivalents and therefore exhibit many of the same properties but are electrically insulating.

The extraordinary properties of these nanomaterials are the reason for the interest in their potential uses. Table 1.1 gives a brief overview of their physical properties. This shows that the physical strength and thermal conductance of both bulk hBN and BNNT are very similar to that of their carbon equivalents, while also being distinct from each other. This is partially because nanotube property

estimates are derived from theoretical calculations and the bulk material properties are experimentally determined. The scale of these values is due to the strong covalently bonded nanostructure of the materials allowing stresses as well as thermal inputs to be spread across their entire in-plane length. The out-of-plane conductance and strength compared to the in-plane of the bulk 2D materials is less impressive but the small shear forces required to force stacked graphene/hBN sheets to slip past each other is advantageous for use as dry lubricants, because of their subsequent low coefficients of friction (0.08-0.18 for graphite[16] and 0.7 for hBN).[17]

Material Property	**hBN** [18]	**Graphite** [19]	**BNNT**	**CNT**	**Graphene**
Youngs Modulus	36.5 GPa	27.6 GPa	1.22 ±0.24 TPa[20]	~ 1 TPa [21]	0.95 to 1.1 TPa [22]
Thermal conductivity (W m^{-1} K^{-1})	600 in plane, 30 out of plane	114 (plane not stated)	~ 2400 [23]	2000-6000 [24]	4840-5300 [25]
Band gap (eV)	5.2 (insulating)	Conducting	5.5 (insulating independent of chirality)[8]	Dependant on chirality	Conducting

Table 1.1. Table of a selection of material properties. Note that many of these numbers are from theoretical calculations and therefore may not be replicable in experimentation.

The chemical stability of these structures is also impressive compared to most organic polymers (eg PTFE degrades at 508 °C)[26] and carbon materials oxidise in air (to form CO_2) at relatively high temperatures with graphene oxide (GO, 558–616 °C), graphene (659–713 °C), graphite (841–949 °C)[27] and CNT (~800 °C)[28] all burning at different points. hBN materials are even more resistant to heat and decompose into boron oxide (B_2O_3), causing samples to increase in mass (by about ~33%)[28] when the temperature rises to 1000 °C.[29] This increases further to 2500 °C in oxygen free environments although this is dependent on the nitrogen content of the decomposition environment and is lower at low pressure.[30]

As could be noted from the increasing temperature of degradation for increasingly multi-layered nanostructures, the relative reactivity of these nanomaterials decreases with the addition of more

layers.[27] Not only do these layers sterically hinder chemical attack of lower layers, but they also donate and accept electron density, stabilising the layers surrounding them.[31] This is more pronounced for the polar B-N bonded materials where the eclipse stacking of the hBN layers places oppositely polarised atoms adjacent to each other, allowing more stabilisation and increasing the energy barrier to reaction.

Due to these properties, carbon and BN nanomaterials have seen a massive surge in research interest (graphene being the most published topic in materials since 2010),[32] with CNT alone seeing proposed uses across the fields of medicine,[33] electronics,[34] optics[35] and composites[36] while hBN already has industrial applications from the makeup industry[37] to aerospace.[38]

A subset of this work has focused on the production of films (both free standing and as coatings) made from these nanomaterials and research into their applications, with CNT based materials being proposed for uses in aeronautical composites,[39] catalyst supports,[40] sensors,[41] biofuel cells[42] and electrodes.[43] hBN based films are less studied but have still generated interest for antibacterial applications,[44] corrosion resistant coatings[45] and thermally conductive composites.[46]

Many of the production methods for these films rely on the functionalisation and/or damage of their constituent nanomaterials or require the addition of various other reagents which make the final product impure. This traditionally takes the form of the nanomaterial being oxidised in acid [47,48] to produce a hydroxylated product more favourable to dispersion in solvent which can then be deposited into a film. The damage to the materials' nanostructure that this oxidation causes, as well as the loss of yield from over-oxidation and post reaction purifications is problematic for applications where specific or expensive nanomaterial films are required (eg. a specific nanotube chirality). Additionally, reliable methods of solution based hBN oxidation have not yet been established within the field, so investigations into this must also be conducted to improve our understanding of these systems.

1.2 Aims of Work

This body of work will aim to improve upon the current state of nanomaterial film production. This will be achieved by:

1. Developing a method that will create a pure nano-material film from CNT and hBN without the need for damaging chemical functionalisation or complicating additives.
2. Comparing these films to those made by the traditional acid oxidation route to verify the validity of this novel production method.
3. Establishing an hBN acid oxidation procedure by applying the traditionally used methods of CNT hydroxylation used in film production.

1.3 Structure of Thesis

1.3.1 Literature Review

The first chapter will summarise current literature covering the functionalisation, dispersion and deposition of hBN and CNT nanomaterials which is required to understand, and put into context, the work undertaken and presented in the subsequent chapters. Current dispersion methodologies will be introduced and evaluated, with reductive dissolution shown to have advantages over traditional oxidative functionalisation methods. The numerous approaches through which this can be achieved that will then also be introduced. Finally, the various methods to produce nanomaterial films will be described, with an emphasis on the theory of EPD.

1.3.2 Characterisation

Following the introduction of the scientific background to the experiments in this thesis, the theory and methodology used to characterise the resulting samples are described. Characterisation theory, sample preparation, data collection and its subsequent manipulation are presented for SEM, EDS, Raman, Thermal conductivity, XPS, TGA, IR, profilometry, XRD, UV-Vis and BET.

1.3.3 Electrochemically Reduced SWCNT for EPD

The first experimental chapter of this thesis presents a novel and superior method of SWCNT film preparation by conducting electrophoretic deposition (EPD) on negatively charged CNT dispersions. The mechanical strength and electrical conductivities of these films are shown to be comparable to traditionally produced oxidised dispersions but are completed using less time, lower field strengths and with higher yields. Additionally, it will be shown that this method produces a pure product with no nano-structural damage compared to the starting material.

1.3.4 Reduced h-BN Dispersion and EPD

The reduced dispersion for the EPD method developed in the previous chapter is successfully applied to hBN nanotubes. The BNNT starting materials are introduced and characterised and then shown to not charge and disperse to the same degree of their CNT equivalents. Because of this this, films produced by EPD are shown to have lower deposition rates but maintain the nanostructure of their starting material. However, to compare these results to the traditional oxidation-based dispersions, a simple hBN oxidation procedure is found to be required.

1.3.5 Acid Oxidation of BNP

This chapter describes a series of solution-based acid etching experiments that attempt to modify/functionalise 2D hBN platelets (BNP), which were used in the place of the less abundant and more expensive BNNT. Initially, acid mixtures alone are used to try to oxidise the hBN surface, but it is shown that these are ineffective despite their wide use in carbon nano-chemistry. Similar experiments, whereby the BNP are kinetically cleaved by sonication in the presence of these oxidising agents, are also shown to be ineffective at producing hydroxylated hBN.

1.3.6 Dispersion of BNP

The final chapter details attempts to exfoliate BNP into solution and conduct EPD on the resulting dispersions. Bath sonication is experimentally determined to be the most efficient benchtop method for BNP dispersion. The resulting suspensions are then used for further acid etching experimentation

that show no significant oxidative functionalisation. All previous BNP acid oxidised samples from chapters 6 and 7 are then dispersed into various solvents and the concentrations of these suspensions used as the final evidence for the inert nature of hBN to the solution-based oxidation reactions. EPD of these same suspensions is shown to be possible, but inefficient compared to the reduced dispersion for the EPD method developed in chapters 4 and 5, which is also applied to the BNP. This shows significantly increased deposition rates but also forms an uneven and mechanically weak hBN film due to the morphology of the BNP starting material.

1.3.7 Conclusions and Future Work

The conclusions drawn from the work conducted for this thesis will be summarised for each experimental chapter. Future work will then be suggested based on preliminary studies that have already been completed in conjunction with the work thus far. Recommendations include the use heteroatom doped nanotubes as a feedstock for the reduced dispersion for EPD method and boron nitride nanofibers (BNF) as a potentially more reactive form of hBN for functionalisation experiments.

2 LITERATURE REVIEW

2.1 DISPERSION OF NANOMATERIALS

An important initial step for the use of nanomaterials in many applications is their dispersion into solution. This allows homogenous mixing with other materials or reagents for even coatings of functionalised additions. The surfaces of boron nitride and carbon nanomaterials do not interact favourably with many solvents and prefer to agglomerate together due to strong inter-nanomaterial Van der Waals forces (16.36 meV $Å^{-2}$ and 95.16 meV $Å^{-1}$ for graphene-graphene and CNT-CNT interactions respectively).[49] Experimentally derived Hansen solubility parameters[50] for hBN (17-19 δD, 4-10 δP, 4-10 δH)[51] and fullerenes (19.7 δD, 2.9 δP, 2.7 δH)[52] re-iterate this problem as very few room temperature liquids (especially common polar protic solvents such as water) exist within the same region of Hansen space. Overcoming these issues has led to a diverse range of tactics being proposed, these methods can be broaldy categoraised into three main approaches: kinetic separation, adsorbed solubilising agents and surface functionalisation. The most recent addition to these methods is the use of charge to reductively disperse materials.

2.1.1 Kinetic Separation

The use of sonication, or shear mixing, has commonly been used to physically separate and individualise nanomaterials, thereby pushing them into a suspension. hBN materials have been reported to produce dispersions in water (0.26–0.32 mg mL^{-1}), DMF (0.34–0.52 mg mL^{-1})[53] and IPA (0.04[54] - 0.06[55] mg mL^{-1}) using sonication alone, while SWCNT have shown similar concentrations in DMF (0.022 mg mL^{-1}).[56] Dumée *et al.*[57] showed that it is possible to increase the efficiency of these dispersing processes by conducting them at lower temperatures (-17 °C in IPA) as this reduces the Van de Waals forces holding the nanomaterials together and may also increase the viscosity of the solvent thereby slowing re-agglomeration.

However, the large forces imposed on the nanomaterials during sonication can be damaging to the dispersed materials' nanostructure and results in the reduction of the aspect ratios of nanotubes.[58] Lee *et al.*[59] showed that sonication of BNNT for as little as 5h can cut the average length of tubes by 50%, and past 20h they are reduced to 10% of their original length. 2D materials have also been observed to reduce in size, with studies using graphene[60] and BN sheets[61] reporting significant reduction in platelet dimensions after sonication. This damage can also lead to covalent bond formation, as observed by Yang *et al.*[62] who produced functionalised (carbonyl, alcohol and carboxylic) MWCNT containing 2% oxygen after sonication in water alone. This has already been purposefully applied to hBN materials[63], but it should be noted that the damage caused by sonication leads to higher nanomaterial surface areas and therefore an increased adsorbed atmospheric oxygen/solvent concentration could also be responsible for these results.

Following the initial dispersion by sonication, many materials will begin to re-agglomerate. This re-bundling process can be slowed by using viscous solvents/polymer melts to kinetically trap dispersed CNTs.[64] More commonly however, chemical stabilising agents are added to the solution to form a thermodynamically stable suspension.

2.1.2 Adsorbed Solubilising Agents

The most common reversable adsorbed stabilising agents added to nanomaterial dispersions are surfactants. The amphiphilic structure of these species allows one side of the molecule to adsorb to the non-polar nanomaterial surface while presenting the other (usually hydrophilic) side to the solvent where is has more favourable interactions and thereby stabilises the system. Common (anionic) surfactants used in conjunction with polar protic solvents are SDS (sodium dodecyl sulphate), triton X-100 (achieving up to 20 mg_{CNT} mL^{-1})[65] and SDBS (160 mg_{CNT} mL^{-1})[66]. These dispersions are created with a significant loss of initial starting material that does not become dispersed, with some studies (for hBN) showing this yield as little as 2-3%.[67] Work by Terao *et al.*[68] uses catechin to illustrate that molecules with non-traditional amphiphilic structures can also be used as stabilising agents, with the

molecular additive containing both aromatic carbon rings that adsorb to BNNT (though Pi-Pi interactions) and hydroxyl groups that interact with the surrounding environment.

Another approach to dispersion stabilisation through adsorbed additives is by polymer wrapping. When in solution, a rigid nanotube/platelet will find itself wrapped/entangled by a large, flexible polymer. When entangled, the surface chemistry of the nanoparticle is effectively that of the polymer and so can be solubilised. C. Zhi *et al.*[69] have demonstrated this by using poly[m-phenylenevinylene-co-(2,5-dioctoxyp-phenylenevinylene)] (PmPV) to fully dissolve BNNTs with dimensions of up to 50 nm by 10 μm. It should be noted however that, due to the sonication process used to individualise the nanotubes before wrapping, these dimensions are likely an over-estimate.

Adsorbed molecules on the surface of these nanomaterials can also be a drawback as they may hinder subsequent functionalisation reactions as well as negatively affecting the electronic and material properties of finished composites.[70] Additionally, the previously mentioned SBDS study[66] showed that oxidised CNT (0.509 mmol/g -COOH and 0.199 mmol/g -OH) can be dispersed at greater yields than with surfactant alone, demonstrating that covalent functionalisation of nanomaterials can be more effective for dispersion.

2.1.3 Surface Functionalisation

As the main issue to overcome when forming stable BNP dispersions is poor solvent-nanomaterial interactions, the most direct way to address this is to chemically modify the materials' surface. This is most commonly achieved using strong acids to oxidise nanomaterial surface, thereby improving the interaction between the now hydroxylated surface and polar protic solvents to create high concentration, stable suspensions.[48]

The various methods used to achieve these effects are explored further in section 2.2 where the different techniques of functionalisation are compared and evaluated in greater depth.

2.1.4 Reductive Dissolution

For CNT, reducing a nanotube by potentiostatic or chemical methods increases its Fermi energy level and results in an overall negative charge across its structure.[71] The mutual coulombic repulsion between the introduced negative charges along individual nanotubes causes the spontaneous exfoliation of the material into solution where it forms a stable dispersion. Shorter, defective CNTs and amorphous graphitic impurities have been shown to diffuse into solution preferentially to higher quality, undamaged CNT and so reductive dissolution also has uses as a purification method.[72] Pénicaud *et al.*[73] used lithium metal and THF to charge CNT and successfully dispersed them in a variety of polar aprotic solvents (NMF, DMF & NMP), achieving concentrations of 2.0 $mg_{CNT}\ g_{DMSO}^{-1}$ in DMSO and 4.2 $mg_{CNT}\ g_{sulfolane}^{-1}$ in sulfolane. Voiry *et al.* [74] showed that it is valid to model the charged nanotubide as polyelectrolytes and predicted that solutions could reach hypothetical concentrations of 10 mg mL^{-1} but experimentally saturated at 4–5 mg mL^{-1}. Reductive dissolution has been further refined by Clancy *et al.*[75] who used sodium naphthalide (in a DMAc solvent) as an intermediate charging agent allowing the dispersion to occur in a single vessel and achieves concentrations up to 2.8 mg mL^{-1}.

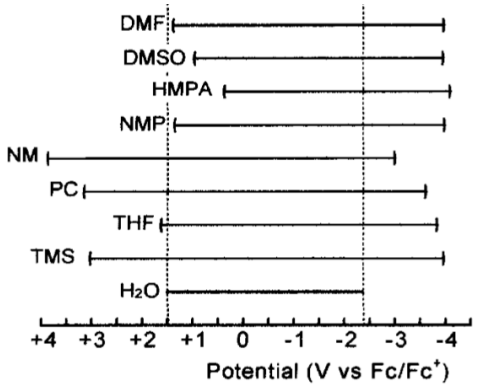


Figure 2.1. An illustrative potential window diagram for common solvents. Note that although this figure indicates at what reduction/oxidation potential a solvent will begin to break down, it does not give information about the rate at which this breakdown will occur.

Image credit: Izutsu *et al.*[77]

The naphthalide anion used in this latter method is thought to have a reduction potential of *ca.* -3.0 V

(measured against standard hydrogen electrode)[76] and so is capable of reducing many reagents (eg. DMSO and DMF) which limits the range of solvents that can be used to those that have a suitably low reduction potential.[77] Solvent candidates can be selected by consulting the potential window of a solvent (Figure 2.1) but this does not consider the kinetics and rate of reaction for the reduction process, so systems first identified by this criteria must still be experimentally determined where it has been found that THF and DMAc are both appropriate solvent selections.

2.2 NANOMATERIAL FUNCTIONALISATION

Due to their nature, the functionalisation of nanomaterials is often required before they can disperse within, or bind to, other mediums. However, the majority of chemical modifications to a materials' surface are predicated on defect site creation which disrupts the nanostructure of the starting material. It should therefore be noted throughout this section that an increase in the functionalisation of any given nanomaterial will be proportional to a decrease in that nanomaterial's innate properties (strength, conductance, etc.).

2.2.1 Oxidation

2.2.1.1 Air Oxidation

As previously explored (Section 1.1), both carbon and BN nanomaterials degrade at high temperatures in the presence of atmospheric oxygen which, when conducted in a controlled manner, can lead to partially oxidised products. Cui *et al.*[78] reported that oxygen intercalates between the h-BN layers when heated at 1000°C so that, when the resulting material is mixed with water, it hydrolyses and exfoliates into a stable suspension of individualised nanoparticles. Chensha *et al.*[79] also took this approach to create oxidised CNT for capacitor applications, finding that tubes heated to 650 °C (for 20 min) doubled the materials' capacitance to 48 F g^{-1}. However, this came at a significant structural cost, as the nanostructure (especially the end caps) of the CNT was significantly damaged and the high

temperatures required, and concomitant energy costs, mean the process is not economically viable for many industrial applications.

2.2.1.2 Radical Hydroxylation

A more niche method of oxidation was introduced by T. Sainbury *et al.*[80] who showed that BN nanosheets can be covalently hydroxylated via a two-step radical reaction with di-T-butyl peroxide (Figure 2.2). The peroxide bond degrades under high temperatures to form two oxygen radicals which then covalently bond to a boron atom on the h-BN surface. The ^{t}Bu group is then removed with hydrogen peroxide and acid to leave a B-OH functionality. This method requires significant amounts of expensive reagents and is overly complicated compared to air oxidation and acid etching, so would only be appropriate for small scale reactions where precise control over the extent of hydroxylation is required.

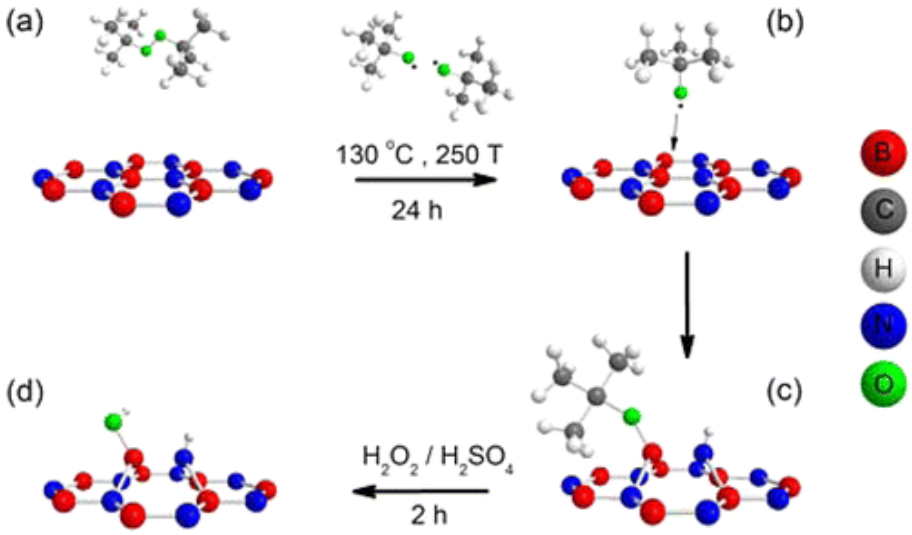


Figure 2.2. Reported two step hydroxylation of the hBN surface. (a) Starting reagents of BNNS and di-T-butyl peroxide. (b) O-^{t}Bu radical formation and attack on B site. (c) B-O-^{t}Bu structure. (d) Final hydroxylated product after the butyl group has been removed by acid and peroxide.

Image Credit: T. Sainbury *et al.*[80]

Taking advantage of a similar radical based methodology, but suffering from similar drawbacks, C. Zhi *et al.*[81] achieved hydroxylation on boron sites of BNNT with pure hydrogen peroxide in an autoclave at 120 °C. The extent of functionalisation was confirmed by the reaction product being soluble in water

up to 250 mg L^{-1} and these hydroxyl groups were used to perform a further esterification reaction with a carboxylic acid to form B-CO_2R

2.2.1.3 Acid Etching

The most widely used methods of oxidation use strong acids and extreme conditions to break the materials' nanostructure and insert carboxylic acid and hydroxyl functionalities into its surface. Work by Rosca *et al.*[82] typifies this approach and uses a high temperature (120 °C) and high concentration nitric acid solution over long periods of time (24-48 h) to successfully oxidise MWCNT. This was evidenced by the products' increased solubility (20-50 mg mL^{-1}) but also led to low yields because large amounts of the original sample were destroyed (60-90% loss). Ciofani *et al.*[83] applied this nitric acid approach to BNNT and produced anchoring hydroxyl functionality (Figure 2.3) onto which a subsequent silanization reaction modified 15% of the material's surface boron sites with 3-aminopropyl-triethoxysilane (APTES). However, this research did not conclusively prove that B-O covalent bonds had formed due to the nitric acid treatment as only the amount of silyl groups were measured as proof of functionalisation which could have been adsorbed to the materials surface. Additionally, other sources claim that BN is completely unaffected by nitric acid alone, to the extent that it is used as a washing step to clean silver nanoparticles from BN samples.[84]

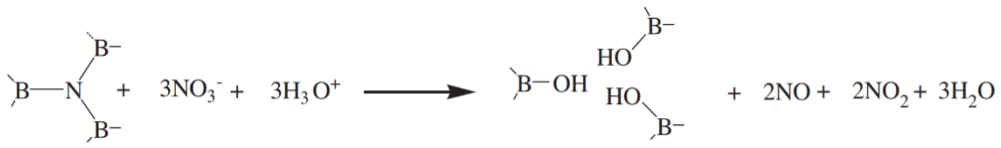


Figure 2.3. Proposed reaction scheme of nitric acid with hBN to yield hydroxyl functional groups on the surface boron sites of BNNT and gaseous by products NO, NO_2 and water.

Image Credit: G. Ciofani *et al.*[83]

There is no doubt however, about the effectiveness of sulfuric/nitric acid mixtures to successfully oxidise carbon nanomaterials. Santangelo *et al.*[85] increased the ratio of H_2SO_4:HNO_3 and found it increased the ratio of resulting carboxylic (acids and anhydrides) to other functionalities (lactones, phenols, quinones/carbonyls and sulphonic groups) in the final product. Osorio *et al.*[86] also

investigated this methodology and found that HCl addition after H_2SO_4/HNO_3 treatment increased total oxygen functionalisation. However, this may be due to the longer acidic environment exposure time these samples experienced and not the specific addition of HCl. Use of purely hydrochloric acid was shown by Datsyuk *et al.*[87] to be an ineffective oxidising agent while the same study suggested piranha solution (a mixture of H_2SO_4 and H_2O_2) treatment increased the carboxylic functionalisation of CNT to 2.0 mmol g^{-1}. Literature focused on the acid etching of hBN is sparse and S. Arya *et al.*[88] report that the material is inert to all acid solutions apart from hot phosphoric acid, which etches the material at 8 nm min^{-1} at 130 °C and 15 nm min^{-1} at 180 °C. Despite this, Nazarov *et al.*[53] applied H_2SO_4/HNO_3 to increase the oxygen content of hBN sheets to ~4 $\%_{wt}$ which led to good dispersions in both water and DMF (also introduced in 2.1.1). These mixed results over the susceptibility of hBN to acid oxidation make the case for further investigation and work presented in this thesis (chapters 6 and 7) will explore this topic further.

2.2.2 Radical Reactions

Reduced nanotubes (as described in 2.1.4) act as both radicals and negative charges which can be used for reactions that lead to a wide range of functionalities as demonstrated in Figure 2.4 taken from work completed by A. Clancy *et al.*[89]

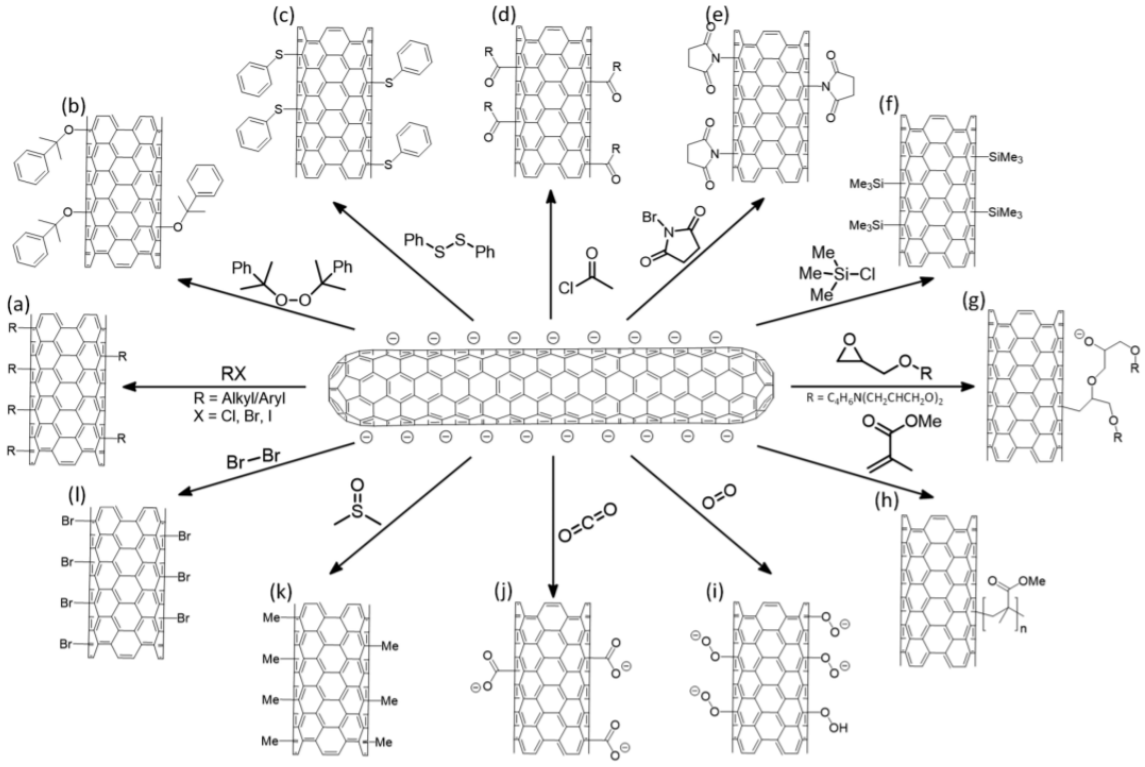


Figure 2.4. Schematic showing the breadth of potential carbon nanotubide reactions. Here are shown the products of reactions with **(a)** alkyl/aryl halides, alkyl/aryl halides*, **(b)** peroxides, **(c)** di-sulfides, **(d)** acyl chlorides, **(e)** N-halo-succinimides, **(f)** chloro-alkyl-silanes, **(g)** epoxides, **(h)** vinyl monomers, **(i)** oxygen, **(j)** carbon dioxide, **(k)** DMSO, and **(l)** bromine.

Image Credit: A. Clancy *et al.*[89]

For the purposes of understanding this thesis, only two of these reactions are relevant: the reaction with R-X halides (Figure 2.4.a,d,e & f) and with gaseous oxygen (Figure 2.4.i). The latter reaction can form B-OOH or degrade into B-OH functionality, but it is more likely that the oxygen desorbs from the nanotube surface, absorbing the negative charge to form a super-oxide anion which thereby effectively oxidises the charged CNT back into its base, neutral state.[90] It is by this reaction with oxygen that excess, unreacted charge can be removed from a reduced nanotube system, but this also leads to the re-agglomeration of the CNT dispersion.

The nucleophilic substitution (S_N2 reaction) of R-X by nanotubide (where R groups can be: alkyl/aryl,[91] succinamides,[92] $SiMe_3$[93]) is very common and versatile. The exact mechanism of this substitution has yet to be definitively proven, but a working model based on the side products of these reactions,[94] the

mechanism of diazonium grafting,[95] and the reduction mechanism of naphthalide[96] has been proposed (Figure 2.5)[5] which also explains the discharge of nanotubide during the grafting process. The halide (X group) selected for this process is usually Br or Cl due to their high electronegativity (causing a highly polar R-X bond) and their ability to form stable soluble ions in solution.

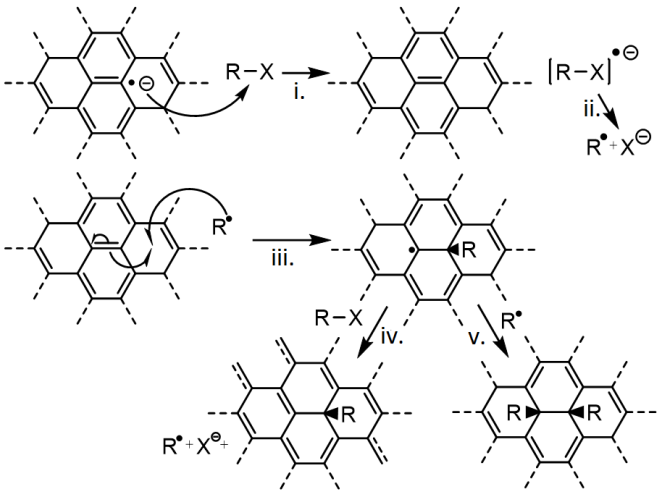


Figure 2.5. Proposed mechanism by which a charged nanotubide reacts with an R-X reagent. The charged radical is transferred from the nanotubide **(i)** to R-X which then dissociates into separate radical and charged species **(ii)**. The radical R group then grafts to the surface of the CNT **(iii)** which leaves a further radical remaining on CNT which is again transferred to R-X species **(iv)** or is quenched by reaction with other radical R reagent in solution **(v)**.

Image Credit: J. Ballentine *et al.*[5]

While the reduction and functionalisation of carbon nanomaterials is a well known, the application of these techniques to hBN materials is an under-developed field. Theoretical DFT (density functional theory) calculations conducted by H. Shin *et al.*[97] showed that pristine single walled BNNT can receive negative charges that are locally restricted to the empty p orbitals of boron atoms within the system. This theory was then tested practically by the charging and functionalisation of BNNT with a bromo-alkyl species (Figure 2.6), achieving a 15%$_{wt}$ addition of grafted hexane and proving that the charge imposed on the hBN has both dispersive and reactive applications. However, no further research into the charging ratios, dispersion potential or other group reactivity has been published on this subject,

suggesting further gaps in our understanding. This is addressed in section 5.4.2.2 of this work where a Br-Hex reaction is used to determine the charging ratio of BNNT.

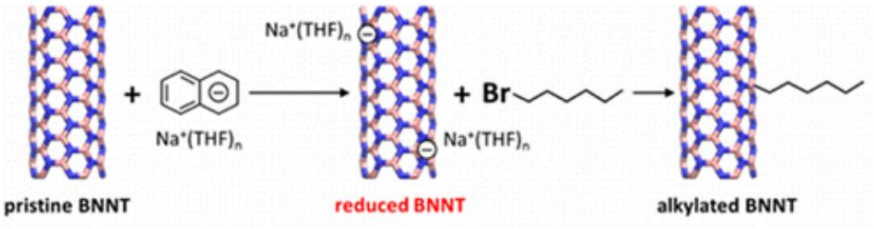


Figure 2.6. Scheme illustrating the reaction of Br-Hex with reduced BNNT. The reduction of BNNT by sodium naphthalide (in THF) leaves negative charges isolated on the BNNT nanostructure. These negative charges act as the nucleophile in an SN2 substitution reaction which form a B-Hex bond and NaBr salt.

Image credit: H. Shin *et al.*[97]

2.3 Nanomaterial Films

A common process utilising dispersions is the production of films and coatings where graphene, CNT, hBN and BNNT are commonly deposited onto a surface to create products of or containing that nanomaterial. For carbon nanotubes, these films are called bucky-papers or bucky-films (in reference to buckminster fullerenes) and can be thin coatings or free-standing films. These films are strong, flexible, chemically inert, thermally conductive and either electrically conductive (carbon) or insulating (hBN), this is due to the innate properties of their constituent nanomaterials, which have numerous potential applications (See section 1.1).

There exists a wide range of methods by which these films can be created[98] each of which impacts on the extent the macro-material can emulate the properties of its constituent parts. For example, the tensile strength and modulus of CNT are as high as 37 and 640 GPa,[99] while these values for the typical bucky paper are only ~10 MPa and ~1.2 GPa.[100] This section will therefore introduce and comment on multiple film production methods.

2.3.1 Filter Deposition

The oldest and most popular method for the manufacture of free standing nanomaterial films dates back as far as 1998[101] and relies on the slow vacuum filtration of dispersions in which the material slowly sediments.[102] This is the most common method used at an industrial scale[103] but is slow and the resulting films are poorly compacted[104] making them fragile. This can be partially counteracted by the modification of the nanotubes used as Zhang *et al.*[105] demonstrated by increasing a SWCNT film's tensile strength (10 to 74 MPa) and modulus (0.8 to 5.0 GPa) by acid etching of the starting nanomaterial. It should be noted however, that this did come at the expense of the film's electrical conductivity (30 kS m^{-1} to 12 kS m^{-1}).

2.3.2 Casting

The simplest method of casting is to place a nanomaterial dispersion onto a substrate and allow the solvent to evaporate in an oven[106] or ambient conditions.[107] As the solvent evaporates, the suspended material becomes more concentrated and begins to interact with itself, which has been reported to result in the self-assembly of structures such as the GO/Ag Janus films reported by E. Ou *et al.*[108]

Generally used for thinner coatings, drop casting is the process whereby small amounts of a nanomaterial dispersion are dropped onto a (sometimes heated) surface and allowed to evaporate. However, drop cast films can easily be uneven as shown by R. Duggal *et al.*[109] Thicker (100 nm) 'coffee stain' rings of deposition can form at the edges of where dispersion droplets were initially placed on the substrate.

To cast even films, a doctor blade can be used to apply the nanomaterial dispersion at an even thickness as it is coated on a substrate prior to drying. C. Xie *et al.*[110] used a glass rod in this role to create CNT films for lithium-sulphur battery cathode materials of controlled and even thicknesses (57, 132 and 180 μm). However, a doctor blade method is less effective for thinner films or less viscous dispersions for which spin coating is more appropriate (Figure 2.7).

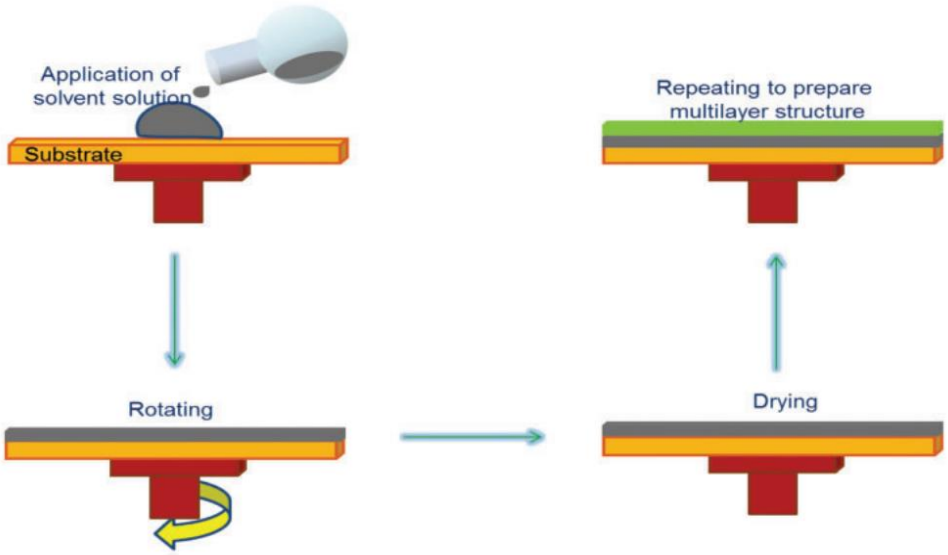


Figure 2.7. Diagram of a generalised spin coating technique. A nanomaterial containing dispersion is applied to the substrate that is spinning such that an even layer of the solution coats it. The solvent then evaporates leaving the nanomaterial only. This then can be repeated to form multi-layered materials.

Image Credit: Z. Khan *et al.*[98]

N. Sahu *et al.*[111] summarise the process of spin-coating into four stages. First, the dispersion is deposited onto the centre of the substrate. Secondly, the liquid is spun so that it is spread across the substrate with the excess being lost to the sides. Next the even coating of the dispersion thins proportionally to its viscosity until it enters the final stage where the thinning of the covering is dominated by the evaporation rate of the solvent. By varying the spin rate, dispersion viscosity and solvent evaporation rate, you can therefore control the film thickness with high precision as Z. Khan *et al.* have summarised for GO films.[98] However, spin coating is only appropriate for small scale, horizontal and flat coatings production and so does not have potential for industrial application.

2.3.3 Synthesis in Place

Another approach to film creation is to grow the nanomaterials directly onto the required substrate. There are a wide range of methods that have been reported for the synthesis of CNT,[112,113] BNNT,[114] and hBN[115] including arc discharge, kinetic ball milling and liquid exfoliation. However, for the production of films, the majority of procedures coat a substrate in a catalyst from which the

nanomaterial is grown by chemical vapour deposition (CVD). An illustrative example of this was shown by D. Wang et al.[116] who grew[117] aligned CNT forests using an iron oxide catalyst, ethylene feedstock, argon carrier gas and 700 °C, which were then compressed to create bucky-papers with nanotubes aligned in the direction of the roller used to flatten them. While these methods may be successful in film creation, the temperatures (as high as 1100 °C for BNNT)[118] required to create the nanomaterials limit the range of substrates that can be used and make useful functionalisation of the nanomaterial postproduction ineffective.

2.3.4 Electrophoretic Deposition (EPD)

Recently, electrophoretic deposition (EPD) has gained more prominence as a nanomaterial (especially CNT) film production method.[119,120] Here, an electric field is applied across a liquid dispersion to concentrate charged nanoparticles onto an electrode causing both their discharge and entanglement on the electrode surface and creating a film (Figure 2.8). The identifiable deposition rate of the particles allows for greater control over the film thickness.

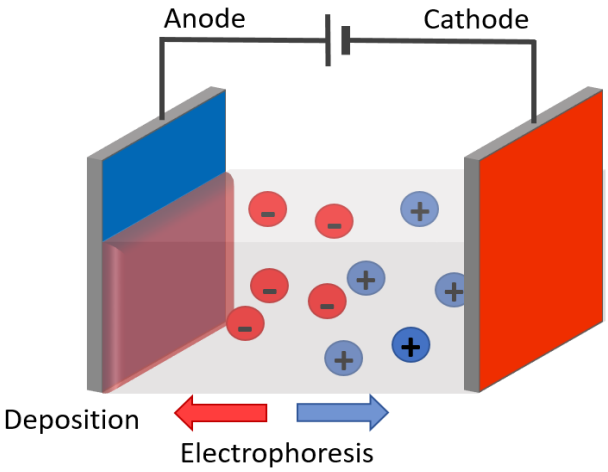


Figure 2.8. Simplified EPD diagram. A potential difference is applied between two electrodes which are immersed in a charged nanoparticle dispersion. The electric field causes the charged particles to migrate to the electrodes where they coagulate into a film deposit.

The variables that control this deposition process and determine the final film are explained with Hamaker's law (Eq. 2.1). Here, the deposited mass of the final film (m) is determined by the

concentration of solids in the dispersion (C_s), the surface area of the depositing electrode (S), the strength of the electric field applied between electrodes (E), the time over which the deposition occurs (t), and the electrophoretic mobility of the nanomaterial in solution (μ). The mobility of the charged material is its velocity relative to the field it finds itself in.[121]

$$m = \mu \times C_s \times S \times E \times t \qquad \textit{Eq. 2.1.}$$

In many of these systems, either through electrode occlusion by insulating deposits, or functionalised charging argents, the material coagulates into a film while still retaining its charge. This is despite the coulombic repulsion that this proximity of like charges would cause. Hamaker and Verwey [122,123] proposed that the deposition process should therefore be visualised as the formation of sediment due to gravitation whereby the pressure exerted by the electric field and incoming particles allows its constituent parts to overcome the energy barrier of mutual repulsion and approach each other close enough so that van der Waals forces can hold the material together.

The energetic environment that this implies is shown in Figure 2.9 where it is implied that there is a certain localised concentration of particles required to overcome the energy barrier. This has led Koelmans et al.[124] to show that a minimum concentration and therefore, a minimum time, are required for film creation meaning that the process cannot be instantaneous.

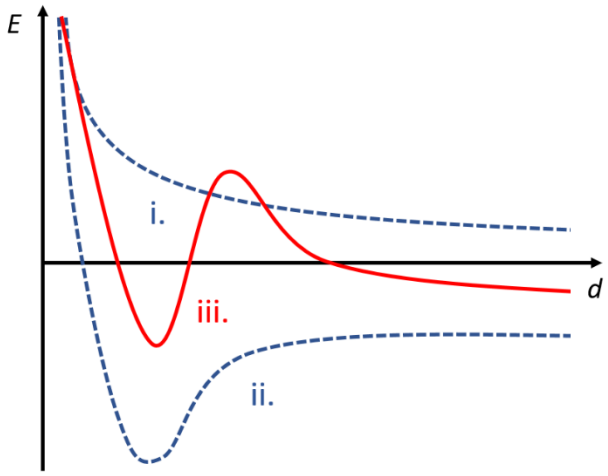


Figure 2.9. Hypothetical interaction energy (*E*) of charged nanoparticles at varying interparticle distances (*d*). The potential energy topography of a charged nanoparticle in dispersion **(iii)** is the summation of the repulsive electrostatic double layer forces **(i)** and attractive van der Waals forces **(ii)** which create an energy barrier to film creation. This is overcome during EPD by the electric field applied to the dispersion, forcing particles close enough together so that they fall into the energy well created by strong nanoparticle van der Waals interactions.

Figure based on work by A. Xiao *et al.*[47]

EPD has been widely applied to produce nanomaterial films. A. Xiao et al.[47] have produced oxidised MWCNT dispersions that can be deposited into free standing, flexible, mechanically strong (>60 MPa tensile strength) and electrically conductive (55 S/cm) bucky papers, although this requires significant loss of starting material during the oxidation procedure and loss of CNT nano-structural integrity. A. Xiao and J. Cho (who conducted similar CNT based work)[48] also required large potential differences (30 and 35 V respectively) to create their films, which would make numerous solvent systems, such as water,[77] inappropriate for use in dispersions (as was explored in section 2.1.4). This issue is more pronounced for the EPD of hBN materials, as M. Raza et al.[45] required 60-120 V to create corrosion resistant BN nanosheet films for copper and Y. Göncü et al.[125] used 100-150 V for the production of biologically inert implant coatings.

There is therefore a gap in the research field that calls for a new method of nanomaterial EPD that requires low voltages, less waste and little nano-structural damage to the final film. This is addressed

in this thesis across chapters 4, 5 and 7. Here, the use of electrochemical reduction to create dispersions of BNNT, CNT and BNP will be shown to be an excellent solution for electrophoretic deposition when compared to the traditional oxidation route of dispersion production.

3 CHARACTERISATION

3.1 ABSTRACT

This section will introduce the various characterisation techniques that have been used to analyse all samples produced for this body of work. The relevant theory of these methods will be described and example values from literature of similar chemical species will be shown to place this work into context. Finally, the practical procedure used to prepare samples prior to, and during, characterisation will also be described.

3.2 Scanning Electron Microscopy

A common way of analysing hierarchical structures comprised of nanomaterials, scanning electron microscopy (SEM) gives a representation of a materials microstructure from which physical characteristics such as alignment, dispersion and void spaces can be visibly identified. Images are created by the rastering of a focused electron beam across a material while measuring the emission of secondary electrons (SE) or back scattered electrons (BSE) excited from its surface (Figure 3.1) which is dependent on topography, local conductivity, and elemental makeup.

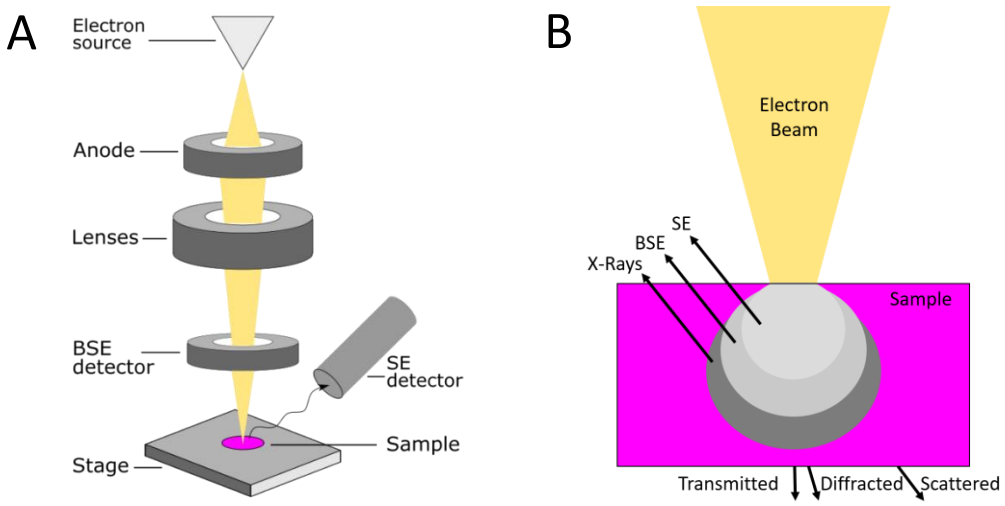


Figure 3.1. Diagrams of an electron microscope. **[A]** The emission of an electron is accelerated by an anode into a beam that is focused by magnetic lenses onto the sample surface from which secondary electrons (SE) and back scattered electrons (BSE) are emitted and measured to create the SEM micrograph. The samples surface that interacts with the incident beam is known as the interaction volume **[B]** and ranges between 100 nm and 5 µm in depth (dependent on the sample type and electron energy). SE are detected from a shallower depth than BSE due to their lower energy (<50 eV) which prevents their escape from all but the top few nm of the imaged material.

Image credit for **[A]**: AnaPath Services GmbH [267]

Samples analysed by SEM in this work were processed depending on investigative requirements. When imaging macrostructures (eg BNNT or CNT films), sections of sample (mm scale) were adhered to conductive carbon tabs with only the edges of these samples being pressed into the tape by needle nose tweezers. Alternatively, when imaging the nanomaterial content of these macrostructures (eg

individual BNP or nanotubes), samples were stirred in acetone and drop cast onto cleaned (by IPA sonication) silicon wafers, that were themselves secured to SEM stubs by carbon tape. Samples were then imaged using either the lower resolution JEOL JSM-840F (>1.8 nm)[126] or the higher resolution Ziess Merlin (0.8-1.6 nm)[127] both of which are maintained by the David Cockayne Centre for Electron Microscopy (DCCM).

Carbon nanomaterials are electrically conductive or semi-conductive and so the discharge of this potentially damaging electron bombardment can be achieved by grounding the sample. However, BN materials are electrically insulating and so samples do not discharge. This build-up of charge can both damage the sample (Figure 3.2) and cause distortions in the resulting SEM images such as oversaturated images or hysteresis streaking. In this work, BN and other non-conducting samples for SEM were therefore covered in 5 – 8 nm of platinum using a Cressington 208HR Pt sputter coater[128] which was both mechanically rotated and continuously tilted by hand during deposition to achieve an even, conductive coating.

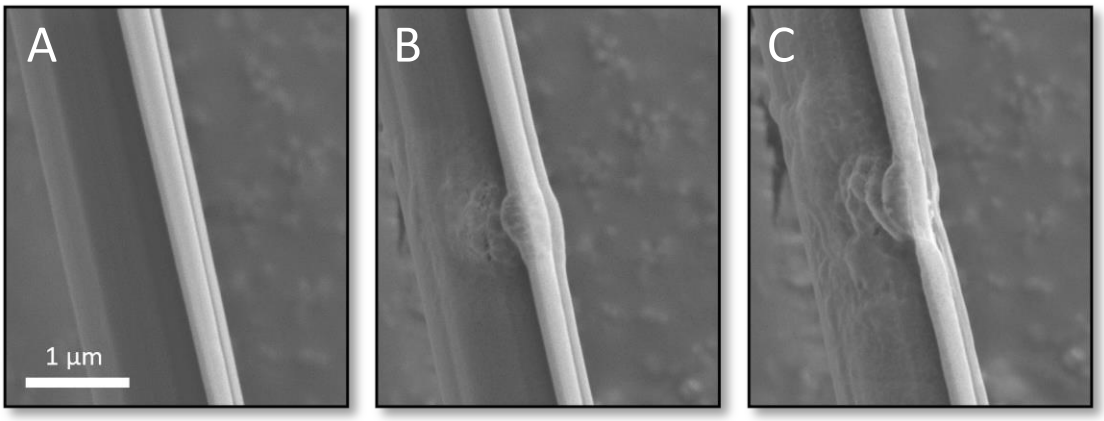


Figure 3.2. SEM Images showing the damage inflicted upon an M.2B precursor fiber from section 0 **[A]** shows the fiber immediately after the electron beam was focused on that area while **[B]** and **[C]** show the results of repeated scans that were focused more closely on the centre of the fiber displayed.

Images taken using these machines were mostly analysed qualitatively as structural features such as pores or crystal impurities were observed and commented upon. However, for BNP samples (Chapters 6 and 7), quantitative analysis of samples sizes was conducted by importing scans into J-Image software where the pixel counted distance of the image could be calibrated using the SEM scale bar

as outputted by the spectrometer (Figure 3.3). Numerous (typically 150- 250) measurements could then be made on the SEM scans for the statistical analysis of particle size for samples.

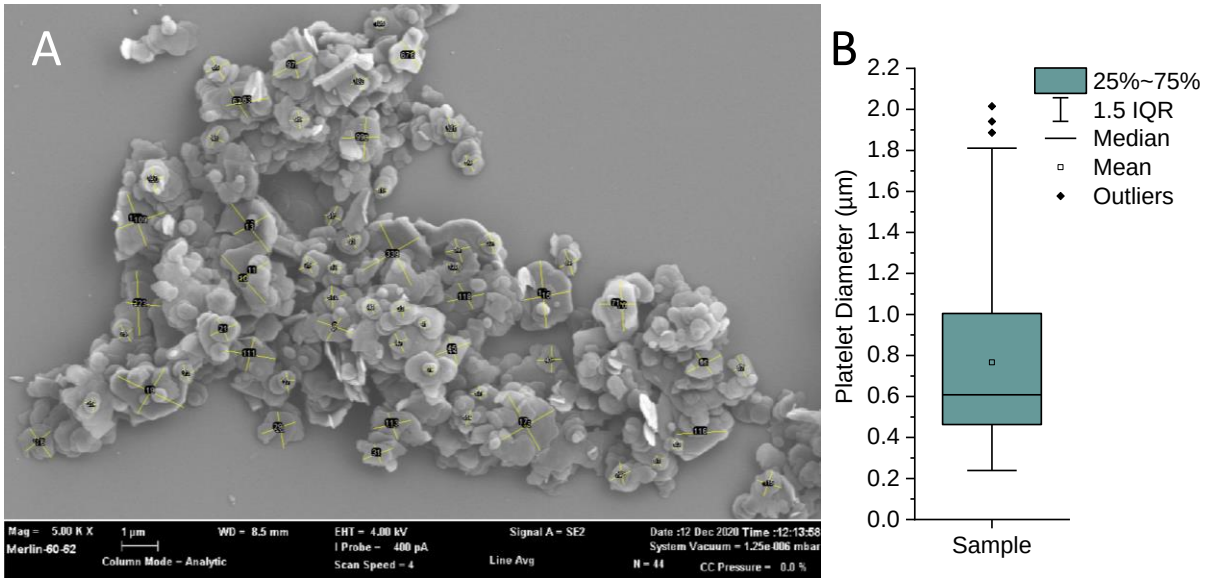


Figure 3.3. Example platelet diameter analysis. SEM raw image as outputted by Ziess merlin SEM **[A]** is imported into J-Image software and calibrated to the scale bar (bottom left). Two perpendicular lines are drawn across visible platelets and the lengths of these lines are recorded. The distribution of these lines is then used for the statistical analysis **[B]** of the diameter of the sample.

3.3 Energy Dispersive X-Ray Spectroscopy

An electron can also be used to identify the elemental composition of a sample if it is assumed that the surface layers of a given sample are representative of its bulk. All elements hold electrons in distinct energetic states. The rastering electron beam excites ground state, low energy, electrons in these atoms, leaving a hole in the atom's electronic structure. When a higher energy electron from the same atom drops down into this hole, it emits an x-ray with energy of the difference between these two electronic states. These X-rays are therefore characteristic of specific elements (Table 3.1) and the intensity of their emission (corrected for excitation and emission probability) can be used to determine the relative concentrations of the elements of their origin.

Element		**$K\alpha_1$**	**$K\alpha_2$**	**$K\beta_1$**
5	B	183.3		

6	C	277		
7	N	392.4		
8	O	524.9		
11	Na	1040.9	1040.9	1071.1
14	Si	1739.9	1739.3	1835.9
26	Fe	6403.8	6390.8	7057.9
29	Cu	8047.7	8027.8	8905.2
78	Pt	66832	65112	75748

Table 3.1. Table of common elemental X-Ray photon emission energies from principal electron shells (in eV). The elements selected are those that are found commonly within this work and will be displayed as part of the elemental mapping used to characterise samples. Reproduced from X-Ray data booklet.[129]

Coupled with the spatial plotting of these X-ray signals, energy dispersive X-ray spectroscopy (EDS) can be used to produce a map of a sample, showing changes in elemental composition across it. In this work, this was achieved by the use of a DCCEM, maintained X-Max^n 150 EDS detector[130] which was coupled to the previously mentioned Ziess Merlin SEM. Samples were prepared in the same manner as for SEM but were not Pt coated and elemental map creation and analysis was conducted using Oxford Instruments AZtec software.

3.4 Raman Spectroscopy

In Raman spectroscopy, samples are irradiated by monochromatic light which interacts with the vibrational modes of bonds/phonons within the material. This interaction is visualised as promoting an electron from a ground state vibrational energy level to a virtual higher energy level. From this higher energy state it can decay back to its original energetic state (called Rayleigh elastic scattering), or relax to a higher or lower energy state (termed stokes and anti-stokes inelastic scattering) in which the energy of the 'emitted' photon is altered ($h\nu = h\nu_o \pm x$ as depicted in Figure 3.4) and a phonon is either emitted or absorbed by the host material.

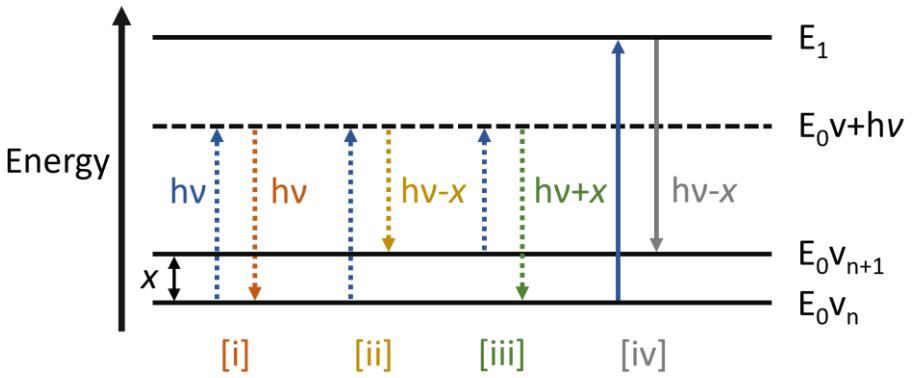


Figure 3.4. Jablonski diagram of the Raman process showing the energetic promotions and relaxations of elastic Rayleigh scattering **[i]**, Stokes scattering **[ii]** and anti-Stokes scattering **[iii]** between the electronic (E_0) and vibrational (v_n) ground states and the virtual energy state $E_0v+h\nu$. When this virtual energy state aligns with a real electronic level (E_1) the excitation is considered resonant **[iv]** and significantly more likely to occur.

When this virtual energy level corresponds to an actual allowed electronic transition, the process is not forbidden, and the quantum yield is dramatically increased and called resonant Raman scattering (Figure 3.4.iv). The energy shifted light that is returned from the sample is then measured and its intensity is plotted against the Raman shift (Δω) that is calculated using Eq. 3.1. (where λ_0 is the excitation wavelength and λ1 is the newly shifted wavelength). The Raman shift value at which signal intensity is observed is characteristic of the material that emits it. For example, cubic BN shows Raman peaks at 1058 cm^{-1} and a E_{2g} stretching Raman peak at 1307 cm^{-1} although this can vary based on the cBN crystal face being imaged and can be hard to detect when the structure contains many impurities.[131]

$$\Delta\omega\ (cm^{-1}) = \left(\frac{1}{\lambda_0(nm)} - \frac{1}{\lambda_1(nm)}\right) \times \frac{10^7(nm)}{(cm)} \qquad \textit{Eq. 3.1.}$$

Single-wall BNNTs can be identified by the distinctive peak at 1370 cm^{-1} thought to be due to an A_1 tangential mode[132] and Wirtz et al.[133] have calculated three radial frequency modes below 810 cm^{-1}. However, multi-wall BNNT do not share these properties and instead display the same indicative peak as planar h-BN between 1365 and 1367 cm^{-1} that represents the E_{2g} stretching mode within the material. [132,134] Further analysis of these BN E_{2g} peaks can show changes to the material. Jung et al.[135]

showed that the reduction in size of bulk hBN to BN quantum dots (BNQD) caused a significant blue shift (1.1 cm^{-1}) in this peak, but the subsequent hydroxylation of these same BQND causes an even larger shift again of 2.6 cm^{-1}. Exfoliation may also cause a blue shift[136] and Gorbachev et al.[137] predict that any observed shift will only occur in BN material of 6 layers or less.

In Carbon nanomaterial Raman spectra, there are three peaks of interest; D (1360cm^{-1}), G (1582cm^{-1}) and 2D/G' (2700cm^{-1}). The G peak is associated with ordered sp^2 graphitic bonding and in CNTs can be separated into the G+ and G- (1590cm^{-1} and 1570cm^{-1}) peaks associated with stretches in the tube axis and circumference respectively.[138] The D peak is associated with the reduction of symmetry caused by introduced defects such as covalently grafted species on the surface of the CNT. The ratio (either by area or intensity) of the D/G peaks can therefore give qualitative information as to the relative grafting densities or nano-structural damage of a set of CNT samples. However, only comparisons between samples with the same original starting material are valid as the background D/G can vary widely between batches.[139,140 ,141]

Samples to be analysed by Raman spectroscopy in this work were manually shredded by needle-nose tweezers and mixed with acetone before being drop cast onto heated (80 °C) glass microscope slides. These slides were then placed into an OMCS maintained, LabRAM Aramis Raman spectrometer equipped with 532 nm green laser and 1800 grating which was zeroed using a Si wafer. A minimum of three spectra at different locations across each sample were taken, normalised, and averaged to calculate errors. For CNT film samples, literature has shown that it is important to have a large number of spectra for D/G analysis[142] therefore 100 spectra, point maps of samples were taken for film samples for which D/G peak heights were analysed automatically by Horiba Scientific LabSpec 6 software.

3.5 Thermal Conductivity Measurements

Thermal conductivity measurements can be broadly classified into two groups; steady state methods (where a constant temperature gradient is established across a material) and transient methods

(where the materials response to a signal is measured). Due to the relatively small scale of the boron nitride fiber samples produced in this work (See section 0), it is difficult to establish stable temperature gradients across them[143] and so the latter transient methods are preferable.

The transient plane source (TPS) method is a well-established (as of 2008, an ISO standard) transient thermal conductivity measurement system in which a wire coil protected by a known thickness of Kapton is sandwiched between two equal samples of material to be tested. The wire coil acts as both heating element and sensor and measures the temperature changes of the sample after a burst of thermal energy. By recording the rate of heat dissipation throughout the sample, thermal conductivity, thermal diffusivity and specific heat capacity of the material can be measured. In this work, TPS measurements were carried out on samples using a Hot Disk TPS 3500 machine which automatically outputted the data that is presented here without further alteration.

3.6 X-Ray Photoelectron Spectroscopy

For a more precise elemental breakdown of a sample and information on the bonding environments of these atoms, X-rat photoelectron spectroscopy (XPS) is used. A beam of X-rays is focused on the sample and the number and kinetic energy of the resulting emitted photoelectrons (usually from the inner 1s electron shells of the atom) are measured. From the kinetic energy of the emitted electron, a binding energy for that electron can be calculated following the photoelectric effect (Eq 3.2) where h is the Planck constant, f the frequency of incident X-rays and E_k is the kinetic energy of the emitted electron.

$$Electron\ Binding\ Energy = hf - E_k \qquad \textit{Eq. 3.2.}$$

The binding energy of an electron is characteristic of its element of origin and by integrating the signal from them and then correcting for relative sensitivities to incident X-rays, you can determine the relative concentrations of each element in any given sample. Individual elemental peaks can be further resolved into separate peaks representing the different bonding environments in which the element

is present. Electron density polarization within bonds due to differences in electronegativity can cause the shielding (by bonds to electron donating groups) or de-shielding (by bonds to election withdrawing groups) of the atomic nucleus.[144] The latter de-shielding of the nucleus raises its electron affinity and so increases the binding energy of the 1s electron shell which is measured during XPS as a distinct and characteristic bonding environment.

Samples for this work were analysed by Dr Philip Holdway of the Oxford Materials Characterisation Service (OMCS) who provided this statement as to their treatment: *"Samples were analysed using a Thermo Scientific K-Alpha XPS instrument equipped with a microfocussed monochromated Al X-ray source. The source was operated at 12 keV and a 400 µm spot size was used. The analyser operates at a constant analyser energy (CAE) 200 eV for survey scans and 50 eV for detailed scans. Charge neutralization was applied using a combined low energy/ion flood source. The data acquisition and analysis was performed with Thermo Scientific Avantage software."*

Data from this analysis included both spectra and elemental percentages and was conducted for each sample multiple times. These elemental proportions were averaged and used to calculate standard deviations which were then presented as is. The spectra were imported into CasaXPS 2.3.22 software in which they were peak corrected based of the carbon peak position (285.0 eV for majority sp^3 containing samples and 284.4 for graphitic samples). A shirley baseline was then imposed on each individualised elemental signal before deconvolution.

The C1s peak is found between 280 and 196 eV and eight studies that analysed this curve for carbon nanomaterials were therefore collected and compared (Figure 3.5.B) to create a model deconvolution that could be used on all samples and so allow these results to be compared. Authors and their work (material analysed in brackets) used for this are as follows: T. Okpalugo (MWCNT & SWCNT),[145] M. Varga (diamond/CNT composites),[146] S. Lee (CNT films),[147] N. Soin (Pt coated CNT),[148] A. Velmakanni (Au coated CNT films),[149] C. Thamaraiselvan (CNT membranes) ,[150] X. Chen (C1s of fullerenes review),[151] R. Blume (C1s of graphitic carbon review).[152]

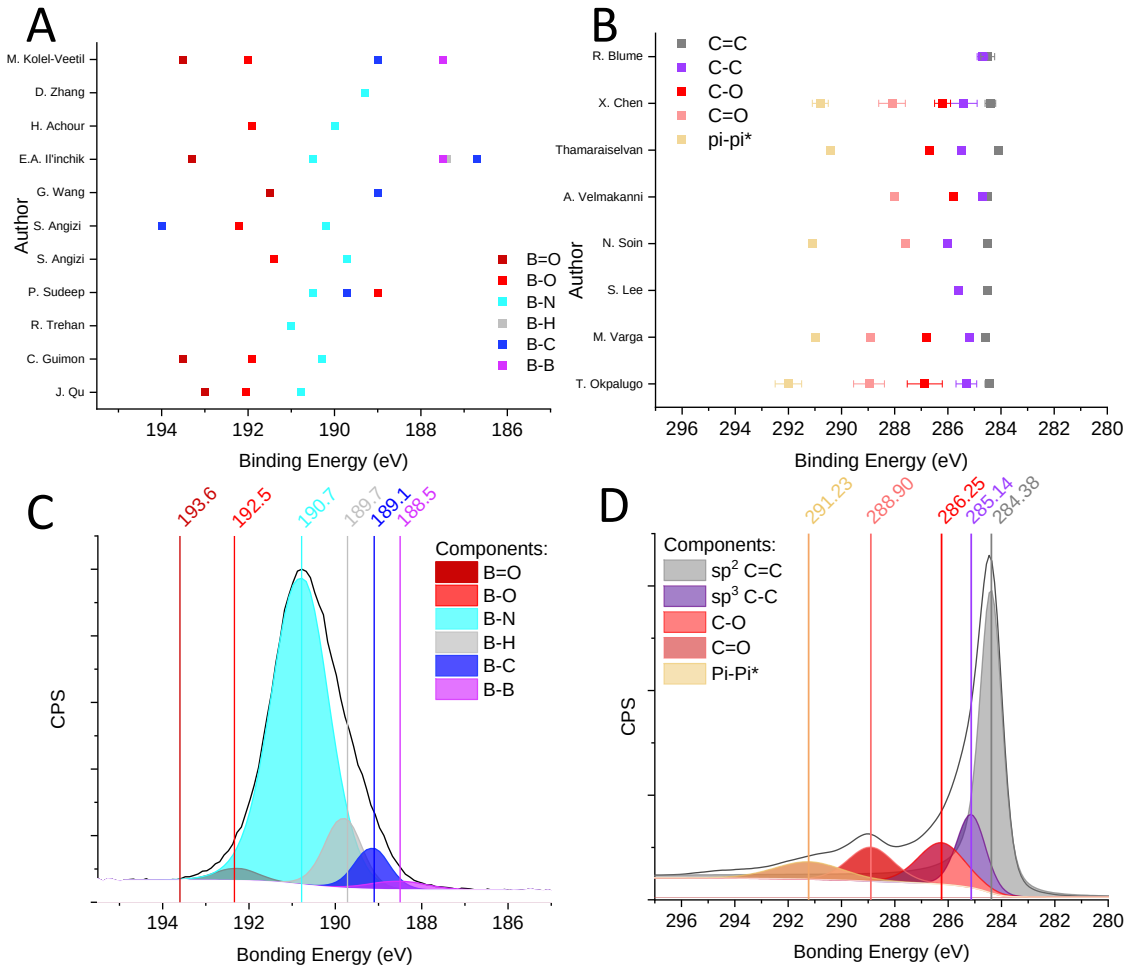


Figure 3.5. Characterisation by XPS graphs. A scatter graph shows the distribution of peak positions assigned to the deconvolution of the B1s **[A]** and C1s **[B]** XPS spectra within literature. A typical h-BN platelet B1s XPS spectra **[C]** from section 6.4.1.3 is used to model the deconvoluted peak positions selected for use in this work. The C1s spectra **[D]** of an archetypal CNT sample from section 4.4.3.2 is similarly used to show the chosen deconvolution peak positions used in this work.

The literature data points were then used as ranges for the deconvolutions of some test spectra using a GL(35)T(3) line shape for all bonding environments bar the sp^2 carbon-carbon bonding which used an asymmetric line shape due to the effects of hole movement within conductive graphitic structures.[153] The peak positions of these test deconvolutions were then used to form the model spectra shown in Figure 3.5.D where deconvoluted peak positions are recorded as follows: sp2 C=C is 284.4 eV, sp3 C-C is 285.1 eV, C-O is 286.3 eV, C=O is 288.9 eV and Pi-Pi* bonding is at 291.23 although this is usually edited out of final bonding percentages.

As was shown in the literature review (section 2.2), the site of bonding within BN nanomaterials is usually thought to be the boron atoms. For the analysis of the hBN materials shown within this work the B1s spectra (185 – 195 eV) was therefore chosen for analysis as it will show the largest changes (if any) in bonding environments as samples are modified either by design or by unforeseen side reactions. The literature covering the deconvolution of the B1s signal is however much more variable than the previously shown C1s. A collation of these literature sources covering various species of hBN, BNNT and BCN is presented in Figure 3.5.A and shows large disagreement as to different boron bonding environment peak positions. The authors and their work used in this section are as follows (with material analysed in brackets): J. Qu (flake hBN),[154] C. Guimon (CVD deposited BN thin films),[155] R. Trehan (hBN, cBN),[156] P. Sudeep (functionalised BN),[157] S. Angizi (BN quantum dots),[158] G. Wang (B-doped graphene),[159] E.A. Il'inchik (boron containing small molecules),[160] H. Achour (plasma functionalised hBN sheets),[161] D. Zhang (amorphous boro-carbon thin films),[162] M. Kolel-Veetil (boron carbide).[163]

The majority of these sources agree that the B1s bonding energy increased with the electronegativity of the bonded component (in increasing energy: B-B, B-C, B-N, B-O) and so the literature peak positions were again used as (albeit wider) ranges for preliminary deconvolutions of samples to find peak positions. These initial deconvolutions showed the need for another peak between the B-N and B-C energies to gain a better fit for the data that came from samples that were more likely to have damaged nanostructures. A B-H peak was therefore created to represent boron atoms that had lost one or more of the 3 planar B-N bonds found within hBN nanostructure and thereby re-gained electron density, increasing the nucleus shielding of the B1s shell. This consequently lower bonding energy peak will be used as a measure of hBN nano-structural damage. By combining the B-H peak with the others previously devised, the final B1s deconvolution model is therefore presented in Figure 3.5.C and consist of the following peak positions (in eV): 188.5 (B-B), 189.1 (B-C), 189.7 (B-H), 190.7 (B-N), 192.5 (B-O) and 193.6 (B=O).

3.7 THERMOGRAVIMETRIC ANALYSIS

Thermogravimetric Analysis (TGA) is simple in its theory and execution. Samples are heated under a constant gas flow (either inert or oxygenated depending on requirements) while their mass is continually measured. As the temperature rises, the samples mass will reduce sequentially as more volatile species within it evaporate, oxidise, or thermally decompose. For many materials and chemicals, the temperatures at which these mass drops occur are known and so by measuring the extent of mass changes at specific temperatures the samples weight percentage (wt%) of that material can be known.

The commonly reported thermal degradation temperature of hBN nanomaterials is 2500 °C [30] under inert conditions and 1000 °C [29] in air where it will oxidise into B_2O_3. This is very similar to the oxidation temperature of cBN which is between 1000-1350 C [164] where the higher range is due to increased crystallinity. More reactive than hBN, carbon nanomaterials have lower oxidation temperatures of 695, 645 and 420 °C for CNT, Graphite and C_{60} (buckyballs) respectively.[165] These high temperatures of oxidation can be utilised in TGA measurements to characterise functionalisation for both carbon and BN nanomaterials. Chemical species attached to the nanomaterials surface usually decompose at a lower temperature than the material itself and therefore the mass loss curves are used to determine the success and extent of grafting reactions.[166] Additionally, the temperature at which the nanomaterial itself degrades can give information about its structure. Studies have shown that CNTs with increasing layers have an increased thermal stability (598.1, 606.3 and 622.6 °C in air for SWCNT, DWCNT and MWCNT respectively).[167] Furthermore an increase in the graphitisation (larger proportion of sp^2 bonded C) within carbon nanomaterials can be identified by an increase their oxidative stability.[168]

Samples characterised by TGA in this work were manually shredded by tweezers and 0.8-1.6 mg were placed in a tared pan. This was then loaded into a Perkin Elmer TGA8000 operating under an anhydrous air flow of 40 mL min^{-1}. Samples where then heated to 170 °C (above the boiling point of

DMAc) where they were held for 10 min. The samples were then further heated at a rate of 10 °C min^{-1} to 950 °C (for CNT samples) or 1100 °C (for BN samples). The recorded mass of the samples was then normalised and plotted against the recorded temperature (as opposed to the programs set temperature). Temperatures of oxidation for each mass loss were determined using the sigmoidal fit gadget of Origin 2021 graphing software.

3.8 Mechanical Tensile testing

Tensile testing is a common characterisation technique used to find the mechanical properties of free-standing film samples. A rectangular sample of known dormitions is clamped in a vice which is then opened at a steady and controlled rate until the material fractures. The force applied to open the vice (F) is monitored and is then divided by the cross sectional area of the material (CSA_0) to calculate the engineering stress[169] (σ_e) being applied to the material Eq. 3.3:

$$\sigma_e = \frac{F}{CSA_0} \qquad \textit{Eq.3.3}$$

This is plotted against the engineering strain (ε_e) calculated by dividing the materials extension (δ) by its original length (L_0) Eq 3.4:

$$\varepsilon_e = \frac{\delta}{L_0} \qquad \textit{Eq. 3.4.}$$

From the graph of ε_e vs σ_e, the ultimate tensile strength (maximum stress), Young's modulus (gradient of the line in the initial linear region of extension) and toughness (integral of the line until fracture) can all be calculated. For materials that may experience large deformations, the true stress and strain (σ_t and ε_t) can be calculated in which the changing cross-sectional area (as the material experiences necking) is taken into account. This was deemed unnecessary for this work as the free-standing films tested were observed to not deform in this manner (section 4.4.2.1).

Mechanical testing in this work was conducted by Xudong Tao of the Assender Research Group and used a Linkam tensile testing machine on free standing nanomaterial films of 3.0 x 0.5 cm dimensions. Film dimensions were measured using a digital micrometer and analysis of the resultant stress/strain graphs were conducted using the linear quick fit (for Youngs modulus) and integrate (for toughness) functions of Origin 2021 graphing software.

3.9 Infrared Spectroscopy

Infrared spectroscopy (IR) is a ubiquitous technique among chemists. All bonds between different elements have characteristic vibrational frequencies that absorb light at specific energies and so by measuring the transmittance of a sample across a spectrum of energies, the specific chemical groups present within it can be determined. The wavelength range of IR spectroscopy is typically 2500 nm to 20000 nm and is presented in wavenumbers (4000 cm^{-1} to 500 cm^{-1}) against transmittance (%). Typically, the 500-1400 range (also referred to as the fingerprint region) represents single covalent bonds; 1600-1800 cm^{-1} range shows double bonds; 2100-2300 cm^{-1} range indicated triple bonds and the 2800-4000 cm^{-1} range shows hydrogen bonding.

Pure carbon nanotubes are rarely characterised used IR spectroscopy. SWCNTs do not support a static dipole moment (as there is no electronegativity difference between C atoms) and so do not strongly absorb IR radiation.[170] Small and broad signals at 1598 and 874 cm^{-1} have been reported as the interactions with tube phonons but may also be graphite.[171] IR is therefore more likely to be used to identify the presence of functionalised groups on the nanomaterials surface such observing the increase in the -CO (1580 cm^{-1}) -COOH (1720 cm^{-1}) signals after a CNT oxidation.[172]

The dissimilar electronegativity of the B-N atoms causes a standing dipole which can interact with the IR frequency. Consequently, hBN displays two characteristic peaks at 1383 cm^{-1} (B-N stretching) and 804 cm^{-1} (B-N-B bending).[173]

Samples for this work had their IR spectra measured using an OMCS maintained Varian Ltd. Excalibur Series IR Spectrometer. Samples were placed on an ATR (attenuated total reflection) setup for measurement with no modification. Other samples were instead ground in an agate pestle and mortar with KBr powder (0.1 mg_{sample} with 150 mg_{KBr}) and then compressed into pellets using a 12 ton press. The pellets were then placed into the spectrometer for measurement as well as a blank KBr standard that was manufactured on the same day with the same KBr powder (to avoid differences in moisture content effecting the spectra).

3.10 PROFILOMETRY

Profilometry is used in this work as primarily the method by which electrode deposited film thicknesses are measured. The films are scratched to expose the electrode surface and the difference between these plateaus is then measured. Additional to this, the roughness/surface morphology of these films are also measured to illustrate the presence of contaminants on their surface. This was conducted using two methods: optical profilometry and mechanical profilometry.

3.10.1 Optical Profilometry

Optical profilometry is a non-contact scanning technique that produces a 3D map of the imaged surface (Figure 3.6). The confocal pinhole microscope used in this process measures the samples optical response at various focal lengths and then uses these images to build up a 3D profile of the material surface which can then be used to find film depth.

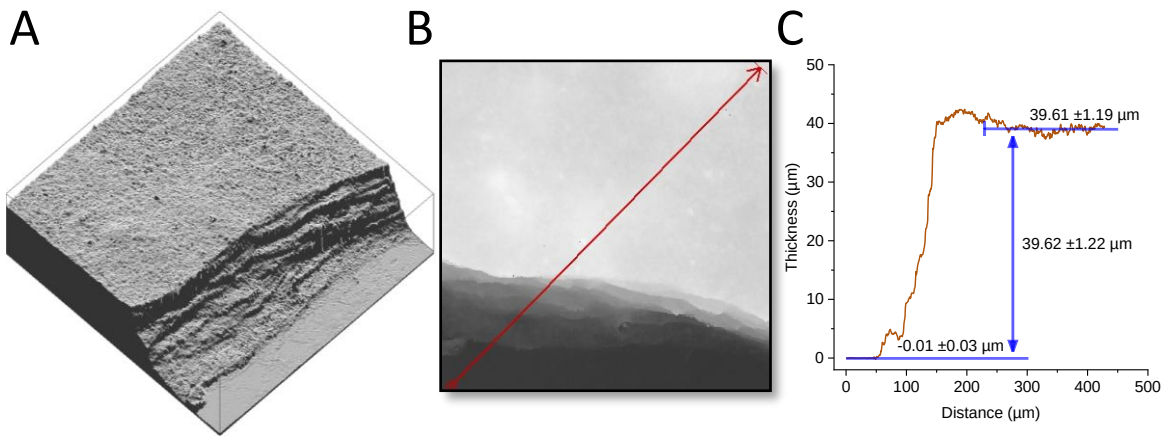


Figure 3.6. Example optical profilometry analysis (1.5 mg_{BNNT} mL^{-1} film sample presented in section 5.4.3). A 3D map **[A]** of the film is taken of a 320 x 320 µm area that includes a scratched area (down to the substrate) along one vertex. Various line profiles **[B]** are taken of this map and plotted **[C]**. The scratched area of the profile is used to level the data and then the difference between the substrate and the films height is calculated.

Samples in this work were analysed using an OMCS maintained Nanofocus µsurf confocal optical profilometer equipped with a x50 magnification lens. A 320 x 320 µm area of the sample is measured and then a minimum of four line profiles (Figure 3.6) are taken and plotted. The plots are levelled using the machines associated µsoft* software and the difference in height between the substrate and film measured. The average and standard deviations of these measurements are then presented.

3.10.2 Mechanical Profilometry

The optical profilometer was not available for use during the period of time in which the majority of this work was conducted. Additionally, its use of light within the visual spectrum makes it unsuitable for use on carbon nanomaterial film samples as CNT absorbs radiation in this range. A contact profilometer was therefore used instead for these samples where a stylus is moved across the sample while its height is measured (Figure 3.7.A).

* The author would like to make a note as to how delightful this software name is.

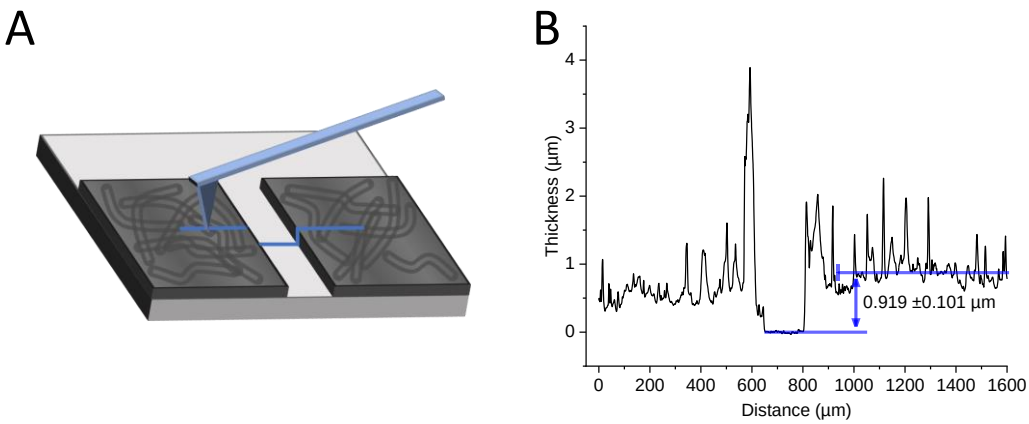


Figure 3.7. Examples of mechanical profilometry analysis (taken from the 20 s EPD of CNT from section 4.4.4.1). Simplified diagram **[A]** of the stylus profilometer path (blue line) across a scratched film sample and the resulting profile **[B]** showing the calculation of the film thickness.

In this work, samples were measured using a Bruker Dektak 6M profilometer equipped with a 12.5 µm radius diamond tipped stylus that has a vertical resolution of 1 Å. Multiple line profiles of each sample were taken, levelled with reference to the substrate, and then film thicknesses were calculated as shown in Figure 3.7.B. Note that the immediate perimeter of the scratch in the film was not used to calculate the thickness as its height has been disturbed by the scoring process.

3.11 X-Ray Diffraction

When X-Rays are incident onto a materials surface, a proportion of them will be diffracted away from their original path as spherical waves from each atom within the structure. Within a crystalline material, these atoms are regularly spaced and so the spherical waves of diffracted X-rays destructively interfere with each other in most directions. These waves do however constructively interfere in specific directions that are described by Braggs Law (Eq. 3.5) where d is the inter layer distance of crystal planes, θ the angle of incident of the X-Ray beam (diffraction angle), n the diffraction order and λ the wavelength of the X-rays.

$$2\,d\,sin\,\theta = n\lambda \qquad \textit{Eq. 3.5.}$$

X-ray diffraction (XRD) characterisation of a sample therefore measures the intensity of diffracted X-rays at various angles around the sample. The peaks on the resulting intensity/angle plot can be used to identify the characteristic crystalline lattice parameters of known materials. In hBN materials, the most intense peak is found at 26.7° and corresponds to the materials (002) crystal plane with other peaks usually noted for the (110), (100), (004), (110) and (114) planes as well.[174] This differs from cBN which is dominated by the (111) plane[175] at 43.2° as well as peaks for the (220), (200), (311) and (400) planes.[176]

Additional information to just material identification can be gained from XRD data. Through analysis of the relative intensities of peaks within a sample, it has been reported that orientation and shape of nanoparticles can be determined[177] with the (002) peak of CNT being identified as decreasing monotonically as nanotubes become more aligned.[178] Furthermore, the relative size of crystalline domains within a sample can be determined by analysis of specific peaks using the Scherrer Equation. Here (Eq 3.6.), the crystalline domain size (D) is determined using the FWHM (β) of a peak at the diffraction angle θ, X-ray wavelength (λ) and the Scherrer constant (κ) which is taken at 0.91 for this work.[177]

$$D = \frac{\kappa \lambda}{\beta \cos \theta} \qquad \textit{Eq. 3.6.}$$

Samples for this work were analysed by Dr Philip Holdway of the Oxford Materials Characterisation Service (OMCS) who provided this statement as to their treatment:

"*X-ray diffraction (XRD) analysis was carried out using a fully automated Bruker D8 ADVANCE eco powder diffractometer employing copper kα radiation (λ = 0.15406 nm) and a LYNXEYE XE detector. The sample was continuously spun during data collection and scanned using a step size of 0.02° 2ϑ between the range of 10°- 90° 2ϑ.*"

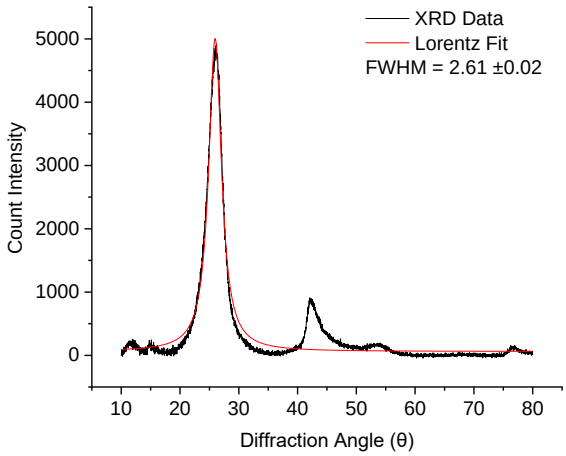


Figure 3.8. Example XRD analysis of BNF (taken from section 0). The baseline subtracted XRD spectra of the h-BN sample is plotted and the (002) peak at 26.4° is fitted using a Lorentz function chosen as the FWHM most closely matches the data that is fitted.

XRD data that was returned from this was processed using Origin software and peaks fitted using a Lorentz function to determine the FWHM used in crystal domain size calculations as shown in Figure 3.8 Once these FWHM values had been used to calculate crystal domain sizes using the Scherrer equation, errors in these values were calculated using Eq 3.7. which uses the same constants while σ_β and σ_θ were given by the Lorentz fitting function.

$$\sigma_D = \frac{\kappa\,\lambda}{\beta\,cos(\theta)}\sqrt{\frac{{\sigma_\beta}^2}{\beta^2}+\frac{sin^2(\theta)\,{\sigma_\theta}^2}{cos^2(\theta)}} \qquad \textit{Eq. 3.7.}$$

3.12 Ultraviolet-Visible Light Spectroscopy

Similar to IR spectroscopy, Ultraviolet-Visible Light Spectroscopy (UV-Vis) is a staple of chemical analysis suites across many fields. The technique uses a higher (compared to IR) energy spectra of light (800-200 nm wavelength) to promote electrons within a sample to higher energetic states. The absorption of this light occurs at characteristic wavelengths and so the technique can be used to identify different species within a given sample. For example graphene gives a characteristic peak at 266.5 nm.[179] Another common use of UV-Vis is for the calculation of solute concentration within solutions. As the spectrometers beam passes through a known distance of solvent containing a light

absorbing solute, the transmittance measured by the machine will be proportional to the solutes concentration as defined in the Beer-Lambert Law. Here (Eq 3.8), the concentration (c) is determined using absorbance (A), pathlength (l), and the molar absorption coefficient (Ɛ).

$$c = \frac{A}{\varepsilon\, l} \qquad \textit{Eq. 3.8.}$$

The molar absorption coefficient (Ɛ) for small molecules in common lab solvents are usually known and can be researched. For more uncommon samples, Ɛ can be practically derived by producing multiple solutions of known concentrations and measuring their absorbance. This data can then be inputted into the Beer-Lambert equation to find a Ɛ value that can then be used for samples of unknown concentration. Due to the large differences even between batches of even the same nanomaterials, literature on Ɛ values for hBN materials is widely conflicting with examples including 874 and 174 mL mg^{-1} m^{-1} for nanosheets and BNP respectively [54] and the different order of magnitude 2367 mL mg^{-1} m^{-1} for just BNP.[55]

Due to this unreliable literature, concentration calculations made using UV-Vis in this thesis are calculated using molar absorptivity coefficients developed for this work. The starting materials of the samples that were to be measured were made up into suspensions of known concentration with by bath sonication in volumetric flasks. These dispersions were then immediately diluted (by hand shaking) into multiple more concentrations that were then placed into 1 cm pathlength quartz cuvettes for analysis by an OMCS maintained Varian Cary 5000 UV-Vis-NIR spectrometer.

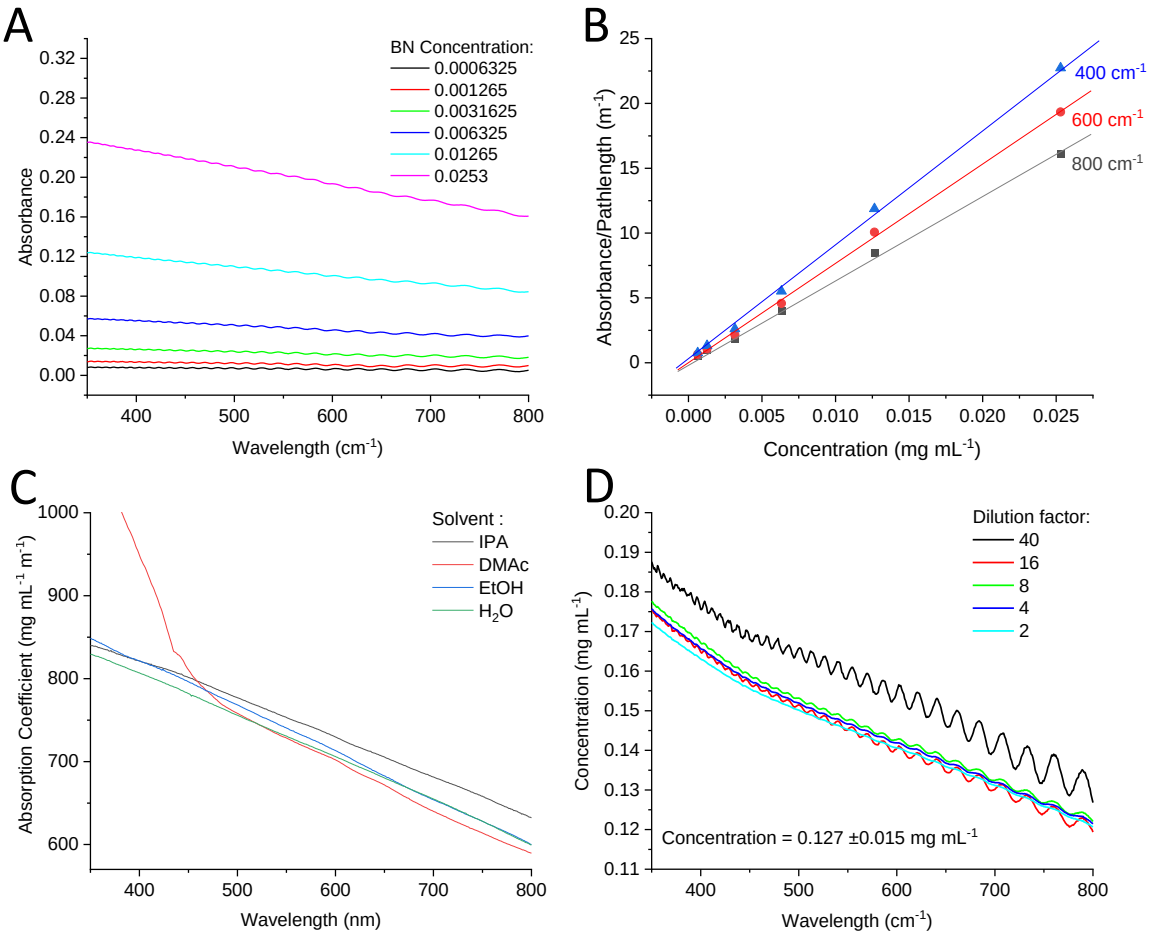


Figure 3.9. UV-Vis Data Processing Graphs. The absorbance spectra of known concentrations of BN in a specific solvent are taken **[A]**. For each wavelength, the gradient of the line from the absorbance/pathlength against concentration plot **[B]** was calculated to find the absorption coefficients at each point in the UV-Vis Spectra **[C].** These points were then used to calculate the concentrations of unknown samples to find an average and standard deviation **[D]**.

The results were then plotted (Figure 3.9.A) where it was noticed that the absorptivity coefficients varied with the wavelength at which they were measured (Figure 3.9.B). To take this into account, Ɛ was calculated for every wavelength (Figure 3.9.C) which was then used to calculate a concentration at every point along the spectra from unknown solutions using the same starting material and solvent (Figure 3.9.D). These concentration ranges were then averaged and used to find standard deviations.

3.13 Brunauer-Emmett-Teller Measurements

To obtain surface area measurements for samples, Brunauer-Emmett-Teller (BET) measurements were ordered. Samples for this work were analysed by Dr Colin Johnston of the Oxford Materials Characterisation Service (OMCS) who provided this statement as to their treatment:

"Barrett-Joyner-Halenda (BJH Pore Size and Volume Analysis) and Brunauer Emmett Teller Measurements (BET) analysis was carried out using a Micromeritics Gemini VII surface area analyser using nitrogen as the adsorbate at liquid nitrogen temperature. For BJH a full adsorption/desorption isotherm was measured totalling 69 points. All samples were degassed at 160 ˚C until a constant weight was achieved prior to analysis."

For BET data presented in this thesis, no further data manipulation was conducted on the results or errors presented by the OMCS report generated by this method.

4 REDUCED SWCNT FOR EPD

4.1 ABSTRACT

There is a significant cost to the final film's utility and production yield caused by the requirements of traditional nanotube film manufacture which involves the oxidation of the starting material. This chapter circumvents these costs by introducing a novel method to produce conductive, mechanically strong, and thermally stable single walled carbon nanotube (SWCNT) buckyfilms which crucially retain the nanostructure of their initial starting material without this need for oxidation, additional modification, additives, or binders.

This process is the first to show an electrochemical charging method used to reductively disperse and individualise CNT samples into a solution that is then coagulated onto the surface of an electrode during electrophoretic deposition (EPD). The resulting thin films and free-standing materials are produced with controllable thicknesses (up to 14 μm), during order of magnitude shorter time periods (120 s), 3-7 times lower voltages (10 V) and with higher yields than traditional methods. Additionally, the physical properties of these films are still comparable to chemically modified traditional films but they are slightly mechanically weaker (8.4 vs 14.9 MPa Youngs modulus) and poorer electrical conductors (229 S cm^{-1} vs 694 ±18 S cm^{-1}) although this gap is expected to narrow as the technology develops. Therefore, this procedure represents a sustainable, versatile, and scalable semi-continuous new method to produce materials for next-generation composites for flexible electronics applications.

4.2 INTRODUCTION

Materials manufactured from entangled carbon nanomaterials across a 2D plane are referred to as free standing “buckypapers” or “buckyfilm” coatings. These are of interest for various industrial applications including mechanical load bearing,[180] thermal management[181] and battery electrode materials[182,183] due to the intrinsic properties of the contained CNT.[184,185,21] The most popular method for the manufacture of these buckypapers and buckyfilms dates back as far as 1998[101] and relies on the slow vacuum filtration of CNT dispersions. This produces a poorly compacted, small-scale product with only limited control over the thickness of the final material.[104] An alternative production method involves drop-casting CNT dispersions.[109] This allows the self-assembly of CNT into a more ordered film but only yields very thin materials (100 nm) and, similar to filtration methods, is not suitable for producing films on an uneven or non-horizontal surface.

A more versatile approach to buckyfilm creation that has been gaining more prominence[119,120] is electrophoretic deposition (EPD). EPD uses an electric field to transport charged colloidal particles from a liquid dispersion onto an electrode. This causes a localised concentration of charged particles, to the point of them overcoming the energy barrier of their mutual repulsion and thereby coagulating into a solid mass creating a film.[122,123] Koelmans *et al.*[124] showed that this is not an instantaneous process but requires time for the particles to coalesce in high enough concentration before deposition can begin (unlike a faradic electroplating processes in which deposition and discharge occur instantaneously). Despite these requirements, the identifiable rate of deposition during EPD allows for greater control over the resultant film thickness and, due to the electrically conductive nature of CNTs, there is theoretically no limit on the size of film that can be produced using this method.[120]

EPD, filtration and drop casting methods of buckyfilm production all share the common issue that the quality of the final film is dependent on the method used to produce the initial CNT dispersion. Due to strong inter-nanotube forces,[49] dispersion is often achieved by sonication, chemical modification or surfactant[186]/polymer[64] addition which can reduce the aspect ratio of the tubes,[58] damage their

nanostructure or introduce further complicating chemical functionality into a final buckypaper respectively. These issues can seriously affect the final properties of a resultant film and can prevent the full utilisation of the intrinsic properties which make CNT materials desirable.

A potential solution[†] to these problems can be found in advances made by Clancy *et al.*[187] within the field of electrochemical dissolution[74,73]. By reducing nanotubes using sodium naphthalide, it has been shown that a non-destructive, reversible method of SWCNT dissolution is possible. This is due to the mutual repulsion of the introduced negative charges along individual CNTs causing samples to spontaneously exfoliate into solutions. The stability of dispersion, individualisation of nanotubes and introduction of charge onto the CNT surface makes this method an excellent candidate for application to EPD for the production of neat CNT buckyfilms.

Here, it is shown that it is possible to produce both free standing buckypapers and buckyfilm coated electrodes using an EPD methodology with dispersions of reduced SWCNT. This method of film manufacture will be compared to a more traditional EPD production method using oxidation-based CNT dispersions building on work previously conducted within the Grobert group by Xiao *et al*[47] as well as others.[48] This comparison demonstrates that this method produces films with little to no nano-structural damage relative to the traditional oxidised dispersions as well as producing films with no impurities within the larger film structure.

[†] pun intended

4.3 EXPERIMENTAL

This section details the experimental methods used to produce CNT films by EPD. The process of CNT oxidation by acid etching, dispersion and EPD used to create comparison films from the Tubal SWCNT are based on the method used by A.Xiao *et al.*[47] while the reductive dissolution of the same SWCNT is based on work done by A.Clancy *et al.*[187]

4.3.1 Materials

Material Name	Abbreviation	Supplier
Single Walled Carbon Nanotubes	SWCNT	Tuball™
Sulfuric acid	H_2SO_4	Sigma 07208
Nitric acid	HNO_3	Sigma 438073
Hydrochloric acid	HCl	Merck 1.00313
PTFE membrane	n/a	Cat#: 776742
Sodium metal	Na	Sigma 262714
Naphthalene	Nap	Sigma 84679
N,N Dimethyl Acetamide	DMAc	Sigma 271012
Methanol	MeOH	Sigma 34860
Ethanol	EtOH	Sigma 32221
Iso-Propanol	IPA	Sigma 59300
Compressed Air	n/a	BOC UN1002

Table 4.1. Materials used in this section as well as the supplier product numbers (where possible) and abbreviations that are used to refer to them within the text.

4.3.2 Methods

Oxidation and purification of O-SWCNT dispersions: 1 g raw SWCNT was purified by stirring for 24 hours in 200 mL 32% HCl solution. This was then vacuum filtered over a 0.22 µm pore PTFE supported membrane wetted with ethanol and then washed sequentially with 100 mL water and 100 mL ethanol. The filter cake was then vacuum dried at 80 °C for 16 hours. 20 mL 97% sulfuric acid solution and 16.5 mL 70% nitric acid solution were combined in an ice-bath. Dried and purified SWCNT was then added

to the acid and the mixture was refluxed at 120 °C for 3 hours. The reaction was halted by pouring the mixture into 160 mL chilled water which was then part filtered over a 0.22 µm pore PTFE supported membrane. The wet filter cake was then divided into six centrifuge tubes and made up to 40 mL with water. Samples were then sequentially centrifuged at 3500, 4000 and 4600 rpm for 5 minutes each. After each spin the supernatant was removed and the pellet re-dispersed in new solvents (water for 5 min; 1:1 water:ethanol for 5 min; and 1:1 water:propanol for 30 min respectively). The pellet was finally re-dispersed in water and centrifuged at 3500 rpm from which the supernatant was taken as the final suspended O-SWCNT product.

Electrophoretic Deposition of O-SWCNT: Combined O-SWCNT supernatants are reduced in volume by roto-evaporation until O-SWCNT began to flocculate. Portions of this suspension are then diluted at a 3:1 solvent:suspension ratio with DMAc. These solutions are then bath sonicated for 2 hours and then immediately used to partially submerge two vertical suspended, parallel plate electrodes held 2 cm apart with a surface area of 2 cm x 2 cm. The electrodes were connected to a Genvolt 73030 high voltage power source and a constant voltage of 30 V (15 V cm^{-1}) was applied for 40 minutes. The depositing electrode (anode) was then removed from the solution and the thick, gel like deposit was allowed to collapse and dry into a black buckyfilm.

Reductive Purification of SWCNT: Under an argon atmosphere, stoichiometrically equal amounts of sodium metal and naphthalene are dissolved in DMAc to produce a 1 mg_{Na} mL^{-1} dark green reducing agent. 50 mL of this reducing solution was poured onto 500 mg raw SWCNT starting material in a 1 L glass cafetiere (with metal handle stand removed). The mixture was swirled gently to wet all CNT and then diluted with 500 mL DMAc. This was left to stand for 2 days without stirring, producing a black opaque solution with large flocculation settled at the bottom which was filtered using the cafetiere steel gauze press to remove the liquid. The wet CNT mass was then transferred to a tri-necked 250 mL flask sealed with rubber suba-seals and dry compressed air was bubbled through the material until discharged. Material was then filtered over a 0.2 µm pore PTFE membrane, rewetted and dispersed

with first EtOH, then a 1:1 EtOH:Water and finally acetone solvents. The final purified material was then divided/spread out by tweezers and dried in a vacuum oven at 110 °C

Reduced SWCNT Dispersions: Under an argon atmosphere, stoichiometrically equal amounts of sodium metal and naphthalene were dissolved in DMAc to produce a 1 mg_{Na} mL^{-1} dark green reducing agent. This was then mixed with the required purified SWCNT in a 5:1 atomic C:Na ratio which causes the swelling of the sample which was then further solvated with DMAc until a 1 mg_{CNT} mL^{-1} solution was produced. This mixture was then stirred with a glass stir bead for 1-3 days until the SWCNT was fully dispersed (homogenous thick ochre solution produced).

Electrophoretic Deposition of Reduced SWCNT: Under an argon atmosphere 25 mL of charged SWCNT solution was placed in a 30 mL glass beaker into which two vertical parallel plate electrodes were suspended, each with a surface area of 2.5 cm x 2.5 cm. The anode consists of FTO coated glass secured by copper tape onto which crocodile clips were attached while the cathode was comprised of copper foil. These electrodes were connected to an Autolab PGSTST128N potentiostat which applies a constant 10 V across the electrodes while measuring the current for a given time. Following the application of this voltage, the anode was covered in a thick, even coating of a CNT gel.

Film drying procedure: Horizontal anodes covered in CNT gel was removed from the glovebox and covered loosely with a plastic box into which dry compressed air was pushed to maintain positive pressure within. The CNT gel on the anode surface collapses into a solid film (leaking clear DMAc solvent) when exposed to this air within 5 minutes. This collapsed film was then allowed to dry in ambient air over 1-2 days.

Cast sample preparation: Cast samples prepared as comparisons were created using the same dispersions as used for EPD. Glass microscope slides were placed in a petri dish and then covered by the CNT dispersion to be cast. The petri dish was left to dry in air until all solvent had evaporated. The now covered microscope slides were removed and processed as samples.

Film Washing Procedure: Dried films were removed from the electrode (if free standing) or suspended while still on the electrode (if not) and submerged in a DMAc bath for 1 hour followed by submersion agitated 1:1 water:methanol solution for 24 hours. When removed, samples were dried in a vacuum oven at 120 °C.

4.4 Results and Discussion

4.4.1 Novel Method of Deposition

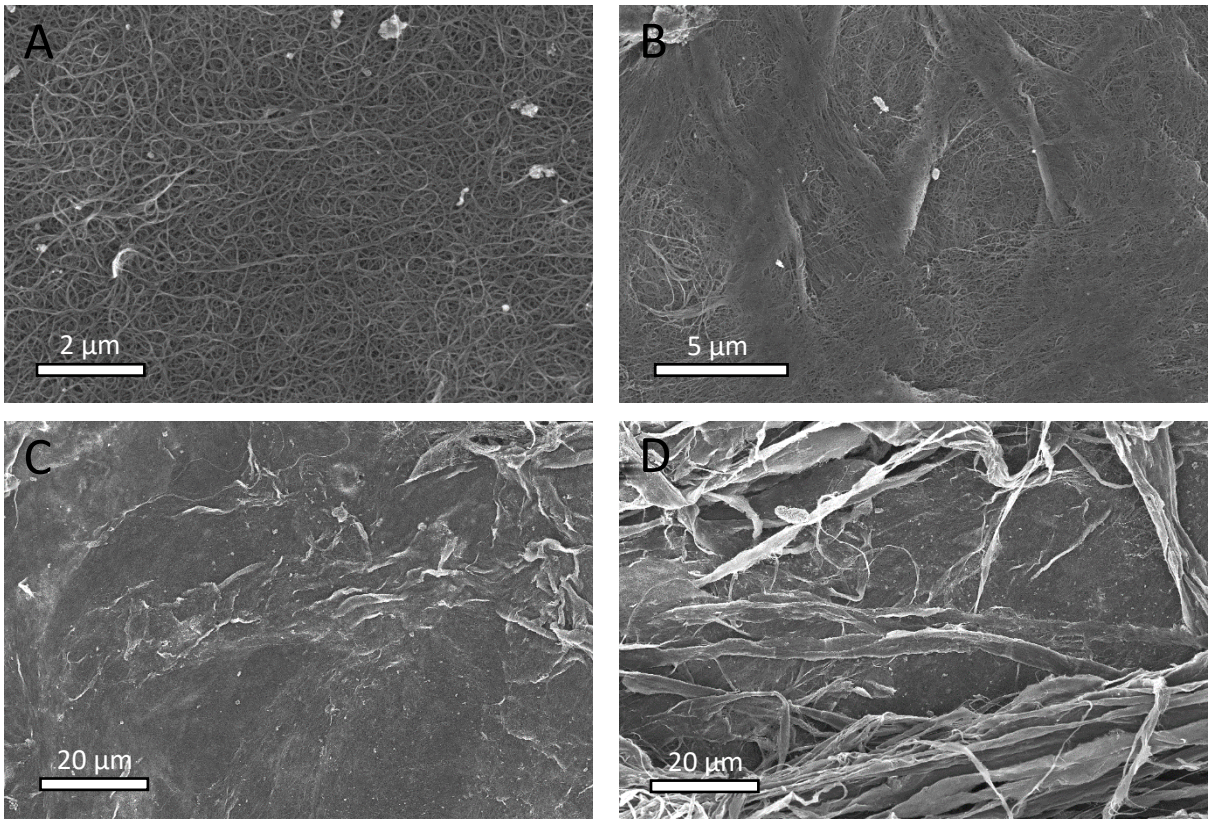


Figure 4.1. SEM of SWCNT Tubal™ starting material. 10kX **[A]**, 5kX **[B]** and 1kX **[C]** magnification shows SWCNT matted together with no significant alignment and a disordered macrostructure while other regions [D] demonstrate the 1D CNT 'rope' structures that some of the material forms. Both matted and rope structures must be broken up during a successful dispersion of the material into solution.

The method to produce CNT buckyfilms described in this chapter is the combination of two established techniques: reduced dispersion and EPD. The initial dry CNT starting material (Figure 4.1) was first reduced under an inert argon atmosphere by a charging solution of sodium naphthalide (NaNap) at a ratio of 5_C:1_{Na}. This reduction caused the CNT mass to swell in size as like charges repel and for the NaNap solution to lose its dark green colouration as the electron transfer occurs. This C:Na charging ratio was chosen as it has been shown to give the highest concentration of CNT into solution[75] and it was assumed that a larger charge would induce a bigger electrophoretic response during EPD.[188] Samples were then diluted to 1.0 mg_{CNT} mL^{-1} and mixed with a glass stir bar (Teflon has been found to

degrade in solution over time) until a thick ochre solution was formed. This ochre solution was observed to be free of visible particulates or CNT flocculation and represents complete individualisation and dispersion of the sample as described by Clancy *et al.*[187]

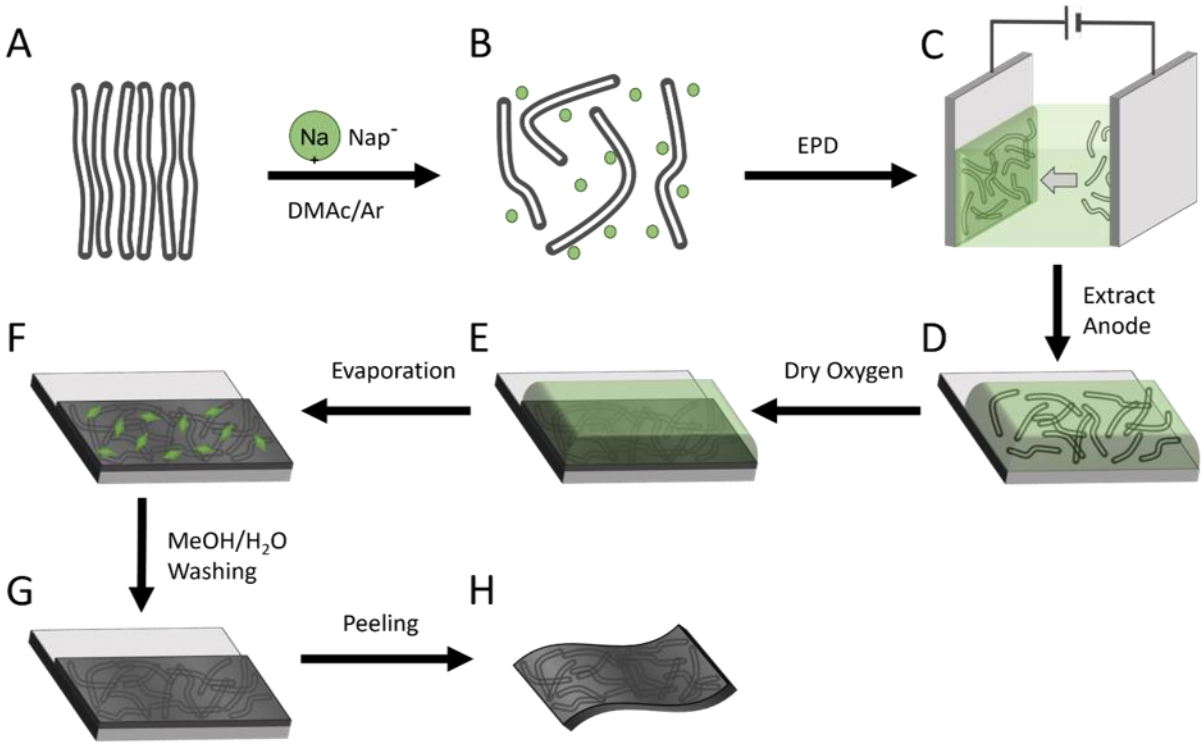


Figure 4.2. A flow diagram illustrating the novel process by which CNT films are created: **[A]** CNT samples are electrochemically charged with a solution of sodium naphthalide under an inert atmosphere causing their dispersion **[B].** In this CNT dispersion a potential difference applied across two immersed electrodes **[C]** causes the formation of a CNT gel on the anodes surface **[D]**. With exposure to oxygen, this gel discharges and collapses into a CNT and solvent components **[E]**. On evaporation of the solvent, sodium crystal impurities ae found on the film surface **[F]** and so a washing procedure produces the final thin **[G]** or free-standing CNT film **[H]** without any impurities.

To compare this chapter's reduced dispersion technique with other, more traditional methods for the EPD of CNT, oxidised CNT dispersions were made using the same Tubal SWCNT starting material that. This was done by oxidation using a sulphuric-nitric acid (H_2SO_4/HNO_3) mixture which is known to degrade the CNT crystallinity but also introduce carboxylic, ketone and alcohol functionality to the nanotube surface[85] allowing them to be suspended into polar solvents. EPD was conducted from these oxidised suspensions using a 30 V potential difference over 30 min which visibly depleted the

dispersion used and produced free standing films that are used throughout this chapter to contrast with the new method described by this work. This system was selected as it represents the most commonly documented 'traditional' method for the EPD of CNT suspensions[48] and it also follows on directly from work conducted within the Grobert group by Xiao et al.[47]

Similarly to the oxidised samples, EPD was conducted by immersing two vertically suspended electrodes 2 cm apart in a beaker containing a CNT dispersion and applying a constant potential difference (10 V as standard) between them (Figure 4.2.C). The maximum field strength of 5 V cm^{-1} used in the method was significantly lower than that used in the literature described oxidation-based methods (15 – 35 V cm^{-1}).[47,48] This may have advantages for wider use as, coupled with the short deposition time, the low potential difference requirement can open this method for use with many solvents that may break down under larger voltages.[77]

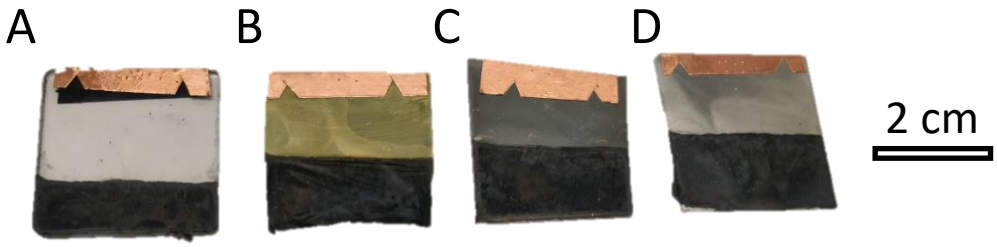


Figure 4.3. Image taken of four different anode materials successfully used to deposit CNT films. The electrodes were cut into 2.5 x 2.5 cm squares and topped with copper tape backed with a conductive adhesive. Although the majority of this work was conducted using FTO coated glass **[A]** in this role, the use of Brass **[B]**, Steel **[C]** and Aluminium **[D]** shows the versatility of this deposition method.

The majority of the films produced in this section were formed using FTO coated glass electrodes (Figure 4.3.A). However, additional testing on reduced dispersions also showed that other conductive electrode materials could be used including copper film as well as brass, steel and aluminium (Figure 4.3.B,C & D). This demonstrates the versatility of this method in coating other materials with the potential of wider applications.

In under 2 minutes, the EPD process was complete, with the anode removed from solution covered in a black gel (Figure 4.2.D) of approximately 3 mm thickness (although difficult to measure accurately while still in the glovebox). The reduced solution used for the EPD was visibly unaffected in consistency or colour and, as long as the concentration remains above ~0.5 mg_{CNT} mL^{-1}, it can be used to create further films (see Figure 4.17.A). In this way it is theoretically possible to re-use charged CNT solutions repeatedly thereby reducing the amount of waste from the process. This is in stark contrast with the oxidised film production method (completed for this work) in which large proportions of the starting material were discarded during the oxidation and purification process (see methods section) through centrifugation and acid damage.

The now coated anode was removed from the inert argon atmosphere it was formed in and placed under a flow of dry air. The use of compressed air in the place of the ambient environment was to prevent atmospheric moisture reacting with any remaining charge on the CNT surface causing hydroxyl functionality decoration[75]. Instead, the removal of excess charge occurred through interaction with oxygen molecules[89] and leaves no damage to the CNT surface or nanostructure. The loss of charge on the nanotubes however, removed the electrostatic force holding up the structure of the thick gel on the anode surface (similar to CNT aerogels produced here[189]) which collapsed into a CNT film wetted by DMAc solvent containing Na and Nap residues (Figure 4.2.E).

On leaving these discharged films to dry, the black CNT film further compacts upon itself (although no shrinkage was observed as seen in other work[47] even in films that would become free standing) and the remaining solvent evaporated to leave a powder on the surface of the material (Figure 4.2.F).

4.4.1.1 Washing Procedure

The white powder found on the surface of the CNT film is a sodium crystal residue which, during the evaporation and drying process, becomes partially imbedded in the film surface (see SEM image Figure 4.4.A). This sodium crystal, as well as remaining naphthalene from the charging solution, needs to be removed to leave a pure CNT film that will not to complicate further applications or uses for of the

material with additional chemical functionalities, as is the case with other EPD methods.[190]

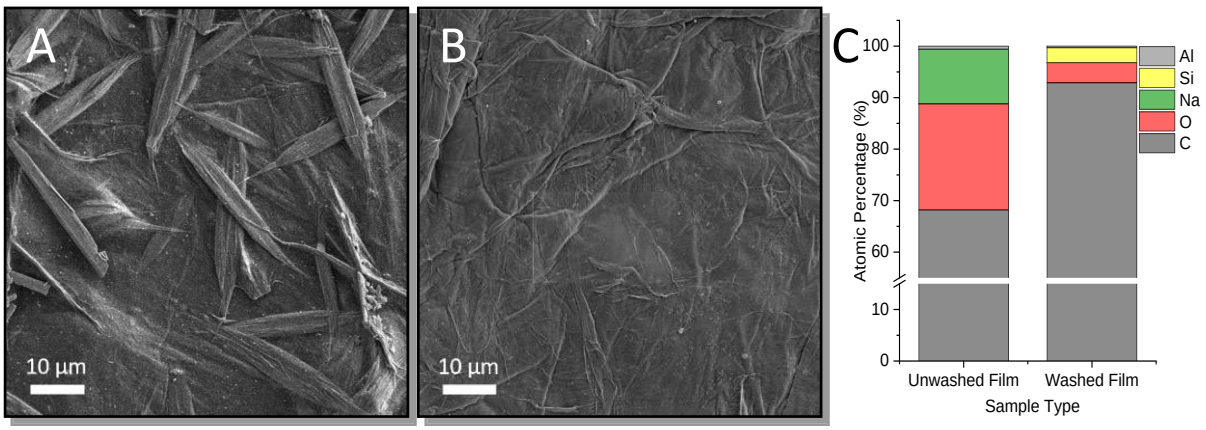


Figure 4.4. SEM images of the surface of the CNT film taken before **[A]** and after **[B]** the washing procedure was carried out. Sodium crystals on the surface of the material (observed as white powder) can be seen partially imbedded in the surface of the film. These are then observed to be completely removed by the washing procedure. EDX measured atomic content of film bulk is compared in **[C]** and shows removal of the sodium content from the CNT bulk.

Residue removal is achieved with sequential washing of the films with DMAc (for the removal of remaining naphthalene) and a MeOH/water solution for 24 hours (to remove the sodium salts). Figure 4.5.A illustrates the profile of films before and after washing showing that the removal of the surface crystal is achieved with no loss of the underlying CNT film thickness. The loss of a sodium atomic fraction in the EDS as well as XPS results of the washed material (Figure 4.4.C and Figure 4.14.F respectively) show the complete removal of sodium not only from the surface crystals but also from the bulk CNT film.

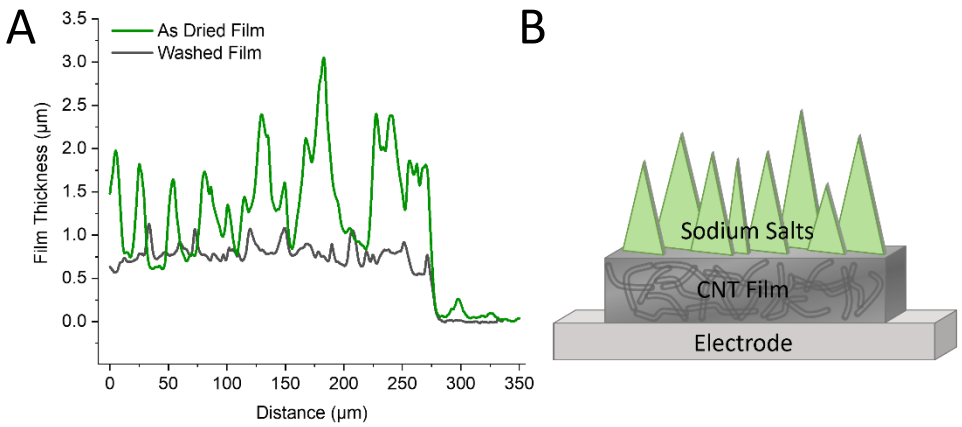


Figure 4.5. The profilometry results **[A]** taken from a thin film before (As Dried Film) and after (Washed Film) the washing procedure showing that only the top rough surface is removed from the material. A simplified diagram of the unwashed films layered structure **[B]** is shown to demonstrate the belief that this profilometry data is the result of the removal of Sodium salts being removed only from the film surface while not damaging the films' structure.

After washing, the now neat CNT film can be peeled away from the surface of the electrode using tweezers to form a free standing and flexible buckypaper. Figure 4.6 shows a representative sample of this final product.

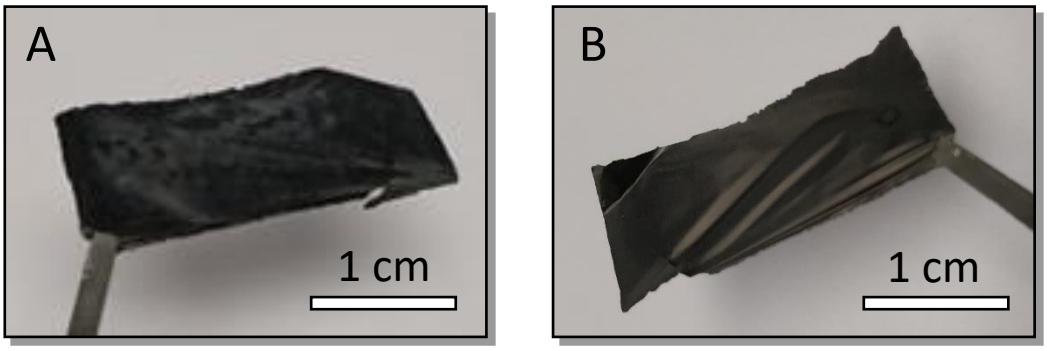


Figure 4.6. Image showing an example free-standing CNT film produced as the final product of the standard method of film production: 120 seconds of deposition at a 10 V potential difference between two electrodes held 2 cm apart immersed in 25 mL of 1 mg_{CNT} mL^{-1} CNT solution charged at a 5_C:1_{Na} ratio. **[A]** shows the unwashed product (anode facing side down) complete with white powder contaminant while **[B]** shows the final washed product (anode facing side up).

4.4.2 Free Standing Film Macro Properties

If this new EPD method is to be useful, the resulting material must utilise the innate assets of its constituent CNTs to have useful material properties. Free standing buckypaper samples produced by reduction and oxidation methods where therefore tested for their material properties.

4.4.2.1 Mechanical Strength

From direct observation, the CNT buckypapers produced by both reduced CNT dispersions as well as oxidised dispersions are flexible and can be bent, folded and unfolded with no apparent damage or degradation (Figure 4.7.A). This is promising for applications in flexible electronics.

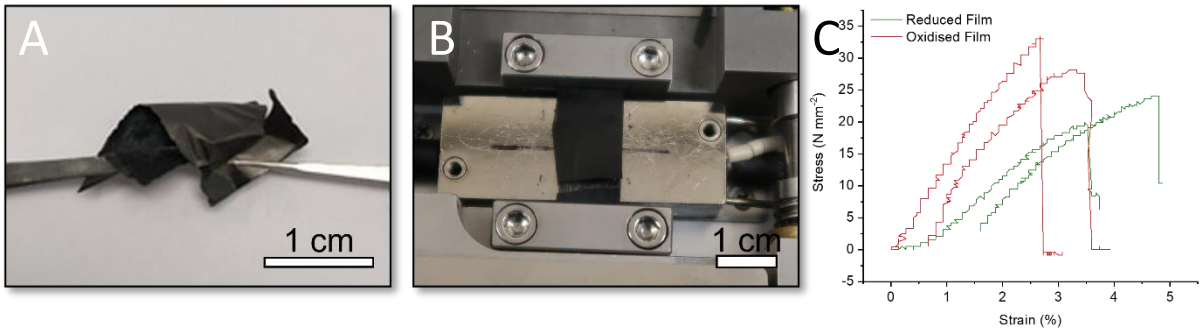


Figure 4.7. Image showing a demonstration of the flexibility of produced free standing films through a 180° bend **[A].** Additional image **[B]** showing a typical fracture of a reduced film sample within the tensile testing machine in which no necking of the sample was observed. The results of these tensile tests* are graphed **[C]** and it is from these that the mechanical properties are calculated.

*Measurements taken by Xudong Tao of the Assender Group

Due to material constraints and experimental priorities, only a small number of free-standing CNT film samples were produced of dimensions that could be measured on the tensile testing machine and so data should be considered only a preliminary study into the mechanical properties of the films. However, the results of the tensile tests (Figure 4.7.C) and the mechanical properties of the films calculated from them (Table 4.2.) show little variation and the errors calculated from them are low. Additionally other studies producing films from single walled CNT have shown similar results (23.6 MPa[191] tensile strength from an unaligned film) so it is believed that these results are still valid and the conclusions drawn from them valuable.

Sample	Youngs Modulus (MPa)		Ultimate Tensile Strength (MPa)		Toughness (MJ m^{-3})	
Reduced	839	±66	21.99	±2.92	0.423	±0.133
Oxidised	1485	±105	30.81	±3.73	0.495	±0.046

Table 4.2. Table of mechanical properties of free-standing films produced using the new reduced EPD method compared to traditional oxidised tubes showing that the traditional method still produces superior mechanical properties.

The mechanical testing results show that the free-standing films produced by the reduced CNT dispersions are significantly inferior to those produced by the traditional method using oxidised dispersions. The traditionally produced material has nearly double the Youngs modulus and a 30% larger tensile strength than the reduced films and, while the reduced films tolerated higher strain rates, the toughness measured from them was still smaller. These results can be explained because CNT surface functionalised with the traditional acid etching method will contain many -COOH and -OH groups that can form strong hydrogen bonds between nanotubes and inevitably result in superior mechanical properties. However, the most likely explanation is the disparity in density between the two sets of samples. The reduced films were found to have a density of 0.34 ±0.07 g cm^{-3} while the oxidised films were 0.53 ±0.04 g cm^{-3}. This will result in significantly more CNT being present at the cross section of the fracture thereby requiring more energy to break. The source of this density discrepancy is explored further in section 4.4.2.3.

The SEM of the materials fracture surfaces demonstrate the difference in tensile properties also. The lower strength but higher strain capable reduced films (Figure 4.8.A and B) show a more ragged edge where CNT has been pulled from the bulk on failure. The stronger but more brittle oxidised material (Figure 4.8.C and D) has a cleaner cut revealing a more homogenous and dense macrostructure.

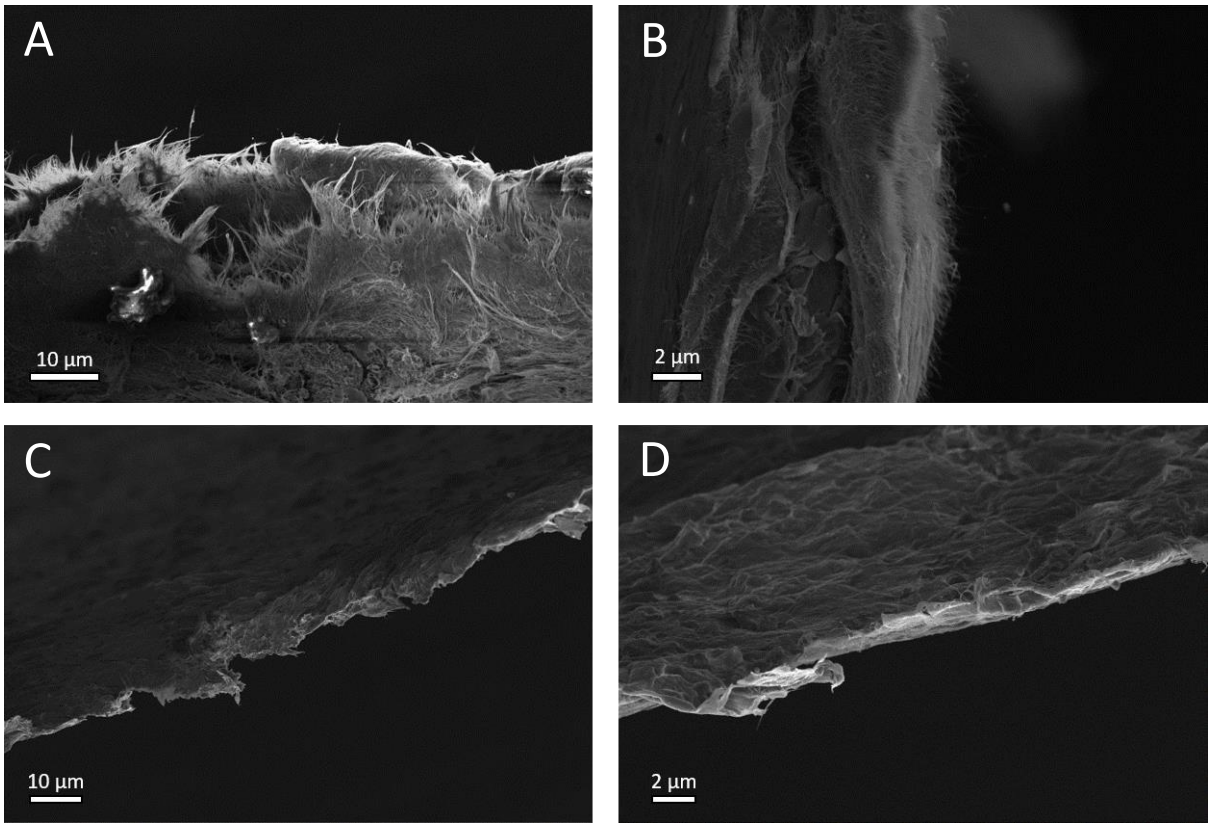


Figure 4.8. SEM images of CNT film fracture surfaces. **[A]** and **[B]** show a reduced film developed in this work which has a more ragged edge and a less homogenous cross sectional macro-structure. **[C]** and **[D]** show the traditional oxidised film fracture surface is more cleanly cut (implying a more brittle fracture) and a more homogenous macro-structure of the cross-section.

While the oxidised films may have stronger mechanical properties than the reduced films, both are still comprised of the same SWCNT starting material. Multi-walled carbon nanotubes have consistently been shown to have superior mechanical properties to their thinner SWCNT alternatives and so it is no surprise that tests conducted by Xiao et al.[47] produced free standing films by the EPD of oxidised MWCNT showed strengths of 60 MPa, double that of this study. While these results are within the same order of magnitude, it must be acknowledged and concluded that if CNT films are required for purely mechanical applications, then the traditional method of production remains the superior technique.

4.4.2.2 Electrical Conductivity of Films

One potential application for CNT films is for use in flexible electronics. While the testing in the previous sections showed that this was possible mechanically, further measurements were carried out using a four-point probe to check the suitability of the free-standing material's electrical conductivity.

Additional to the standard EPD films, cast films using the same dispersions as their EPD equivalents were also measured. The oxidised films were produced using a higher potential difference than that of the reduced films and it was hypothesised that this greater force acting upon the nanotubes may produce films of greater density. It is known that the density of a film is proportional to its conductivity and so the measurement of cast films was therefore conducted to check that the EPD process itself was not causing any difference between samples.

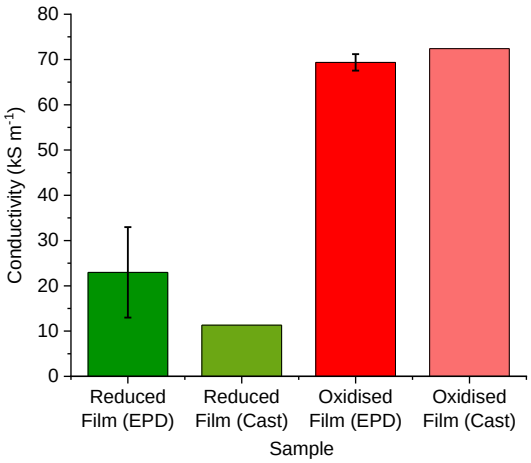


Figure 4.9. Chart showing the sheet conductivities (measured by four-point probe*) for free standing films produced by the two EPD and Cast methods. This clearly shows that the hydroxyl bonded oxidised CNT films are superior. Error bars were calculated from measurements of 3 samples produced by EPD for both oxidised and reduced CNT while Cast films were only created once from residual CNT samples and therefore statistical analysis was not possible

*Measurements taken by Bianca Baur of the Grobert group.

The conductivities of the films were measured and are shown in Figure 4.9. The cast film measurements are very similar to the films produced by EPD and so any differences in

density/conductivity due to the field strength between electrodes was discounted as a source of significant error in the differences between the reduced and oxidised materials. These differences were significant however with the reduced film having a notably lower conductivity of 229 ±99 S cm^{-1} compared to the oxidised films 694 ±18 S cm^{-1}. Previous studies have shown that unfunctionalized SWCNT networks have similar conductivities in thin films[192] (250-400 S cm^{-1}) or thicker ones[191] (170 S cm^{-1}) although these results are still on the higher end of many studies.

The large difference between the reduced and oxidised films is initially counter-intuitive to theory as damage to the CNT nanostructure caused by oxidation should cause a reduction in conductivity of individual nanotubes and thereby make the whole structure less conductive. However, many studies have also found that acid treatments increase the conductivity of CNT films both neat[193] and as fillers in composites.[194] Similar to the explanation in mechanical differences, this is thought to be due to the hydrogen bonding of the oxidised CNT improving inter-nanotube interactions, reducing tube-tube distances and and thereby increasing the electrical conductivity between nanotubes. Additionally, the differences in density (0.34 vs 0.53 g cm^{-1}) between the reduced and oxidised samples mean fewer CNT are available in the reduced samples cross section to facilitate charge transfer. This sub-optimum performance due to a lower density of the reduced films is because of cavities found in them.

4.4.2.3 Sub-optimal Macro Property Explanation

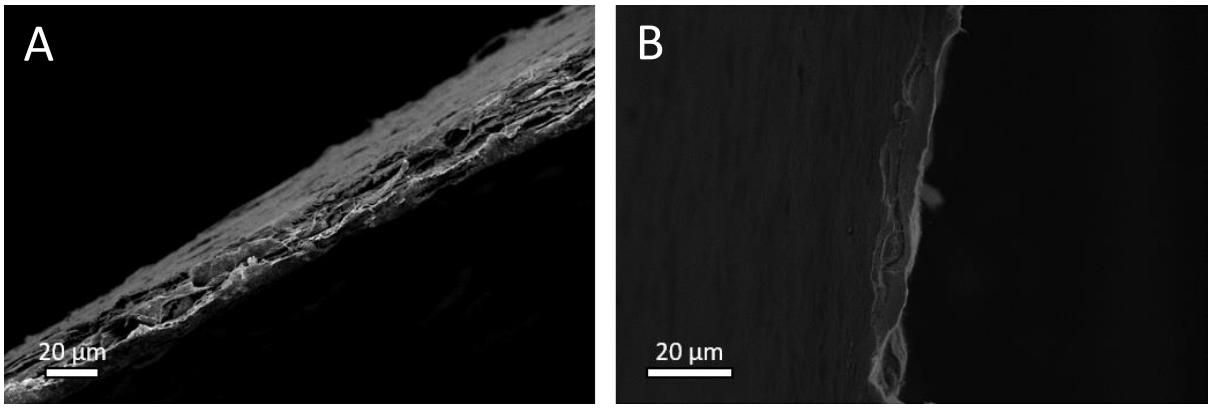


Figure 4.10. SEM of CNT film cross sections demonstrating differences in macro-structure. The reduced film **[A]** cross section shows a layered structure with numerous pores both between and inside these layers. The oxidised film **[B]** is also layered but does not exhibit any holes/gaps/pores and is therefore a denser material.

For both the mechanical and electrical conductivity testing that was conducted on the free-standing films, the properties of the oxidised produced films were consistently superior to those of the new reduced method developed in this work. While some of this can be explained by the hydrogen bonding present on the oxidised nanotubes, as has been previously explored, another possibility is the presence of cavities found within the reduced film macrostructure.

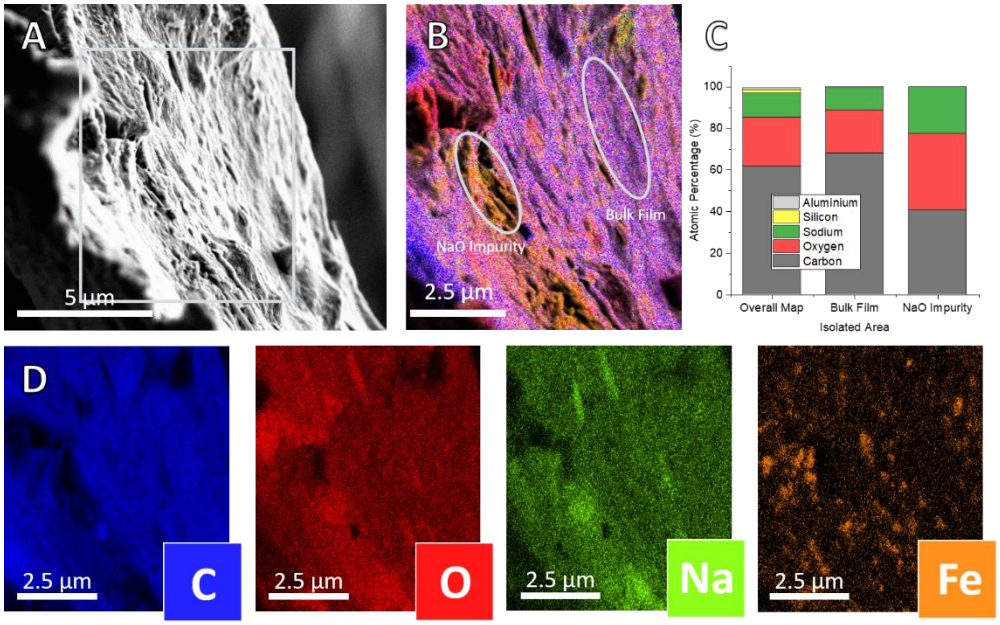


Figure 4.11. Microscopy of unwashed CNT film cross section. **[A]** SEM image of CNT film edge obtained by tearing film. **[B]** EDS image of cross section with isolated regions for further analysis highlighted. **[C]** Bar chart showing atomic composition of different regions of the EDS image (note that Al and Si content can be explain by the SEM sample mount). **[D]** individual atomic maps showing both sodium oxide and iron oxide localisations within the film structure. The iron content is a relic from the starting material synthesis.

SEM and EDS of the cross sections for reduced films both before and after the washing procedure were taken and are shown in Figure 4.10. These images show inconsistencies both in texture and composition within the films' macro-structure. Atomic composition analysis (Figure 11.C) confirms that these impurities are localised and of a similar constitution as the sodium crystals found on the surface of the films after drying, being comprised of sodium and oxygen. These impurities are assumed to be non-conductive (as are most ionic salts) and poorly attached to the surrounding CNT (as were the surface residues that would fall from the CNT film surface when inverted).

While these impurities are in the unwashed film, their presence is assumed to inhibit the mechanical strength and electrical conductivity of the final film product. However, after the washing procedure, previous results indicated that these salts were completely removed from the material. To ensure that this was the case throughout the thicker free-standing materials, further SEM and EDS were carried out on the cross sections of washed films and are presented in Figure 4.12. The SEM shows dark

patches across some areas of the cross section implying either elemental variation or the shadow cast by empty cavities. EDS and atomic analysis (Figure 4.12.C) of these areas compared to the bulk material shows that these regions are a mixture of cavities as well as small residues of sodium salts. The sodium content found in these regions was 1.2 % compared to the unwashed film proportion of 22.5 % and the overall sample EDS map found negligible sodium. This order of magnitude difference found in only the thickest (and so most difficult to wash) films shows that the washing procedure is still effective and valid for use on the more numerously produced thin films used in this study.

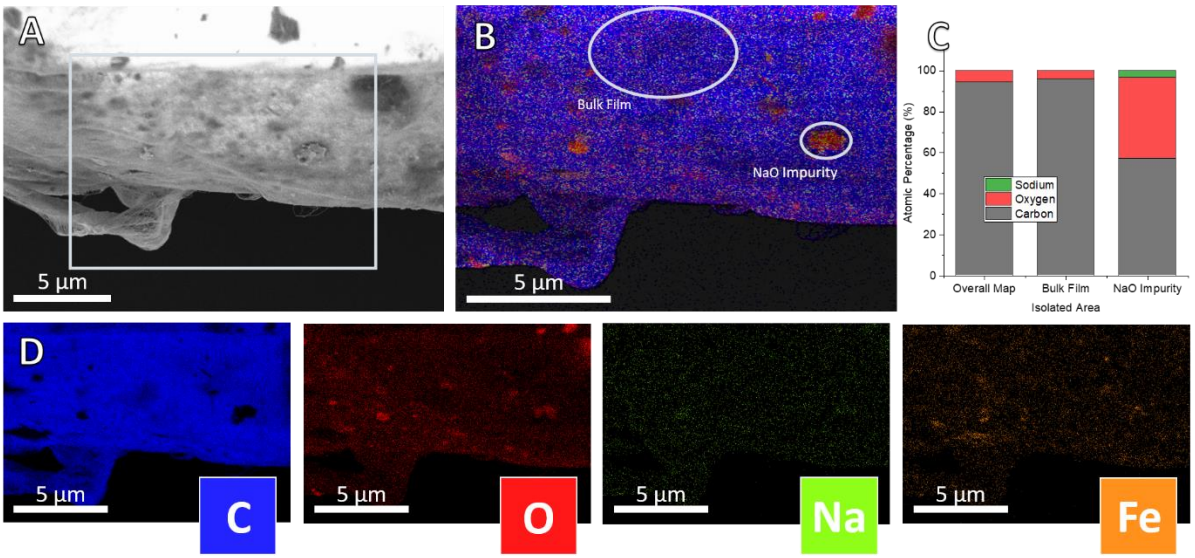


Figure 4.12. Microscopy of washed CNT film cross section. **[A]** SEM image of CNT film edge obtained by tearing film showing cavities within film structure. **[B]** EDS image of cross section with isolated regions for further analysis highlighted. **[C]** Bar chart showing atomic composition of different regions of the EDS image showing majority of sodium is removed but remains in some locations. **[D]** individual atomic maps showing oxide and cavity localisations within the film structure.

Despite the washing procedure being shown to be effective at impurity removal, the presence of these cavities can explain the poor performance of the reduced films compared to the traditional oxidised films. The holes within the film structure reduce the density of the material so reducing its electrical conductivity as well as providing weak points throughout its macrostructure through which crack propagation can occur leading to early mechanical failure.

While this does seem to be a downside to the material produced by the reduced dissolution method, the presumed increase in surface area of the films that should be created by these pores can potentially have advantage in catalytic or electrode applications where strong materials with a larger surface area are desired. This possibility could be taken even further by utilising the chemistry developed by De Marco et al.[189] where the reduced CNT gel could be held in place by the cross linking of 1,4-diiodobenzene to create high surface area, conductive aerogels from CNTs. Additionally, the very proof of viability for the reduced dispersion for EPD method for film production may allow the deposition of nanomaterials impervious to the traditional oxidation approach (which will be shown in section 7.4.2.3 for BNP).

4.4.3 Film Nano-Structure

The CNT film produced by the reduced dispersion method does not improve upon the mechanical and electrical properties of the traditional oxidised procedure. However, the final product is still flexible, mechanically strong, and electrically conductive. This has been achieved using a fabrication method that is simple, fast and gives a high yield while needing low voltages. Arguably the most important feature of this method is the complete retention of the starting material's nanostructure during its incorporation into the film.

This section will show that, in contrast to the traditional oxidation method, the CNT nanostructure of the starting material is maintained into the final film product using the reduced dispersion for EPD. The nanostructure of CNTs define their properties and much research and effort has gone into creating or separating nanotubes of specific proportions or chiralities[195] which could be lost/degraded using the traditional oxidation method.

4.4.3.1 Raman Analysis

For CNT structures, the relative intensity of the D (1360 cm^{-1}) and G (1582 cm^{-1}) peaks within their Raman spectra indicate the relative amount of non-graphitic and graphitic bonding within a sample respectively[140,139] and so are a good indication as to change in the material's nanostructure.

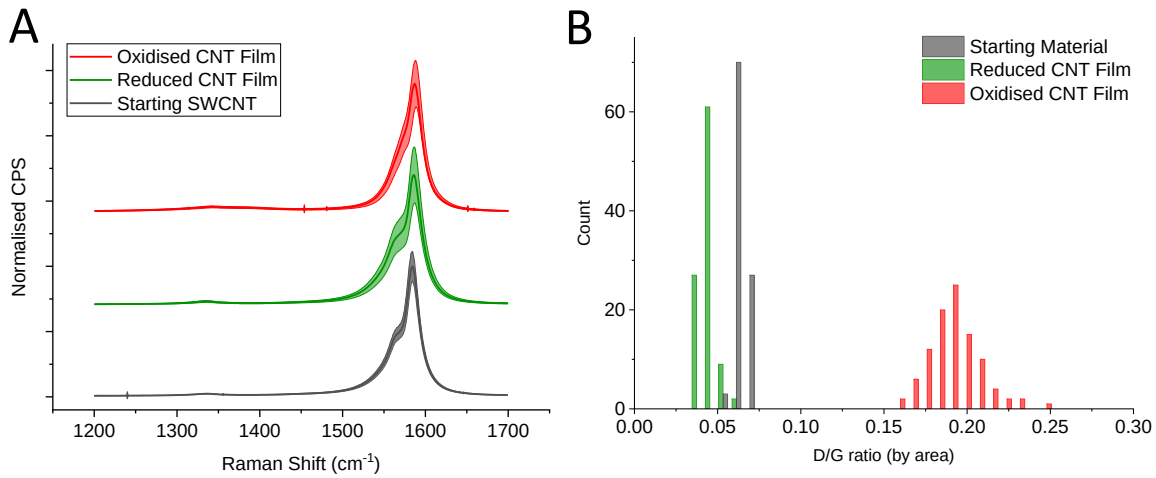


Figure 4.13. Raman results comparing the CNT starting material, reduced film and oxidised film. The average of a hundred spectra with standard deviations is shown in **[A]** and show that the D peak is very small for all samples. A histogram of D/G ratios (by area) from these Raman spectra **[B]** shows that the reduced film retains the nanostructure of the starting material.

Figure 4.13 shows the cumulative results for Raman spectra of the oxidised, reduced and starting CNT. Due to the high crystallinity of the SWCNT used for this study, the D peaks are small for all spectra so the relative areas for the D and G peaks were compared and used to create the D/G ratio distribution. As can be seen, the D/G ratios for the starting material and reduced films are very similar, showing no change of graphitic structure within the CNT. This is in contrast to the D/G distribution of the oxidised film CNTs which have both a wider distribution of D/G ratios (implying CNT dis-uniformity within the sample) as well as higher ratios (implying lower levels of graphitisation compared to the starting material).

4.4.3.2 XPS Analysis

Film samples were analysed *via* XPS analysis and a comparison was made to the starting material. The comparison of the C1s XPS spectra (Figure 4.14.D) with the final washed film produced by this works method, shows that the carbon bonding environment is 84.2 ±1.2% constituted of sp^2 C=C bonds (284.4 eV)[151] as is expected of a graphitic material. This is very similar to the sp^2 C=C content of the starting material (Figure 4.14.A) at 83.7 ±0.7%, but the spectra vary slightly in their respective sp^3 C-C (285.1 eV)[146,196] and C-O (286.3 eV) bonding content: the finished film has a lower oxygen bonding content (3.0 ±0.2 % vs 8.2 ±0.3 % respectively). These minor differences are insignificant however, when compared to the damage that is caused to the CNT nanostructure by purposeful functionalisation as illustrated by the C1s XPS of the comparative oxidised CNT film (Figure 4.14.B). A summary of these differences is shown in Figure 4.14.E in which the non-graphitic C-C, C-O and C=O content of the oxidised tubes is nearly double (30.2%) that of both the starting material (16.2%) and the reduced dispersion produced washed films (15.8%). This loss of graphitic structure affects the individual nanotubes within the film and emphasises that the traditional oxidation method is inappropriate for applications where retention of the initial nanostructure is required.

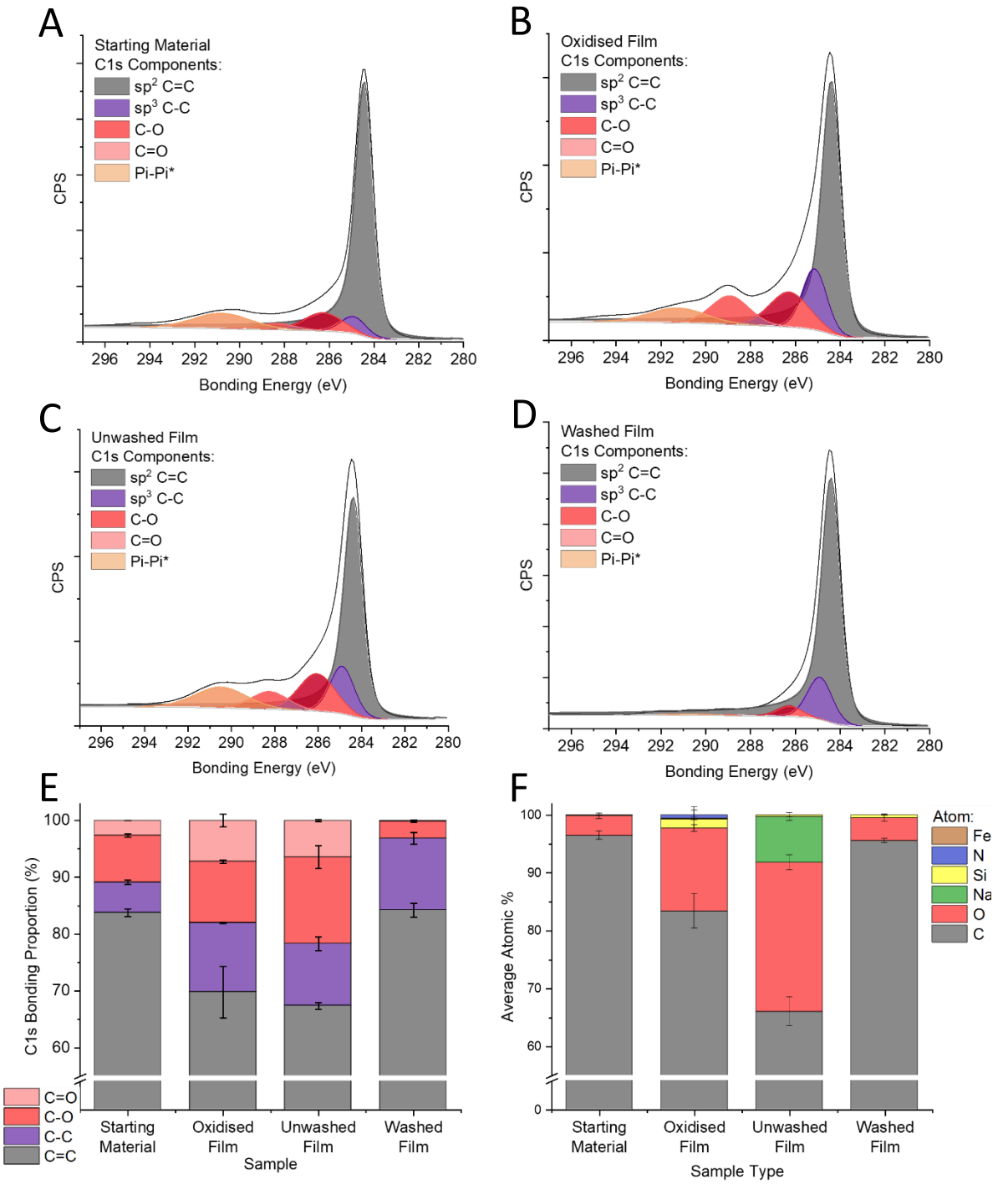


Figure 4.14. XPS analysis showing CNT retention of nanostructure after film production compared to traditional oxidation methods. De-convoluted C1s XPS analysis of Tubal SWCNT starting material **[A]**, traditionally oxidised CNT produced films **[B],** unwashed reduced film **[C]** and final, washed film **[D]**. A summary of these C1s deconvolutions **[C]** shows that the final washed films contain significantly less carbon-oxygen bonding than the oxidised film and the same sp^2 C=C bonding to the starting material implying little or no change to the nanostructure. XPS atomic composition analysis **[F]** similarly shows no change in the film compared to the starting material while the oxidised film contains significantly more heteroatom content.

4.4.3.3 TGA Analysis

One way in which this retention of CNT nanostructure can be demonstrated to benefit the final CNT film is through analysis of thermogravimetric (TGA) data (Figure 4.15). The starting material CNT decomposes in air at 701 ±14 °C while the oxidised CNT film decomposes at the much lower temperature of 627 ±7 °C in addition to a gradual loss of mass prior to this point due to its various defects. This contrasts with the reduced film product of this work which decomposes at 689 ±6 °C re-enforcing the point that the retention of nanostructure from the starting material has occurred. These results are consistent with literature that has shown an increase in graphitization of CNT samples can lead to an increased oxidation temperature by as much as 155°C.[168]

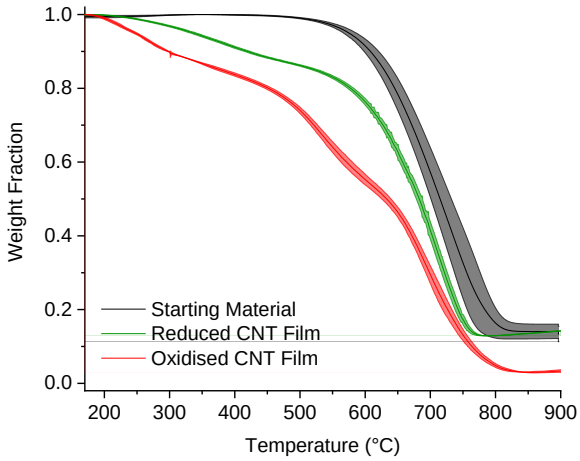


Figure 4.15. Thermogravimetric analysis of CNT samples. The average TGA curve for a material is plotted with the error between values for each point coloured on either side. The starting material CNT powder's decomposition temperature (701 ±14 °C) is compared to that of the films produced by EPD using the reduced (689 ±6 °C) and traditional oxidation (627 ±7 °C) methods. The mass losses at <500 °C in both film samples are presumed to be residual small organic molecules trapped within the dense film structure which is not seen in the loosely packed and unprocessed starting material. The mass loss at 520 °C for the oxidised film can be identified as amorphous and oxidised carbon created during the acid etching process prior to the films deposition and has been observed previously by *A.* Mahajan *et al.* [268]

4.4.4 Mechanism of Deposition

While it has been shown that this method of CNT film production allows for the retention of CNT nanostructure, to fully allow others to take advantage of this technique it is important to understand

in depth the deposition process so that its adaptation to other materials can be as smooth as possible. To this end, multiple studies were conducted by altering controllable variables.

4.4.4.1 Deposition Rate

The simplest parameter to control that effects film deposition when creating CNT films by EPD is the time over which the deposition takes place (Hamakers law, Eq 2.1). Films were therefore produced from a 1 mg_{CNT} mL^{-1} reduced solution using a 5 V cm^{-1} field strength while varying the time for which this voltage was applied between 0 and 60 seconds (where 0 was measured by immersing an electrode, connected to the circuit, in the solution but refraining from turning on the potentiostat).

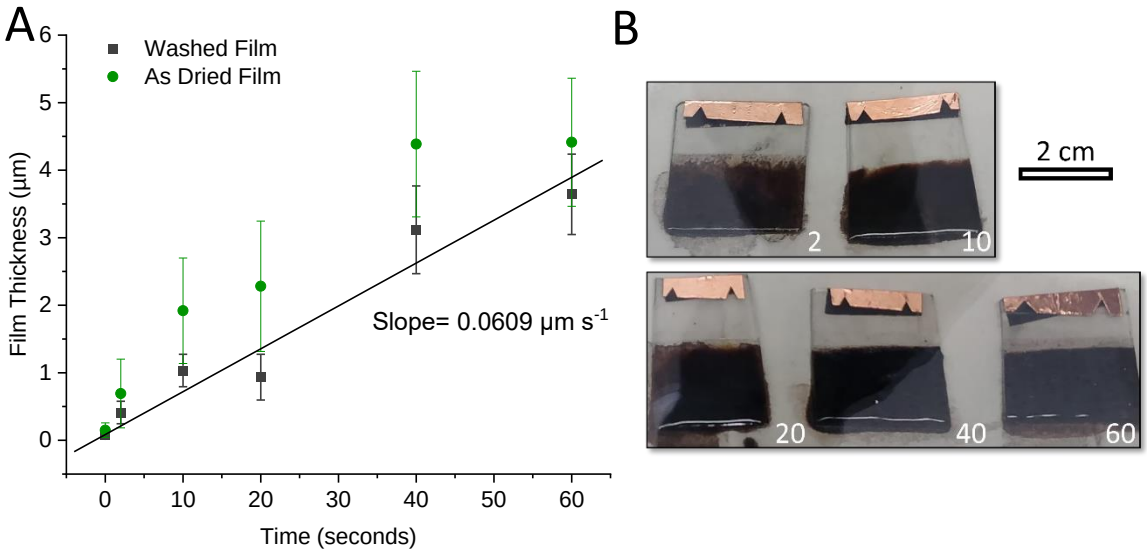


Figure 4.16. The thickness of films produced both before and after washing is plotted against the time taken for EPD **[A]** and shows the expected trend of proportional increase of deposition with time although this begins to lose linearity past 60 seconds due to vertical slippage. The slope is calculated to show the rate of deposition. The CNT gel phase of the manufacture process is imaged **[B]** for each of these times (numbered in seconds on each image) and illustrates the increase in CNT coverage.

The results of this variation are shown in Figure 4.16 and display the expected linear relationship (as all other variables described by Hamakers law remained constant) between deposition time and the resulting film thickness. Using this data, as well as the average reduced films density (calculated as 0.34 ±0.07 g cm^{-3} from free standing films), a deposition rate of 0.122 mg cm^{-2} s^{-1} was determined. This is significantly faster than the rate calculated for the comparative oxidised CNT which was found

to be 0.056 mg cm^{-2} s^{-1} (from an average density of 0.53 ±0.04 g cm^{-3}), in part due to the longer deposition times required for film creation. Additionally, the complete depletion of the oxidised CNT dispersion after EPD implies a lower concentration of nanomaterial within the oxidised system which will further reduce the speed of deposition.

4.4.4.2 Concentration of CNT Solution

As mentioned, concentration of the nanomaterial suspended within the dispersion has a large effect on the viability of a film creation within an EPD system as well as the final films' thickness/deposition rate (variable C_s in Hamakers law, Eq 2.1). The variation of the dispersion concentration was therefore tested by producing five 30 mL reduced solutions of concentrations varying between 0.1 and 1.33 mg_{CNT} mL^{-1} and conducting EPD on them for 120 s using a 5 V cm^{-1} field strength between an FTO anode and a copper foil cathode.

The thickness of the resultant films was plotted against this CNT concentration in Figure 4.17.A and shows a sigmoidal relationship. This trend can be explained by dividing the graph into three distinct conceptual regions (Figure 4.17.B).

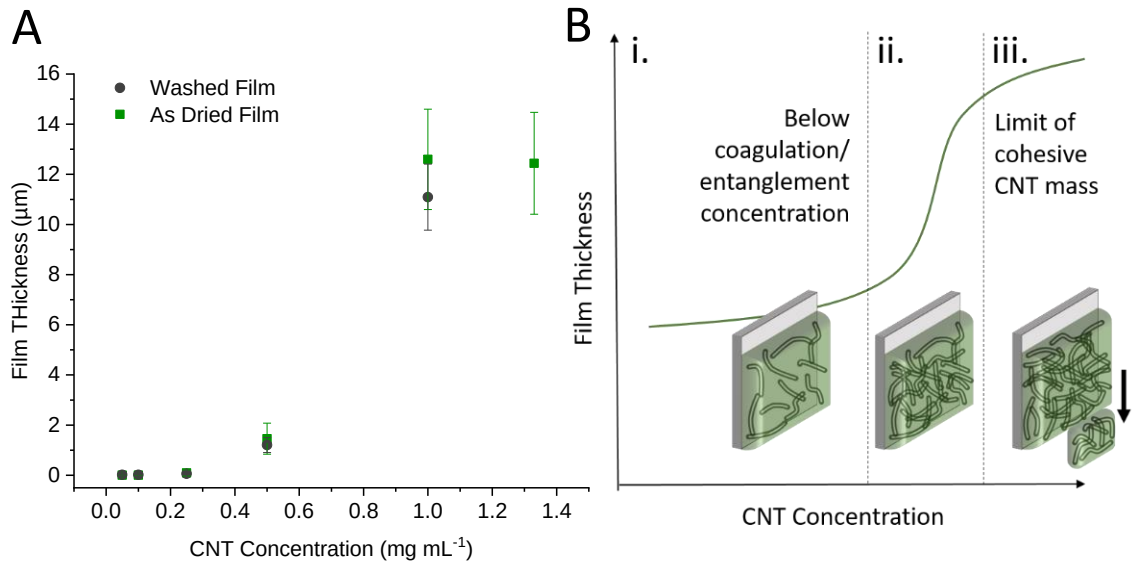


Figure 4.17. The thickness of films produced in different concentrations of CNT solution **[A]** shows a sigmoidal relationship. This sigmoidal relationship between thickness and CNT concentration is explained in **[B]** by dividing the curve into three hypothetical regions in which different forces effect the deposition of CNT. Note: that the final 1.33 mg mL^{-1} washed film result is missing due to delamination of the film during the washing procedure.

Below a certain concentration (Figure 4.17.B*i*) there is not enough CNT concentrated either in the solution on locally on the anode to overcome the charge induced inter-CNT repulsion and so no film can be formed. In the next region (Figure 4.17.B*ii*) the local CNT levels at the anode are above the critical concentration required for coagulation and so the film thickness is proportional to the amount of CNT available in solution that can be transported by electrophoresis to the anode within the 120 s over which the experiment is conducted. However, this increase in film thickness with CNT concentration is not infinite (Figure 4.17.B*iii*) as it has been observed that the weight of the CNT gel that forms on the electrode becomes too large to be self-supporting and either falls away into the dispersion or causes large sections of the film to slide away from the electrode, thereby limiting the final dried film thicknesses to approx. 10 µm. This sliding effect can be seen in the images of Figure 4.16.B where the very top of the CNT gels (closest to the Cu tape connections) show a slightly thinner CNT covering. It is thought that further work could improve upon this limiting thickness by altering the

C:Na charge ratio within the dispersion, thereby changing the inter-tube repulsive forces governing the gel structure, although this would, in turn, limit the CNT dispersion concentration.[75]

4.4.4.3 Field Strength Variation

As shown, film deposition rate (as represented by final film thickness after a fixed period of EPD time) is governed by the CNT concentration of the dispersion but is also altered by the speed at which CNT can be concentrated on the surface of the anode. It is unsurprising therefore, that when the force acting upon the CNT solution is enlarged by increasing the potential difference applied across the two electrodes, that the film thickness is increased proportionally as predicted by Hamakers law (variable E in Eq 2.1.) and shown experimentally in Figure 4.18.A

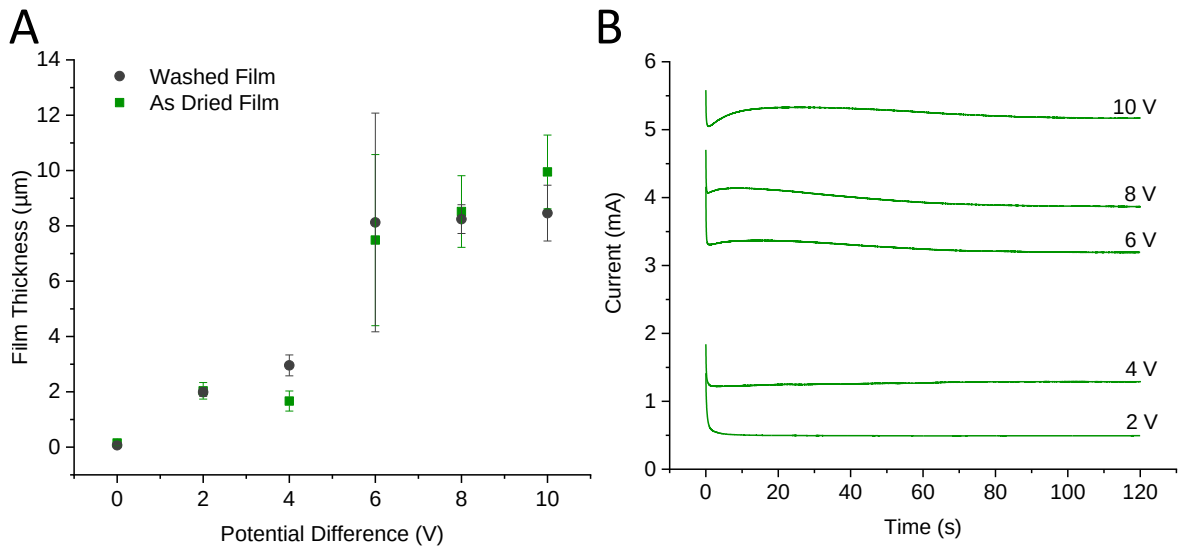


Figure 4.18. The relationship of varying potential difference between the electrodes during a 120 second EPD on 1 mg_{CNT} mL^{-1} solution and the final film thickness (both of before and after washing) is shown to be linear **[A]**. The relationship between the potential difference and the current flow between the electrodes is also shown **[B]**.

These films were manufactured using a 1mg_{CNT} mL^{-1} solution and it is interesting to note that with even the smallest measured field strength of 1 V cm^{-1} (2 V potential difference), this was enough force to concentrate CNT on the anode in large enough amounts to cause deposition. This shows that other solvents, that may be more prone to decomposition, could be used in this method, thereby broadening its versatility and application.

Another notable result from the variation of field strength data was the relationship between the current output of the EPD setup and the final film thickness produced. The current/time graphs for each deposition are plotted together in Figure 4.18.B showing the current output is a function of the voltage applied. The increased force acting upon the charged CNT caused by the larger field strengths causes a faster deposition rate and so a larger current flow and thicker resulting film.

The current flow during EPD can additionally be used to calculate the total charge transfer that occurs during film formation (as opposed to waiting for the film to dry before measurement). When plotted against the final thickness of these materials (Figure 4.19), a linear relationship is observed. Despite the EPD process being possible without charge transfer at the electrodes as proposed by Hamaker,[122] these results indicate that charge transfer can be used as an alternative measure of EPD film thickness during production instead of waiting until after the final material is dry to make these measurements. It is therefore hypothesised that this alternative measurement system could be opened up to wider industrial applications.

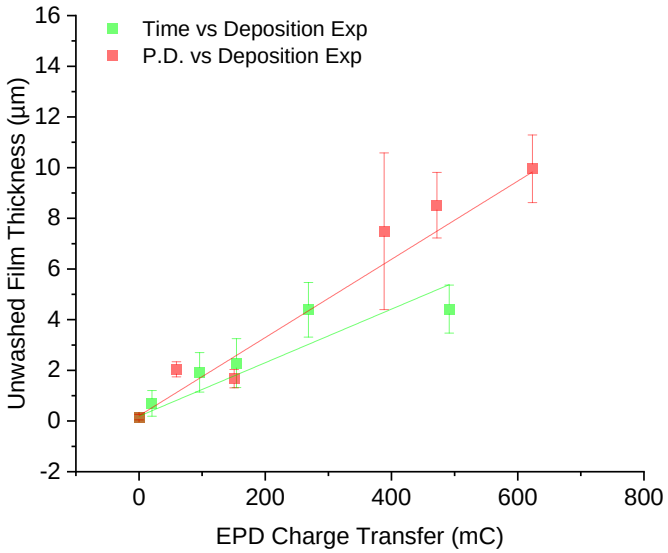


Figure 4.19. Using the integration of the measured current-time curves created during EPD, the total charge transfer for a deposition can be calculated and is shown here to be directly proportional to the final film thickness of the washed film for the results from both the time and potential difference (P.D.) variation experiments.

4.4.4.4 Explanation of Current-Time Result

Even further understanding of the CNT deposition process can be inferred from the current output of the electrodes during EPD. A typical current/time curve for one of these experiments can be said to be split into three hypothetical regions as is displayed in Figure 4.20.

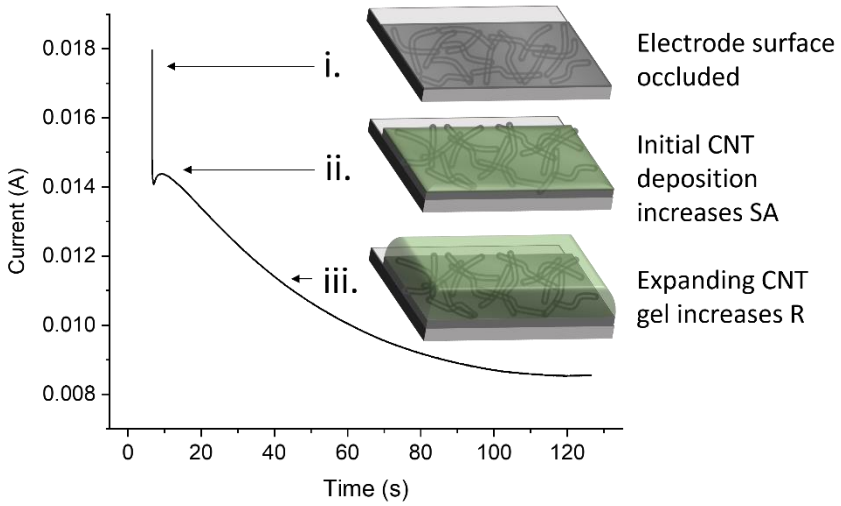


Figure 4.20. The theoretical chronology of deposition is explained through the analysis of a typical current/time curve recorded during EPD by analysing three sections. SA refers to surface area and R refers to electrical resistance.

Initially (Figure 4.20.*i*) the controlling potentiostat sets the voltage between the electrodes and immediately the surrounding CNT, within the dispersion, contacts the electrode surface occluding it from the remaining solution and thereby effectively increasing the electrode's resistance and thereby reducing the current measured. Next, as the localised concentration of CNT becomes high enough to form a film on the electrodes' surface, the electrically conductive CNT film artificially increases the electrodes' surface area and so temporarily increases the current observed (Figure 4.20.*ii*). This effect is not observed when the nanomaterial being deposited is not electrically conductive (see section 5.4.5.3). Finally, the film thickness grows further and the electrical resistance between the solution and electrode steadily increases, thereby reducing the current. It should be noted that the current does not decrease due to the depletion of CNT in solution as the fraction of overall CNT formed into a film (approx. 3 % for a 2.5 cm x 1 cm x 12 µm film sample from a 30 mL solution) is negligible.

4.4.4.5 Error Check: Solvent and Reducing Agent

While the information extracted from the current/time graphs can be corroborated by their relationship to the final film products and theory, potential sources of error within these measurements must also be investigated if only to eliminate them as possibilities.

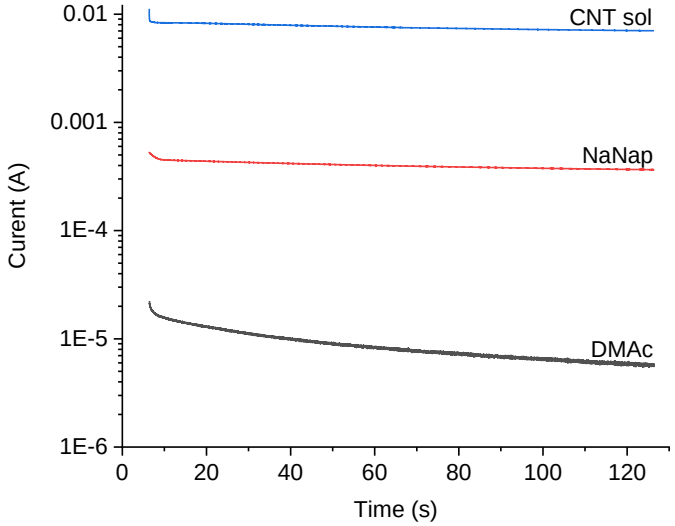


Figure 4.21. Current/Time graph of electrodes held at 10 V immersed in 25 mL of three different solutions: a typical 1 mg mL^{-1} CNT dispersion; a 0.2 mg mL^{-1} sodium naphthalide charging solution and pure DMAc solvent. This shows that the vast majority of current measured during EPD of nanotube is due to the nanotubes.

A likely source of this error is that the current flow measured is the result of processes other than the deposition/discharge of CNT forming a film. Other potentially charged particles within the solution are from the NaNap charging solution and from the breakdown of the solvent at the electrode. By conducting EPD on solutions of the same charge concentration of NaNap and of neat DMAc at 10 V (highest V possible to induce largest response, if any), their current/time curves can be compared to that of a typical reduced CNT deposition in Figure 4.21. This shows that the current signal from the CNT is orders of magnitude larger than the signals from both the NaNap solution and DMAc, meaning that results from CNT EPD can be fully attributed to the nanomaterial with no error.

4.5 Summary and Conclusions

This Chapter has described and demonstrated the value of a novel method for producing neat free-standing and thin CNT films. The reduction and subsequent dissolution of CNT, in high enough concentration (>0.5 mg mL^{-1}), is shown to be an excellent dispersion for EPD. This can produce films with a controlled thickness (0-14 µm) in a short amount of time (5-120 s), using field strengths (1-5 V cm^{-1}). A washing procedure for the removal of remaining discharged reducing agent from produced films was confirmed to remove all impurities from the film surface leaving a pure CNT material with only minor impurities found in the centre of the macrostructures of only the thickest samples. The removal of these impurities due to this washing process causes cavities to be formed in the centre of these thicker films leading them to have worse electrical conductivity and mechanical strength than a comparison film made using an oxidation method.

Despite this, the reduced dispersion manufactured film was then proved to be comprised of CNT with near identical nanostructure to that of the starting material, which contrasts more favourably with the traditional methods of film production. This was further emphasised by showing that the reduced film retained its thermal degradation resistance compared to the oxidised films.

Finally, the variables that control the EPD mechanism were investigated, and it was shown that the deposition process follows the expected trends as laid out by EPD coagulation theory and Hamakers Law but can additionally still be predicted by current measurements. It is anticipated by the author that this work will provide useful method for film production that can be both expanded for use in CNT film production but also adapted to apply to other nanomaterials.

5 REDUCED BNNT FOR EPD

5.1 ABSTRACT

This chapter develops the scope of the reduced dispersion for EPD method developed in Chapter 4 by proving the viability of producing free-standing films and coatings from hexagonal boron nitride nanotubes (BNNT). Similarly structured to CNT, but electrically insulating, this novel starting material has never before been charged by electrochemical reduction. This work demonstrates that the BNNT used do not accept as high a charge density as SWCNT ($<41_{BN}:1_{Na}$ vs $5_{CNT}:1_{Na}$) but still produces films of pure nanotube with no nano-structural damage from the process as determined by Raman, TGA and XPS analysis. This is the first report to detail pure BNNT film fabrication by EPD, so it is not comparable to other literature methods for this nanomaterial as was possible using the oxidised CNT discussed in Chapter 4. Despite this, BNNT reductive dispersion for EPD is shown to produce films up to 35 µm thick (compared to <14 µm for SWCNT) at a deposition rate measured at 2.03 µg cm^{-2} min^{-1} (significantly lower than 0.122 mg cm^{-2} s^{-1} for reduced CNT).

5.2 INTRODUCTION

Boron nitride nanotubes (BNNT) are analogous to carbon nanotubes (CNT), and are made from hexagonally bonded alternate boron and nitrogen atoms in the place of carbon. BNNT structures that consist of ionic B-N bonds make the material electrically insulating[8] while still retaining a strength[20] and thermal conductivity[23] similar to CNT (see section 1.1.). BNNT may even surpass CNT in some areas, as recent measurements have shown that it can form stronger binding interfaces with polymers when incorporated into composites[197] and can improve the thermal conductivity of ceramic films.[198]

These properties within composite materials are interesting for a wide range of applications. For example, thin films have been produced by annealing precursors to a chosen surface at high temperature to produce superhydrophobic (170° contact angle) coatings.[118] However, BNNTs relative novelty and expense as a material has meant that limited research has so far been conducted into their application for neat films and near zero have used EPD for their production. Therefore, to appreciate the true extent of potential applications for BNNT films, studies using the cheaper and more widely available 2D BN nanomaterials should be examined (as is additionally explored in this works chapters 6 and 7).

EPD has been employed for use in the fabrication of these 2D BN materials because it is, as Walsh et al.[199] express, "*capable to do deposition on complex geometry shapes with achievable, controllable thickness, easy setup, and low cost process set-up*". These systems have been used to create chitosan/BN films[44] with antibacterial properties; BN nanosheet corrosion resistant copper coatings[45] as well as BN medical surfaces with high potential for bioactive materials.[125] 2D boron nitride platelets (BNP) are analogous to graphite in structure and these applications described in literature utilise the chemical stability and electrical insulation properties that they share with BNNT. However, due to its 1D morphology, BNNT has further potential uses for mechanical applications. Additionally, while these examples show the range of applications for BN material films, they all contain none-BN additives which can restrict the utilisation of the BN material properties. Alternative methods require the

chemical functionalisation of the BNNT prior to dispersion and deposition[200] which can damage the materials nanostructure by interrupting its B-N bonds to create other functionalities.

Chapter 4 of this thesis introduced and explored the novel reduced dispersions for EPD method to create nanotube films without the need for chemical functionalisation or additive inclusion. This chapter applies this method to BNNT film manufacture, proving its viability, and exploring the differences this change in starting material imposes on the method.

5.3 EXPERIMENTAL

A series of experiments were designed and are described here to show how the reduced dispersion and deposition method (Chapter 4) can produce both coatings and free-standing films of pure BNNT, free of additives and with no nano-structural damage.

5.3.1 Chemicals

Material Name	**Abbreviation**	**Supplier**
Boron Nitride Nanotubes	BNNT	BNNT Materials LLC
Boron Nitride Nanotubes	BNNT	BNNT Materials LLC SP10-R
Boron Nitride Nanotubes	BNNT	BNNT Materials LLC SR10-RX
Boron Nitride Platelets	BNP/003	3M^{TM} 003
PTFE membrane	n/a	Cat#: 776742
Sodium metal	Na	Sigma 262714
Naphthalene	Nap	Sigma 84679
N,N Dimethyl Acetamide	DMAc	Sigma 271012
Methanol	MeOH	Sigma 34860
Ethanol	EtOH	Sigma 32221
Iso-Propanol	IPA	Sigma 59300
Acetone	n/a	Sigma 32201
1-Bromo Hexane	Br-Hex	Sigma B68240

Table 5.1. Materials used in this section as well as the supplier product numbers (where possible) and abbreviations that are used to refer to them within the text.

5.3.2 Methods

Reductive dissolution of BNNT: BNNT 'puffball' samples (resembling cotton balls as shown in Figure 5.1.A) were taken into an argon atmosphere and then partially separated into smaller chunks using two pairs of needle nose tweezers. Using 1 mg_{Na} mL^{-1} sodium naphthalide (NaNap) charging solution used in CNT EPD (section 4.3.2), the BNNT chunks (small portions of the BNNT 'puffball') were immersed in the charging solution at stochiometric ratio of 5_{BN}:1_{Na}. This mixture was then made up to

a 1 mg_{BN} mL^{-1} concentration with additional anhydrous dimethyl-acetamide (DMAc) and then further separated with tweezers, followed by mixing by glass stir bead for multiple (1-3) days. The dispersion was considered completed when there were no remaining visible clumps of the original 'puffball' (although, unlike in previously described CNT dispersions, some BNNT was still visible as a cloudy, fibrous suspension).

Electrophoretic deposition of BNNT dispersions: Vertically aligned, parallel electrodes of 2.5 x 2.5 cm dimensions were suspended and then immersed into the BNNT solution while held 2 cm apart. The anode was made from fluorine-doped tin oxide (FTO) coated glass and the cathode from copper foil and both were connected by crocodile clip to an Autolab PGSTST128N potentiostat which applied a constant 10 V potential difference between the electrodes while measuring the current. The BNNT film created was removed from solution and taken out of the argon glovebox.

Film drying and washing procedure: The drying and subsequent washing steps taken for BNNT films is identical to that used for the CNT films in section 4.3.2

Charge concentration investigation (bromide substitution): Five samples of 5 mg BNNT SP10-R were divided into five 20 mL vials equipped with small (5 mm) glass stir beads. 0.25, 0.5, 1.0 and 2.0 mL of the 1 mg_{Na} mL^{-1} NaNap charging solution was added to four of these vials and all were made up to 10 mL by DMAc addition. All were stirred over 2 weeks and then had their UV-Vis spectra determined. Following this, each solution had the sociometric equivalent of their sodium content added in 1-bromo-hexane. This caused the solutions to lose any remaining green colouration, being replaced by yellow. The samples were filtered over a 0.22 µm pore PTFE supported membrane wetted with EtOH and washed with further EtOH and acetone before drying in air prior to further analysis.

5.4 Results and Discussion

5.4.1 Starting materials

Unlike the relatively large amounts (gram scale) of high-quality CNT (>90 G/D ratio[201]) that could be used in experiments previously, BNNT manufacture is still limited. The samples that were provided by BNNT LLC were therefore analysed prior to EPD, and sample recycling was often used to save material throughout this study.

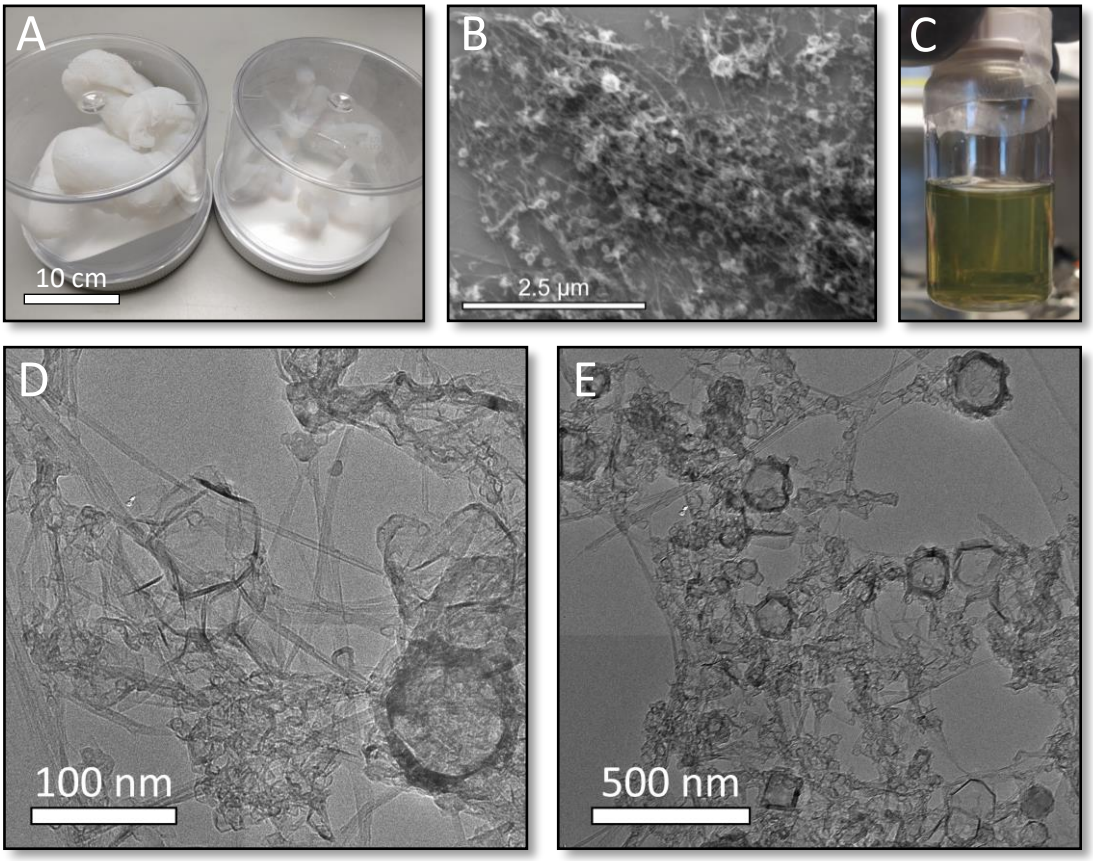


Figure 5.1. BNNT starting materials. Image **[A]** of the SP10-R *(left)* and SR10-RX *(right)* BNNT 'puffballs' as provided by the manufacturer before processing. SEM **[B]** image of SP10-R showing the nanotubes are comprised of fibrous tubes and large BN bulbs remaining from the synthesis procedure which charge during imaging creating the slight distortion seen in the micrograph. Image **[C]** of a BNNT sample (cloudy suspension) immersed in NaNap charging solution (green solution) showing incomplete charge transfer. TEM images* **[D]** and **[E]** emphasising the size difference between the BN Bulb and nanotube structures.

*TEM taken by Dillon McGurty of the Grobert Group.

BNNT LLC manufacture their product by a HTP (high temperature and pressure) method[202] using laser ablation to create BNNT cotton-like 'puffballs' (Figure 5.1.A) of many entangled BNNT which must be physically shredded/separated into chunks before use in solution otherwise they were found to collapse into small fibrous clumps that do not disperse into solution. Under SEM (Figure 5.1.B) the starting material mass appeared to be made up of BNNT tubes and bulbs (encapsulated boron nanoparticle surrounded by hBN) which are indicative of the HTP method of synthesis.[203] Further transmission electron microscopy (TEM) images (Figure 5.1.D-E) confirm the manufacturer's claims[202] that these nanomaterials have larger dimensions (up to 200 µm in length with 1-5 h-BN walls) to that of the CNT that were used in chapter 4 (≥5 µm[201] length with 1 graphene wall).

The size disparity between these BNNT and the previously successful CNT is an issue as the electrochemical reduction of the nanomaterial by NaNap was found to be unable to individualise and disperse larger multiwalled CNT (produced by D. McGurty *et al.*[204]). Additionally, the polar covalent nature of BNNT nanostructure makes reduction of BNNT less likely compared to CNT, as point charges introduced onto the BN surface cannot move and so act as a localised repulsion to further reduction reactions. This trend is shown in the simulated nanotubes calculated by Shin *et al.*[205] where BNNT models constantly showed lower electron affinities compared to the analogous CNT structures (0.40 eV for BNNT compared to 1.98 eV for CNT where both have a (5,5) armchair structure).

With a lower charge and larger dimensions, it is no surprise then, that these BNNT samples do not fully disperse into solution when charged. Figure 5.1.C shows this issue as a cloudy BNNT suspension which can be observed within a dispersion that also retains much of the green NaNap charging solution colouration meaning that full charge transfer onto the BNNT has not occurred. Despite these issues, initial EPD testing of these partially charged BNNT samples showed that films would still be created given a longer period of time (10-30 mins) and so further testing was therefore continued.

5.4.2 Charging of BNNT

The initial experiments that were carried out to estimate variables required for BNNT charging and deposition showed that the BNNT material was not fully reduced for the amount of NaNap solution that it was combined with. Additionally, the longer EPD times required to create films (BNNT=20 min vs CNT=2 min dispersions) implied a lower nanotube charge, as the nanomaterial was less effected by an electric field and so moved to the electrode surface more slowly. To investigate the degree to which the BNNT samples were charging, an experiment was designed immersing the same amount of BNNT in varying amounts of NaNap. The differences between these samples were then be measured to determine the charge transfer.

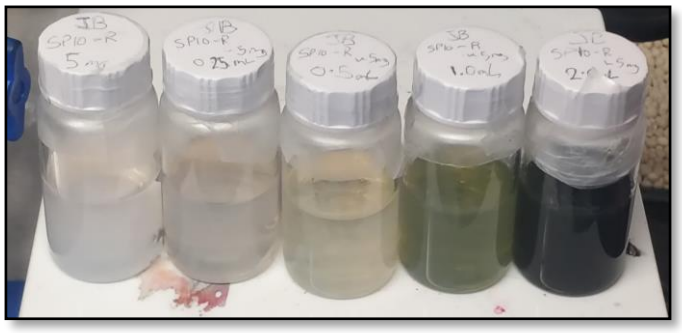


Figure 5.2. Image showing the dispersion/charging samples lined up in increasing (from *left* to *right*) NaNap concentration as indicated by increasing green colouration. Here 5 mg of BNNT was placed in 10 mL of varying concentrations of NaNap solution and left to disperse/charge. Note the parafilm surrounding the vial caps used to prevent oxygen contamination of samples during glovebox transfers.

5.0 mg of shredded BNNT was added to 0, 0.25, 0.5. 1.0 ad 2.0 mL of 1 mg_{Na} mL^{-1} NaNap solution and each made up to 10 mL with DMAc solvent. These samples, after stirring, are displayed in Figure 5.2 and it can be seen by eye that complete charge transfer (denoted by a loss of green colour) has not occurred in at least the three more concentrated samples to the right.

5.4.2.1 UV-Vis Spectroscopy Analysis

While the eye can observe significant differences between colouration, UV-Vis spectroscopy can quantify these differences. Attempts to produce absorption coefficient curves for NaNap solutions proved unsuccessful as they showed no consistent or repeatable trend possibly due to air mediated

discharge. The BNNT concentrations were determined instead, within the variously charged dispersions. It was assumed that the higher the charge transfer to the nanotube, the higher the resultant BNNT concentration[75] shown by UV-Spectra. This trend would continue until the maximum charging is achieved at which point the BNNT concentration should not increase further.

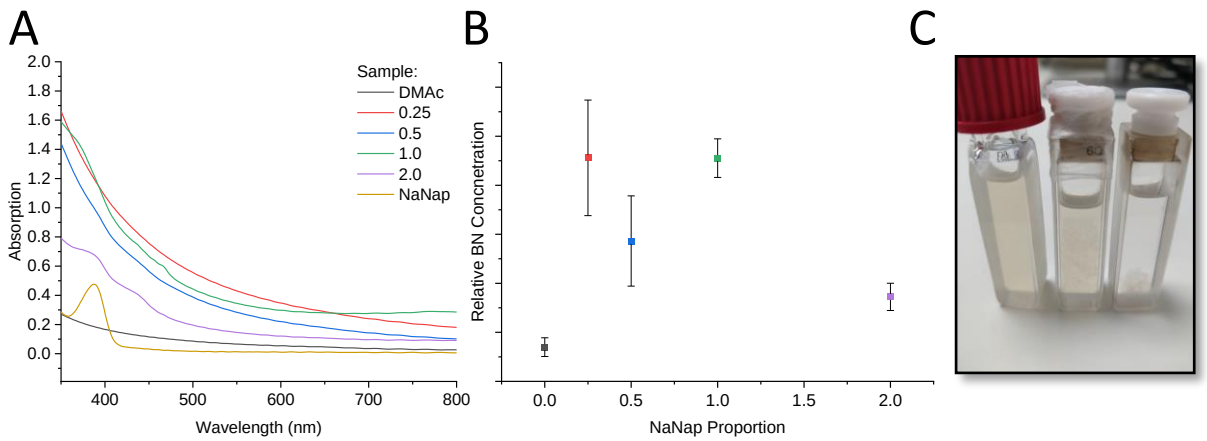


Figure 5.3. Results of UV-Vis analysis of the variously charged BNNT. The spectra **[A]** for the NaNap charging solution, DMAc and 'charged' BNNT samples showing the 350 – 800 nm region from which BNNT concentration is calculated. Graph **[B]** showing the relative concentrations of BN material suspended within each sample calculated using the Beer-Lambert law using a molar absorptivity coefficient calculated using BNP powder suspended in DMAc. Image of UV-Vis samples in cuvettes **[C]** showing the cloudy coagulation of BNNT in the more oxygen exposed samples (*right*) compared to the better sealed samples (*left*).

The UV-Vis absorption curves are displayed in Figure 5.3.A. To calculate the BNNT concentrations (Figure 5.3.B) from this UV-Vis data, molar absorptivity coefficients from BN platelets (derived and used in section 7.4.1) were used. This was because it was impossible to create standard solutions of known concentrations for the BNNT due to their large dimensions which caused them to coagulate too rapidly, and so the chemically similar BNP dispersed in DMAc were used instead. As this is the case, only trends in relative BNNT concentrations are valid as the calculated numbers may be misleading. Furthermore, the UV-Vis spectrometer was situated outside the glovebox and so oxygen induced discharge of samples (as described in lit review 2.2.2) transported for analysis to it may be another source of error. Discharge of BNNT and their subsequent coagulation due to presumed

oxygen/air contamination over time can be seen in Figure 5.3.C (right hand cuvette with cloudy material at bottom of the container).

The relative BNNT concentration results show that the nanotube concentration is lowest for uncharged BNNT, implying that the charging solution does have an effect. Nevertheless, no trends are observable within the charged solutions. This may be due to the possibility that the maximum possible BNNT charge transfer has already occurred with the 0.25 mL sample, implying a charge ratio of $<41_{BN}:1_{Na}$ which would limit the density surface decoration for any future radical based functionalisation reactions.

5.4.2.2 Bromide Substitution

To gain more substantial data on the amount of charge transferred to the surface of the BNNT, a complimentary study was performed. a S_N2 halide substitution reaction was designed in which these charges would result in the addition of hexane chains to the BNNT surface as detailed in Figure 5.4.

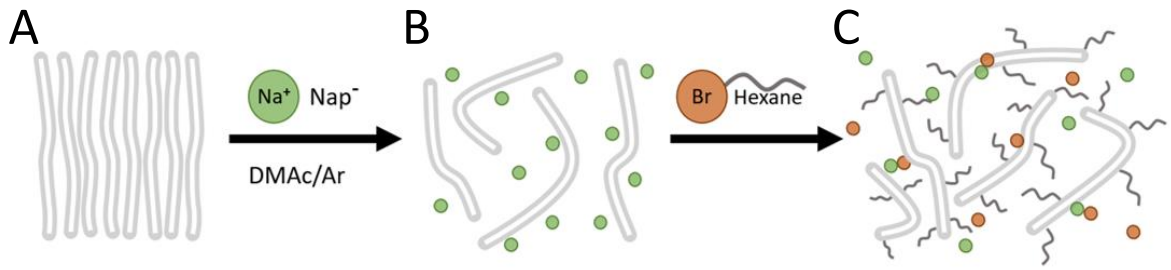


Figure 5.4. Schematic of proposed reaction. BNNT starting material **[A]** is charged by NaNap reducing agent causing its dispersion **[B]**. The negative point charges on the BNNT surface then react with the bromo-alkane in a substitution reaction resulting in the decoration of the BN surface with covalently linked hexane **[C]** while the solution contains a sodium bromide salt.

This halide substitution is common in CNT chemistry[89] and Shin *et al.*[205] describe the same reaction, reporting that the binding energy between an alkyl radical and a charged BNNT could be -3.86 eV. They also achieved a 15% weight fraction addition of hexane experimentally. It was therefore hypothesised that the proportion of BNNT-Hex bonding found when this reaction was completed would be indicative of the charging of the BNNT.

As many REDOX reactions are reversable, there was a possibility that the charging ratio of the BNNT was in an equilibrium based on the concentration of charged naphthalide in solution. Enough Br-Hex was therefore added to discharge every theoretical sodium introduced charge in the system simultaneously, preventing any reversible reactions that would first discharge the BNNT onto the Nap and artificially lower the recorded BNNT-Hex bonding.

After the combination of Br-Hex and the differently charged BNNT samples, any remaining green coloration of the solution disappeared and samples were washed, dried and sent for XPS analysis. The XPS results were expected to show an increase in C atomic content as well as C-C and B-C bonding proportions as the BNNT charging ratio increases, plateauing when the BNNT charging limit being reached.

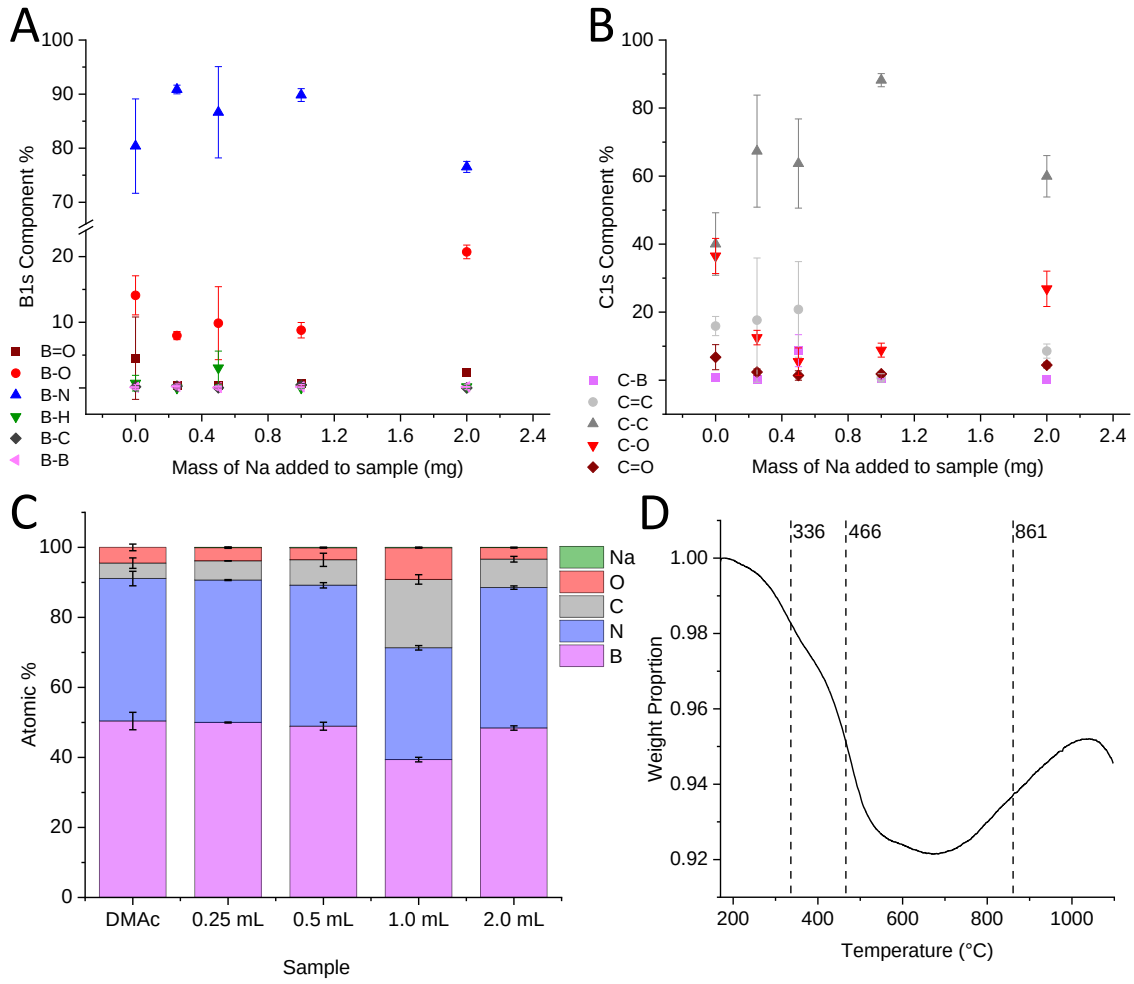


Figure 5.5. Analysis of Br-Hex reaction with 'charged' BNNT. XPS summary of the B1s **[A]** bonding regimes found within BNNT samples showing the expected high B-N bonding proportion but little of the expected B-C bonds with no obvious trends. The XPS summary of the C1s bonding environment **[B]** also shows no trend in the C-C bonding as is expected of a successful functionalisation. This lack of trend is again repeated in the atomic fraction breakdown **[C]** of the same samples. A TGA **[D]** signal of the 2.0 mg_{Na} shows evidence of hexane presence by the mass loss at 466 °C.

The actual XPS results do not show any significant differences or trends across the B1s (Figure 5.5.A) spectra. As expected, the B-N bonding proportion dominates but the predicted increase in B-C bonding for charged BNNT samples was not present and remained negligible in all samples. This may be due to the small scale of the reacted boron sites (implying a very low charging ratio) in relation to the majority of the boron found in internal BNNT shells as well as the boron nanoparticles held within the previously described bulb structures. The carbon atomic content (Figure 5.5.C) of the charged samples does increase from 4.3 % in the uncharged BNNT sample to 7.3% and 8.1% in the 0.5 and 2 .0 mg_{Na}

charged samples respectively. The C1s deconvolutions (Figure 5.5.B) show that this is due to an increase in sp^3 C-C bonding (40 % to >60 %) implying the increased presence of hexane. This observation is backed by the 5.7% mass loss at 466 °C shown in the TGA (Figure 5.5.D) of the 2.0 mg_{Na} but is much lower than the 10% mass loss reported for a similar reaction by Shin *et al.*[205]

The XPS results are, similar to the UV-Vis, inconclusive. The increase in atomic carbon bonded in sp^3 does imply hexane bonding, but shows no trend that would allow the charging ratio of the BNNT to be determined. Additionally, the lack of significant increase in B-C bonding could imply that the hexane is not covalently bonding to the BNNT surface but is instead detected as an impurity within the sample having reacted with the cation on the naphthalide molecule (as no bromine atomic signal was detected, it is concluded that a reaction did take place). This is confirmed by comparison of IR spectra for the starting material and reacted BNNT-Hex (Figure 5.6) in which no C-C or B-C single bonds can be seen created in the fingerprint region.

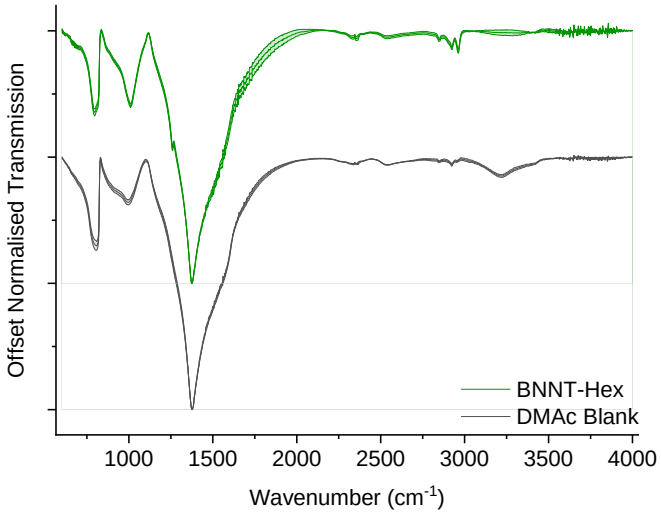


Figure 5.6. Normalised IR spectra of BNNT immersed in DMAc and reduced BNNT reacted with 1-bromo-hexane (BNNT-Hex). No new single bonding signal is detected in the fingerprint region (<1500 cm^{-1}) of the BNNT-Hex spectra, implying no significant reaction creating a B-C or C-C bonds has occurred.

5.4.3 BNNT Film

Despite the charging ratio of the BNNT being unknown, the deposition of the nanomaterial onto an electrode's surface by EPD does still occur. The final product of these procedures was observed through manual handling to be flakier and weaker than its CNT counterparts and broke apart when attempts were made to remove it from the depositing electrode's surface (Figure 5.7.A). This was despite the thicker (25 – 35 µm) film depth and longer constituent nanotubes which should have increased the films mechanical properties.

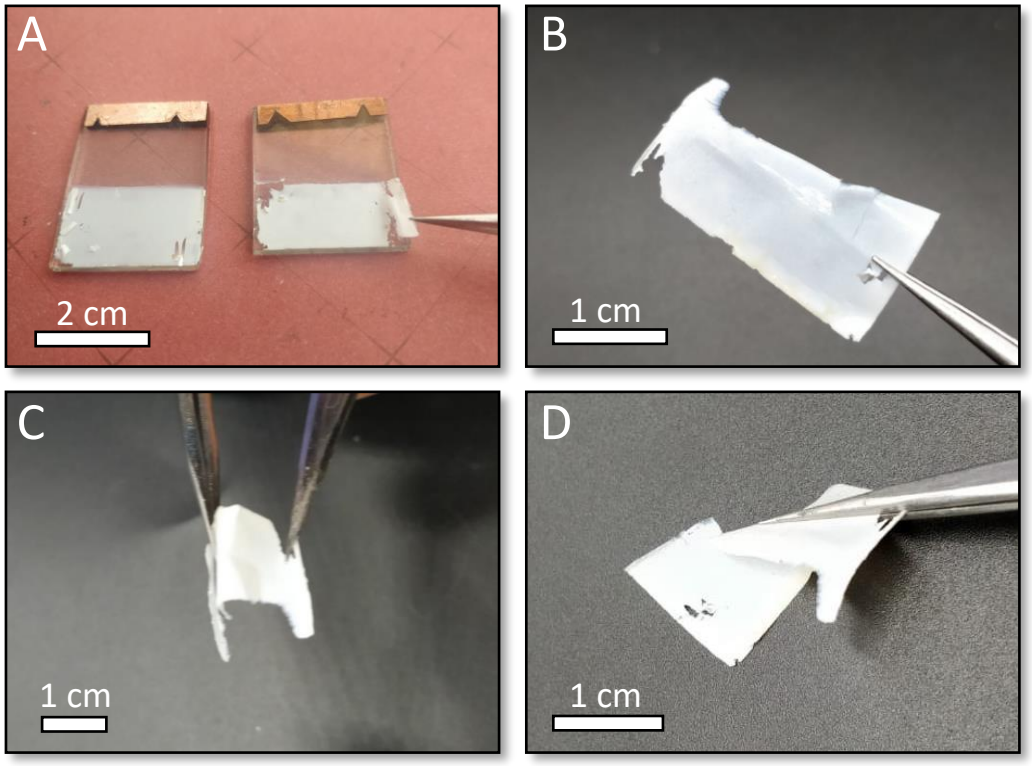


Figure 5.7. Images of BNNT films. BNNT films on electrodes crumbling **[A]** during peeling despite high thickness of the film. Free standing BNNT film **[B]**. Demonstrations of film flexibility by bending **[C]** and folding **[D]** although note the beginnings of a tear due to the latter.

Free standing film samples that were extracted from the electrode (Figure 5.7.B) where found to be less flexible and more delicate than their CNT equivalents as they could bend (Figure 5.7.C) but would then tear when folded or bent transversely (Figure 5.7.D). These problems with free standing film extraction and their subsequent delicacy made it impossible to produce samples suitable for

mechanical testing and so no quantifiable comparison to the CNT films could be made. Additionally, due to their electrically insulating nature, sheet conductivity measurements (measured by Bianca Bauer of the Grobert group) showed no signal and could not be compared to the products of chapter 4. Additionally, under SEM (Figure 5.8) these samples appear to contain a porous structure similar to their CNT equivalents.

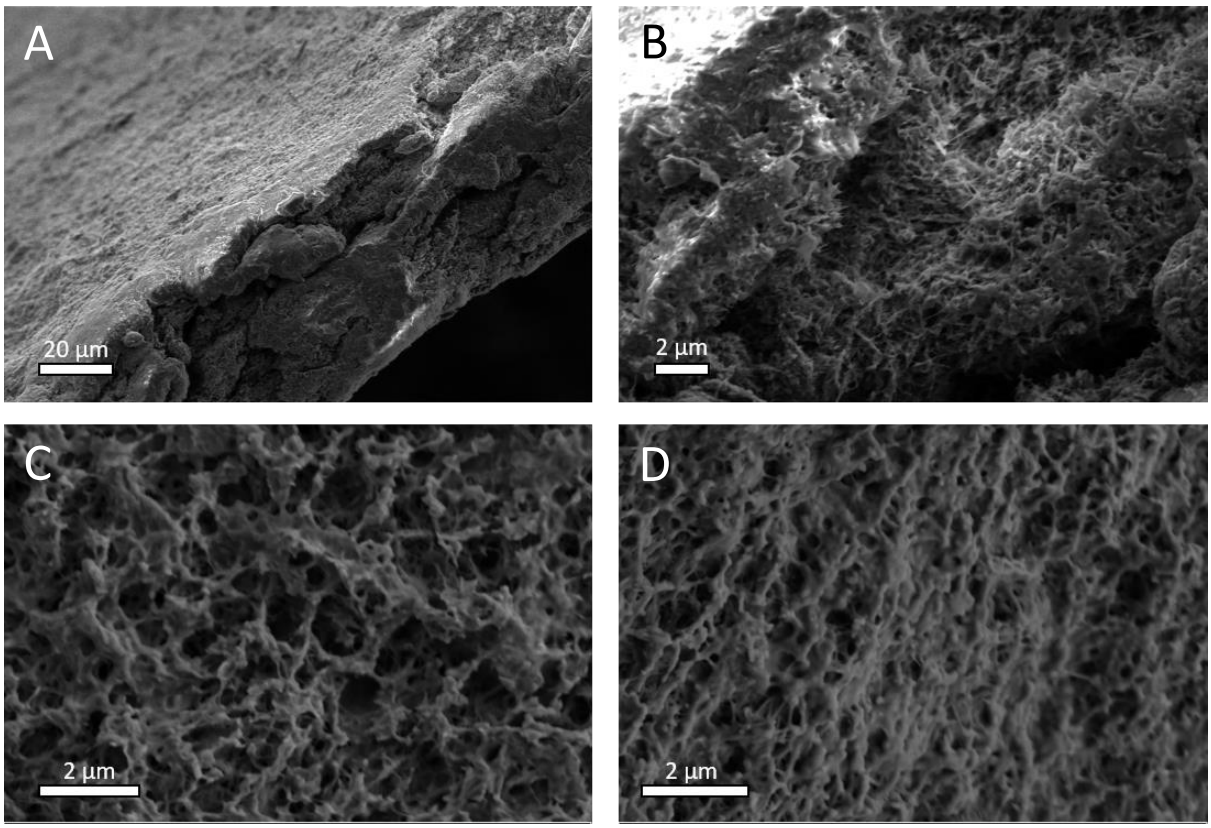


Figure 5.8. SEM of BNNT film cross section. The film does not have an obvious layered structure **[A]** similar to its CNT equivalents and similarly, individual nanotubes do not appear to lie parallel to the electrode plane **[B]**. BNNT instead form a 3D, interconnected/tangled network with areas are more **[C]** and less **[D]** densely packed.

Due to these cavities, the average density of the BNNT films produced in this work was found to be 0.31 ±0.3 g cm^{-3}. This is statistically identical to the CNT (calculated in section 4.4.4.1 at 0.34 ±0.07 g cm^{-3}) and supports the proposal in section 4.4.2.3 that the density of the films created by the reduced dispersion EPD method is due to the drying procedure and not other variables. This is thought to be

because the drying stage introduces sodium salt impurities into the film macrostructure which has the largest influence on the final films' density once these are washed away to leave cavities.

5.4.4 Nanostructure retention

While the films' macro properties may not be fully understood, the main advantage of this new reduced dispersion EPD method was identified in Chapter 4 as being the retention of nanostructure from the starting nanomaterial. BNNT films that were manufactured using this method were therefore analysed to investigate if this remains the case.

5.4.4.1 Raman

The Raman spectra of a typical film sample produced during the concentration variance (section 5.4.5.2) and time variance (section 5.4.5.1) experiments were compared to the SP10-R BNNT starting material. The full spectra (Figure 5.9.A) did not show the expected h-BN peak at 1370 cm^{-1} [185] but instead a sharp peak was found at 1332 cm^{-1}. On examination of the broader peaks from the glass slide on which the BNNT were mounted for analysis, it was seen that these peaks had also moved. The Si-O-Si asymmetric stretch expected at 1100 cm^{-1} [206] was redshifted by 40 cm^{-1} and found at 1060 cm^{-1}. This systematic error (despite Si calibration of the spectrometer) allows the peak at 1332 cm^{-1} to be confidently identified as the T_{2g} stretch of h-BN.

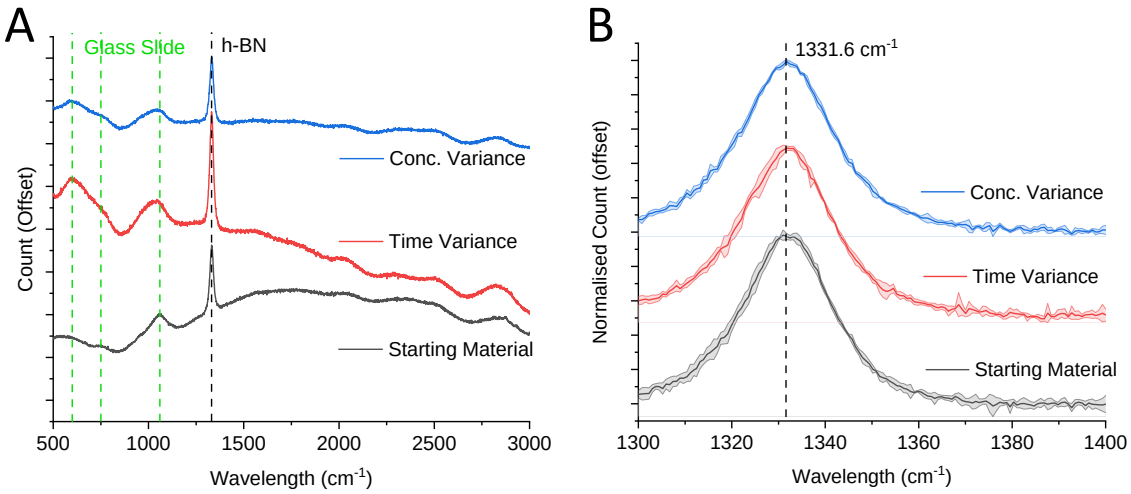


Figure 5.9. Raman spectra of BNNT starting material compared to BNNT films created during the concentration and time variance experiments (see later section 5.4.5). Typical full Raman spectra **[A]** show the distinctive E_{2G} h-BN peak at 1331 cm^{-1} which is red shifted by ~40 cm^{-1} although the Si-O-Si peaks of the glass slide are similarly shifted. The comparison of the normalised and averaged (with error lines) h-BN peaks **[B]** shows no change induced by the reduced dispersion EPD method.

The averaged h-BN peaks for these samples (Figure 5.9.B) show that, despite the red shifting of the data, the samples are very similar. The peak position of the starting material 1331.6 ±0.78 cm^{-1}) is statistically identical to that of the time and concentration variance film samples (1331.5 ±0.45 cm^{-1} and 1331.7 ±0.60 cm^{-1} respectively). Furthermore, the peak FWHM are again statistically identical at 21.4 ±0.80 cm^{-1}, 21.3 ±0.43 cm^{-1} and 22.8 ±0.97 cm^{-1} for the starting material, time variance and concentration variance. These identical peaks are evidence that the BNNT nanostructure for the starting material and final films remains unchanged despite the charging and EPD processes.

5.4.4.2 XPS

As previously mentioned, the deconvoluted B1s spectra may not be able to detect small changes to the BNNT surface when compared to the bulk of boron held within the multi-layered structure. However, when examining overall changes to this nanostructure, it is still useful.

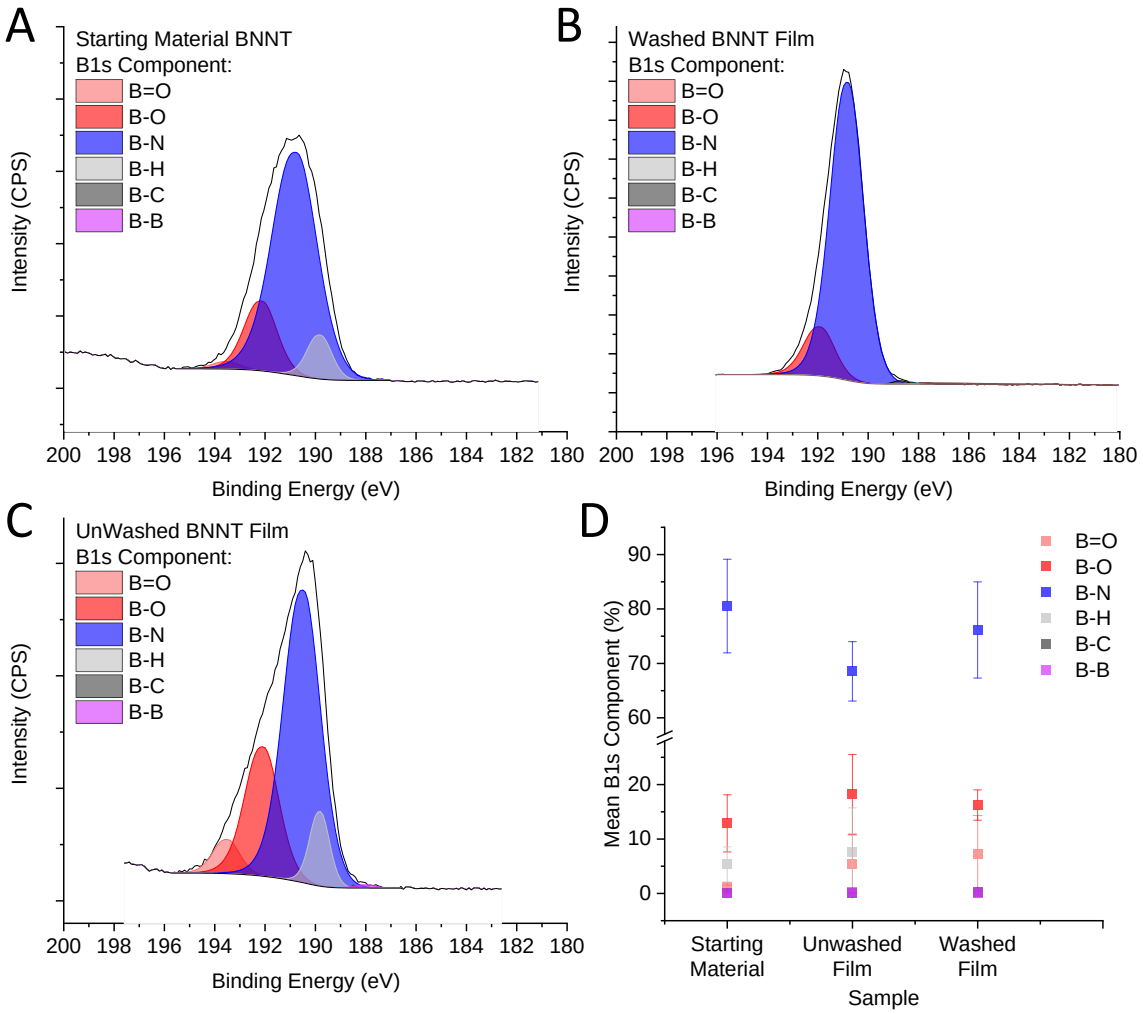


Figure 5.10. B1s XPS analysis of BNNT films produced by reduced dispersion method. Typical deconvoluted B1s spectra of the starting material **[A]** as well as the washed **[B]** and unwashed **[C]** BNNT films. A summary of the averaged B1s components **[D]** is graphed and shows the B1s environment is statistically the same as the starting material implying the retention of h-BN nanostructure.

Figure 5.10.A-C shows typical deconvolutions of the B1s spectra comparing the BNNT starting material with the washed and unwashed films produced by reduced dispersion EPD. While the B1s of the starting material and the washed film are similar, the unwashed film shows larger variance. This is reflected in the averaged B1s deconvolutions plotted in Figure 10.D. The expected largest bonding proportion of B-N consists 80.5 ±8.6 % of the starting material compared to the similar 76.1 ±8.8 % of the washed final film and the much lower 68.5 ±5.4 % of the unwashed film. B-O is the next largest bonding fraction and follows the trend of a smaller starting material proportion (12.8 ±5.2 %)

compared to larger washed film (16.2 ±2.8 %) and larger still unwashed film (18.2 ±7.3 %). The remaining B-C, B-B, B=O and B-H were all found to be statistically negligible.

While the B1s spectra show that the samples' nanostructure has remained relatively the same, analysis of the C1s (Figure 5.11) can give information about the type of impurities within the system and therefore help develop the understanding of the reduced dispersion EPD method.

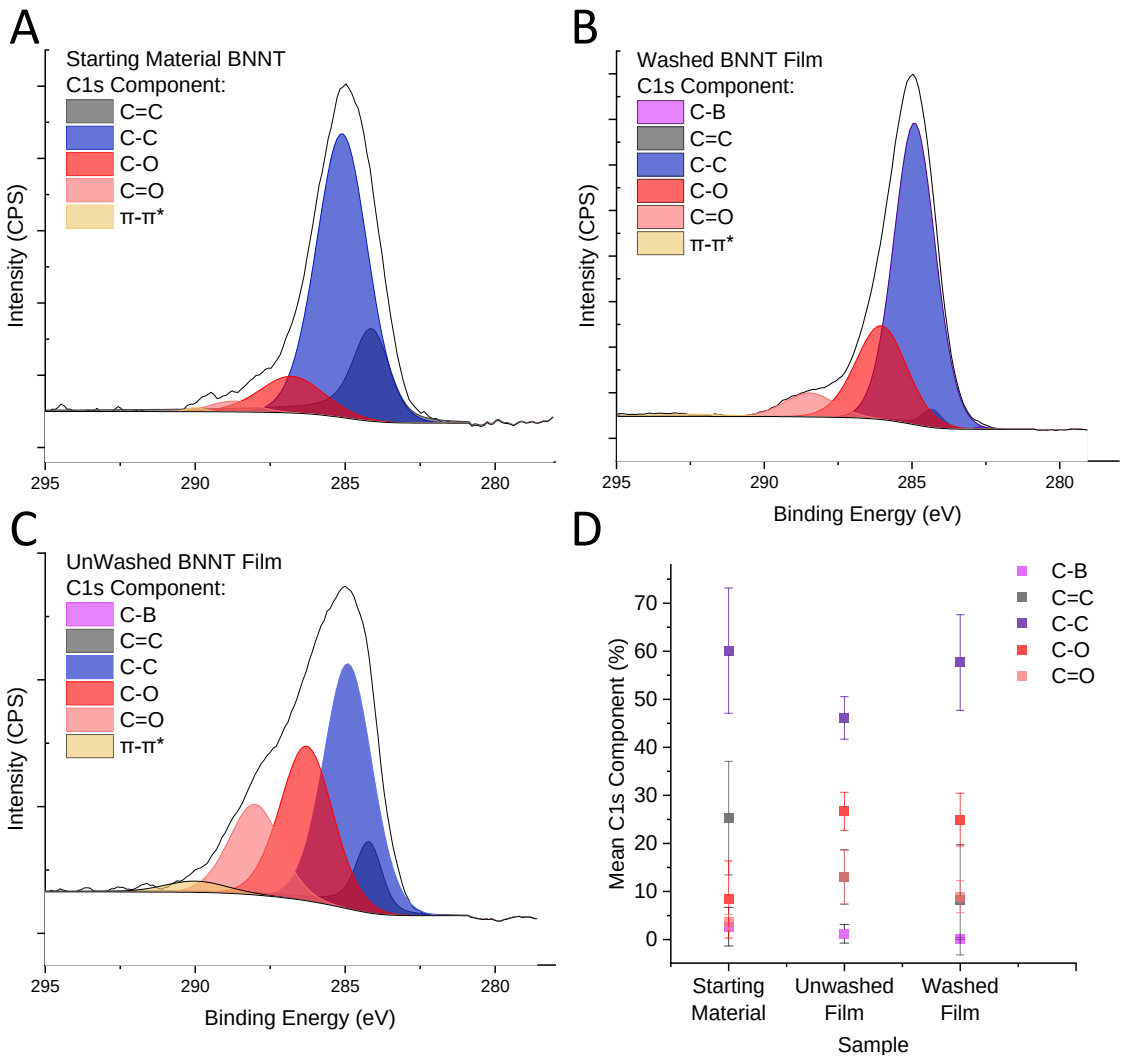


Figure 5.11. C1s XPS analysis of BNNT films produced by reduced dispersion method. Typical deconvoluted C1s spectra of the loose starting material **[A]** as well as the washed **[B]** and unwashed **[C]** BNNT film. A summary of the averaged C1s components **[D]** is graphed and shows the C1s environment varies significantly between samples. Low carbon content or addition of different carbon containing species may be responsible for these variations.

The C1s of the starting material contains a significantly larger (25 ±11 %) sp^2 component compared to the other samples. This is thought to be due to the graphitisation of carbon containing species during the high temperature BNNT synthesis of the material in which it has been shown segregated B-N and C=C bonding is energetically preferential to B-C-N bonding.[207] These sp^2 species are removed by the reducing NaNap solution which preferentially reduces amorphous carbon species.[75] Their further removal, in addition to the remaining naphthalene, is evidenced by the drop in C=C bonding from the unwashed film to the washed samples (13.0 to 8.2 %).

Another large bonding environment is that of C-O, which is not significantly present within the starting material due to high temperature synthesis. XPS of the solvent DMAc should contain a C-N (285.78 eV [208]) component or O=C-N (~288 eV [209]). These bonding regimes may explain the increase in the C=O and C-O components of the unwashed sample as these signals overlap.

The majority of all the carbon bonding environments consist of C-C bonds which are presumed to be from impurities within the BNNT and solvent residues trapped within the films' macrostructure. The smallest C-C proportion is from the unwashed material, but this will be due to the increase in other impurities and not the loss of the formerly mentioned residues.

This can be seen most clearly in Figure 5.12 where the non-BN component of the unwashed film (14.9%) is significantly larger than that of that of the starting material (7.8%) and washed film (11.1%) showing the additional impurities which are washed out. Further proof of this is in the detection and then removal of the 0.9 % Na content from the unwashed film, paralleling the same result found in the CNT based films of Chapter 4. However, there may still remain traces of sodium and cavities within the film, especially as the BNNT films were thicker than the CNT films making washing harder to conduct thoroughly.

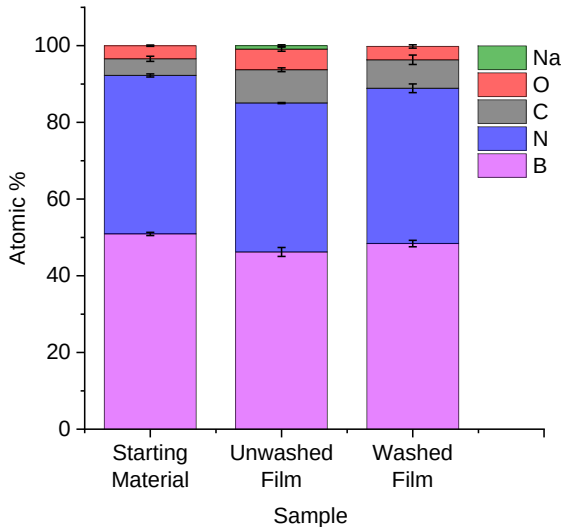


Figure 5.12. Summary of BNNT film sample atomic breakdowns as measured by XPS. The unwashed samples show an expected reduction in its BN proportion compared to the starting material which is nearly fully recovered by the washing procedure.

In conclusion, the XPS results for these films have further proven that the reduced dispersion EPD method produces films with little or no damage to the constituent nanotubes. While the film washing procedure may need improvements, this is a minor issue compared to this significant achievement.

5.4.4.3 Thermogravimetric Analysis

TGA was used as final proof of the BNNT nanostructure retention. Under inert conditions, h-BN can reportedly remain intact up to 2500 °C [30] and in air will form B_2O_3 starting at 1000 °C [29] . This will cause the increase in the samples' mass due to the addition of oxygen. Boric acid (H_3BO_3) is a common feedstock used in the synthesis of BNNT and also thermally decomposes into B_2O_3 between 450 and 800 °C [210] so the lack of TGA increase in this range can also be used as evidence for the purity of both materials.

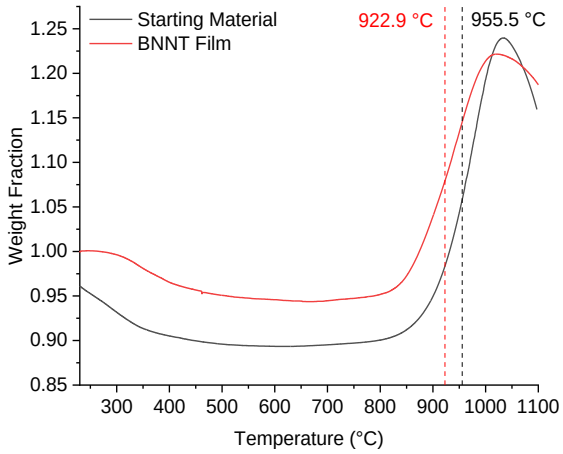


Figure 5.13. Thermo-gravimetric data comparing the BNNT starting material and films produced using the reduced dispersion EPD method. Both samples degrade in atmospheric oxygen and increase in mass as their structures break down into boron oxide.

The XPS atomic breakdown of the BNNT starting material and resultant film explored in the previous section showed that the non-BN component of both samples was approximately 10% and it is assumed that it is these species that are removed from the samples in the 5-10 % mass drops observed in the first 400 °C of the TGA (Figure 5.13). This is because this temperature range does not correspond to any of the boiling or decomposition points of the other species known to be in the sample (naphthalene at 217 °C or DMAc at 165 °C). The oxidation of the BNNT starting material resulting in the mass gain from 89.9 % to 124.1 % was half complete at 955.5 °C. This is similar to the reduced films' mass gain at the lower temperature of 922.9 °C from 94.7 % to 122.2 %. The 32.6 °C between these degradation temperatures is larger than the difference between the CNT reduced films and their starting materials but smaller than the difference between the oxidised CNT films and starting nanotubes and confirms that little or no damage has been done to the BNNT nanostructure.

5.4.5 Mechanism

While the mechanism of deposition was explored for the CNT films, the BNNT system differs due to its electrically insulating starting nanomaterial, lower charge density and retention of charged naphthalide ions within the dispersion. A study of the basic variables controlling the deposition

process was carried out to confirm similar trends when applying the reduction EPD method to the new nanomaterial.

5.4.5.1 Time vs Deposition

Similar to the CNT based investigation into the same variable (part 4.4.4.1), the time for EPD was varied from between 1 to 30 minutes and the resulting BNNT films' thicknesses determined (Figure 13). Films were produced using a 1 mg_{BNNT} mL^{-1} reduced solution at the theoretical charging ratio of 1_{Na}:5_{BN} although, as previously explored, the actual fully dispersed BNNT concentration and charging ratios are likely to be significantly lower than this. Despite this, the excess of charging solution was used to ensure that the maximum possible charge was transferred to the nanotubes thereby ensuring that the 5 V cm^{-1} field applied to the solution had the largest possible effect.

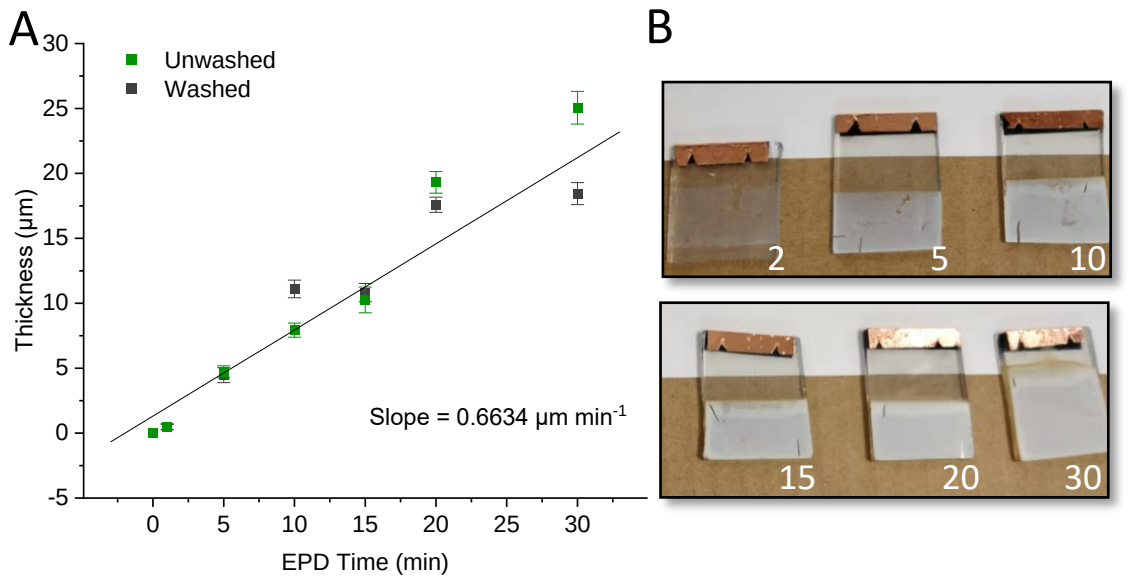


Figure 5.14. Results of varying the time of EPD. Graph **[A]** of film average thickness variation (both washed and unwashed) with time showing a linear trend of slope 0.66 µm min^{-1} from a 1 mg_{BN} mL^{-1} suspension theoretically charged at 1_{Na}:5_{BN} ratio and held at a 10 V potential difference. Images of the resultant dried and washed films **[B]** visually show the increase in film thickness with time (written to the bottom right of each film. Note the scratched points on all films when thickness measurements were taken using optical profilometry.

The results of this time dependency trial (Figure 5.14.A) again show a trend explained by Hamaker's Law (Eq 2.1.) from which a film thickening rate of 0.663 µm min^{-1} was calculated which is one-sixtieth

the rate of CNT deposition (0.011 µm s^{-1} for BNNT compared to 0.609 µm s^{-1} calculated for CNT in section 4.4.4.1). From this, the deposition rate of 2.03 µg cm^{-2} min^{-1} (3.39 x10^{-5} mg cm^{-2} s^{-1}) is calculated. This is significantly lower than both the 0.122 mg cm^{-2} s^{-1} (of reduced) and 0.056 mg cm^{-2} s^{-1} (of oxidised) CNT produced films. These slower deposition rates are due to the larger size and lower charge density of the BNNT compared to CNT. As explained previously, (section 2.3.4.) Hamaker's Law (Eq 2.1) predicts that the rate of deposition is dependent on the electrophoretic mobility of the dispersed nanomaterial. The lower charge density on the BNNT compared to previous CNT experiments means that the force exerted on an individual tube by the same electric field during EPD is less (as laid out by Coulomb's law). Additionally, the larger size of BNNT increase their drag within solution, reducing terminal velocity. Taken together, these effects decrease the materials mobility and therefore increases the time taken for BNNT to concentrate at the electrode for its subsequent coagulation. This satisfactorily explains the reduced rate of deposition for BNNT.

5.4.5.2 CNT Concentration vs Deposition Rate

The previous CNT investigation had shown that (within the conditions explored) a minimum concentration of ~0.5 mg_{CNT} mL^{-1} was needed to allow a film to be produced (section 4.4.4.2). A similar experiment was set up to determine the concentration threshold for BNNTs, with concentrations of nanotube varying between 0.2 and 1.5 mg_{BNNT} mL^{-1} 'charged' at the same ratio and deposited at 5 V cm^{-1} for 20 minutes.

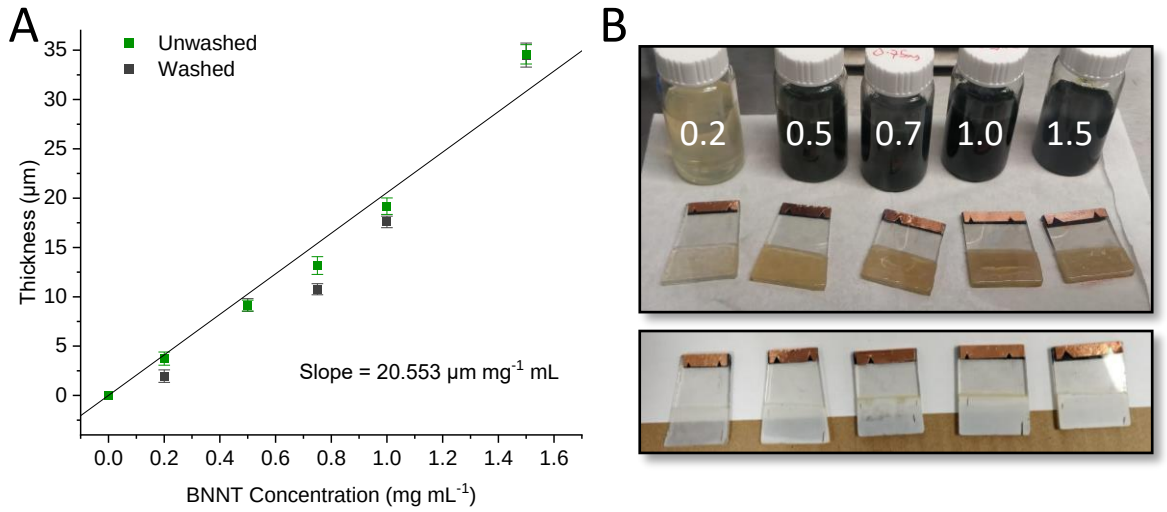


Figure 5.15. Results of varying the BNNT concentration of EPD dispersion. The average thickness of the unwashed and washed BNNT films are plotted **[A]** against the solution concentration (between 0 and 1.5 mg_{BN} mL^{-1}) used to make them. The images **[B]** show the suspensions (labelled with their respective BNNT concentrations) used for EPD of the displayed gel phase BNNT films before air discharge *(top).* These same samples, as final dried films *(bottom)* on both a white and coloured background for contrast is also shown.

Shown in Figure 5.15, all concentrations used in this study resulted in a film of significant thickness. This means that all the conditions used for this series of experiments were, unlike the CNT equivalent, sufficient to allow enough BNNT to concentrate within the time allotted to coagulate, entangle and deposit and therefore follow the trends predicted in Eq 2.1.. Also dissimilar to the CNT equivalent experiment, the thickness of films continued to increase linearly with concentration and did not plateau at any particular thickness. For CNT systems, this upper limit in thickness was thought to be due to the mutual repellence of charged nanotubes that had not fully discharged when deposited. The resulting gel that formed on the electrode could not support its own weight and so fell/slipped from the vertically held surface. It was therefore hypothesised that lowering the charging ratio on the nanotubes may lead to thicker films as it would increase the density of this gel, thereby supporting more nanotube mass for less perpendicular overhang as was shown in Figure 5.15.B.

5.4.5.3 Current/Time Graphs

Current measurements were taken during the EPD of the reduced dispersion BNNT and are presented in Figure 5.16. It will be shown that these can be used to further understand the deposition process as well as being a useful way of determining EPD progress during deposition.

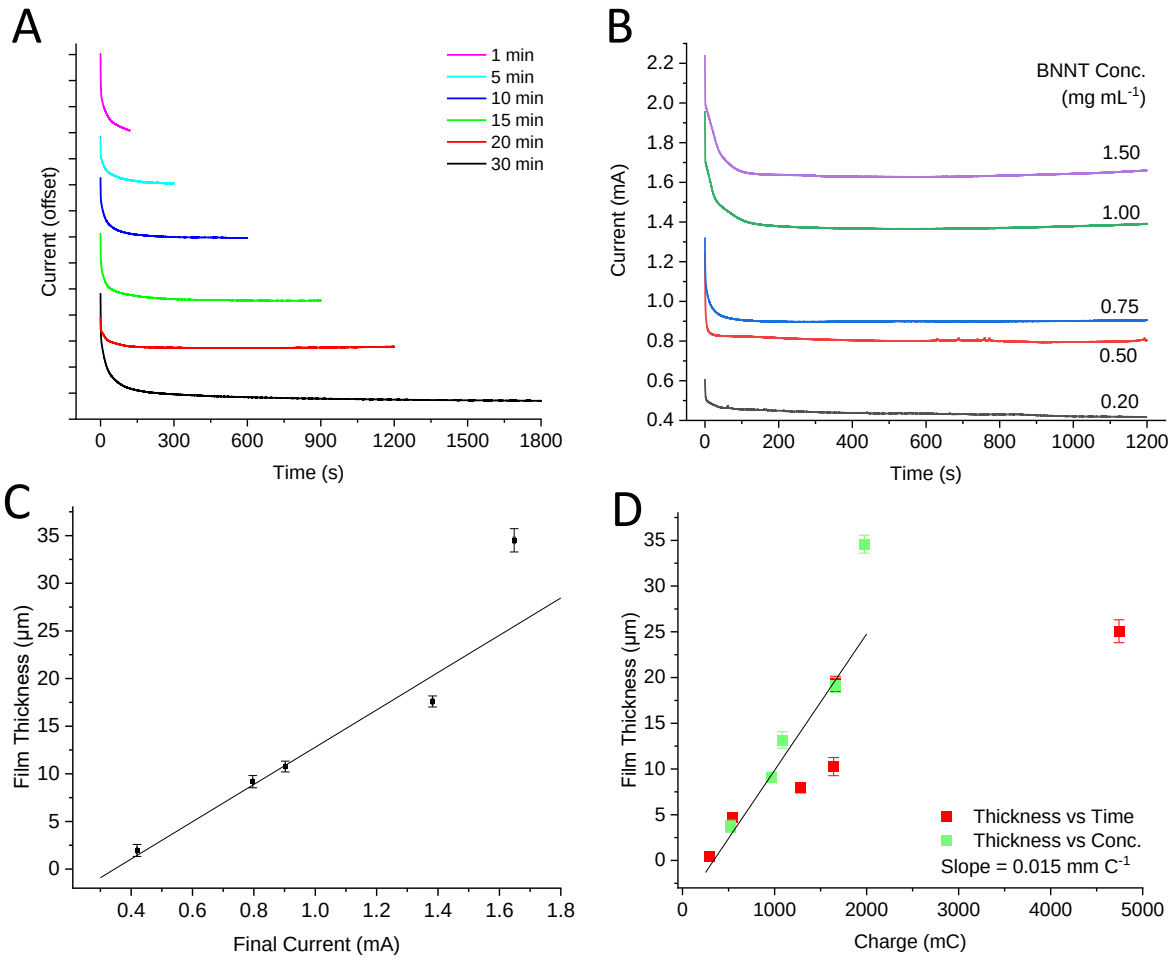


Figure 5.16. Current/Time curve measurements taken during the EPD of differently timed film production **[A]** and varying BNNT concentrations **[B]**. The average current of the final 60 s of the EPD of varying BNNT concentrations **[C]** shows the expected linear relationship. The total charge transfer during EPD of all experiments are plotted **[D]** against their resulting film thickness with the slope calculated for all data points excluding the two thickest results.

The current/time curves display a hyperbolic asymptote (Figure 5.16.A) with no secondary peak as was observed in the CNT measurements. BNNT is not electrically conductive, therefore the increased surface area on the electrode, due to the initial nanotube deposition, does not increase the amount

of area available for approaching BNNT to discharge upon and so no brief current increase is observed. This is more evidence for the current/time curve description that was explained in section 4.4.4.4.

Also, similar to the reduced dispersion EPD of CNT, the final current of the BNNT EPD was proportional to the final thickness of the film produced. Figure 5.16.B-C show this trend while also confirming that the deposition current for BNNT (1.4 mA) is significantly larger than that measured for the same concentration of NaNap charging solution (0.3 mA). This shows that the majority of the current measured is due to the BNNT. It is thought that this proportional relationship could be used to determine the thickness of a film as it is being deposited.

Another way that immediate film thickness measurements could be achieved would be by measuring the total charge transfer that has occurred during the EPD as is plotted in Figure 5.15.D and shows a linear relationship for both the concentration and time variance experiments. The largest of the time variance measurements has a disproportionately large charge transfer and was not included in the trend calculations. This is because these electrodes were more immersed in the BNNT dispersion (as can be seen in the images of Figure 5.14.B) in order to produce larger free-standing films but therefore also recorded larger currents. This error could be corrected by using the total mass of the BNNT deposited in place of the thickness.

5.5 Summary and Conclusions

This chapter has shown that the novel reduced dispersion EPD method of nanotube film production is possible for application to the electrically insulating starting material BNNT. This has produced electrode coatings of thicknesses between 3 and 35 µm that can be extracted as free-standing films. These BNNT films are electrically insulating but were qualitatively found to be mechanically weaker than their CNT equivalent. Due to the lower charging limit of the BNNT structure ($<41_{BN}:1_{Na}$) the system required longer deposition times which resulted in lower deposition rates (2.03 µg cm^{-2} min^{-1}). However, this lower charge density nanotube also led to an increased density of the gel phase during deposition and therefore higher thickness limits.

Crucially, this method has again been shown to maintain the nanostructure of the starting material that has been used as its constituents. This was shown with Raman, XPS and TGA data, the latter two of which were used to confirm that the film washing steps developed for CNT were also effective for BNNT. These washing steps may have introduced cavities within the film macrostructure as the density of the produced films (0.31 g cm^{-3}) was shown to be similar to the CNT equivalent. This shows that the density of the resultant films is determined, in the majority of cases, by the discharge and drying of the films and not by other variables.

Finally, the variables of concentration and time were investigated and shown to both have the expected linear relationship with film thickness and it is suggested that the current/time curves measured during EPD could be used to predict the thickness of the final film before drying/washing.

6 ACID OXIDATION OF BNP

6.1 ABSTRACT

Boron Nitride Nanotubes (BNNT) are highly expensive and manufactured in low quantities, so it is necessary to find cheaper, mass-produced alternatives so that the discoveries using electrophoretic deposition (EPD) made in previous chapters can be utilised more widely. The most common method of EPD for nanomaterials is to oxidise their surface to allow better solvent interactions, but this procedure is poorly researched for boron nitride (BN) materials. This chapter documents the application of multiple acid etching techniques to BN in an attempt to oxidise the surface of boron nitride platelets (BNP). Characterisation of the BNP samples were carried out using IR, Raman, SEM, EDS, XPS, XRD and BET, which demonstrated that the platelets used are inert to the range of chemical oxidation methods used, but led to damage of materials' bonding nanostructure by sonication procedures.

6.2 INTRODUCTION

Chapters 4 and 5 focused on describing and explaining a novel method for the dispersion and deposition of nanotubes to make neat films of controllable thickness. However, boron nitride nanotubes (BNNT) are relatively expensive and manufactured by batch processes in small quantities[211] which makes them currently inappropriate for industrial scale applications. BNNT are however a very small share ($44 million per year in 2022)[212] of a much larger and more developed worldwide hexagonal boron nitride market that is predicted to be valued at $956.9 million a year by 2030.[213] Boron nitride platelets (BNP) are one of the common products of this market and are made up of multilayer hexagonal boron nitride (hBN) similar to the carbon-based analogue graphite. BNP are commercially available in large, cheap quantities that are chemically similar to multilayer BNNT, meaning advances made using them could later be applied to BNNT.

BNP also retain the desirable material properties of hBN (thermal stability, electrical insulation, thermal conduction) and various studies have already been conducted that show the wide range of potential applications this material can have. Predictably, most literature focuses on the thermal applications of BNP containing both ceramic[214] and plastic[215] composites, though others take this a step further using 3D printing to align BNP to produce directional thermal conduction.[216] Alignment has also been shown to be possible using iron nanoparticle attachment and magnetic fields[217], although work showing that thin coatings of BNP can be used as fire protective coverings of other materials[218] is more directly relevant to the EPD research done previously in this thesis (Chapters 4&5).

Given BNP's wide range of applications, similarity to BNNT and relative abundance, they are an excellent material candidate to be used for EPD coatings. Throughout the literature, the standard method for nanomaterial dispersal is through the oxidation of its surface to form favourable interactions with polar solvents and so create stable solutions for EPD. The oxidation of the hBN surface of these BNP is therefore the objective of this chapter. This should simultaneously increase

our collective understanding of hBN reactivity, provide a new route for BNP suspension and provide a comparison to the future dispersion of BNP by the reduction method explored in previous chapters.

6.3 EXPERIMENTAL

This section describes the different methods by which BNP oxidation was conducted. Four BNP starting materials (003, 0075, 015 and CFA-50M) with varying surface areas (20, 10, 4 and 3.5 $m^2 g^{-1}$ respectively) were subject to the four commonly used nanomaterial acid etching oxidation techniques. The amount of acid used in each case was significantly in excess of the BN sample and reaction temperatures were set at the boiling point of the solutions. These conditions were imposed to ensure that any reaction that might occur would do so to the maximal amount and therefore most likely to be detected in subsequent sample characterisation.

6.3.1 Chemicals

Material Name	**Abbreviation**	**Supplier**
Boron Nitride Platelets 003	003 BNP	3M™ 003 Grade
Boron Nitride Platelets 0075	0075 BNP	3M™ 0075 Grade
Boron Nitride Platelets 015	015 BNP	3M™ 015 Grade
Boron Nitride Platelets CFA-50M	CFA-50M BNP	3M™ CFA-50M Grade
Nitric Acid	HNO_3	Honeywell-007-004-00-1
Sulphuric Acid	H_2SO_4	Sigma 30743
Hydrogen Peroxide	H_2O_2	Sigma 216763
PTFE membrane	n/a	Cat#: 776742
Methanol	MeOH	Sigma 34860
Ethanol	EtOH	Sigma 32221
Iso-Propanol	IPA	Sigma 59300
Acetone	n/a	Sigma 32201

Table 6.1. Materials used in this section, supplier product numbers and abbreviations that are used to refer to them within the text.

6.3.2 Methods

HNO_3 Etching: 20 mL nitric acid (70%) was added to a 200 mg BNP sample in a 100 mL tri-necked round bottom flask equipped with a vertical reflux condenser and glass protected thermocouple. The

mixture was covered in aluminium foil to prevent ambient light being incident on the setup. The mixture was then stirred with a 10 mm teflon stir bar at a temperature of 85 °C for 18 hours.

H_2SO_4/HNO_3 Etching: 15 mL sulfuric acid (95.0-97.0%) was cooled in an ice bath and 7 mL nitric acid (70%) was added and swirled until mixed and cool. This nitrating solution was added to 200 mg of a dry BNP sample in a 100 mL tri-necked round bottom flask equipped with a vertical reflux condenser (topped with silica drying beads) and glass protected thermocouple. The mixture was covered in aluminium foil to prevent ambient light incident on the setup and was then stirred with a 10 mm teflon stir bar at a temperature of 85 °C for 18 hours.

H_2SO_4 Etching: A 200 mg of a dry BNP sample was mixed with 25 mL of sulfuric acid (95.0-97.0%) in a 100 mL tri-necked round bottom flask equipped with a vertical reflux condenser and glass protected thermocouple. The mixture was stirred with 10 mm Teflon stir bar at a temperature of 120 °C for 18 hours.

Piranha Solution Etching: A 30 mL hydrogen peroxide solution (30%) was cooled in an ice bath then 10 mL of sulfuric acid (95.0-97.0%) was added slowly. This solution was added to a 200 mg BNP sample in a 100 mL tri-necked round bottom flask equipped with a vertical reflux condenser and glass protected thermocouple. The mixture was stirred with 10 mm Teflon stir bar at a temperature of 100 °C for 18 hours.

Etched Sample Washing: After being heated in the oxidising solutions for the 18-hour periods, the etched BNP samples were cooled to room temperature and 50 mL of water was added through the top of the reflux condenser to dilute the oxidising mixture. Samples were then vacuum filtered over a 1 μm pore PTFE membrane on a Teflon mesh and Teflon frit, initially wetted with 2 mL ethanol. This was then washed (with stirring by glass rod) sequentially with 80 mL de-ionised water, 30 mL 0.1 g mL^{-1} potassium hydroxide solution, 20 mL de-ionised water and 30 mL ethanol. The resulting BN white powder was then dried in a vacuum oven at 100 °C overnight. All samples of etched BN (approx. 130

mg in a typical sample) were then stored in glass vials and re-dried in the same vacuum oven the night prior to individual analysis.

Sonication of BNP in Acid: A 200 mg BNP sample was placed in a tri-necked 250 mL round bottom flask. 22 mL cooled (0 °C ice bath) H_2SO_4/HNO_3 acid mixture was then added and vertical reflux condenser placed on top. The flask was then held (by clamp on the middle flask neck) in a heated 60 Hz, IND1250D PACKED bath sonicator so that the BN/Acid suspension within the flask was fully submerged. The suspension was then simultaneously refluxed and sonicated at 70 °C for 28 hours or 18 hours (non-continuous over multiple workdays). The sample was then left to cool to room temperature, at which point 50 mL ice water was added in parts through the reflux condenser. The solution was then swirled and washed, as previously described, in preparation for analysis.

6.4 Results and Discussion

6.4.1 Chemical Etching of BNP Experimental Theory

As explored in section 2.2.1.3 of the literature review, and re-introduced in 6.2, numerous sources have claimed that it is possible to oxidise hBN materials and introduce hydroxyl functionality to their surface by mixture with acids alone.[53,82,83,85,86] In this work, four BN platelet samples of varying surface area were mixed with four common acid oxidising solutions (Figure 6.1) to find and confirm a system that would consistently return high yields of oxidised BNP.

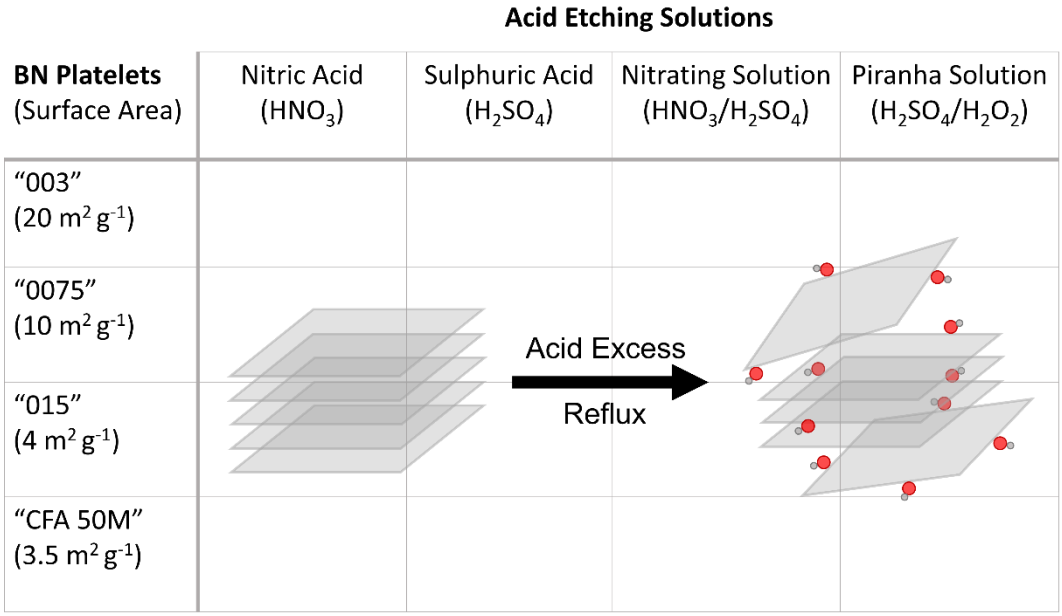


Figure 6.1. Schematic diagram of acid-BNP reaction overlaid onto a table showing an overview of the scope of this experimentation. Four boron nitride platelet starting materials of varying surface area are separately immersed in four common acid etching solutions. The amount of acid is stoichiometrically far in excess of the BNP, and the temperature of the system is maximised to the systems boiling point to ensure that a reaction (if possible) will occur. If the reaction is successful, this should result in the addition of hydoxyl functionality (represented by red and white circles) to the BN sheets and possible exfoliation of the original material.

The four BNP starting materials (003, 0075, 015 and CFA 50M) have varying surface areas (20, 10, 4 and 3.5 $m^2 g^{-1}$ according to manufactures specifications[219]) and should therefore present different amounts of hydroxylation when oxidised. The actual surface areas of the 003 and 015 material were later found to be 12.70 ±0.03 $m^2 g^{-1}$ and 3.33 ±0.01 $m^2 g^{-1}$ respectively as measured by BET (see section

6.4.2.5). Despite this slight discrepancy, it is still expected that a steeper increase in the BN oxidation signifiers, when characterising reacted samples for the higher surface area materials, will indicate a more successful method.

The etching solutions were selected based on literature and availability of materials. Nitric acid has been reported to hydroxylate up to 15% of boron sites[83] of a hBN starting material, although other sources have cast doubt on this.[84,88] Neat sulfuric acid and the nitrating solution (a sulfuric and nitric acid mixture) is commonly used to oxidise carbon nanomaterials[86] but has also been shown to be effective when applied to BN systems.[53] Similarly, piranha solution (a sulfuric acid and hydrogen peroxide mixture) has been shown to oxidise graphite[220] as well as etch away BN material from Si based substrates.[221] All of these acid systems are common to most laboratories and have a long history of use within industry, meaning that any successful etching methods could be scaled up.

All sixteen experiments (4 BNP x 4 Acids) were conducted under reflux conditions (boiling point of the acid solutions) to ensure the highest temperature possible at atmospheric pressure. This was done to force any reaction that might occur to do so to its greatest extent so as to be more easily detected. The reactions were carried out over an 18-hour period to provide enough time for any etching process to occur. This is similar to the times used in literature[83], but is significantly longer than times used for carbon nanomaterial oxidation (30 min used in section 4.3.2) as BN is known to be less reactive.

6.4.1.1 IR Analysis

After the acid solution exposure, washing, and drying procedures had been carried out on the chemically etched BNP samples, they were initially characterised by IR spectroscopy. The most easily identifiable region of interest within the spectra is between 3200-3600 cm^{-1} which indicates the presence of N-H and O-H bonds. These moieties would be expected if the chemical etching has been successful in oxidising the BN surface which would then be decorated with hydroxyl functionality as shown in Figure 6.2.A.

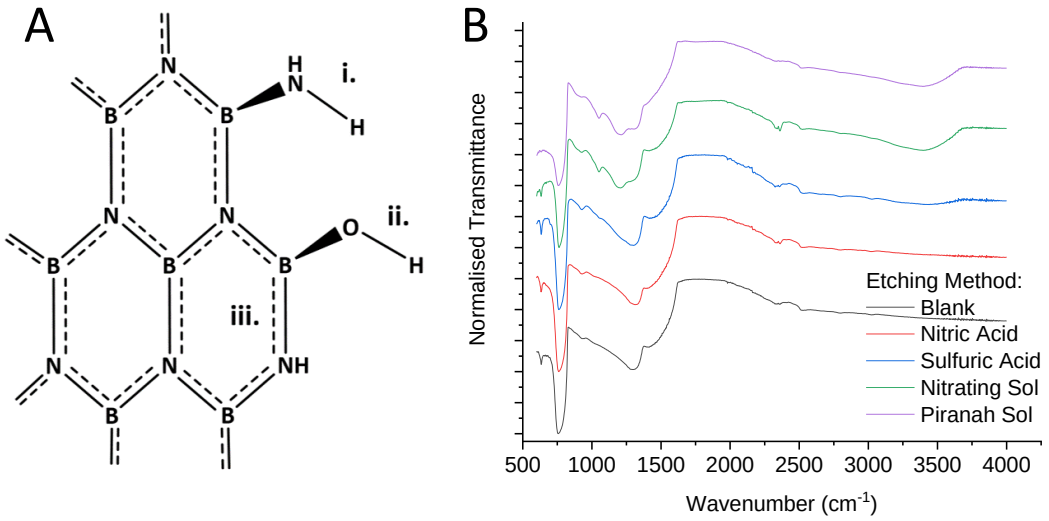


Figure 6.2. Example IR analysis of hBN. A bond diagram **[A]** of the terminating edge of hBN highlighting the **[i]** N-H, **[ii]** O-H and **[iii]** B-N bonds which would be created by a successful oxidation reaction. The staggered plot of normalised IR spectra of the acid etched 015 BNP samples **[B]** have been measured using attenuated total reflection (ATR). These show promising results from the Nitrating and Piranah solutions which display broad hydrogen bonding peaks in the 3500 cm^{-1} region compared to the starting material (blank) that are indicative of the oxidation reaction being successful.

Initially the IR analysis was conducted using ATR-IR and results from these studies were promising. Figure 6.2.B. shows an example set of IR spectra for the low surface area (large flake size) 015 BNP samples that have been chemically etched. The expected characteristic BN peaks at 1383 cm^{-1} and 804 cm^{-1} are present but, importantly, a broad peak at 3400 cm^{-1} emerges weakly for the sulfuric acid etched material but, much more significantly, for the nitrating and piranha solution exposed BNP. This was not the case, however, for nitric acid mixed BNP whose spectra was near identical to the starting material blank implying no reaction has taken place.

IR analysis was conducted by both ATR-IR and transmission IR using a sample containing compressed KBr discs (characterisation section 3.9). The latter method was used to re-take the IR spectra of all chemically etched samples as the ATR gives poor quality spectra due to the interference caused by the orientational differences of individual BN platelets on the ATR surface. The resulting KBr plated spectra are more reproducible and give more defined bond peaks which can be seen in Figure 6.3.

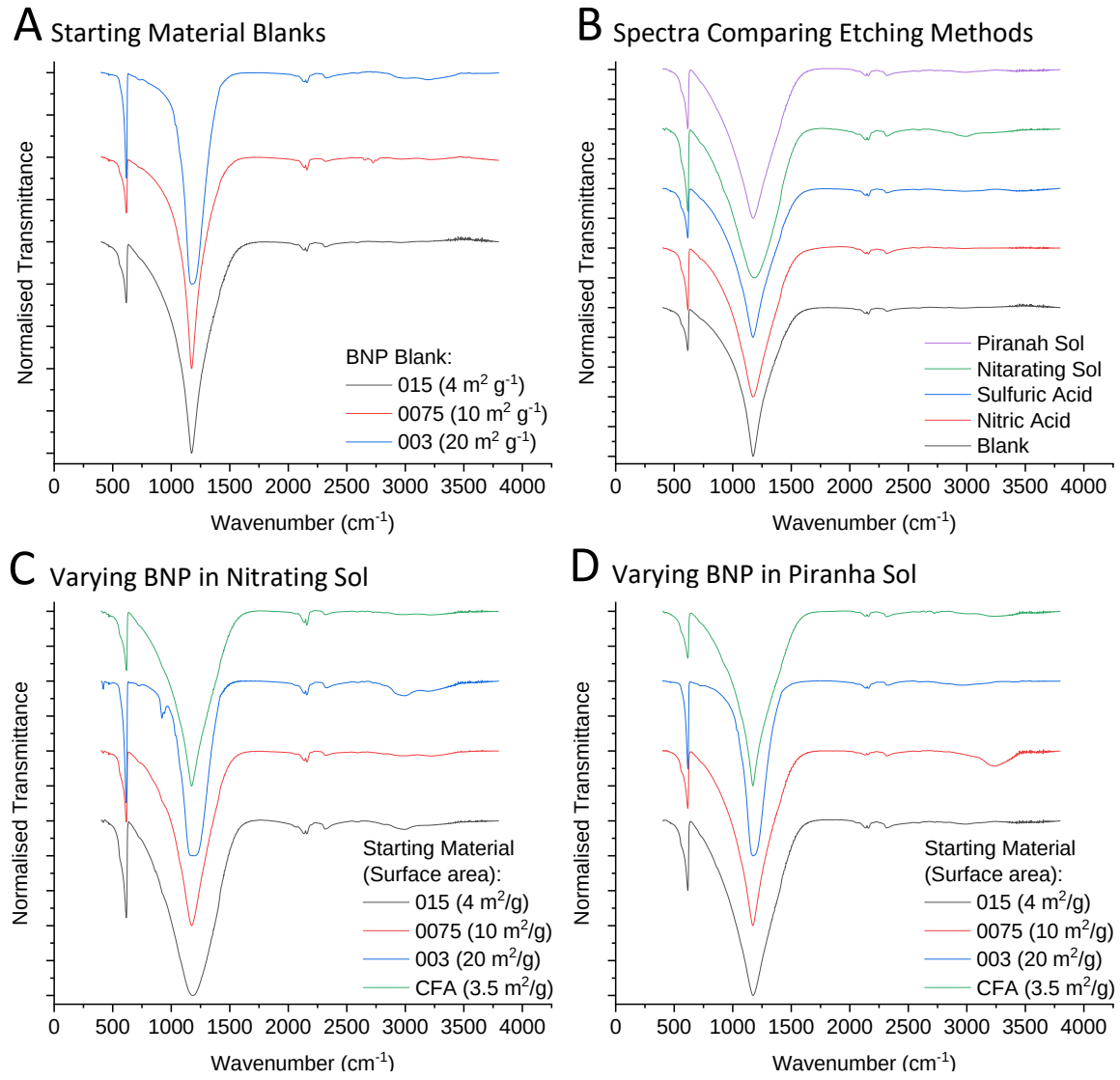


Figure 6.3. Relevant IR spectra of BNP samples taken using KBr plating method (section 3.9). The starting material BNP (Blank) spectra **[A]** were compared to the spectra of the 015 (low surface area) material etched under all investigated oxidising conditions **[B]** from which the initially promising hydrogen bond peaks seen for the piranha and nitrating solutions were d educed. The spectra for samples etched using these more promising nitrating (H_2SO_4/HNO_3) **[C]** and piranha ((H_2SO_4/H_2O_2) **[D]** solutions are then further examined. Here, only a few spectra (003 BNP with nitrating sol and 0075 with Piranha sol) show O-H bonding peaks in the 3500 cm^{-1} region.

The spectra (Figure 6.3.A) for the blank BNP starting materials (heated for 18h in water then filtered and dried as other samples) show only significant peaks at 1383 cm^{-1} (B-N stretching) and 804 cm^{-1} (B-N-B bending).[173] There are additionally CO_2 anomalies at 2200 cm^{-1} which are a product of the analysis method and can be discounted due to their ubiquity throughout all samples. There were also a slightly

larger signal in the 3000 – 3500 cm^{-1} range for the 003 BNP blank which is thought to be due to its larger surface area and larger amount of pre-existing terminating edges containing O-H and N-H moieties.

The KBr plated IR spectra, comparing the effects of the different etching environments (Figure 6.3.B), show significantly less signal within the hydrogen bonding range compared to the ATR results, with only the nitrating solution (H_2SO_4/HNO_3) showing a resolvable peak. The nitric acid etched BNP materials again show no variation from the blank and does not support the claims made by G. Ciofani et al.[83] who claimed nitric acid treatment of hBN created hydroxyl functionality which could be used to anchor further additions to the hBN surface. It is possible that the latter study could have mistakenly conflated its success in the subsequent silanization of BN for success in hydroxylation when the two process may have been unrelated as the Si content of the final product was the only measure used for success. Additionally, other studies have used nitric acid as a hBN cleaning reagent[84] where the acid solution is used to clean away silver nanoparticles leaving pristine and undamaged BN. For these reasons it is therefore reasonable to conclude that hBN is inert to Nitric acid treatment.

Due to some acid etched BNP samples within the set displaying peaks in the O-H and N-H IR region, the IR spectra of all BNP treated by the nitrating and piranha solutions were plotted (Figure 6.3.C-D). If oxidation had been universally successful in these reactions, the O-H peak at 3500 cm^{-1} should have increased for larger surface area materials. However, no significant correlation between surface area (by type of BNP starting material) and hydroxyl functionality was observed. Additionally, no B-O bonding signal is observed which would have appeared as peaks at 1350 cm^{-1} (B-O asymmetric stretch) and 860 cm^{-1} (B-O symmetric stretch).[222]

As results suggesting successful oxidation of BNP samples was mixed, further analysis was therefore required.

6.4.1.2 Raman Analysis

Study of the peak position and full width half maxima of the E_{2g} Raman peak for BN samples can give information about the relative size of BN crystallites as well as potential exfoliation of the sample. This peak has therefore been isolated and plotted for each chemically etched BNP in Figure 6.4 which is sorted by BNP starting material.

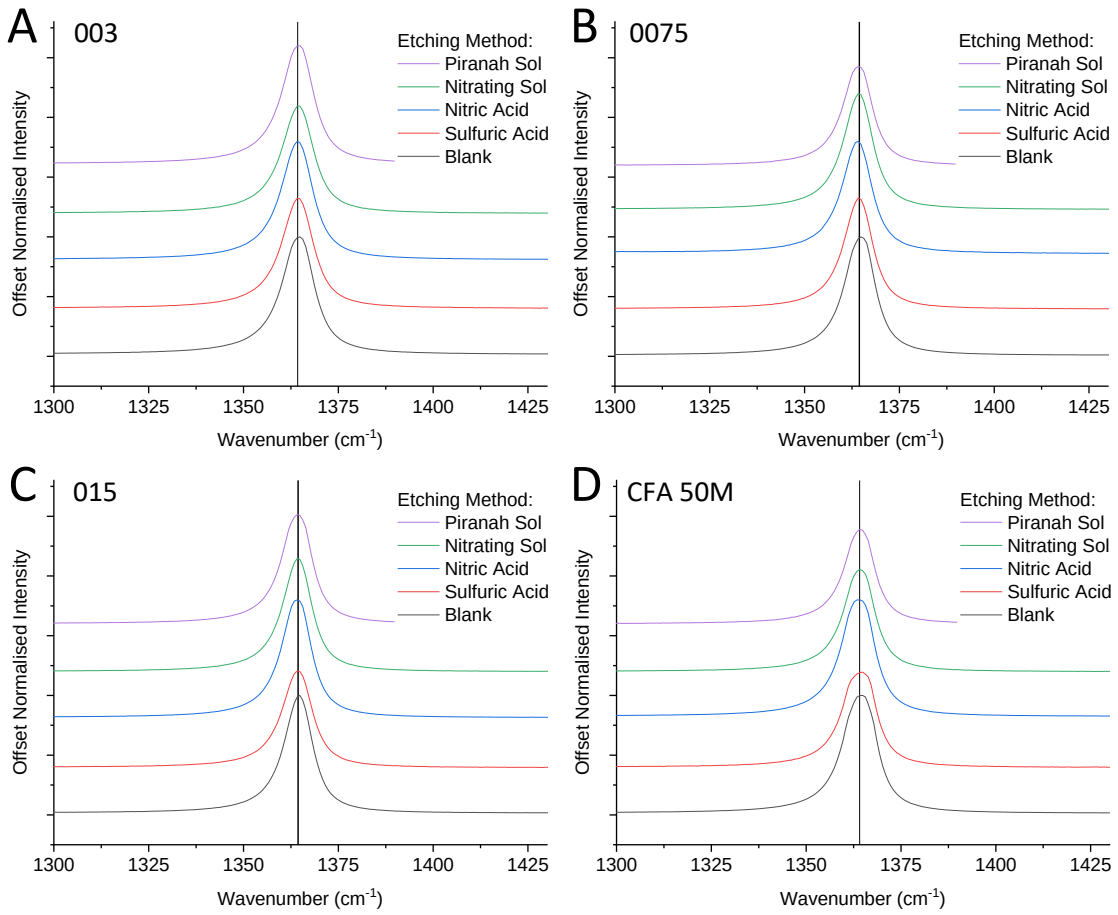


Figure 6.4. Collated Raman spectra focussing on the B-N indicating peak at 1364 cm^{-1} (indicated by the solid black line on the spectra). Each individual plot shows the results from different etching solutions on a single starting material which vary in surface area. These surface areas are **[A]** 20 m^2 g^{-1}, **[B]** 10 m^2 g^{-1}, **[C]** 4 m^2 $g^{-1}$and **[D]** 3.5 m^2 g^{-1} for the 003, 0075, 015 and CFA grade BNP as stated by the manufacturer.

The Raman spectra (Figure 6.4) are very similar for all samples within the same set and have not changed significantly, despite acid treatment. If oxidation has occurred to a significant degree, it would be expected that the hydroxylated platelets would be more likely to spontaneously exfoliate or at least not re-stack due to more favourable BN-solvent interactions. This reduction in BN size or

oxidation would be shown as a blueshift in the E_{2g} peak of between 1.1 – 2.2 cm^{-1}.[135,136] To quantify any potential peak shift of the BNP Raman spectra, the E_{2g} peaks were fitted using a Lorentz function and the results are plotted in Figure 6.5.

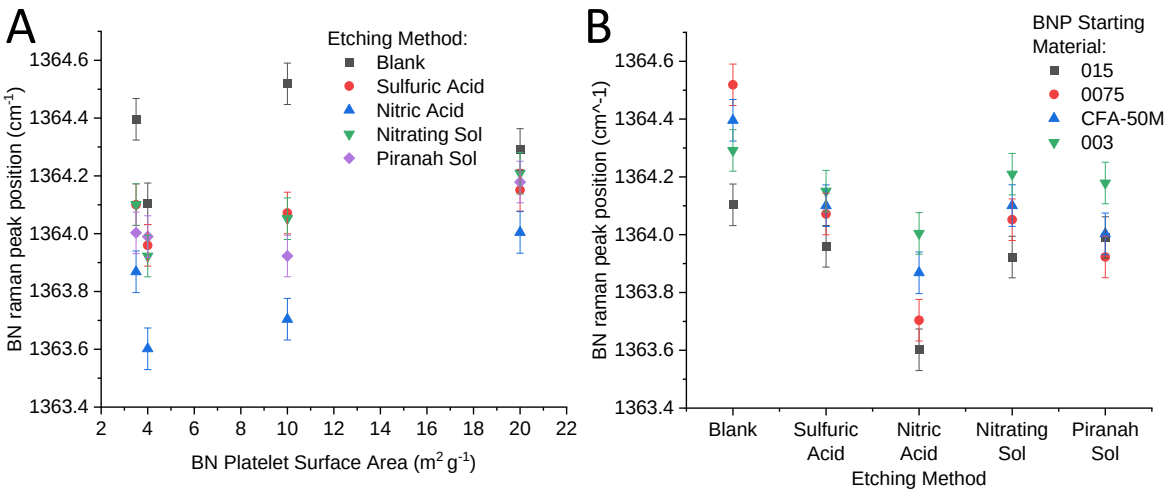


Figure 6.5. Secondary analysis of the BN E_{2g} Raman peak around 1364 cm^{-1}. The variation in peak position is compared to the **[A]** BN surface area and **[B]** etching method in order to determine any trends within the data.

Secondary analysis of the BN E_{2g} Raman peak (Figure 6.5) shows that the peak position's variation is not greater than 0.8 cm^{-1} from the starting materials' blank. This small shift allows the BNP to be assessed as still consisting of >6 monolayers hBN sheets as predicted by Gorbachev *et al.*[137] Additionally, this small the peak position shift is also to a lower energy (redshift). Furthermore, there are no significant trends between starting materials or etching methods so, overall, it is reasonable to assume that the chemical oxidation has made no resolvable change to the BNP nanostructure. This is not necessarily proof of the oxidation reaction failing as the smallest size of BNP used here are on the 0.1 – 1 µm scale which will be shown to not change significantly (SEM in section 6.4.1.5). Most noted shifts in hBN Raman spectra from literature are determined from materials on the quantum dot scale (1-10 nm) and therefore the oxidation of the larger BNP surface may not lead to significant changes.

6.4.1.3 XPS Analysis

In the absence of strong evidence for BNP oxidation from acid etching using IR (weak) and Raman (inconclusive), XPS was undertaken to find atomic content percentages as well as to investigate boron bonding environments which should display a measurable increase in B-O as oxidation occurs. Additionally, successfully hydroxylated BN samples of increased surface area should also show an increased proportion of hydroxylation and oxygen atomic composition when compared to samples treated by the same method of lower surface area. The results of this characterisation are displayed in Figure 6.6 while the method of deconvolution for the B1s spectra can be found in section 3.6 of the characterisation chapter.

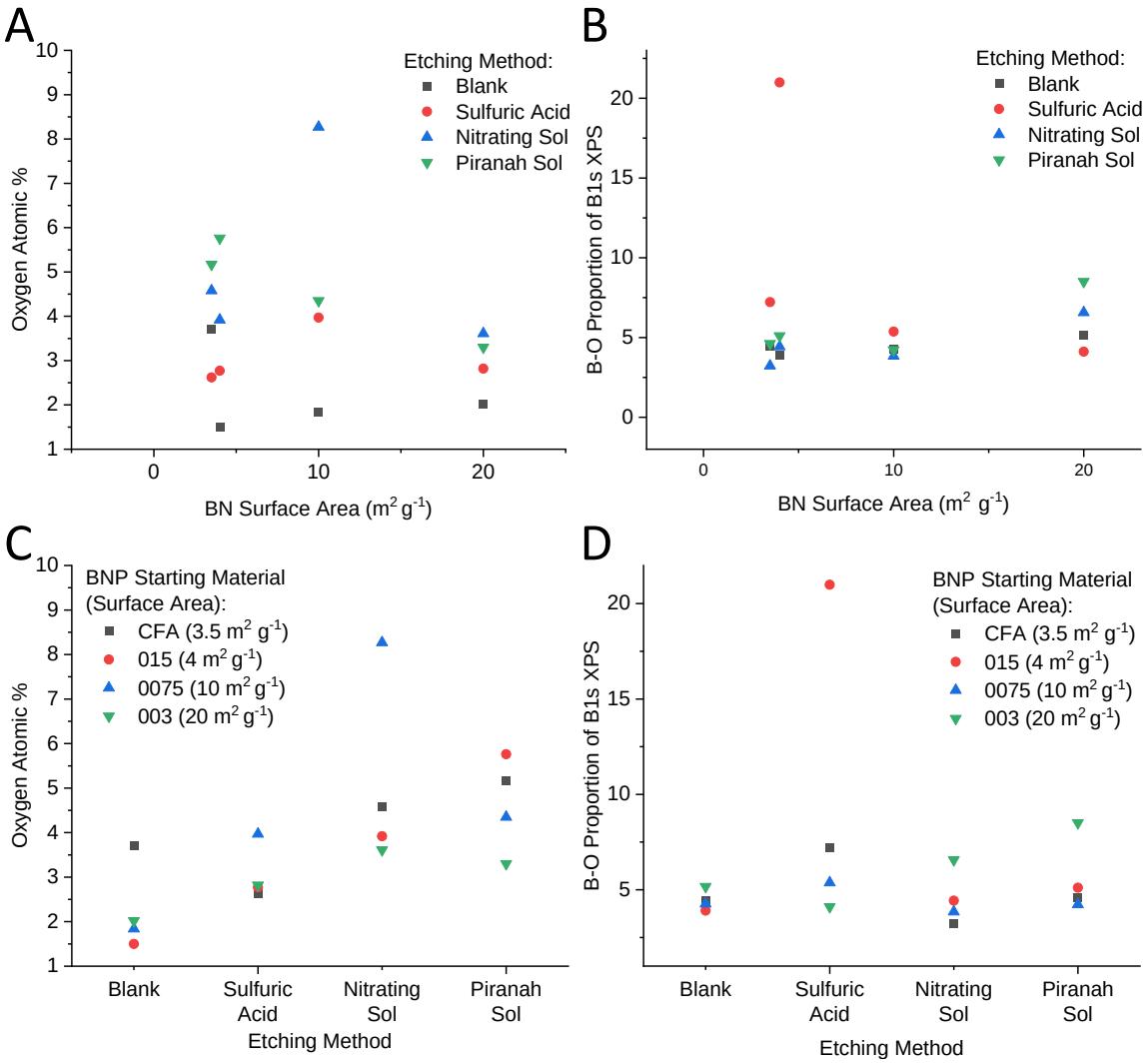


Figure 6.6. Results from the XPS analysis of acid etched BNP samples. Atomic percentages of oxygen (with error bars calculated from multiple XPS readings) within the BNP samples are compared with respect to **[A]** the samples reported surface area and **[C]** the etching method used. Additionally, the B-O bonding proportion within the B1s deconvolution is plotted with respect to the same surface area **[B]** and etching method **[D]** variables.

The oxygen atomic percentage and B-O bonding proportion can be compared to the samples' surface areas (Figure 6.6.A and B). The atomic composition of oxygen increases in all samples compared to their starting material, as predicted for an oxidation reaction. However, the proportion of B-O bonding within the same samples does not significantly increase (and in some cases, decreases). The 015 sample etched in H_2SO_4 does not follow this trend but is assumed to be anomalous, as FTIR and Raman analysis showed no significant variation from its starting materials. It is therefore thought that the

additional atomic oxygen content is from adsorbed or intercalated oxygen containing molecules of solvent or acid reagents that have not covalently bonded to the BN surface.

Despite this possibility, the same data was compared to the etching method used for the oxidation to illuminate trends in the acids used. Figure 6.6.C and D, show that all oxidising solutions caused an increase in both the oxygen and B-O content of the samples. Again, however, no overall trend was observed and results could be explained by adsorption and intercalation of oxygen containing solvents or air. It must be concluded therefore that either the oxidation methods used for this section are unsuccessful in their stated purpose, or that their success is unmeasurable through the techniques used so far.

6.4.1.4 EDS Analysis of Oxygen Distribution

The previous IR, Raman and XPS analysis showed that the BNP nano-structure appears mostly unchanged by the chemical etching solutions that have been exposed to them. However, XPS indicated that there is a significant increase in atomic oxygen content within the samples compared to the blanks, which implies that this increase cannot be discounted as poor drying procedures (as the blank samples were washed and dried using the same method). To investigate the distribution of oxygen within these samples and determine its origin, EDS maps were taken of the nitrating solution etched BNP samples and examples of this analysis are displayed in Figure 6.7.

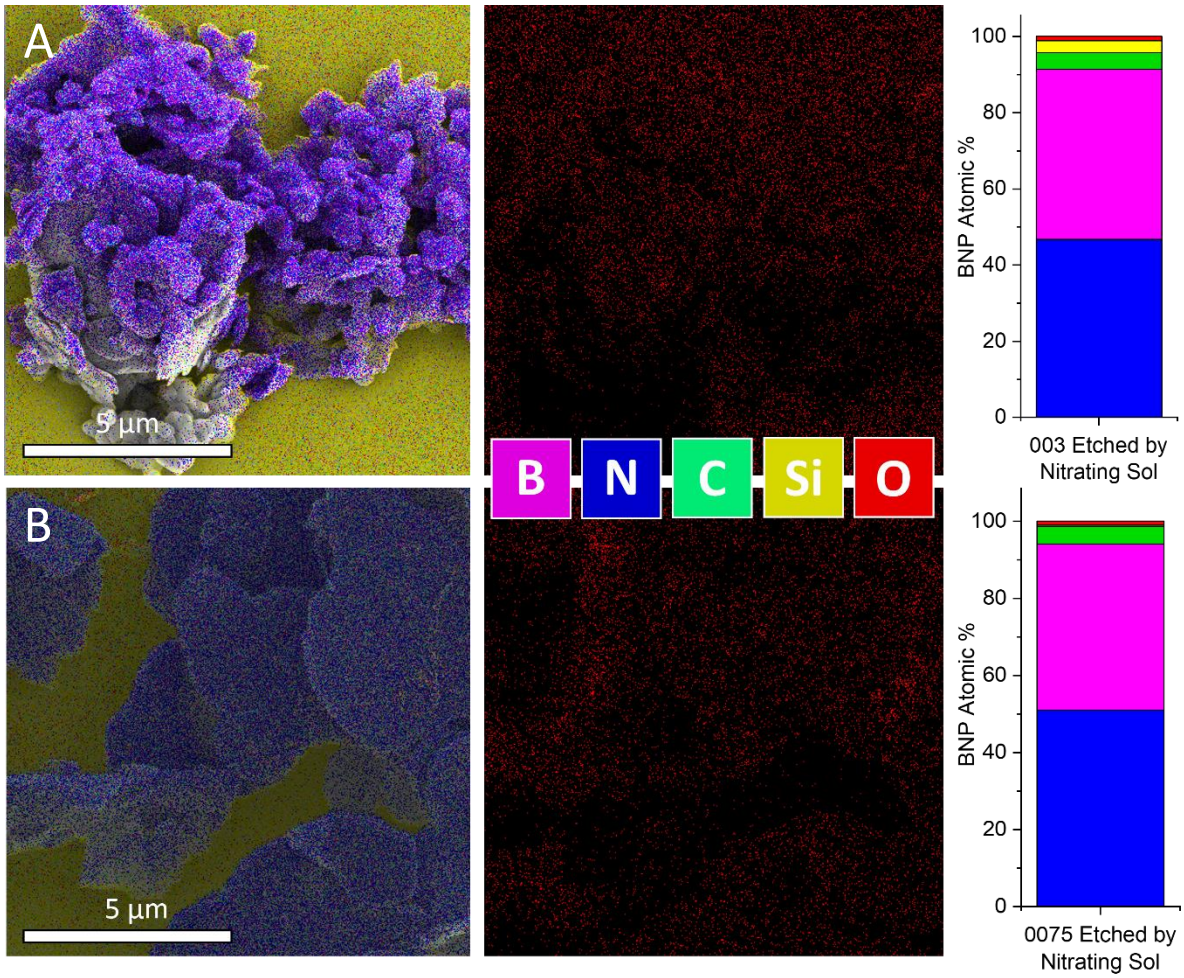


Figure 6.7. EDS elemental maps of BNP samples chemically etched by the nitrating solution (H_2SO_4/HNO_3). The maps presenting all elements as well as just oxygen are shown next to a stacked column chart showing the elemental breakdown for the 003 **[A]** and 0075 **[B]** etched samples. These examples were chosen as they displayed the lowest and highest (respectively) oxygen atomic percentage within their etching environment under XPS analysis.

Neither sample shows localised concentrations of oxygen (Figure 6.7). When oxidised, BN structures can form boron oxide (B_2O_3) which can appear as small deposits of high oxygen content within the sample. Any boron oxide that might have formed during the etching reaction would have been washed away, as it is moderately soluble in water (36 g L^{-1}).[223] There are also no detectable increases in oxygen concentration at the more reactive terminating edges of the 2D platelets. These edges are more visible on the larger 0075 material (Figure 6.7.B) which shows a larger oxygen concentration on the silicon wafer than the BNP itself.

Overall, this EDS data has confirmed that any oxidation that has occurred is not localised but spread evenly (and thinly) across the entire BNP sample. As XPS has shown that this oxygen content is not covalently bonding to the hBN, it must be assumed that the even coating shown in the EDS is adsorbed to the BN surface, so implying that the BNP are inert to the oxidation reaction.

6.4.1.5 SEM Analysis of BNP Size Distribution

Another, more crude way of checking the success of acid etching is by the measurement of the BN platelets' size before and after the oxidation process. In future sections of this work (0), it is shown that hBN based fibers have their structures completely broken down by acid oxidation and it was hypothesized that a similar significant reduction of these chemically etched samples will indicate a successful oxidation reaction despite it leaving little chemical trace. Numerous SEM images (representative examples shown in Figure 6.8) of BNP samples were taken before and after chemical oxidation. These were used to calculate the diameter distribution of the nitrating solution etched samples.

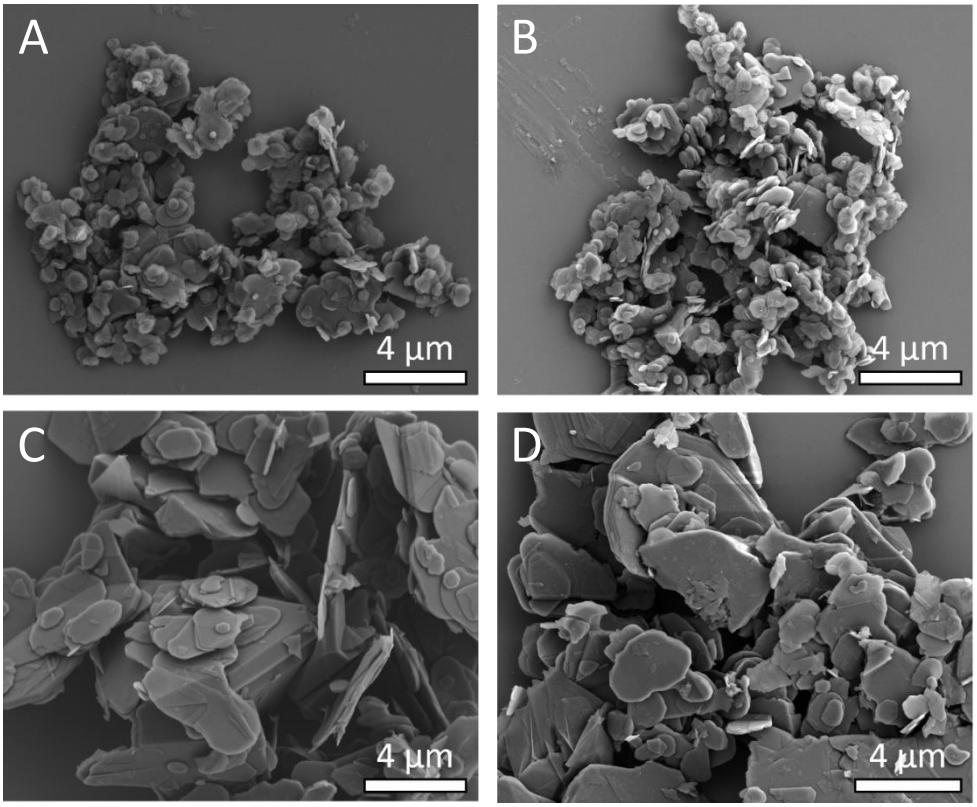


Figure 6.8. Example SEM images of BNP samples. The high surface area 003 BNP starting material before **[A]** and after **[B]** acid etching are compared to the low surface area and larger platelet sized 015 before **[C]** and after **[D]** the same process.

As was shown previously by the EDS maps and now re-iterated here, the chemical oxidation solution alone does not significantly change the BNP size or structure when observed by eye. When quantified, this observation is borne out as the average platelet diameter for 003 samples did not change significantly after oxidation, going from 0.79 ±0.55 µm to 0.71 ±0.59 µm (median sizes being 0.605 and 0.542 respectively). Similarly, the 015 sample did not change statistically but even increased in size from 1.94 ±1.53 µm to 2.86 ±2.08 µm (median being 1.50 and 2.42 respectively). This clearly shows that no significant loss of hBN has occurred to the platelets through chemical oxidation.

6.4.2 Kinetic Cleavage Assisted Etching

The characterisation of the initial chemical etching of the BNP starting materials analysed in the previous section has shown that minimal, if any, oxidation or hydroxylation has been achieved by

heated reagent mixing alone. While this is unfortunate, it is consistent with other literature sources that have claimed that oxidation of hBN can only be achieved through more extreme conditions.[200]

A commonly cited and easily implemented way of introducing more extreme conditions into the BNP/etching solution system is the use of sonication. Sonication is most associated with 2D nanomaterial research with exfoliation, but C. Backes *et al.*[224] hypothesised that the rates of exfoliation (peeling) and nano-sheet cleavage (tearing) were linked, as expressed in Eq 6.1, where a was empirically calculated to be 0.8 ± 0.1.

$$\langle E_{Peeling} \rangle = a \times \langle E_{Tearing} \rangle \qquad \textit{Eq. 6.1.}$$

It is thought that this relationship is because as the material thins through exfoliation, it becomes weaker and thus more susceptible to lateral tearing. In this work, it was thought that by damaging the materials' nanostructure through the kinetic cleavage induced by sonication, the broken terminating edges of the smaller hBN can be used as a more reactive substrate onto which the oxidising acid solutions used previously could be more able to react (see Figure 6.9).

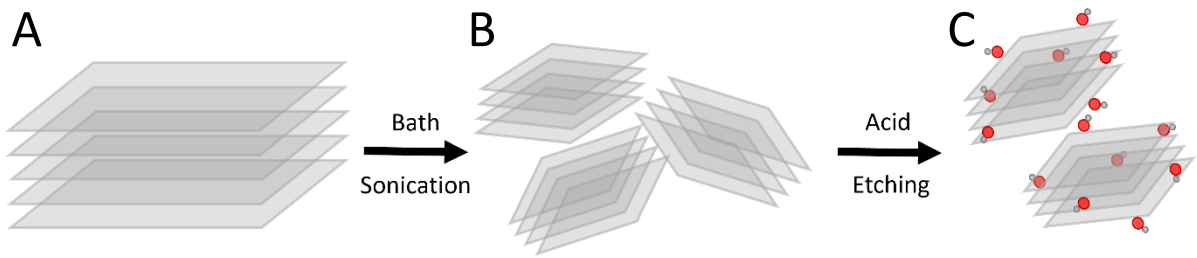


Figure 6.9. Schematic Diagram showing the proposed method of action for the cleavage and subsequent etching of the BNP. The BNP starting material **[A]** fractures due to the kinetic forces applied to it within the bath sonicator. These smaller BNP **[B]** will have a larger surface area as well as an unstable/unreacted terminating edge which it is hypothesized to be more reactive towards the acid etching solution in which the material is immersed thereby hydroxylating the surface of the material **[C]**.

This approach has been utilised across a wide range of literature with sonication being widely recognised as a cause of nano-structural damage. For carbon materials, sonication has been used to exfoliate and reduce the size of graphene platelets[60] and has even been shown to cause oxidation

when CNT are sonicated in water.[62] Further evidence for when applied to BN materials has shown platelets being oxidised when sonicated in a pressurised autoclave[53] as well as showing significant reduction in flake size after treatment.[61] Additional to this, studies have shown that sonication for periods of time as short as 5 hours can lead to a cut in BNNT length of up to 50% and this can be further enhanced by the addition of other chemical reagents within the reactor, such as ammonia which 'unzips' and 'de-caps' the BNNT, to leave an oxidised end product.[225]

To test the veracity of acid sonicated hBN methods to achieve BNP oxidation, the reflux experimental setup used in the previous chemical etching section (6.4.1) was modified by clamping the reaction vessel into a 500 W, 60 Hz bath sonicator. The use of a water bath limited the maximum temperature at which the reaction could be conducted to 70 °C, below the 85 °C used previously for the nitrating solution (H_2SO_4/HNO_3), but it was thought that the reactivity of the BNP would be more dependent on the cleavage of its bonds than on the temperature of reaction (which had done little in the previous section).

The nitrating solution (H_2SO_4/HNO_3) was selected for these experiments because of the partial evidence of oxidation success from section 6.4.1.1, as demonstrated by the FTIR results, as well as its common use in carbon nano-chemistry including this work (section 4.3.2 CNT oxidation). Samples of both the high and low surface area BNP (003 and 015 respectively) were sonicated at 70 °C for 18 and 28 hours non-continuously. The 18h time was selected so as to directly compare those results to the chemical etching of the same time period and the longer 28 hour time was used when initial testing showed little change over the shorter period, but falls in line with similar times used by B. Mapleback *et al.*[200] Blank samples were also produced by sonicating BNP samples in water at temperature.

6.4.2.1 FTIR Analysis

As with the chemical etching (Section 6.4.1), the initial characterisation of the sonicated BNP was conducted by IR and results are presented in Figure 6.10. Due to variations between the spectra of

the same sample, cleaved BN samples have been presented as an average line flanked by standard deviations.

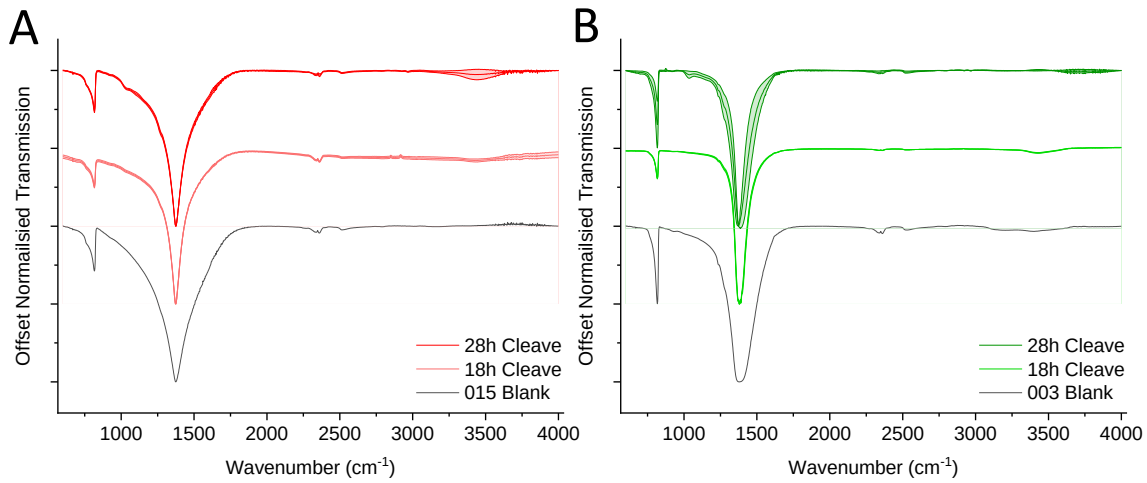


Figure 6.10. IR spectra comparing the blank (sonicated in water only) BNP samples to those sonicated in nitrating solution (H_2SO_4/HNO_3) for 18 and 28 hours. The acid sonicated BNP results are presented as an average and standard deviation of multiple spectra due to variation within sample measurements. Both the lower 015 **[A]** and higher 003 **[B]** surface area materials are shown.

The IR spectra for all samples show the characteristic hBN signals from the B-N stretching and B-N-B bending modes, but the slightly lower peak positions of 1377 and 802 cm^{-1} respectively. As with previous IR spectra of the 003 material, its higher surface area leads to a slightly bigger O-H signal in both the blank and samples, due to relatively more adsorbed solvent molecules compared to the 015 material. Despite this, there appears to be no significant change in the 3500 cm^{-1} region of the spectra between the acid sonicated and blank samples. This is not the case for the 015 samples as the 28h acid sonicated sample shows a significant increase in hydrogen bonding in this region as well as an unidentified single bond stretch peak at 1036 cm^{-1} which is suspected to be a B-O as it is very similar in energy to C-O primary alcohol bond (1050-1085 cm^{-1}).

This may be evidence that oxidation may have been achieved in the 015 sample. However, as this was not shown in the 003 sample, which is chemically identical to the 015 starting material, further investigation is warranted.

6.4.2.2 Raman Analysis of Nanostructure

Samples were subjected to Raman analysis and the hBN E_{2g} peaks for the 28h cleaved samples (which showed potential in the IR spectra) are presented in Figure 6.11.

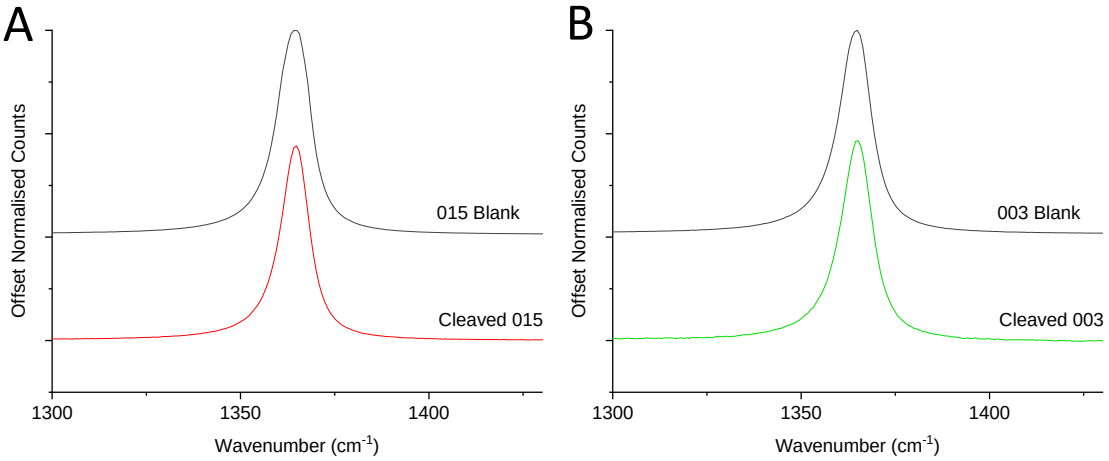


Figure 6.11. The hBN E_{2g} peak from the Raman spectra of the 28h sonicated (cleaved) samples are compared to the sonicated blank samples. Very little difference between the spectra can be observed in either the 015 **[A]** or 003 **[B]** systems.

The peak position of the cleaved 003 was blue-shifted by 0.4 cm^{-1} (1364.3 – 1364.7 cm^{-1}) while the cleaved 015 sample was similarly shifted by 0.3 cm^{-1} (1364.1 – 1364.4 cm^{-1}). These blue-shifts are again not significant enough to show that the material has been exfoliated[136] or significantly reduced in size[135] but may be explained as poorly re-stacked BN. Partial exfoliation by sonication and then re-stacking has been shown to distort the (002) plane of the hBN nanostructure and cause slight blue-shifting of the E_{2g} peak.[226] However, this slight difference is still very small and the FWHM of the peaks have shrunk (9.826 to 9.523 cm^{-1} for 003 and 9.874 to 8.595 cm^{-1} for 015), which is a sign of increased BN crystallinity,[227] the opposite of what would be expected if the BN was being cleaved and oxidised. The results obtained using Raman are therefore inconclusive.

6.4.2.3 XPS Analysis

For the initial experimentation using chemical etching alone (section 6.4.1), the expected XPS results for a successful hydroxylation reaction were an increase in both oxygen atomic content of the samples

and an increase in the B-O and B=O content of the B1s. These criteria for success remain the same for the sonicated samples and so the XPS results for the starting material, sonicated blank and acid sonicated samples are therefore displayed in Figure 6.12.

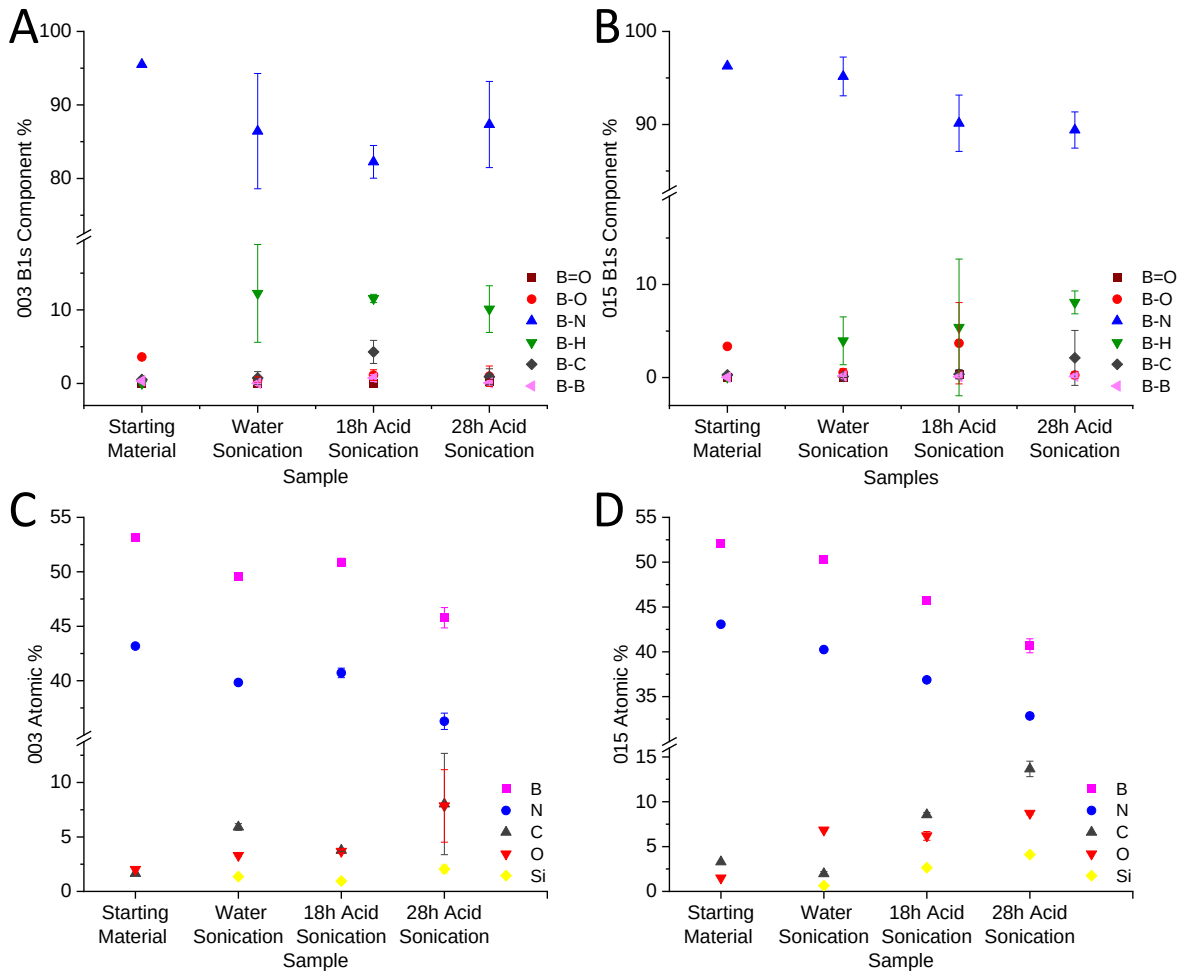


Figure 6.12. Result summaries for XPS characterisation of sonicated BNP samples. The proportions of boron bonding environments as found by the B1s deconvolution of XPS from the high surface area 003 **[A]** and low surface area 015 **[B]** BNP shows a reduction in B-N bonding but no significant or consistent corresponding increase in B-O bonding. The atomic percentage composition of the same 003 **[C]** and 015 **[D]** samples show a reduction in BN and an increase in oxygen and carbon.

The oxygen atomic content of both samples (Figure 6.12.C-D) follows the expected trend for samples becoming sequentially more decorated by hydroxyl functionality. The 015 samples especially demonstrate this with the oxygen content of the material increasing from the starting materials 1.50 % to 6.85 ±0.07 % for the water sonicated material to 8.72 ±0.16 % for the 28h acid sonicated material. This oxygen increase is matched by a consistent decrease in total BN proportion (95.2, 90.5 ±0.3, 82.61

±0.6 and 73.5 ±1.1 % for the starting material, blank, 18 h and 28 h sonication's respectively) which would also be consistent with a successful acid etching removing BN material and attaching other moieties onto its surface.

The evidence for functionalisation shown by the oxygen atomic content is not supported by the breakdown of boron bonding environments. The deconvolution of the B1s spectra for the 003 and 015 samples (Figure 6.12.A-B) show a decrease in B-O bonding for all samples (with the exception of the 18h acid sonicated 015 which still showed no significant increase). Instead, there was an increase in the B-H bonding proportion (to as much as 8.1 ±1.2 % in the 28h 015) which can be used as a proxy for damage to the BN structure. Taken together, these results indicate that the BN structure was damaged by the sonication, but this did not cause covalent oxidation of the BN surface.

6.4.2.4 SEM Analysis

In section 6.4.1.5, the size distribution of platelet diameters for the acid immersed samples were found to not change significantly due to chemical etching alone. However, the sonication that was used for these experiments has been shown to cut up hBN structures and the XPS analysis of them showed an increase in B-H bonding, indicating damage had been inflicted. SEM images for all samples were therefore taken and used to find platelet diameter distributions which are presented in Figure 6.13.

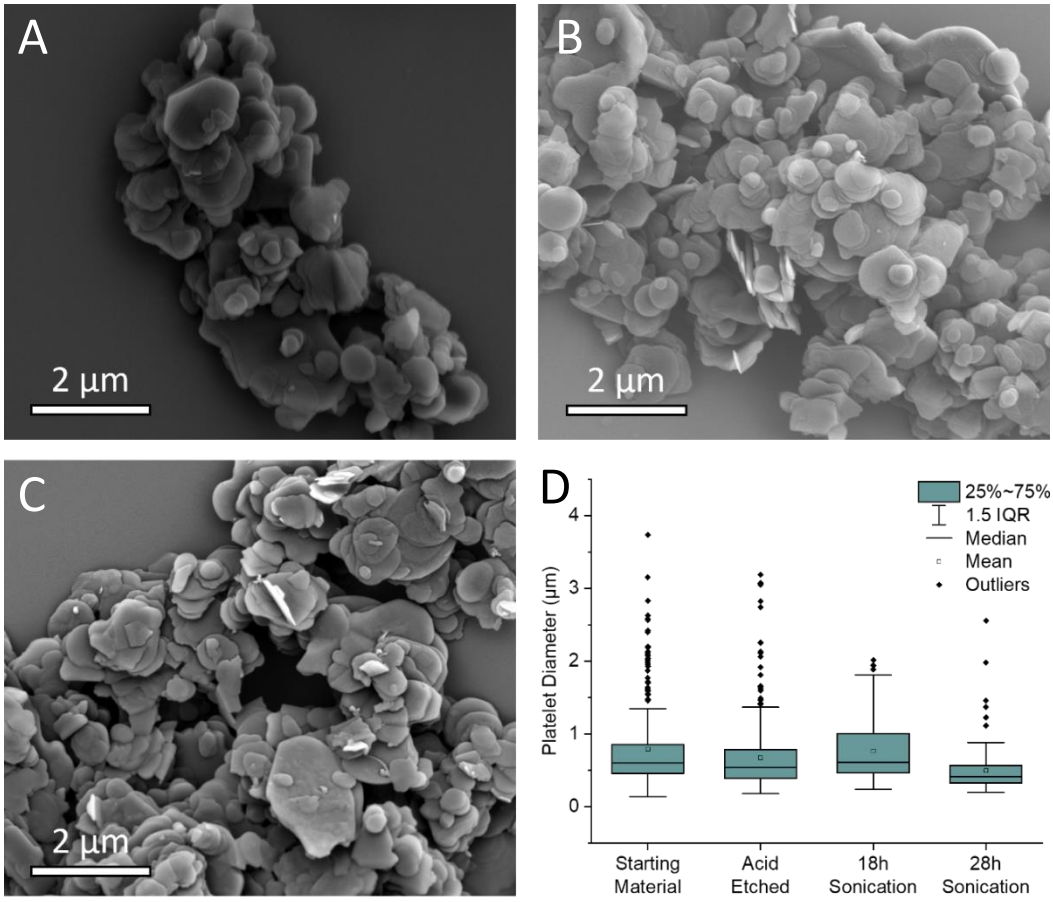


Figure 6.13. Example SEM images from a selection taken of each of the 003 BNP samples drop cast onto Si. The starting material **[A]** can be compared to the BNP after sonication in acid for 18 **[B]** and 28 **[C]** hours. The distribution of diameters of platelets for these samples is then plotted **[D]** and shows a slight decline in platelet size as more extreme conditions are imposed.

The 003 results (Figure 6.13.D) show a decrease in the average and median diameter from the starting material (0.79 ±0.54 and 0.605 µm respectively) and the most harshly treated 28h acid sonicated sample (0.50 ±0.32 and 0.41 µm respectively). There is no similar trend in the 015 set however, as the average diameters for these samples increased with more sonication from the 1.94 ±1.53 µm of the starting BNP to 2.92 ±1.93 µm. Work conducted by K. R. Paton *et al.*[228] predicts that that the exfoliation rate of similarly structured graphite is dependent on the flake size of the nanomaterial, as shown in Eq 6.2, and can explain why the larger 015 material did not see a size reduction.

$$\gamma_{min} = \frac{[\sqrt{E_{S,G}} - \sqrt{E_{S,L}}]^2}{\eta L} \qquad \textit{Eq. 6.2.}$$

Eq 6.2. was constructed by modelling exfoliation as shear-induced interlayer sliding in a solvent [229] and predicts the minimum shear rate (γ_{min}) as a function of the surface energies of graphene and solvent ($E_{S,G}$ and $E_{S,L}$) as well as the solvents' viscosity (η) and nanomaterials' flake length (L).

Despite trends in the average platelet diameters being observed, the large range of platelet sizes within individual samples leads to wide standard deviations for each result, both before and after the oxidation. This makes the diameter distributions of all samples for each of the same starting material statistically identical. It must therefore be concluded that the sonication and acid etching of the material had no resolvable effect on the diameter of platelets measured and that kinetic cleavage of the planar bonds within hBN by sonication has not been achieved or has only succeeded at a level that is unmeasurable by this technique.

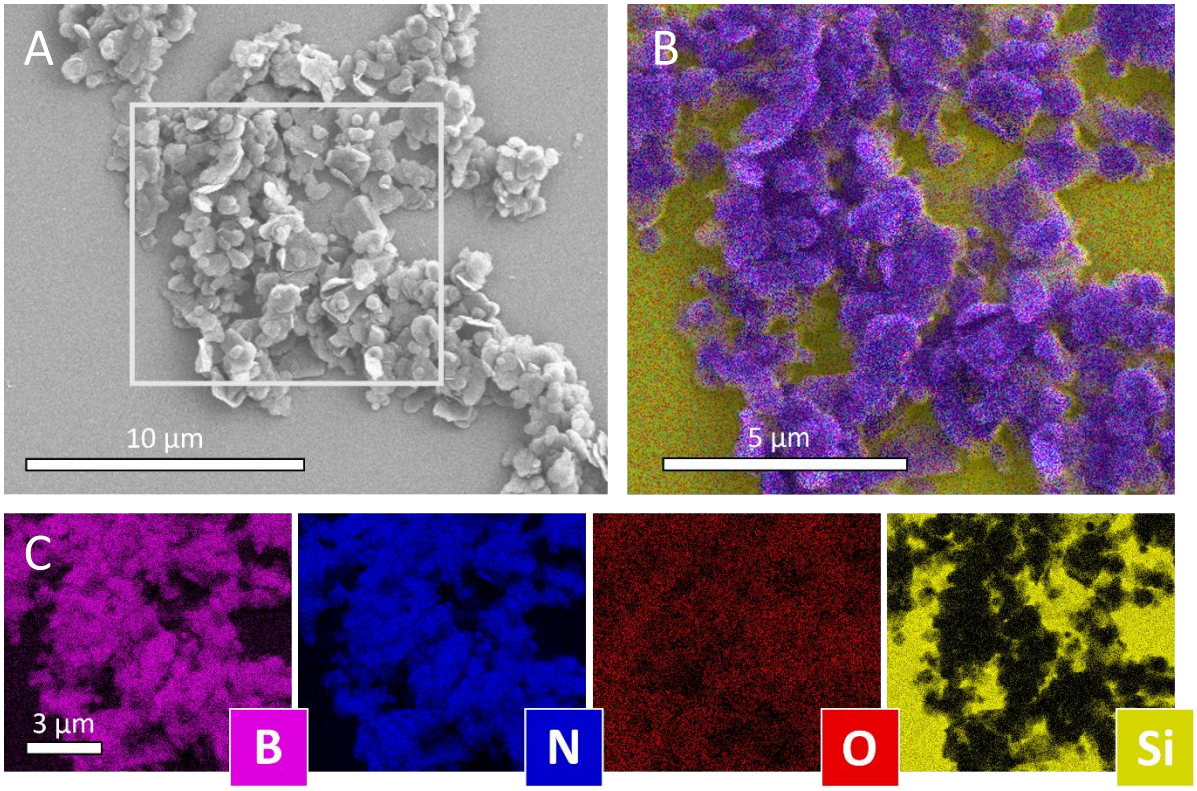


Figure 6.14. Example EDS images of the 003 18 hour acid sonication sample. The SEM image **[A]** shows the region used for the elemental mapping **[B]** of the sample. This map is a composite image made from the different elements B, N, O, Si and C which are also shown **[C]**.

The higher surface area 003 material does not show any localisations of oxygen concentration across

the BN sample (Figure 6.14), which is measured as having a 0.8 % proportion of oxygen content compared to 90.2 % BN, 4.4 % carbon and 4.1 % silicon. The visible similarity in oxygen concentration across both the BNP and the Si substrate onto which they are placed shows that this oxygen is ambient and must be adsorbed onto the sample from the atmosphere or processing solvents. The solvent origin is more likely as when a region of Si substrate is measured alone it consists of 88.3% Si and 11.7 % C.

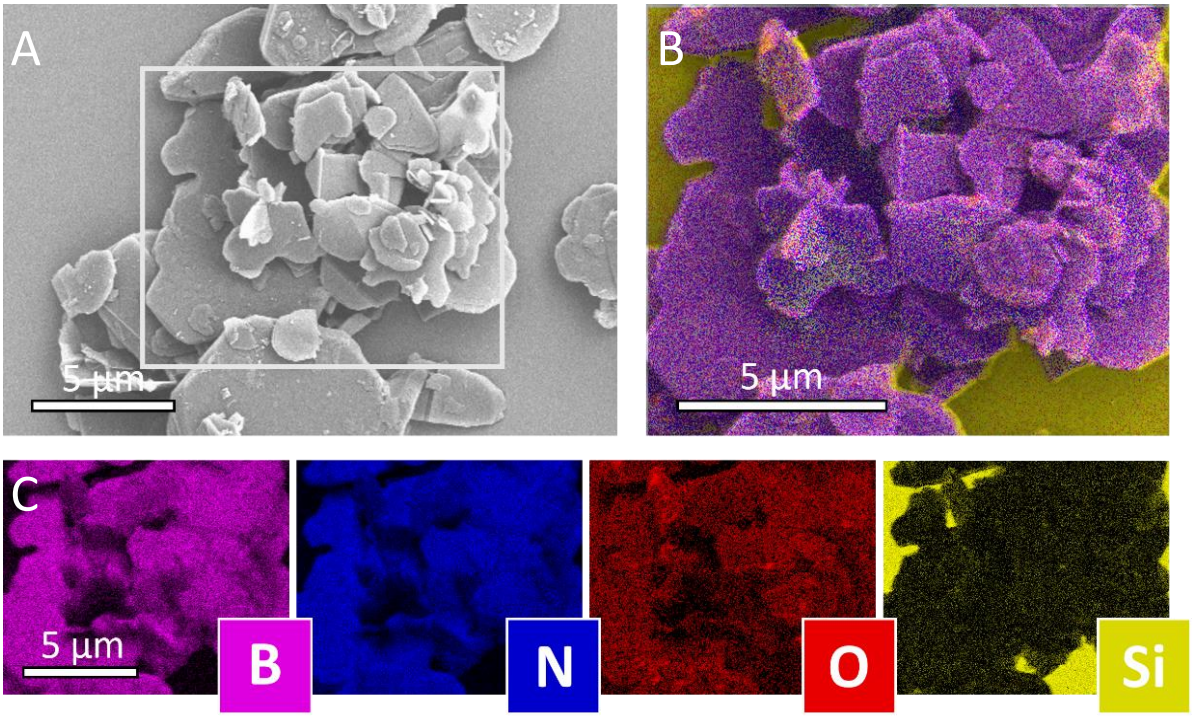


Figure 6.15. Example EDS images of the 015 18 hour acid sonication sample. The SEM image **[A]** shows the region used for the elemental mapping **[B]** of the sample. This map is a composite image made from the different elements B, N, O, Si and C which are also shown **[C]**. The oxygen map displays small regions of higher concentrations.

The majority of the 18 hour acid sonicated 015 sample (Figure 6.15.) is similar to the 003 in that its composition consists of 0.9 % oxygen, 92.7 % BN, 5.5 5 C and 0.9 % Si. However, while the majority of the oxygen does evenly cover both the Si wafer (measured at 97.2% Si and 2.7 % C) and the BNP as if adsorbed, there are small spots of regional density observed on the surface of some of the flakes. These regions are less than 100 nm across and are thought to be small flakes of BN that have been sheared away from the starting material by the sonication process and potentially reacted with the

acid to give the higher oxide density observed. Additionally, the small scale of these flakes explains why the average platelet size for the material was unchanged by the process, as their loss would be insignificant to the much larger BNP.

6.4.2.5 Surface Area Analysis

The SEM diameter analysis and Raman nano-structural analysis indicate that the BNP were unaffected by the acid sonication process. However, the increase in B-H bonding in the XPS implies some damage had been achieved even if this did not result in oxidation. Damage to the BN sample would be expected to increase its surface area as the BNP break apart. Brunauer-Emmett-Teller (BET) measurements were therefore commissioned for all samples to determine their surface area.

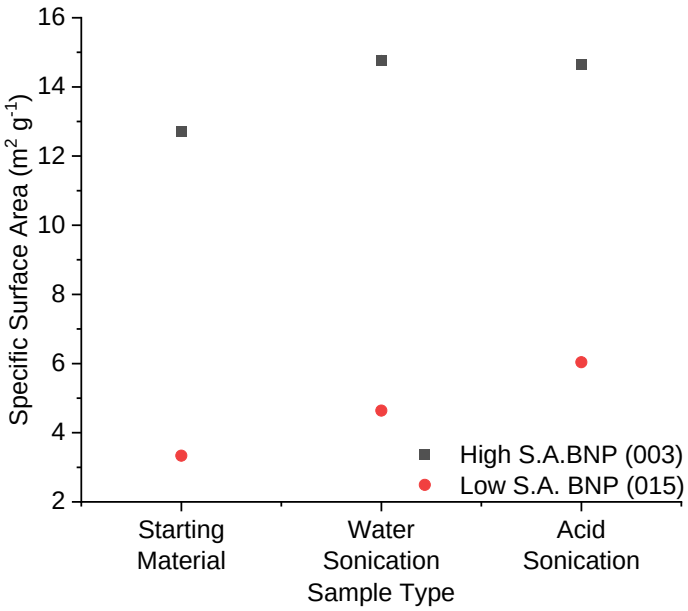


Figure 6.16. Surface area measurements from BET analysis of BNP samples. This shows an increase in surface area compared to the starting material due to the sonication process in both water and acid but is less conclusive between the two. Note that error values provided by the BET technician have been plotted on this graph but fall within the plotted symbol.

Figure 6.16 reflects the XPS results and shows the more harshly treated BNP (sonicated and acid immersed) for both the 015 and 003 materials have a higher specific surface area and are presumed to be more damaged than those less exposed to these conditions. The lower surface area 015 samples best exemplify this trend and showed an increase in surface area due to sonication alone from the

3.33 ±0.01 m^2 g^{-1} of the starting material to 4.64 ±0.04 m^2 g^{-1} of the water blank. Additionally, the presence of acid solution caused a further significant increase in surface area to 6.04 ±0.07 m^2 g^{-1}. However, the higher surface area 003 samples might have grown in area due to sonication alone from 12.70 ±0.03 m^2 g^{-1} (starting BNP) to 14.78 ±0.08 m^2 g^{-1} (blank) but did not increase further when sonicated in acid which was measured at 14.65 ±0.05 m^2 g^{-1}. This discrepancy between 015 and 003 samples clearly shows that it is the sonication that causes the BNP damage and not the acid etching. This conclusion is further reinforced by a null result in the previous chemical etching experiments.

6.4.2.6 XRD Confirmation of Crystallite Purity

As a confirmation of the conclusions drawn from the other characterisation methods, XRD analysis was conducted on all sonicated samples. It was assumed that every BN platelet consists of a single crystal domain and this would usually lead to the application of the Scherrer equation to XRD results in order to estimate the average crystal size.

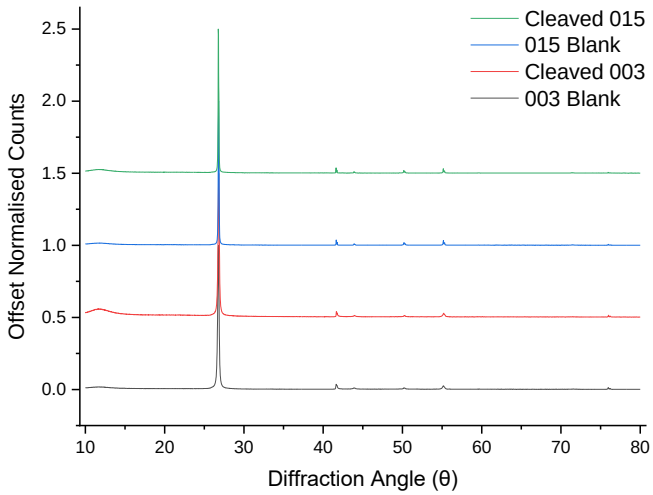


Figure 6.17. XRD graphs of sonication cleaved BNP samples. Full signals from the water sonicated blanks and acid sonicated (cleaved) samples are displayed together showing the 002 (26.7°), 100 (41.6°), 101 (43.8°), 004 (50.2°) and 110 (55.0°) plane peaks of the hBN.

However, SEM (section 6.4.2.4) has shown that even the smallest BN platelets used in this work are larger than the 200 nm limit usually accepted for the Scherrer equation's use.[230] This limit is imposed as the broadening of the XRD peaks caused by size variation at this scale is too small to measure

accurately making resultant crystal size calculations using these figures unusable. The XRD results (Figure 6.17) comparing the acid sonicated (cleaved) and water sonicated (blank) samples was therefore used to show the purity of sample (as no other crystal structures detected) and retention of the hBN nanostructure (no conversion to any of BN's allotropes).

6.5 Summary and Conclusions

A total of twenty different oxidation of hBN experimental conditions were tested and analysed in this study to functionalise the surface of the platelets. Reaction conditions were designed with the highest concentrations, temperatures, and stoichiometric ratios available in the laboratory to force any chemical reaction that might occur to do so to its fullest extent. BNP with a range of surface areas were selected as starting materials to show trends of relative hydroxylation for successful acid etching solutions, and the acid mixtures used on these materials had previously been claimed in literature (2.2.1.3) to have chemically oxidised both other nanomaterials as well as hBN.

Despite this experimental design, characterisation by IR, Raman, XPS, EDS and SEM showed that no single etched BN sample deviated from its initial chemical structure in any significant way that was detectable across more than one analysis method. It was therefore concluded that hBN platelets are inert to the chemical procedures used in this study and that an alternative avenue for the hydroxyl functionalisation of hBN should be investigated.

In numerous studies, the sonication of boron nitride materials leads to damage of its nanostructure. It was hypothesised that if this damage was inflicted at the same time as the material was exposed to an oxidising solution, the exposed and reactive terminating edges of the newly cleaved BN material could be oxidised, creating the desired hydroxyl decorated BNP. The previously used chemical etching equipment was therefore transferred to a bath sonicator. Two BNP samples of different surface area were used for both water blank sonication as well as acid sonication sample production and these were characterised in the same manner as the previously investigated chemically etched platelets.

The results for these sonicated samples were mixed. The IR and Raman spectra as well as the SEM based diameter distributions of the material implied no change had occurred from the starting material. However, XPS, BET, XRD and EDS characterisation showed that the materials' nanostructure had been significantly damaged by the introduced sonication but did not promote detectable BNP oxidation.

7 EXFOLIATION AND DISPERSION OF BNP

7.1 ABSTRACT

This chapter details a collection of investigations into the dispersion/suspension of boron nitride platelets (BNP). It is shown that bath sonication is the most efficient benchtop method of BNP suspension and despite a decrease in average diameter and an increase in surface area, these dispersed platelets are still inert to acid oxidation as shown by XPS and IR analysis. Measurements of dispersibility for the 'oxidised' BNP samples in multiple solvents of varying Hansen solubility parameters were taken to investigate the surface functionality of the treated BNP samples without interference from bulk hBN. The improvement of suspension in polar-aprotic DMAc indicates no H-bonding hydroxyl group introduction onto these samples and so confirms their lack of oxidation. However, this dispersion in DMAc allows the EPD of the BNP sample to be carried out, showing a trend of increased deposition proportional to platelet nano-structural damage. The 'oxidised' BNP films, however, are thin and uneven in coating compared with the reduced dispersion EPD method introduced in Chapters 4 and 5. This is shown to create BNP coatings up to 1.37 µm thickness but was found to be mechanically weak, chemically impure, and as a result reduced in its potential applications.

7.2 INTRODUCTION

In chapter 6 various grades of Boron Nitride Platelets (BNP) were introduced as a cheap and more plentiful source of chemically pure hBN which could be used as an industrial scale alternative to the BNNT used in chapter 5. Numerous attempts to oxidise these BNP were carried out by chemical and kinetic etching methods but these were shown to be ineffective at decorating the hBN surface with oxide or hydroxyl functional groups. It was reasoned that this would allow the material to be more easily dispersed into solution using polar protic solvents prior to EPD, as is standard practise for carbon nanomaterials.[47,120] As this was unsuccessful, direct exfoliation of BNP into solution was investigated.

For the analogous field of graphite exfoliation to form graphene, alternatives to the production of graphene oxide (GO) are centred around sonication in select solvents.[232] 0.01 mg_{Gr} mL^{-1} of 100% <6 layer graphene has been reported for sonication in the common solvent NMP (N-methyl-pyrrolidone)[233] while concentrations of 0.03 mg mL^{-1} and 0.1 mg mL^{-1} have been shown using the less environmentally friendly *ortho*-dichlorobenzene[234] and pentafluorobenzonitrile[235] respectively. Some evidence points to the success of longer sonication periods of time (460 hours yielding 1.2 mg mL_{NMP}^{-1})[236] but this comes at the cost of increased nano-structural damage of the final product. More recently, Kai Ling Ng *et al.*[237] have combined shear mixing and sonication using the green solvent of IPA to create graphene using a method that also shows promise for application to BNP.

Graphite has an interlayer binding energy between 35 and 56 meV $atom^{-1}$ [238,239] which is significantly lower than that of bulk hBN (85.9 meV $atom^{-1}$)[240] despite these two materials having the same interlayer distances. However, the polar B–N bonds and its eclipsed-stacking structure stabilise hBN. This means that the exfoliation of the BNP used in this work will be more difficult, but previous studies have shown that it is possible to achieve modest dispersion concentrations of BN in IPA (0.04-0.06 mg mL^{-1})[55,54] and even higher values using surfactants (up to 0.5 mg mL^{-1}).[241] Previous work from chapter 4 showed that the minimum CNT concentration required for EPD is 0.5 mg_{CNT} mL_{DMAc}^{-1} and if this can

be achieved with BNP, this will represent a significant advance in the scalability and application of the EPD of exfoliated BNP.

7.3 EXPERIMENTAL

This chapter describes the methods by which BNP samples were dispersed into solution by various techniques and then used as the feedstock for further acid oxidation reactions. The BNP solutions were measured by UV-Vis spectroscopy (see section 3.12) and standard solutions for this analysis were made here. BNP solutions made from previously 'oxidised' BNP samples (inverted commas used due to the questionable validity of describing the samples as oxidised) were then used for EPD. The reduced dispersion method of film deposition was then used on BNP for comparison.

7.3.1 Chemicals

Material Name	**Abbreviation**	**Supplier**
Boron Nitride Platelets 003	003 BNP	3M^{TM} 003 Grade
Nitric Acid	HNO_3	Honeywell-007-004-00-1
Sulphuric Acid	H_2SO_4	Sigma 30743
Hydrogen Peroxide	H_2O_2	Sigma 216763
PTFE membrane	n/a	Cat#: 776742
Sodium metal	Na	Sigma 262714
Naphthalene	Nap	Sigma 84679
N,N Dimethyl Acetamide	DMAc	Sigma 271012
Methanol	MeOH	Sigma 34860
Ethanol	EtOH	Sigma 32221
Iso-Propanol	IPA	Sigma 59300
Acetone	n/a	Sigma 32201
1-Bromo Hexane	Br-Hex	Sigma B68240
0.025 mm thick, uncoated Copper Foil	Cu foil	Alfa Aesar 49686RG

Table 7.1. Materials used in this section as well as the supplier product numbers (where possible) and abbreviations that are used to refer to them within the text.

7.3.2 Methods

Sonication based BNP Exfoliation: 3.75 g 003 grade BNP was shaken with 150 mL IPA in a 250 mL glass reagent bottle. For **bath sonication**, the bottle was then sealed, placed in a bath sonicator (IND1250D, 700W, 60 Hz) so that the liquid contents of the flask were immersed in water, the mixture was sonicated for 3 hours at room temperature after which it was shaken again. For **probe sonication,** A UP100H Ultrasonic processor equipped with a 3 mm steel probe tip at 100% amplitude (1 cycle) was immersed in the suspension and the flask opening covered with parafilm after which the suspension was probe sonicated for 3 hours (temperature change is negligible). For **shear mixing**, a Greaves mixer impeller was immersed in the BNP/IPA solution and turned at 5000 rpm for 3 hours during which 10 mL additional IPA was added every hour, after which the top 120 mL of suspension was bath sonicated for 2 minutes. 80 mL of the resultant white suspensions for all three methods was split between two 50 mL centrifuge tubes and centrifuged at 500 rpm for 1 hour. The supernatant was collected and left to sit overnight. Samples were then taken from this settled suspension to measure BN concentration by UV-Vis spectroscopy. The remaining centrifuged samples were then re-shaken and vacuum filtered over 1 μm pore PTFE membrane on a Teflon frit and washed with 50 mL ethanol before being dried overnight in a vacuum oven at 60 °C.

Acid Etching of 'Exfoliated' BNP: 200 mg of bath sonicated 'exfoliated' BN and 18.4 mg of probe sonicated 'exfoliated' BN were acid etched using the same method as the sonication etching experiments of section 6.3.2. Samples were then washed and dried in the same manner as in the same section 6.3.2, which recovered 153.6 mg and 2.91 mg sample of the bath sonicated and probe sonicated starting material respectively. The resultant samples joined the other acid exposed samples from chapter 6 as being denoted 'Oxidised BNP' irrespective of the degree of functionalisation achieved.

Known BNP Concentration Solution: 5.06 mg 003 grade BNP was shaken with 100 mL solvent (IPA, Water, EtOH and DMAc) in a 100 mL volumetric flask. The sample was bath sonicated for 1 hour and

left to settle overnight. Suspension was again bath sonicated for 4 hours at 55 °C, then allowed to cool to room temperature (returning to its original volume). 2, 1, 0.5, 0.25, 0.1 and 0.05 mL volumes of solutions are then pipetted into vials and diluted to 4 mL with additional solvent before being used to calculate UV-Vis absorbances for known concentrations.

Solvation of 'Oxidised' BNP: 50 mg of the 'Oxidised BNP' samples (derived from the 003 grade starting material) were placed in a 50 mL polypropylene centrifuge tube and shaken with 50 mL of solvent. The centrifuge tubes were then sonicated at room temperature in a 50-60 Hz, 500 W bath sonicator for 3 hours, followed by centrifugation at 500 rpm for 60 min. The supernatant was analysed by UV-Vis then re-shaken with the centrifuged pellet and vacuum filtered over a 0.2 µm pore PTFE membrane where it was washed with three 50 mL aliquots of the next solvent it was to be dispersed in. The order of solvents used was IPA, Water, DMAc and finally EtOH.

EPD of BNP Suspensions: The 'Oxidised BNP' samples dispersed by DMAc described in the previous section were shaken and re-sonicated for 3 hours before 25 mL of each are placed in a 50 mL beaker in which were held two 2.5 x 2.5 cm copper foil electrodes held vertically parallel with a separation of 2 cm. A potential difference of 10 V was applied across these electrodes for 120 s after which the electrodes are dried horizontally in ambient laboratory conditions before analysis.

Reduced Dispersion and EPD of BNP: 15 mL of a 2 mg_{Na} mL^{-1} NaNap charging solution (section 4.3.2) was mixed under argon with 89.5 mg 003 BNP and 78 mL DMAc and left to stir overnight by glass stir bead. While still under an argon atmosphere, 25 mL aliquots of this mixture were sequentially placed in a 50 mL beaker into which was immersed the EPD setup described in section 4.4.1. EPD was conducted at 10 V for 120 seconds on both FTO and copper foil depositing electrodes as well as 1200 s (20 min) on FTO.

7.4 Results and Discussion

The successful acid oxidation of BNP and consequent production of stable, dispersed hydroxyl functionalised BNP solutions was shown to be improbable due to the high chemical stability of BNP compared to the carbon nanotubes these acid etching techniques were developed for. An investigation into the exfoliation of the BNP starting material without initial oxidation was devised. The 003 grade BNP was selected for this experimentation as it has the smallest radius range and therefore should be the slowest to sediment out of solution as predicted by Stoke's Law (Eq 7.1) where r is the radius of the particle, Δρ the density difference between the dispersed and continuous phases, g the acceleration due to gravity, k_B the Boltzman constant and T temperature).[242]

$$Rate\ of\ Sedimentation \propto \frac{r^4\,\Delta\rho\,g}{k_B\,T} \qquad \textit{Eq. 7.1.}$$

7.4.1 Exfoliation of BNP

The 003 grade BNP was exfoliated by three common benchtop methods: bath sonication, probe sonication and shear mixing. The method of exfoliation and subsequent separation of suspended and un-suspended BNP by centrifugation was developed in consultation with Kai Ling Ng of the Grobert Group and was originally developed for the production of graphene from graphite.[237]

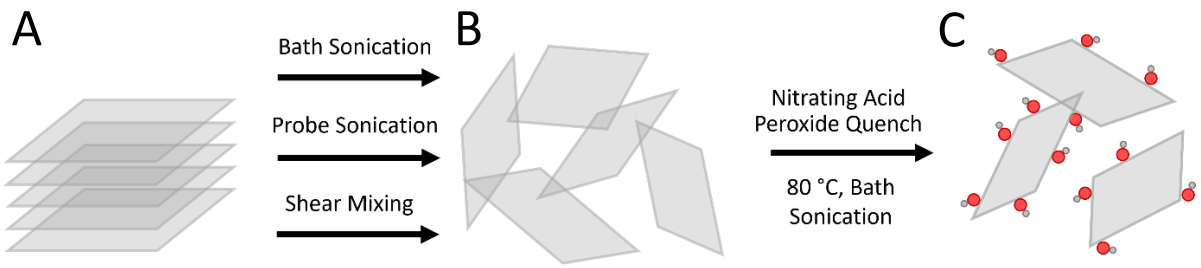


Figure 7.1. Schematic showing the proposed steps of hBN exfoliation and oxidation. 003 BNP **[A]** are exfoliated into single or few layer hBN sheets **[B]** with higher activity towards the acid etching solutions used previously and so create hydroxylated hBN sheets **[C]**.

It is thought that the energy input into the solvent/BNP system during sonication will cause both the tearing and the peeling of the material.[224] Following Stoke's Law (Eq 7.1), these smaller, exfoliated

hBN will have lower rates of sedimentation and are thus more likely to stay in the supernatant during centrifugation. The average exfoliated hBN material should therefore have a smaller size, few hBN layers and a higher surface area:volume ratio which combined would indicate they could be less inert to oxidation compared to the starting BNP. A final effort to oxidise this exfoliated BNP was also planned as shown in Figure 7.1.

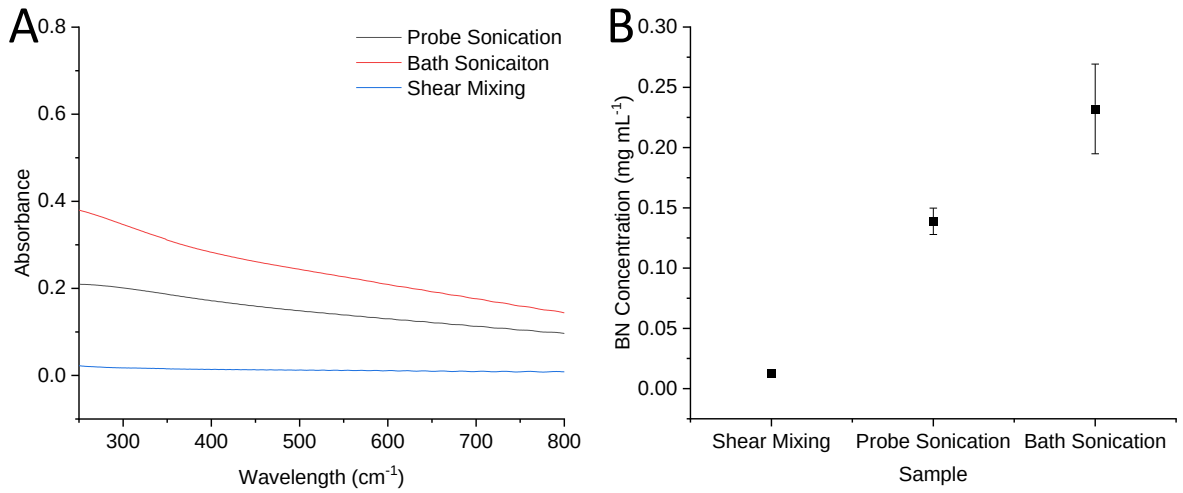


Figure 7.2. Example UV-Vis absorbance spectra **[A]** for the supernatant (1/8 diluted) of the IPA suspended 003 BNP that has been exfoliated by three different methods. The calculated concentration of BN remaining in solution after both exfoliation and centrifugation **[B]** is compared showing that bath sonication is the most effective in exfoliating BNP.

The exfoliation and centrifugation of the BNP was successful and produced cloudy white dispersions that did not visually clarify within 100 hours of suspension (Appendix Figure 11.1.). The concentrations of exfoliated BNP in the centrifuged supernatants are summarized in Figure 7.2., which represent the yield of each exfoliation method. The shear mixer produced the lowest yield at 0.0127 ±0.0029 mg_{BN} mL_{IPA}^{-1}, the probe sonicator yielded the significantly larger 0.1389 ±0.0110 mg_{BN} mL_{IPA}^{-1} but the bath sonicator proved most effective at 0.232 ±0.037 mg_{BN} mL_{IPA}^{-1}.

These figures are low when compared to some literature BN ultrasonication in water (0.26–0.32 mg mL^{-1}) or DMF (0.34–0.52 mg mL^{-1})[53] and even smaller compared to exfoliations that have used surfactants (0.5 mg mL^{-1})[241] to aid with BN suspension. However, they are larger than other studies of

BNP suspension in IPA which have reported 0.06 mg ml^{-1} [55] and 0.04 mg ml^{-1}.[54] This demonstrates that nanomaterial studies using different starting materials are not directly comparable and divergence between this work and literature is expected.

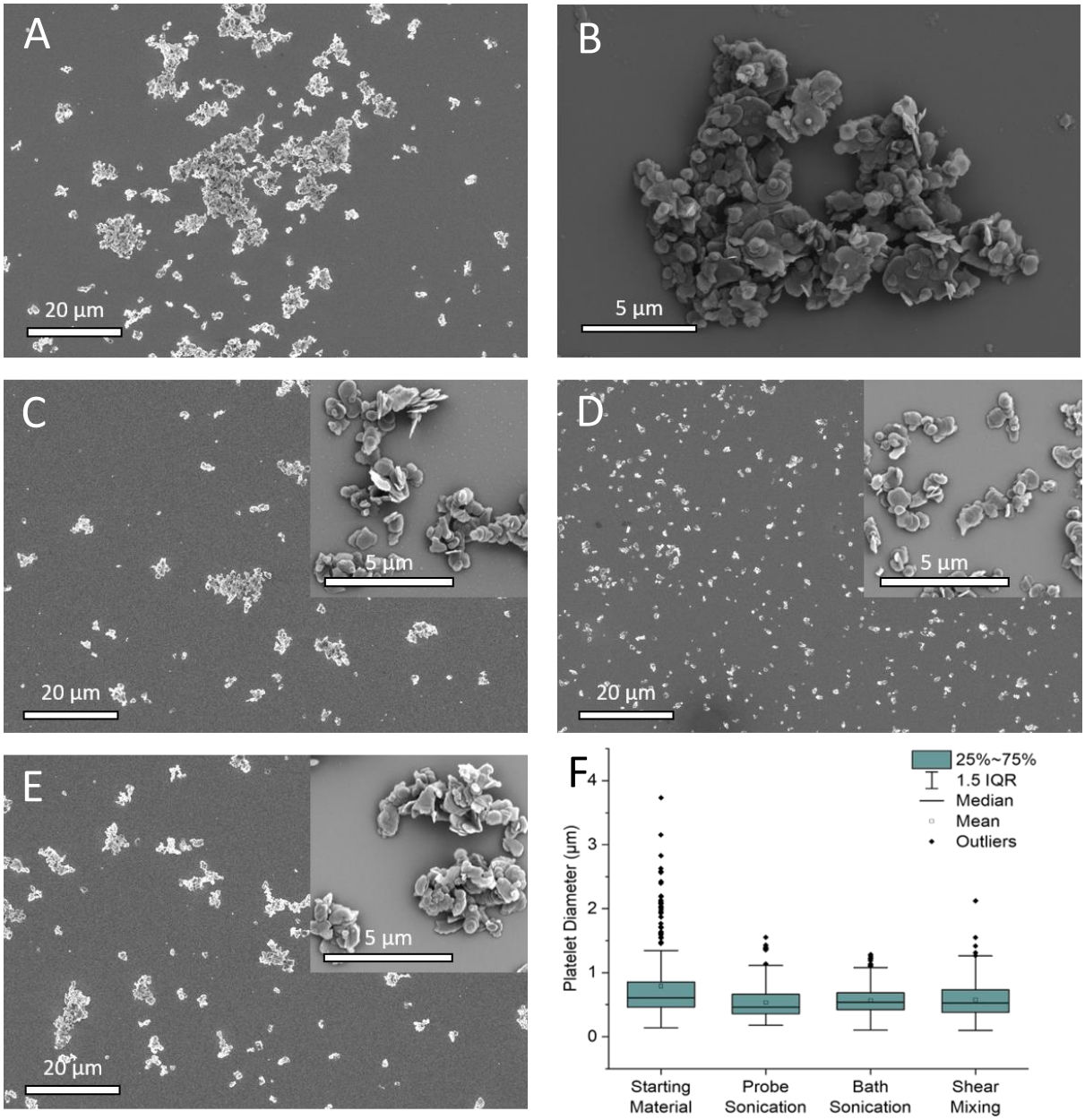


Figure 7.3. SEM images showing the BNP starting material compared to platelets exfoliated in this work. The pristine starting material **[A]** and **[B]** is shown alongside 003 platelets exfoliated in IPA by probe sonication **[C]**, bath sonication **[D]** and shear mixing **[E]** are compared showing that the bath sonicated samples are less agglomerated than other methods. The analysis of the diameter distributions for these samples **[F]** shows a significant drop in larger platelets for all dispersed materials.

Despite the differences in BNP concentration with the extant literature, previously sonicated BNP samples XPS results have indicated significant damage is incurred on the structure of the BNP samples due to sonication (see section 6.4.2). To investigate this for these exfoliated samples, SEM (Figure 7.3) and EDS (Figure 7.4) were conducted on all samples to ensure that the exfoliation processes had not destroyed the samples (or even hydroxylated them as one paper has proposed).[63]

On examination of the SEM images, it was noted that the bath sonicated samples (Figure 7.3.D) appeared less agglomerated than the others. However, the BNP do not show any other significant visual variance (torn edges, increased debris etc.) between exfoliation methods and the starting material. Results of the average diameter measurements (Figure 7.3.F) also indicate little difference between exfoliated samples (0.57 ±0.21μm, 0.57 ±0.21μm and 0.53 ±0.25μm for the bath, shear and probe methods respectively) but does show that, compared to the starting material (0.79 ±0.54 μm), a minor decrease in diameter has occurred.

The decrease in the average size of BNP is unlikely to be due to fractures or breakages caused by the exfoliating process, as significantly longer sonication in acid (section 6.4.2) gave an average BNP diameter of 0.77 ±0.43 μm which is identical to the 003 starting material. This reduction in the size of BNP is instead most likely because the larger sized BNP are centrifuged into the sediment and removed. This effect has been used by W.Gao *et al.*[243] to select specific BNP sizes (0.7 μm) by first removing all large particles with a low power centrifuge (3-5 krpm) followed by the removal of smaller particles with a high power centrifuge (16-20 krpm).

While the exfoliation methods are selective for size only, due to their centrifugation, the material that is initially pushed into dispersion may be selective based on its structure. It is possible that the fraction of more pre-damaged or pre-oxidised BNP within the original sample would be pulled into the dispersion preferentially. Alternatively, the exfoliation technique may indeed damage the BNP enough to induce favourable interactions with the solvent but not at the scale detectable by visual inspection

by SEM. In both of these hypothetical cases, the BNP found in the dispersion would be chemically distinct from the starting material.

All exfoliated samples do show very similar atomic content measured by EDS, with the bath sonicated sample showing 84.6 % BN, 6.0 % C and 2.3 % O (for 7.1 % Si) which is near identical to the shear mixed (84.4 BN, 7.7 C, 1.5 O for 6.3 Si) and probe sonicated materials (84.1 BN, 5.7C, 1.5 O, for 8.7 Si). However, EDS maps (Figure 7.4) show no significant regional concentrations of heteroatoms within any of the BNP samples and these maps and atomic breakdown values are not dissimilar enough to the starting material (Appendix Figure 11.3) to be taken as evidence for any reaction occurring. The C and O content increases are thought to be adhered solvent as their concentration increases when examining the Si surface not containing BN sample (78.7 % Si, 14.5 % C, and 3.1 % O for 3.7 BN).

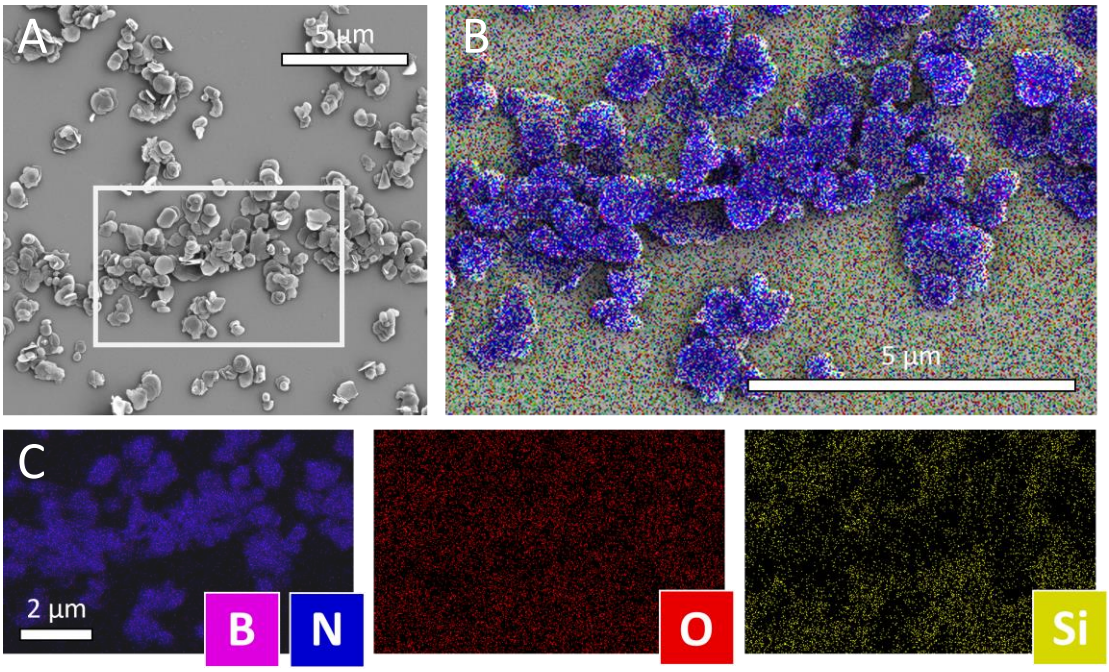


Figure 7.4. Example EDS map of bath sonication exfoliated BNP. A region containing both BNP and Si substrate is selected from the SEM **[A]** and is mapped according to its elemental makeup **[B]** which are further broken down into maps for specific elements of interest **[C]**. These show that there is clearly no oxygen addition to the BNP due to exfoliation alone. This is the case for all samples exfoliated by alternative methods also.

7.4.1.1 Acid Etching of Exfoliated Material

Section 7.3 of this thesis concluded that BNP were inert to surface hydroxylation by solution-based acid oxidation. However, it was thought that the 'exfoliated' BNP material produced would be more susceptible to reaction due to its reduced layers and reduced stability from pseudo-bonds formed between eclipsed stacked N atoms donating electron density into vacant B orbitals of adjacent layers.[244,240]

Exfoliated samples were dried to remove the exfoliating solvent (IPA) and then subjected to the same acid sonication treatment as described in chapter 6. Due to a lack of sample mass from the less efficient exfoliation by shear mixing, the acid sonication of this sample did not yield any product for analysis. However, IR and XPS was conducted on both the probe sonicated and bath sonicated samples after acid etching to examine any changes in their nanostructure.

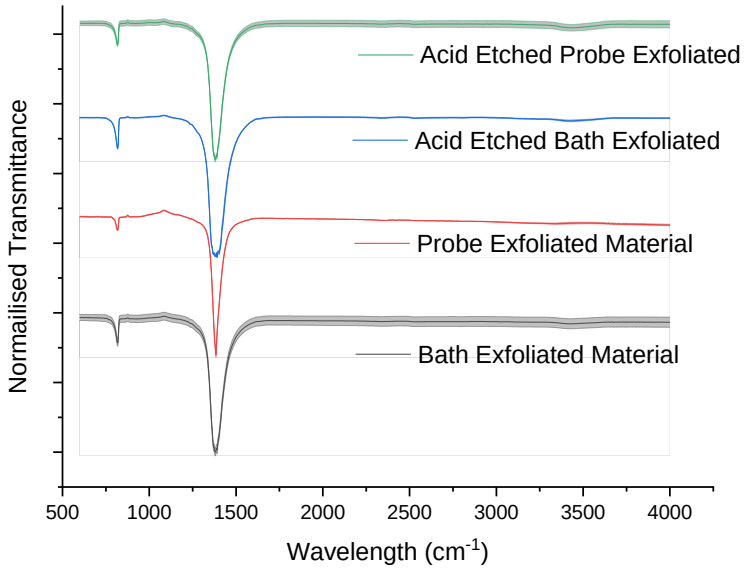


Figure 7.5. Comparison of IR spectra for the exfoliated and acid etched exfoliated materials showing no significant increase in any peaks associated with BN hydroxylation.

No detectable change was observed within the IR spectra (Figure 7.5) recorded for both the starting exfoliated material or the subsequent acid etched sample of the same type. The expected O-H indicating region between 3200-3600 cm^{-1} does appear to bow slightly for the acid etched probe exfoliated material, but this is not enough to conclusively prove a significant reaction.

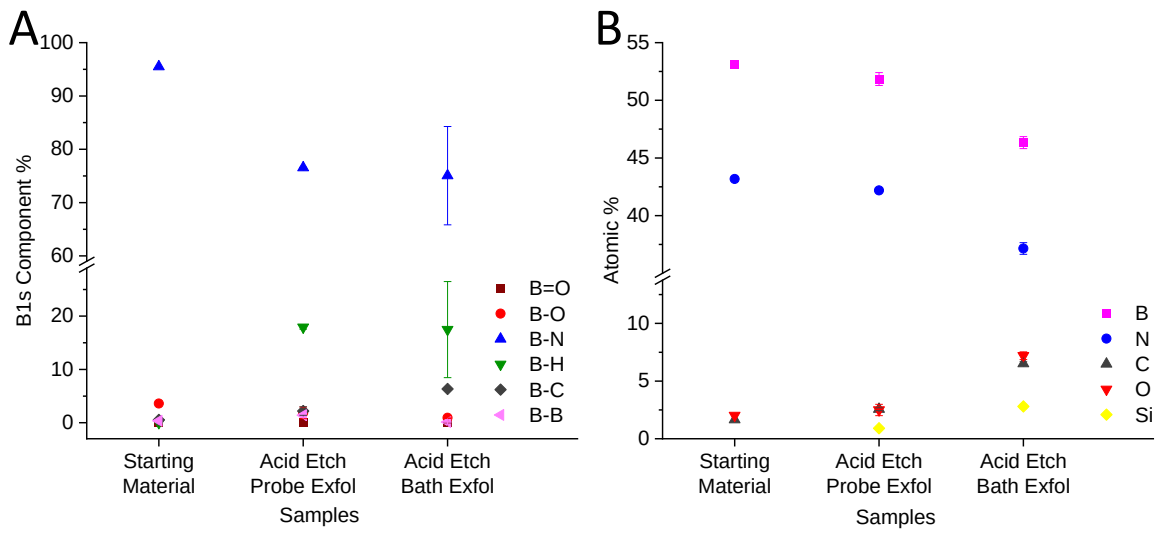


Figure 7.6. XPS of acid etched exfoliated samples. The results of the deconvolution of the B1s XPS spectra **[A]** shows that significant damage is inflicted upon the BN nanostructure but does not cause any heteroatom bonding. Analysis of the sample's atomic constituents **[B]** shows a decrease in BN content but is thought to be likely due to a decrease is platelet agglomeration.

The B1s XPS spectra of the starting, and acid etched, exfoliated BNP were deconvoluted to investigate the contribution of each bonding environment to the sample. Comparison of these B1s results (Figure 7.6.A) of the 003 starting material (95.5 % B-N, 0.01 % B-H, 3.6 % B-O and 0.53 % B-C) and the acid etched 'exfoliated' samples show a decrease in B-O bonding proportion (1.86 ±1.08 % and 0.94 ±0.13 % for probe and bath sonication respectively) which is the opposite to what would be expected of an oxidised BNP sample. The most significant difference between the starting material and samples is in the B-H bonding environment (17.92 ±0.35 and 19.48 ±9.01 % respectively). These B-H increase in the B1s results indicate that the nanostructure of the BNP has been damaged but not reacted with any heteroatoms.

The atomic composition (Figure 7.6.B) of the probe sonicated acid etched sample (94.0 ±0.74 % BN, 2.6 ±0.12 % O, 2.5 ±0.49 % C) also follows this conclusion and does not deviate from the starting material (96.3 % BN, 1.65 % C, 2.02 % O). The bath exfoliated acid etched sample does however show an increase in both carbon and oxygen content (83.5 ±1.02 BN, 6.5 ±0.16 % O, 7.2 ±0.33 % C 2.8 ±0.19 % Si) which it thought due to the increase in surface area (and subsequent increase in adsorbed

molecules) caused by the reduction in re-agglomeration shown previously in the bath exfoliated BNP SEM and not by a successful oxidation reaction.

To conclude, this final oxidation attempt has again indicated that the chemical stability of hBN makes it inert to acid etching methods used for carbon nanomaterials despite exfoliation.

7.4.2 Solvation of BNP Samples

BET measurements of the 003 BNP starting material found that it has a surface area of 12.70 ±0.03 m^2 g^{-1}. Using the density of hBN (2.1 g cm^{-3}), a surface area to volume ratio for the material can be calculated at 26.7 x10^6 m^{-1}. This ratio implies that the majority of any spectroscopy signal used to analyse BNP samples will return results reflective of the bulk hBN and not the surface functionality of the material. While many spectroscopy techniques used for BNP analysis in this work have limited penetration depths and so may reflect a larger effective surface area to volume ratio, a possibility remains that any successful oxidation of the BNP surface conducted in all previous experimentation may have been unmeasurable.

An alternative way in which only the surface of the BNP samples can be measured is through their interactions with different solvents. It is well established that 'like dissolves like' and therefore it is postulated that a more oxidised BNP material decorated by polar and hydrogen-bonding hydroxyl functionality will be more stably suspended in polar-protic solvents than unfunctionalized material. To demonstrate their possible surface chemistry, the 'oxidised BNP' samples from throughout chapters 6 and 7 were dispersed in four different solvents at the same initial concentration of 1 $mg_{O\text{-}BNP}$ mL^{-1}. After bath sonication and centrifugation, the dispersions' concentrations in solution were measured by UV-Vis (extinction coefficients were calculated for each individual solvent system using the 003 starting material). The concentration of 'oxidised' BNP in each solvent and an example UV-Vis spectra used to calculate them is displayed in Figure 7.7.

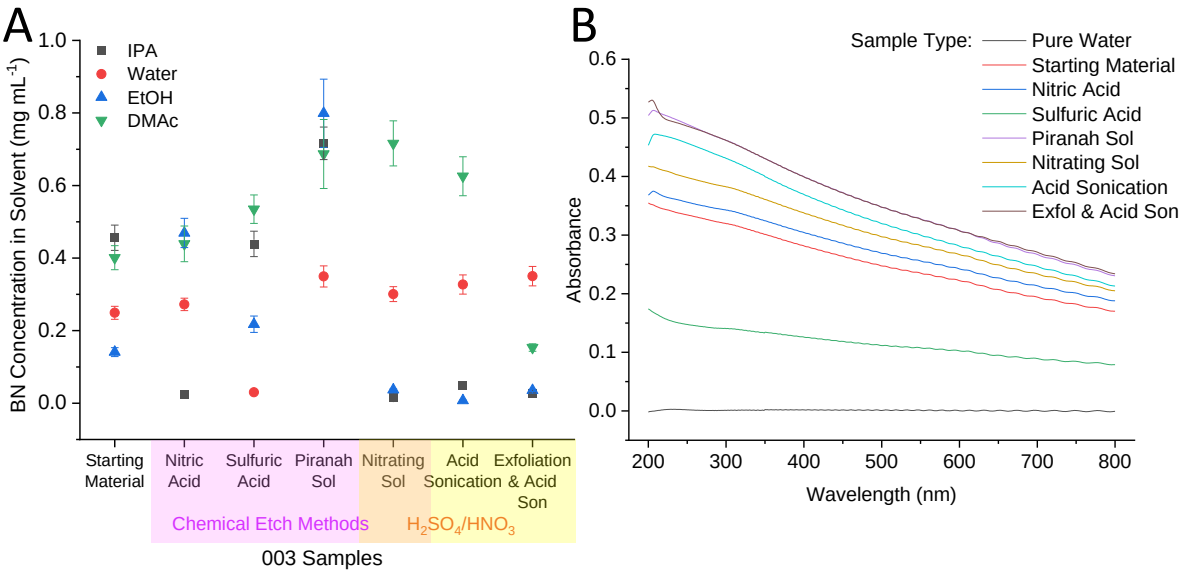


Figure 7.7. Summary of BNP sample dispersion experiments. The BNP products from previous experiments were dispersed by bath sonication in various solvents and the concentrations **[A]** calculated using UV-Vis data and the Beer-Lambert Law. An example of these UV-Vis spectra **[B]** for samples (1/8 dilution) dispersed in water is shown for illustration of the linear relationship between absorption and BN concentration.

The ability of a solvent to dissolve a solute can be predicted using Hansen solubility parameters (HSP) which break down a solvent's properties into atomic (dispersive) interactions (δD), permanent dipole-permanent dipole interactions (δP) and hydrogen bonding interactions (δH).[50] The HSP of the solvents used for the dispersion of the BNP samples are presented in Table 7.2.

Solvent Name	**δD**	**δP**	**δH**
IPA [245]	15.8	6.1	16.4
Water [246]	15.5	16	42.3
Ethanol [246]	15.8	8.8	19.4
DMAc [247]	16.8	11.5	9.4

Table 7.2. Table of Hansen Solubility Parameters (HSP) for solvents used for the dispersion of BNP samples. The Dispersion (δD), Polar (δP) and Hydrogen bonding (δH) terms for each solvent is displayed.

When these values are plotting in 3D, it is found that solvents that are able to dissolve a specific solute, cluster together in the same spatial region. By calculating the centre of this region, the HSP values for

the solute can be estimated[246] and this has already been used as evidence for the oxidation of CNT.[248] For nanomaterials, the definition of what is considered dissolved varies, but studies have been published finding the HSP coordinates of C_{60},[52] CNT [249] and BNNT[250,251]. These sources do not always agree, as dispersion concentration is also dependant on material size and the mechanism of exfoliation.[237]

The position of BNP in HSP space has been placed at {17-19 δD, 4-10 δP, 4-10 δH}[51] and explains why the 003 starting material was most dispersible in IPA (0.456 ±0.035 mg mL_{IPA}^{-1}) and DMAc (0.401 ±0.033 mg mL_{DMAc}^{-1}) but not in the H-bonding (causing greater difference between the BNP and solvent δH values) water and EtOH (0.249 ±0.018 mg mL_{Water}^{-1} and 0.141 ±0.012 mg mL_{EtOH}^{-1}). DMAc remains the solvent with the highest concentrations of BNP (max 0.716 ±0.062mg mL_{DMAc}^{-1} for nitrating solution chemically etched BNP) for most of the 'oxidised' BNP samples, while the concentrations in water remain lower than DMAc for all samples (max 0.349 ±0.029mg mL_{Water}^{-1} for piranha solution chemically etched BNP).

None of the 'oxidised' BNP samples show significant movement in HSP space toward the H-bonding water and EtOH, this is attributed to the lack of oxidization on the BN surface. Thus, by combining this lack of HSP movement with the previously explored XPS and IR and EDS results for these samples, it must again be resolved that the initial conclusion that BNP are inert to solution-based acid oxidation is correct.

7.4.2.1 EPD of Solvated BNP Samples

While the concentrations of the modified BNP in solution achieved in the previous section were low, there is a possibility that EPD may still be successful, as the critical concentration required for BNP deposition is unknown for this system and may yet be achieved. An exploratory investigation was therefore launched to test this theory using the solutions suspended in DMAc from the previous section which were placed in the EPD setup of Chapters 4 and 5 (Figure 7.8.B).

2.5 cm x 2.5 cm Cu foil was used for both electrodes and the depositing electrode acted as the cathode as the samples would be positively charged by the addition of oxidised groups the BN surface as was the case for the previously investigated O-SWCNT of chapter 4. A 10 V potential difference was applied (5 V cm^{-1} field strength) between the immersed electrodes for 120s (a time selected because it was the maximum time used in the SWCNT depositions section 4.4.4.1. It was found that BNP were deposited on the Cu foil electrode, but no film was created due to a combination of the low BNP concentration in solution and short deposition times.

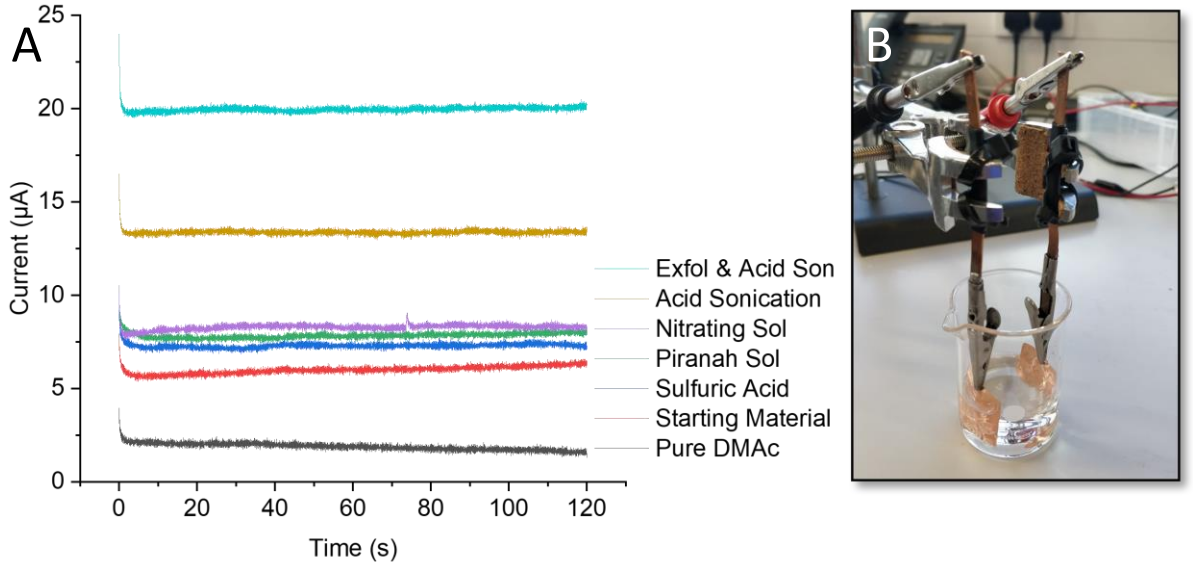


Figure 7.8. Electrophoretic deposition (EPD) of DMAc dispersed 'oxidised BNP' samples. 25 mL aliquots of DMAc dispersed BNP samples from previous experiments were placed in the EPD setup **[B]** used for film manufacture although under ambient conditions rather than Ar. The resulting current measurements for each dispersed sample was measured **[A]**, showing a trend of increasing current with increased damage to the BNP initially used.

The current/time curves for these experiments were measured (Figure 7.8.A) and, from the difference in current measured between the EDP of pure DMAc (end current of 1.3 μA) and the BNP dispersions (max end current 20.1 μA), it can be concluded that the migration of charged BNP in solution is responsible for the increase in signal. The chemically etched samples (sulfuric and piranha) show similar total charge transfers to each other (0.876 mC and 0.942 mC respectively) which are both bigger than the unmodified starting BNP (0.720 mC) and DMAc blank (0.227 mC), implying that the

modification of these BNP has in some way effected their electrophoresis. However, the most obvious trend in charge transfer during EPD is between the BNP treated by the same nitrating solution (H_2SO_4/HNO_3 mixture), but with differing amounts of sonication applied to the sample. Chemical etching alone (0.994 mC) is smaller than acid etching and sonication (1.605 mC) which is, in turn, smaller than the exfoliated and sonicated material (2.396 mC). These examples of increasing charge transfer during EPD correspond with both an increase in B-N nano-structural damage, as evidenced by the sequential increase in the B-H components (see sections 6.4.1.3, 6.4.2.3 and 7.4.1.1) of these samples' B1s XPS spectra as well a gradual increase in the dispersion concentration in water shown in the previous solvation investigation.

The current and charge transfer is not, however, coupled with the BNP concentration in DMAc (Appendix Figure 11.2.) which implies that not all of the material dispersed in the solvent is being affected by the electric field equally, which could imply chemical differences between deposited and bulk BNP. Insufficient BNP sample was deposited during these EPD to conduct XPS analysis therefore EDS on the depositing Cu electrodes was conducted as an alternative.

Figure 7.9.A and B show example results of this EDS analysis for the exfoliated and acid etched 003 sample (selected as an illustration due to the high charge transfer shown during EPD). These elemental maps show no localised concentrations of any atom across the sample and are similar to both the starting material (Appendix Figure 11.3.) and previous EDS maps of 003 sample presented throughout this work. A summary of the atomic content for all 'oxidised' BNP samples Figure 7.9.C shows that the deposited BNP are all very similar in makeup and comprise of on average 89.5 ±7.3 % BN with 0.6 ±0.1 % oxygen and a higher than usual 5.9 ±1.3 % carbon content. While this high carbon proportion could indicate a reaction with the BN material, previous XPS deconvolutions of the C1s spectra for the bulk of these samples (6.4.1.3, 6.4.2.3 and 7.4.1.1) has shown that this is not the case and is instead attributed to adhered solvent. This is further proved by the DMAc blank sample which shows a large (15.5 %) C content on what should be a pure Cu foil.

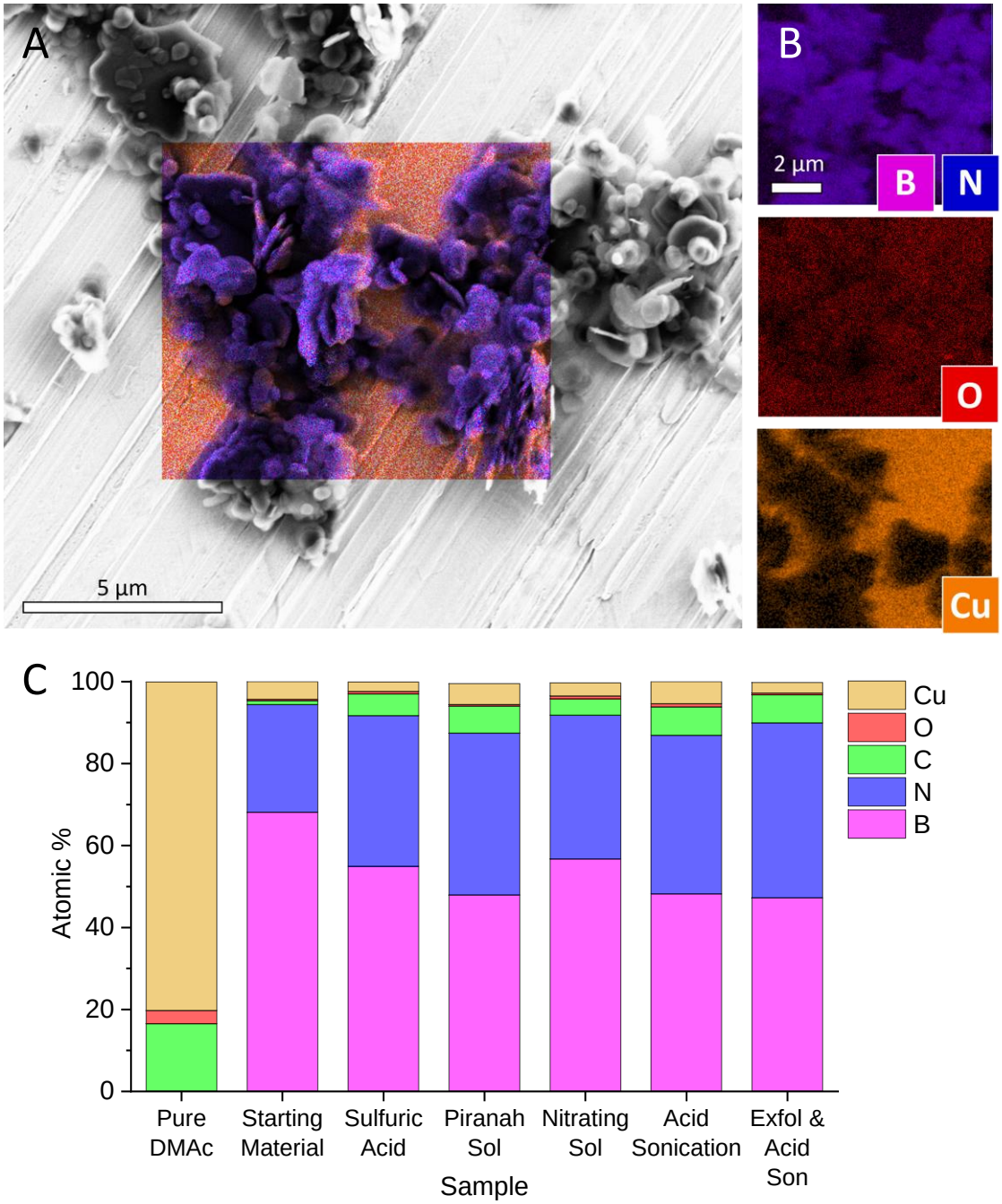


Figure 7.9. EDS of deposited BNP samples. An example EDS map **[A]** for the largest BNP covered electrode as predicted by the charge transfer during EPD (exfoliated and acid sonicated 003 sample) is shown to illustrate the homogeneity of distribution for all atoms of interest **[B]** within the sample. The total atomic content for all samples **[C]** is also measured in this way and shows no trend in samples' constituents other than an increase in carbon content which may be attributed to the sample preparation process.

7.4.2.2 Issues

The investigation into the differences of deposited BNP as suggested by the de-coupling of dispersion concentration and charge transfer during EPD is moot if the actual deposition is insignificant. Using the relationship calculated between total charge transfer and film thickness determined for BNNT deposition (section 5.4.5.3), the hypothetical film thicknesses that should be achieved for each of the 'oxidised' BNP EPD was calculated and is presented in Figure 7.10.A. This was considered a valid comparison as the electrode surface area and immersion depth remain constant between these two studies and used the same field strength. Due to the flexibility of the Cu foil and its resulting uneven surface, these thickness values could not be verified by profilometry, but the predicted scale (nm) of these films makes them inappropriate for many electrical applications. For example, film thicknesses required to electrically insulate wires on the kV scale are a minimum of 1.2 µm at 10 kV to 4.0 µm at 30 kV[252] for ethylene propylene rubber (EPR), which has a similar electrical permittivity (3.5 at 50 Hz) to the out of plane hBN (3.29 to 3.76).[253]

While these film thicknesses may be on the correct scale for use as insulators in microchip production[254] the reality of the film produced can be seen in Figure 7.10.D-E. Images of the Cu foil depositing electrodes show minimal to no visible BNP coverage on the 003 blank and small, isolated regions of deposition across what was predicted (by charge transfer) as the most successful 'oxidised' BNP deposited film. It is unclear if this uneven deposition is due to the mechanics of EPD[255] or the agglomeration of BNP in solution, which are then deposited themselves. These results imply that it would require a much longer EPD time, using much higher concentrations of BNP, to create a complete covering or film.

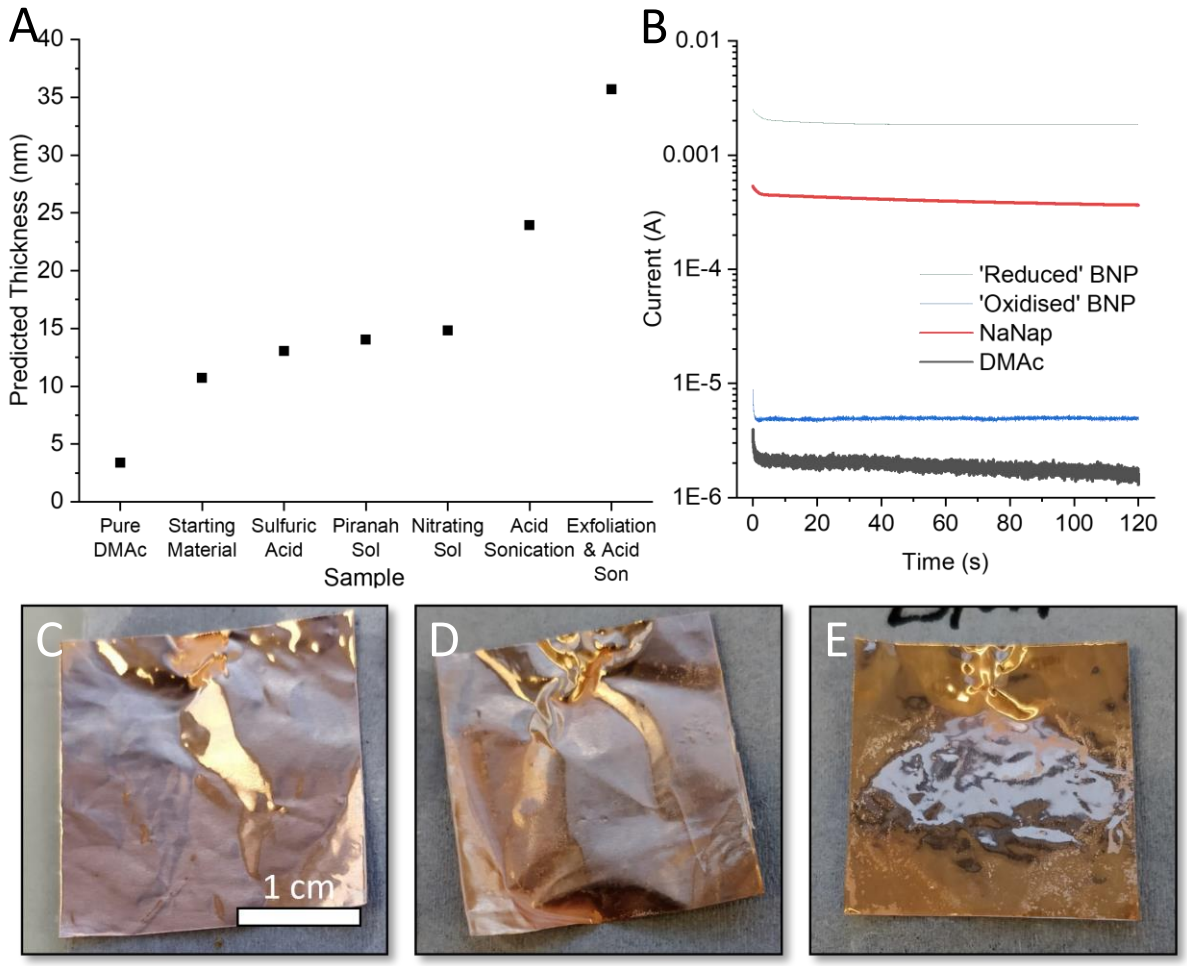


Figure 7.10. Issues with the EPD of DMAc dispersed BNP. Using the relationship between total charge transfer and film thickness determined for BNNT films (section 5.4.5.3) and the current/time graphs for the DMAc dispersed EPD, the predicted BNP thickness of these films **[A]** is shown to be very low. The current/ time graph for a NaNap charged 003 BNP sample subjected to EPD using the same conditions is shown **[B]** to have nearly three orders of magnitude higher current signal than the 'oxidised' samples. The dried Cu foil depositing electrodes of the pure DMAc **[C]**, 003 starting material blank **[D]** and the exfoliated/ acid etched 'oxidised' BNP **[E]** show the minimal deposition that has occurred.

In addition to the uneven and incomplete BN coverage, the current/time graph of the 'oxidised' BNP are orders of magnitude smaller than those for the NaNap charging solution, which are in turn an order of magnitude smaller than an NaNap dispersed 003 BNP displayed in Figure 10.B. The charge transfer for this experiment was 226.5 mC (1000 times larger than that of the exfoliated acid etched 003) and resulted in a visible BNP covering of the electrode.

7.4.2.3 EPD of electrochemically reduced BNP

Due to the success indicated by the NaNap dispersed 003 BNP EPD, further experimentations using this system were conducted. The principles for this procedure were the same as for the dispersion and deposition of nanotubes for chapters 4 and 5 and summarised in Figure 11.

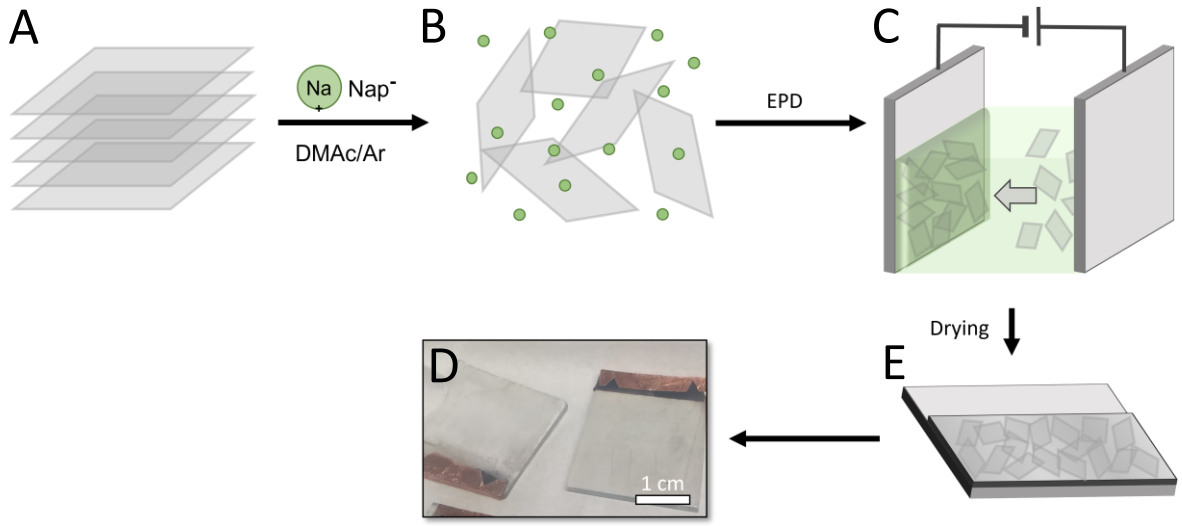


Figure 7.11. Schematic diagram for the reduced BNP EPD process. Unmodified 003 grade BNP **[A]** is charged using the NaNap reducing solution causing the BNP to become charged and partially suspened in the DMAc solvent **[B]**. This suspension is placed between two electrodes where an electric field induces the charged BNP to migrate and deposite onto the electrode surface **[C]** from where it is removed and then dried **[E].** The final product is a controllable thickness of BNP film coating covering the electrode **[D]**.

Dry 003 BNP was mixed under an argon atmosphere with NaNap charging solution and made up to 1 mg_{BN} mL^{-1} at a charging ratio of $1_{Na}:5_{BN}$, which is an over-estimate, as evidenced by the continued green colour of the solution after mixing. This is similar to the mischarging of BNNT in section 5.4.2, but was used despite this, so that these BNP samples could be directly compared to the BNNT and CNT EPD methods which used the same conditions. Vertically held, parallel electrodes were immersed in this BNP dispersion 2 cm apart where a 10 V potential difference was applied between them while the current was measured (Figure 7.11.C). The previous section of this chapter already demonstrated that this measured current is orders of magnitude larger than both the NaNap charging solution and the 'oxidised' BNP dispersions. The EPD was conducted using rigid FTO covered glass electrodes so

that further measurements of the resultant films could be made. Washing of the resultant coatings was found to remove the BN film, implying weak inter-BNP interactions unlike the entanglement found within nanotube films.

7.4.2.3.1 Profilometry of BNP 'Films'

EPD was conducted for 120 s and 1200 s to compare results with same time period used in CNT and BNNT experiments respectively. Both of the resultant films were then analysed by optical profilometry where 3D maps of the films' surface as well thickness measurements were taken and are presented in Figure 7.12.

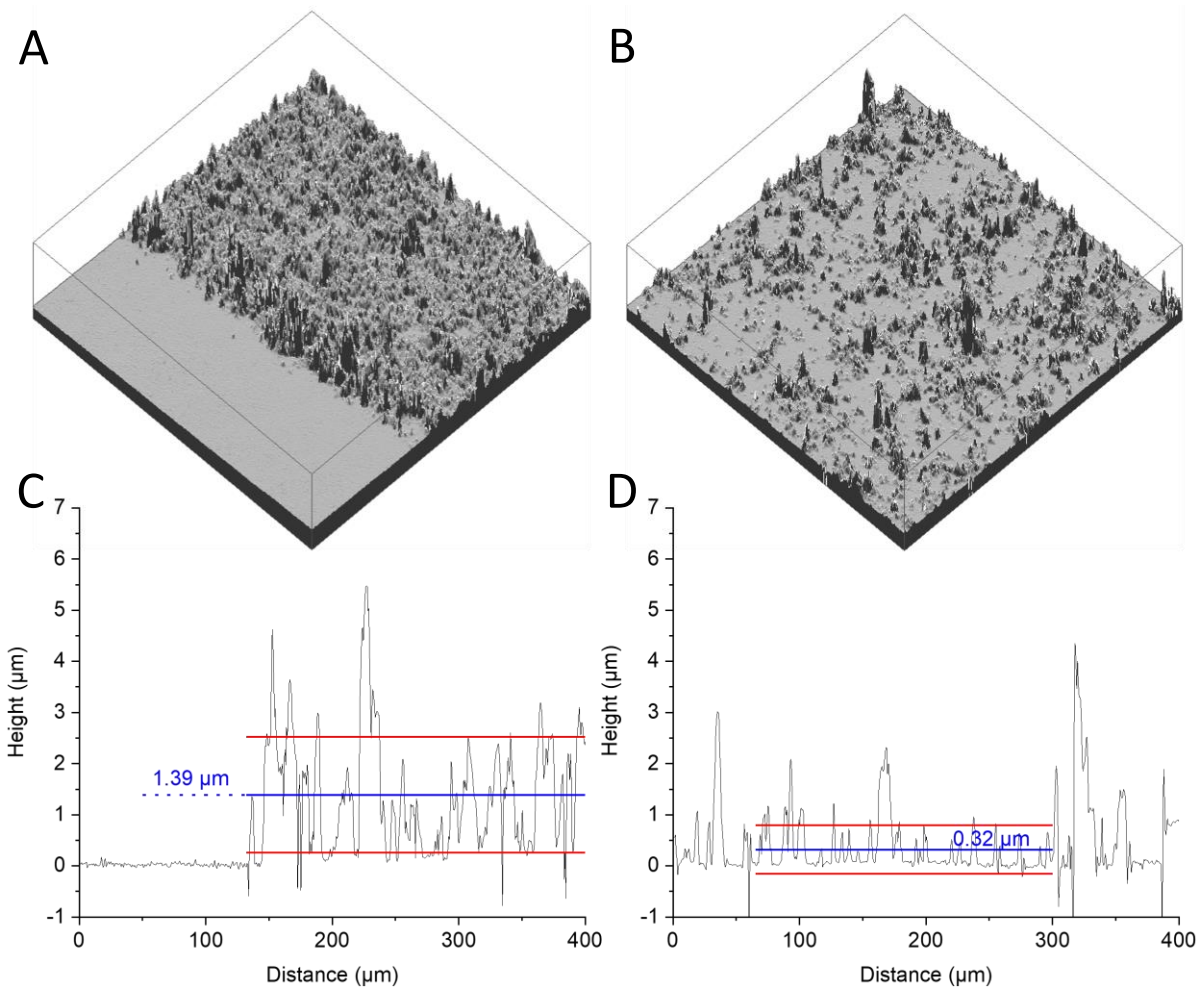


Figure 7.12. Optical profilometry of reduced dispersion BNP EPD depositing electrodes. The 3D maps for the FTO glass electrodes of the 1200 s **[A]** 120 s **[B]** depositions are compared showing clumps of BNP depositing. Example line profiles taken from these maps show the uneven surface of the BNP deposits for both the 1200 s [A] and 120 s [B] samples.

As expected and predicted by Hamakers Law (Eq. 2.1.), the longer 1200 s deposition shows a significantly larger covering of BNP which was found to have an average thickness of 1.37 ±1.28 µm while the 120 s experiment showed a thickness of 0.47 ±0.62 µm. The very large standard deviations proportional to the thickness results can be explained when observing the 3D maps used to calculate them (Figure 7.12.A-B). The films appear to be comprised of small regions of isolated thickness, implying that the BNP deposited onto the electrodes in clumps and not as dispersed and individualised platelets. Furthermore, washing procedures conducted on these samples, that were used previously for nanotube films, completely washed away the deposited BNP from the electrode surface. This shows a significant drawback in this method of deposition and explains the large film thickness error

values, which contain sodium crystals that could not be washed away, as evidenced by EDS atomic mapping of the samples in Figure 7.13.

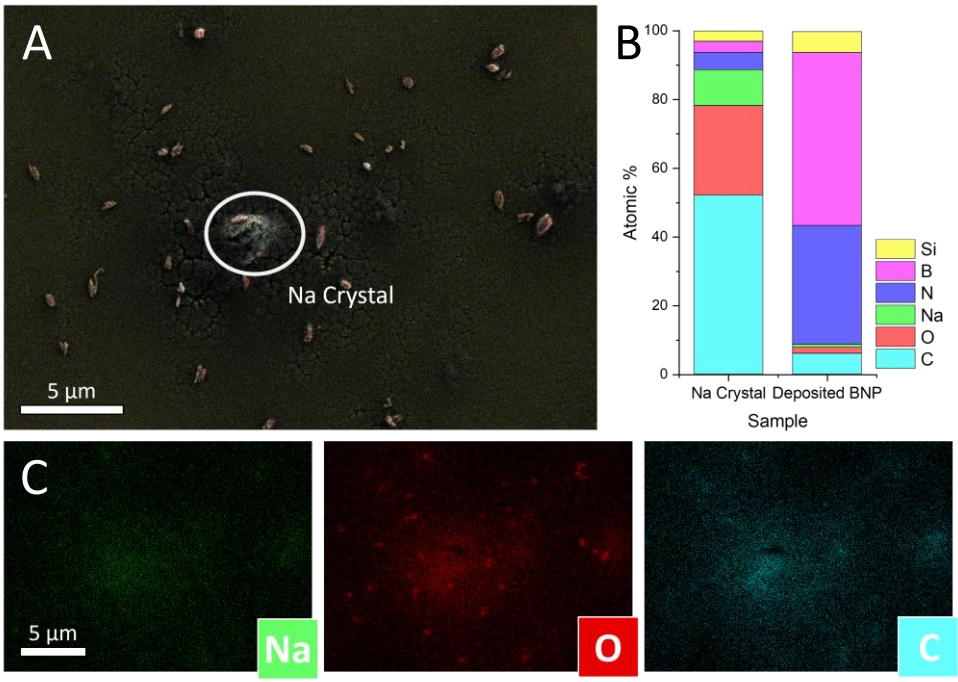


Figure 7.13. SEM with overlaid EDS atomic map **[A]** of the Na crystal found on the clear surface of the depositing electrode from reduced BNP dispersion EPD. The measured atomic content of the Na crystal region is compared **[B]** to that of the deposited BNP and the individual atomic maps **[C]** show the Oxide localisation.

The EDS mapping of the sodium crystals showed an atomic composition of 8.3% BN, 10.4% Na, 26.1% O and 52.1% C which is consistent with the sodium crystals found on top of and within the nanotube films explored in chapters 4 and 5. This contrasts with the bulk deposited BNP (Figure 7.13.B) which measured as 84.9 % BN, 0.9 % Na, 1.8 % O and 6.02 % C. This is very similar to the BNP material deposited after suspension in DMAc (Sect 7.4.1) which showed 89.5 % BN with 0.6 % O and 5.9 % carbon content.

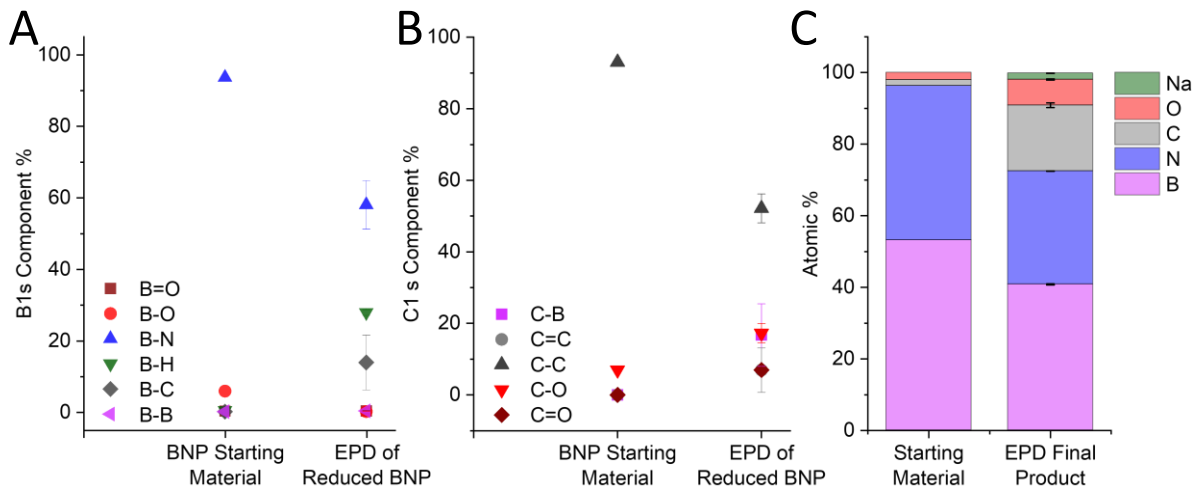


Figure 7.14. XPS of reduced dispersion BNP EPD 1200s sample compared to starting material. Results of the B1s deconvolution **[A]** show damage to the BN nanostructure with a possible increase in B-C bonding. This increase is borne out in the C1s deconvolution **[B]** which showed an increase in C-B bonding in addition to the increase in oxygen bonding associated with remaining solvent. The atomic breakdown **[C]** of these samples also show this increase in C and O.

BNP from the 1200 s sample was scraped from the dried depositing electrode and sent for further analysis by XPS (no analysis was done on the 120 s sample as not enough BNP could be recovered). The atomic breakdown analysis of the deposited BNP (Figure 7.14.C) showed larger deviations from the starting BNP than the EDS results and exhibited a composition of 72.5 ±0.2 % BN with large impurities of 7.2 ±0.2 % O, 18.4 ±0.7 % C and 1.8 ±0.03 % Na. This heteroatom content is significantly larger than the 1.7 % C, 2.0 % O and 0 % Na found in the 003 grade starting material but is expected due to the unwashed nature of the sample, meaning sodium crystals and DMAc solvent must still be held within the sample.

The C1s deconvolution (Figure 7.14.B) of the sample show the C bonding environments completely diverge from the 93 % C-C and 7 % C-O regime of the starting material to form 52.1 ±4.0 % C-C, 17.3 ±2.7 % C-O, 7.0 ±0.8 % C=O, 6.9 ±6.2 C=C and even 16.7 ±8.7 C-B bonds. This wide range of environments is again attributed to the unwashed nature of the material which would usually remove any products of the side reactions that this divergence represents.

The B1s similarly shows a degradation in structure going from a 5.8 % B-O and 93.5 % B-N boron environment to 0 % B-O, 57.9 ±6.8 % B-N, 27.7 ±0.8 % B-H and 13.8 ±7.7 % B-C environment. This shows that only significantly damaged BNP material (evidenced by the high B-H proportion) can be successfully dispersed and deposited onto the electrode by BNP. This conclusion is supported by the same trend being observed in the deposition of 'oxidised' BNP from section 7.4.2.1.

7.5 Summary and Conclusions

This chapter has focused on the exfoliation and/or suspension of boron nitride platelets (BNPs) in various solvents. Initially, it was found that bath sonication was the most efficient benchtop route to produce BNP suspension in IPA when compared to probe sonication and shear mixing. This was shown by the higher BNP concentrations (0.232 ±0.037 mg_{BN} mL_{IPA}^{-1}), visually (by SEM) less agglomerated product, as well as a 100-hour stability test on the suspension. All methods were shown to reduce the size of BNP but this was hypothesised to be due to the size-selection effects of centrifugation. The exfoliation processes have no obvious influence on the BN atomic makeup that could not be explained by an increase in surface area.

It was hypothesised that these exfoliated BNP with higher surface area and fewer stabilising, eclipse-stacked, hBN layers may be less inert to oxidation, so samples were exposed to similar acid oxidation treatments as in chapter 6. IR and XPS analysis of these samples showed no significant change in the BNP bonding environment, and it was again concluded that BNP are inert to acid based chemical oxidation despite exfoliation.

Due to the surface area:volume ratio (6.04×10^{-6}) of the BNP used in this and chapter 6, it is possible that molecular characterisation techniques used previously may not be able to distinguish the surface modification of BNP from the bulk hBN majority. As solvent-BNP interactions are largely determined by the chemical functionality of the BN surface, the ability of different solvents of varying Hansen solubility parameters to disperse 'oxidised' BNP samples from across chapters 6 & 7 were used as a final check for BN hydroxylation. Suspension in polar protic solvents did not significantly improve while the least H-bonding solvent (DMAc) remained the most efficient dispersant of nearly all 'oxidised' BNP samples with an improved yield in most cases. Through this, the original conclusion that BNP are inert to acid based chemical oxidation was upheld.

The dispersal of these 'oxidised' BNP samples in DMAc was of use for their deposition by EPD. The current/time curves of these EPD and resulting charge transfer values (max 2.396 mC) showed an

increase proportional to the damage to the 'oxidised' BNP samples used (as expressed by the B-H signal of their B1s XPS spectra), but independent of BNP concentration in DMAc. This implied that the deposited BNP may be chemically distinct from the bulk dispersed material, but EDS showed no significant variation in atomic makeup. Additionally, the predicted BNP film thickness (max 35.7 nm) was low and actual films were observed to be uneven and consist of agglomerated BNP isolated from each other on the electrode surface, making it inappropriate for many applications.

Finally, deposition of BNP by the reduced dispersion for EPD method was investigated. It was found to be successful at producing thin, uneven, films of BNP covering the electrodes of thicknesses up to 1.37 ±1.28 μm. However, the resulting dried film was not mechanically strong as it could not be washed as this would remove the film from the electrode surface.

8 SUMMARY AND CONCLUSIONS

The initial objective of this thesis was to investigate and further our understanding of the reactivity, dispersibility and deposition of primarily hexagonal boron nitride nanomaterials by applying science to them developed for use on analogous carbon structures. The approach taken to address these outstanding scientific questions was through the development of a novel method of nanomaterial film production. This was achieved by the amalgamation of reductive dispersion and electrophoretic deposition techniques and by applying experimental conditions that surpass the traditional oxidation based methods currently in use. This approach has been successfully applied to CNT, BNNT and BNP while the latter has additionally been subjected to a parallel study investigating the utility of the oxidation techniques used on carbon materials. This parallel work aimed to create stable suspensions of oxidised BNP for EPD which could be compared to the reduced dispersion for EPD method. This concluding chapter summarises the main findings of the thesis, presents the conclusions reached, and identifies results of interest that future researchers can build upon for further applications across the field.

8.1 REDUCTIVE DISPERSION OF CNT CAN BE APPLIED SUCCESSFULLY TO EPD

The fourth chapter of this thesis introduced a novel method to produce conductive, mechanically strong, and thermally stable SWCNT films. This represents a step change in the field as using this methodology will allow the retention of SWCNT nanostructure without the need for additional chemical modification, additives, or binders as was previously the case. It was shown that the electrochemical reduction and subsequent suspension of CNT by sodium naphthalide is an excellent dispersion for use in electrophoretic deposition which can produce films of a controllable thickness (0-14 µm) in a short amount of time (5-120 s), using low field strengths (1-5 V cm^{-1}).

When compared to materials produced using the current standard oxidation based methods, the final free standing product of this work was found to have a lower mechanical strength (8.4 vs 14.9 MPa

Youngs modulus) and electrical conductivity (229 S cm^{-1} vs 694 ±18 S cm^{-1}). Analysis of the cross section for these thicker films found void spaces caused by the removal of sodium crystals during the washing of samples and it is these holes that are assigned blame for the films' macro-property failings. Contrary to this, TGA comparisons of the same samples showed this work's product degraded at a significantly higher temperature than the pre-oxidised standard (689 vs 627 °C) which illustrates the main advantage of this novel method: that the nanostructure of the CNT used are not altered or damaged by the procedures required to form them into a film.

8.2 Reductive dispersion for EPD can be applied to BNNT

Further developing the scope and applications of the novel reduced nanotube dispersion for EPD method developed in this thesis, the fifth chapter demonstrated the possibility of using electrically insulating boron nitride nanotubes in the place of CNT. BNNT have never before been shown to be dispersed by electrochemical charge, nor been subject to neat film creation by EPD, therefore the successful completion and display of this work represents a significant contribution to the field.

It was found that the charge ratio on BNNT was significantly lower ($<41_{BN}:1_{Na}$) than for CNT ($5_{C}:1_{Na}$) and subsequently EPD deposition rates were slower (2.03 µg cm^{-2} min^{-1}) but it is hypothesised that this allowed thicker/denser gel phases to form on the depositing electrodes allowing resultant BNNT films to be thicker than CNT (up to 35 µm). The nanotubes within films were again found to have near identical nanostructures to the starting material feedstock, showing the dispersion and EPD processes were not damaging. However, the similar film density to CNT equivalents (0.31 g cm^{-3}) and poor mechanical performance implies a similar issue with washed away sodium crystal pores.

8.3 BNP are inert to acid oxidation

Numerous literature sources have described methods of hBN functionalisation by acid oxidation using similar methods to those that are standard practice in carbon nano-chemistry. In this study, when multiple grades of BNP were subjected to numerous acid mixtures, they were found by all analysis

techniques to be inert to these conditions, with the BNP not deviating from their initial state. Experiments designed to damage the BNP structure using strong oxidative conditions were performed with the aim of introducing functional groups onto the presumed more reactive hBN defects introduced during the sonication process. Analysis of the BNP samples showed only an increase in hBN nano-structural damage, and the conclusion reached was that the BNP samples had not been damaged or oxidised under the conditions employed. A final BNP chemical oxidation was made using pre-exfoliated BNP with the assumption that this less stabilised and higher surface area starting material would be more reactive. The results also showed no observable damage or oxidation, with the conclusion that the 2D, eclipse stacked hBN platelets are inert to acid oxidation.

8.4 DISPERSIONS OF BNP ARE APPLICABLE TO EPD

A key process in EPD efficiency is the suspension of nano particles in the reaction vessel fluid. Of common benchtop methods, bath sonication was found to be the most efficient route to BNP suspension, achieving a concentration up to 0.232 mg_{BN} mL_{IPA}^{-1} and a visually less agglomerated product. Bath sonication was therefore used to suspend all 'oxidised' BNP samples from previous studies in various solvents. The increase in sample concentrations found in polar-aprotic solvents, as well as no significant rise in the polar protic solvents, confirmed that the oxidation methods employed in this study are unable to introduce h-bonding hydroxyl groups onto the hBN surface and the inertness of this substance to acid oxidation. However, these BNP suspensions were found to deposit BNP during EPD. A clear conclusion from these experiments is that current/time measurements of these experiments predict that more nano-structurally damaged samples would deposit at faster rates while retaining their molecular integrity and properties. Indeed, assessments of the deposited material did not show significant difference between it and the bulk BNP in solution.

Finally, the reduced dispersion for EPD method was applied to BNP samples. It was found to be successful at producing thin, uneven films of BNP from a charge transfer during EPD that was orders of magnitude greater than those found for the 'oxidised' BNP dispersions. It was observed that the

resulting dried film was not mechanically strong, as it could not be washed. While it can be concluded that the technique has met with some success, the lack of mechanical strength means that that the resulting film was probably not chemically or nano-structurally pure and further development will be needed to identify how to improve on this.

9 FUTURE WORK

Given the breadth of potential research avenues within the field of nanomaterial functionalisation, dispersion and deposition, the conclusions made by this thesis can be built upon to conduct further investigations. Here, two potential routes for further study are presented and some initial work reported and described. This preliminary work provides a proof of concept and makes the case for these investigations to be taken further.

9.1 REDUCTIVE DISPERSIONS FOR EPD OF DOPED NANOTUBES

The successful application of reductive dispersion for use in the EPD nanotubes described in chapters 4 and 5 shows the biggest improvement on current EPD methods by the retention of nanostructure seen between the starting material and final film. While this has been shown for both carbon and boron nitride nanotubes, the retention of nanostructure is arguably most significant for heteroatom doped nanotubes. This is because the current standard oxidation based methods of nanotube dispersion preferentially target heteroatom dopants[256] thereby limiting the dopant levels of materials that can be deposited by EPD.

To investigate the viability of the reductive dispersion for EPD method being applied to doped nanotubes, boron doped SWCNT (B-CNT) were produced by Dillon McGurty (of the NbD research group) who provided this statement on their synthesis (additionally illustrated in Figure 9.1.A):

"*Boron doping of SWCNTs was attempted using a substitutional synthesis technique adapted from commonly employed procedures within the literature. SWCNTs and boron oxide (B_2O_3), at a ratio of 2:5, were combined in ethanol (250 mL) and sonicated for 30 minutes. The solvent was then allowed to evaporate away before collecting the powder mixture. This was transferred to an alumina boat that was centred in a tube furnace which was purged in argon (0.5 slm) before heating to 1100 °C and holding for 2 hours. The powder was then washed thoroughly by dispersing the powder in a combination of ethanol and DI water (1000 mL) which was boiled and then filtered and collected. After*

collection, the washing step was repeated in water before rinsing the final product with more boiling water (1000 mL)."

These B-CNT were subjected to the reductive dispersion and EPD as described in section 4.3.2. Film thicknesses were measured by profilometry (Figure 9.1.B) and the rate of deposition was calculated as 0.0409 μm s^{-1}, with the film achieved after 60 s of deposition being 2.8 ±1.3 μm thick. The undoped SWCNT (section 4.4.4.1) deposition rate (0.0609 μm s^{-1}) and 60 s thickness (3.6 ±0.6 μm) are higher than those measured here and this is thought to be due to the less dispersed nature of the B-CNT suspensions used (also evidenced by large error values from profilometry, which indicate clumps of material depositing together). Despite this, these experiments show that both reductive dispersion and EPD will work on these B-CNT and Raman D/G ratios (Figure 9.1.C) and imply that the nanotubes' nanostructure remain very similar before (0.100 ±0.019) and after (0.106 ±0.014) EPD.

XPS atomic breakdowns of these samples (Figure 9.1.D) re-iterate the successful Na removal by washing of the films, but also indicate that the initial boron doping of the CNT was not as successful as initially thought. This is due to the starting B-CNT material not measuring a significant boron signal to be counted in the atomic makeup of the sample. Additionally, the low C-B (0%) and B-C (2.9 ±4.1 %) bonding proportions found in the C1s and B1s deconvolutions (Figure 9.1.E-F) must lead to the conclusion that boron doping has not occurred.

While these experiments have shown the materials being investigated hard to manipulate under even chemically extreme conditions, this leaves the field open to further exploration which can be taken in many different directions. Nanotubes can be doped with many different heteroatoms[257,258] for a range of applications, so the ability to easily deposit them from solution in thin films with no damage to the dopant level or nanostructure, demonstrated in this work, will be a useful and worthwhile area for future study.

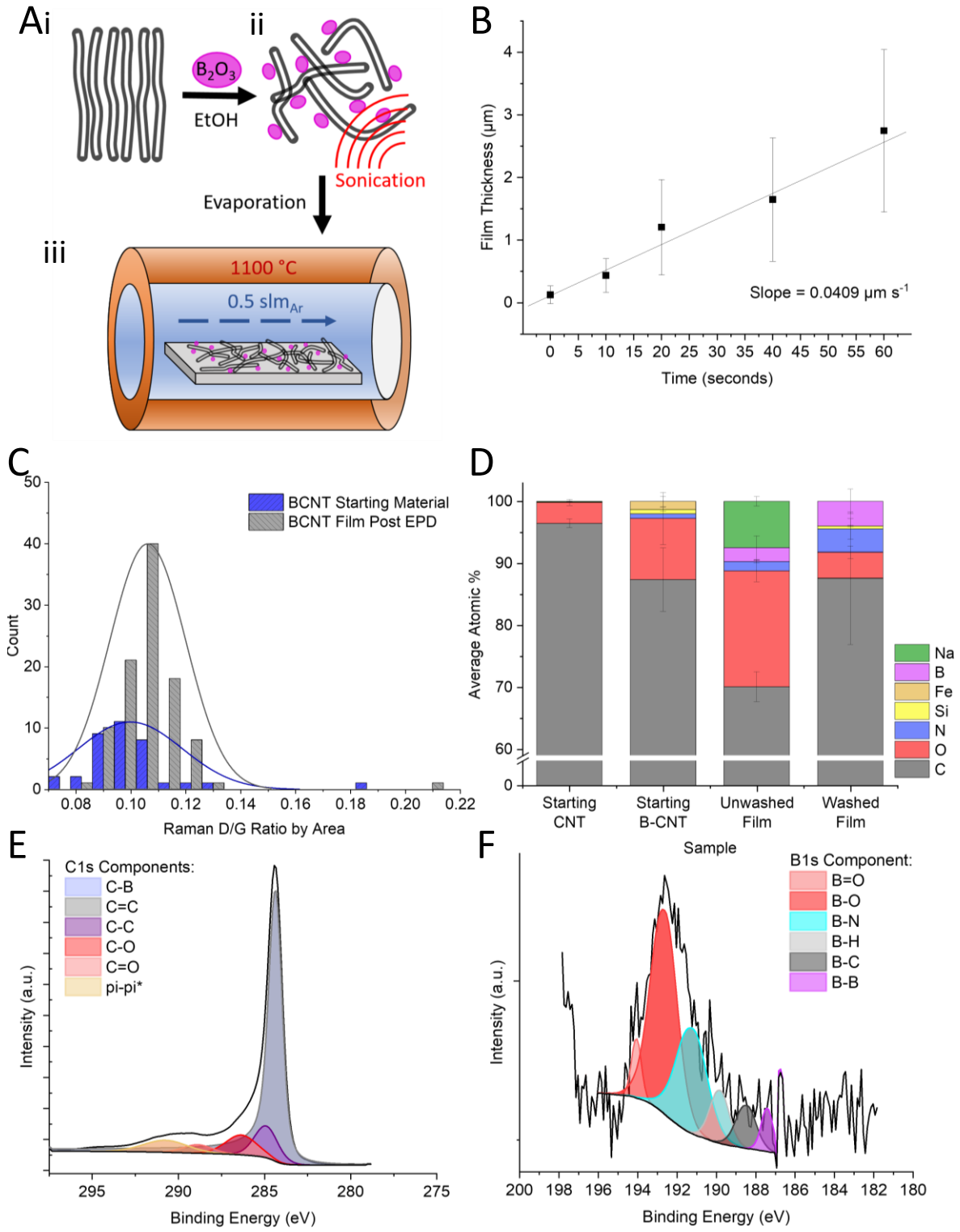


Figure 9.1. Analysis of B-doped CNT reductive dispersion EPD. Schematic for the formation of B-CNT shows the starting SWCNT **[A]*i*** combined in ethanol with boron oxide and sonicated **[A]*ii***. The solvent was then evaporated, and the boron coated CNT were heated at 1100 °C in a tube furnace under an argon atmosphere **[A]*iii***. The resulting material was reductively dispersed and EPD was carried out which shows a similar deposition rate **[B]** to work presented in chapter 4. Raman D/G ratios of the nanotubes before and after deposition **[C]** are statistically identical showing retention of nanostructure. (Continued on next page)

However, XPS atomic analysis **[D]** showed very little boron present in the pre-EPD B-CNT and C1s **[E]** and B1s **[F]** of the same sample confirm minimal B-C bonding implying that the initial doping has been unsuccessful.

9.2 Impure hBN as Sources for Oxidation Reactivity: BNF

Chapters 6 and 7 showed the difficulty of modifying boron nitride platelets by acid oxidation. The BNP used had a high purity and stabilised eclipse stacked hBN nanostructure with low surface area to volume ratios and few reactive terminating edges. These made the attempted reactions using common acid oxidation methods unsuccessful. However, the demand for a thermally conductive, electrically insulating hBN material, that is functionalised by polar hydroxyl groups, remains for applications in EPD (as explored in this work) as well as composites[259] and catalysis.[260] A potential route towards this goal of functionalised hBN is the use of an alternative, less pure (and thereby more reactive) starting material such as boron nitride fibers (BNF).

Similar to analogous carbon fiber manufacture, the most common methods for BNF production follow a methodology in which a principally BN containing polymer (eg. poly-aminoborazinyl)[261] is synthesised and then spun into a fiber. This fiber is then pyrolyzed under inert conditions to remove heteroatoms and fuse the remaining BN into a hBN lattice.[262] More recently, an alternate approach by J. Lin *et al.*[263] heated melamine and boric acid in an aqueous solvent which was then frozen and freeze-dried to produce ultra-fine BN containing precursor fibers that were pyrolyzed to make h-BN nanofibers. The resulting material made from these methods is comprised of both amorphous and hexagonal BN and so does not achieve the same thermal or mechanical properties of pure hBN[264] but increases the potential for chemical reactivity. To explore this possibility, preliminary experimentation was conducted to investigate BNF as an alternative to BNP.

BNF for this investigation were manufactured (Figure 9.2.A) by dissolving melamine and boric acid (1:3 molar ratio respectively) in water at 85 °C which was then rapidly frozen (typically by liquid nitrogen). This ice was then freeze dried to reveal M.2B (melamine di-borate complex)[265] fibers which were

pyrolyzed at 1300 °C under argon to produce the hBN. Analysis showed that an increase of melamine concentration in the initial solution over 0.1 mol L^{-1} (12.6 g L^{-1}) results in BNF fibers forming a porous and self-supporting 3D network of interconnected M.2B fibers in the shape of the container in which they were initially frozen (Figure 9.2.B). SEM analysis of M.2B fibers was problematic as charging caused damage to the material (see section 3.2) but images obtained showed ribbon shaped solid crystals which became hollow and porous when pyrolyzed (Figure 9.2.C) as well as reducing in size.

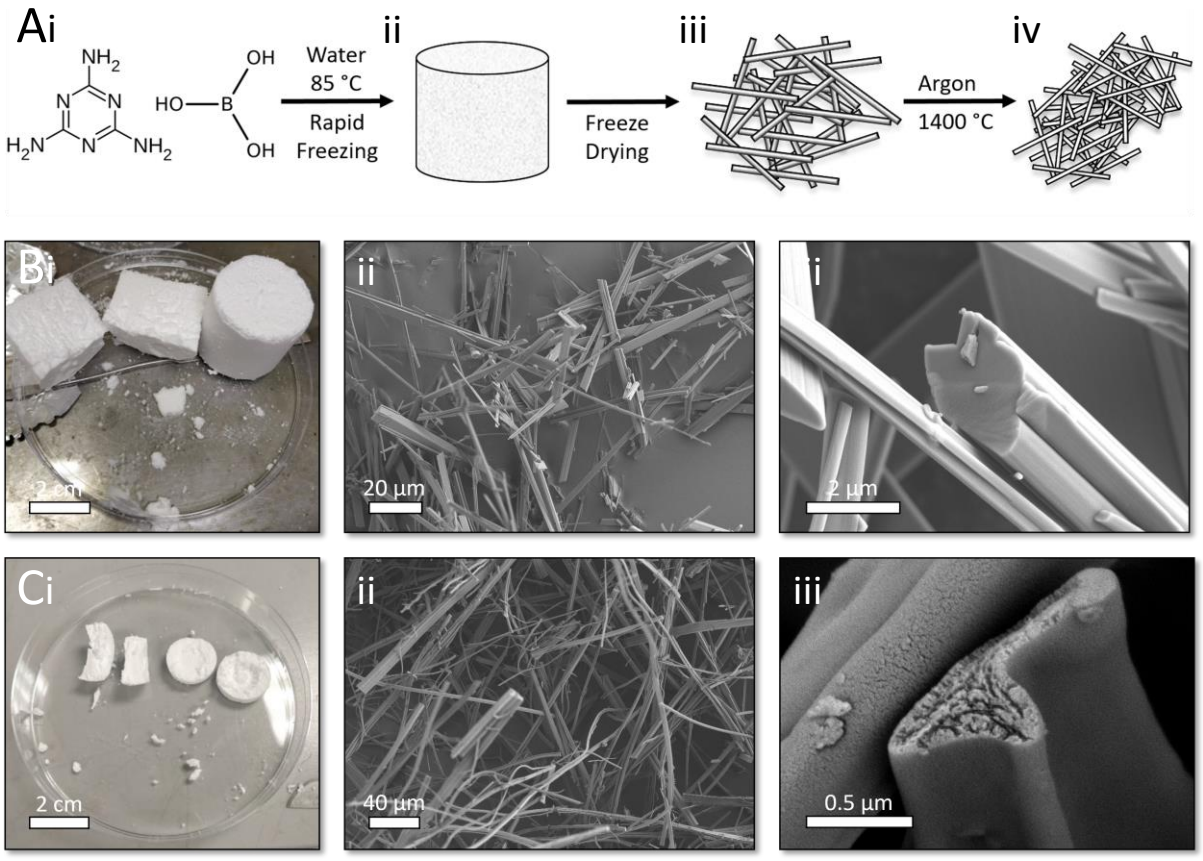


Figure 9.2. Summary of produced BNF. Diagram shows the process used to manufacture BNF by dissolving melamine and boric acid **[A]*i*** in water (1:3 ratio) and then rapidly cooling this solution (typically with liquid nitrogen) into an ice **[A]*ii*** which is then freeze dried to leave a M.2B crystal network **[A]*iii*** that can be pyrolyzed at 1400 °C under an argon atmosphere to form hBN fibers **[A]*iv***. When the melamine/boric acid concentration is high enough, the resulting material forms a homogenous self-supporting structure, taking the shape of the container in which they were frozen **[B*i*]** and are comprised of enmeshed flat ribbon-like fibers **[B]*ii*** made from solid M.2B crystal **[B]*iii***. After pyrolysis, the BNF retain their shape but shrink in size **[C]*i*** and become porous **[C*iii*]**.

The nanostructure of these pyrolyzed BNF was confirmed with TEM imaging (Figure 9.3.A-B) where

2D hBN platelets fused together by aBN can be observed across the BNF. The average size of these constituent hBN platelets was measured at 10.5 ±6.9 nm from TEM (42 measurements), although this conflicted with the value (55.3 nm) calculated from the Shearer equation using the BNFs XRD spectra. The mixed aBN and hBN BNF structure of the material is also present in the Raman spectra (Figure 9.3.C) as the sharp E_{2g} hBN peak at 1367 cm^{-1} is barely visible above the broad aBN signal centred on the same coordinate, which increases (implying a relative increase in aBN) when the BNF material is exposed to the acid oxidation reagents used for BNP in chapters 6 and7.

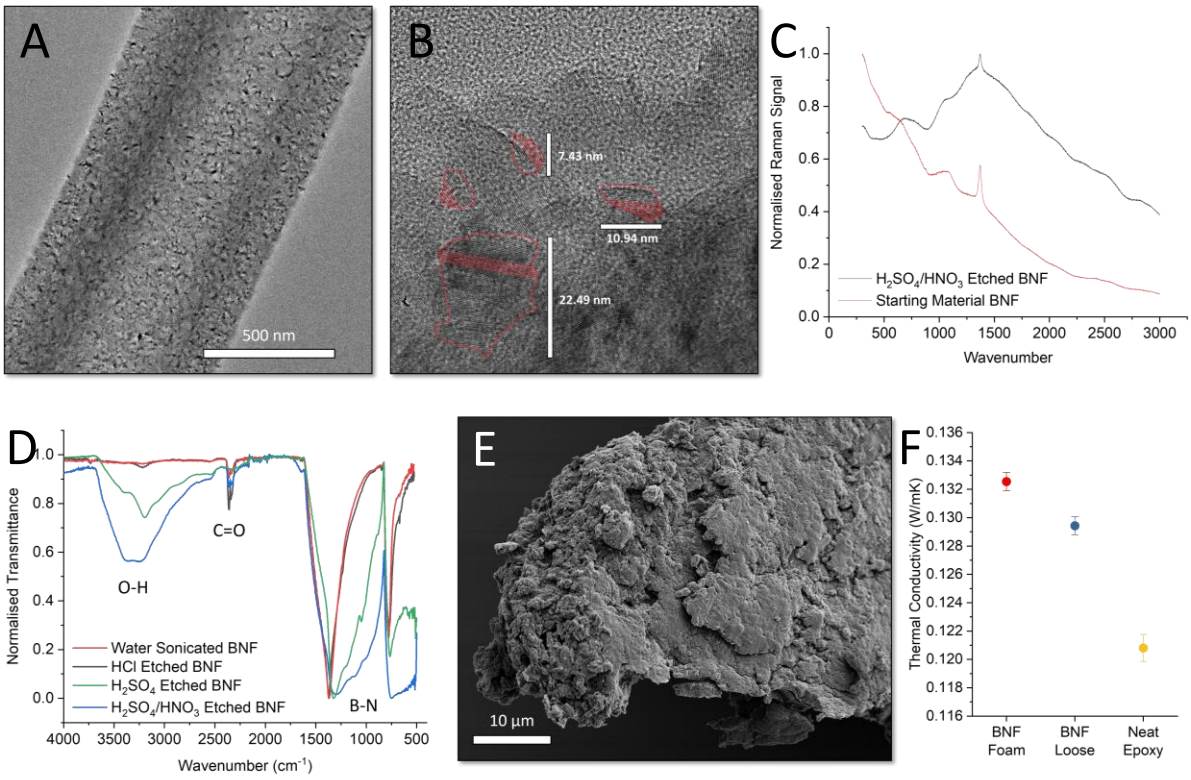


Figure 9.3. Summary of investigations into BNF. TEM images of the fiber cross section **[A]** and edge **[B]** show that the BNF structure is comprised of 2D hBN platelets (of average size 10.5 ±6.9 nm) fused together. Raman spectra **[C]** of BNF showed that these platelets are fused together with amorphous BN which proportionally increased after acid etching. FTIR analysis **[D]** showed a significant increase in O-H (3400 cm^{-1}) content after both H_2SO_4 and H_2SO_4/HNO_3 acid etching but this caused the destruction of the BNF macrostructure as seen in SEM **[E]**. An application of these BNF as fillers for thermally conducting composites is demonstrated by thermal conductivity measurements of samples set in epoxy **[F]**.

BNF oxidation was conducted in the same manner as attempted for BNP (section 6.4.1) and the IR spectra (Figure 9.3.D) of these initial samples are promising due to the large increase in O-H signal found in the H_2SO_4 and H_2SO_4/HNO_3 treated samples implying successful hydroxylation. However, this potential functionalisation success is tempered by a low reaction yield (80%$_{Mass}$ drop compared to starting BNF) and the loss of the BN fibrous structure. SEM images (Figure 9..E) show that the product is a rough paste with no obvious order to it. Future researchers will therefore need to design experiments to understand and control the extent of damage that these oxidation conditions inflict upon the BNF material.

Finally, the potential for the self-supporting 3D BNF structures was demonstrated by comparison of epoxy infiltrated composites (Figure 9.3.F). The thermal conductivity of neat epoxy (120.8 ±1.2 W K^{-1}) was improved by the incorporation of loose BN fibers (129.4 ±0.8 W K^{-1}), but when this same polymer was infiltrated into the 3D BNF (as H. Fang *et al.*[266] have similarly done with BN foams) it produced an even higher thermal conductivity of 132.5 ±0.8 W K^{-1}.

This foray into macro-materials' properties clearly shows the breadth of possibilities and potential for BNF research and projects building on the acid etching techniques and BN dispersions developed in this thesis.

10 BIBLIOGRAPHY

1. Raimond, J. M., Brune, M., Computation, Q., Martini, F. De & Monroe, C. Electric Field Effect in Atomically Thin Carbon Films. *Science (80-.).* **306**, 666–670 (2004).
2. Ozdemir, S., Taniguchi, T., Watanabe, K., Geim, A. K. & Novoselov, K. S. Stacking Order in Graphite Films Controlled by van der Waals Technology. *Nano Lett.* **19**, 8526–8532 (2019).
3. Ebbesen, T. W. *et al.* Electrical conductivity of individual carbon nanotubes. *Lett. to Nat.* **382**, 54–56 (1996).
4. Iijima, S. Helical microtubules of Graphitic Carbon. *Nature* **354**, 56–58 (1991).
5. Ballentine, J., Clancy, A., Rubio, N. & Shaffer, M. Investigation into the Carbon Nanotubide Initiated Grafting of Vinyl Monomers. (Imperial College London, 2017).
6. Zhang, W. *et al.* Chirality dependence of the thermal conductivity of carbon nanotubes. *Nanotechnology* **15**, 936–939 (2004).
7. Charoenpakdee, J., Suntijitrungruang, O. & Boonchui, S. Chirality effects on an electron transport in single - walled carbon nanotube. *Sci. Rep.* **10**, 18949 (2020).
8. Chacham, H. *et al.* Stability and Band Gap Constancy of Boron Nitride Nanotubes Stability and Band Gap Constancy of Boron Nitride Nanotubes . (1994).
9. Glavin, N. R. *et al.* Amorphous Boron Nitride: A Universal, Ultrathin Dielectric for 2D Nanoelectronics. *Adv. Funct. Mater.* **26**, 2640–2647 (2016).
10. Hattori, Y., Taniguchi, T., Watanabe, K. & Nagashio, K. Layer-by-layer dielectric breakdown of hexagonal boron nitride. *ACS Nano* **9**, 916–921 (2015).
11. Tian, Y. *et al.* Ultrahard nanotwinned cubic boron nitride. *Nature* **493**, 385–388 (2013).
12. Bello, I. *et al.* Cubic boron nitride films for industrial applications. *Diam. Relat. Mater.* **14**, 1784–1790 (2005).
13. Majety, S. *et al.* Semiconducting hexagonal boron nitride for deep ultraviolet photonics. *Quantum Sens. Nanophotonic Devices IX* **8268**, 82682R (2011).
14. Rubio, A., Corkill, J. L. & Cohen, M. L. Theory of graphitic boron nitride nanotubes. *Phys. Rev. B* **49**, 5081–5084 (1994).
15. Chopra, N. G. *et al.* Boron Nitride Nanotubes. *Science (80-.).* **269**, 966–968 (1995).
16. Spreadborough, J. The frictional behaviour of graphite. *Wear* **5**, 18–30 (1961).
17. Saito, T., Hosoe, T. & Honda, F. Chemical wear of sintered Si3N4, hBN and Si3N4–hBN.pdf. **247**, 223–230 (2001).
18. SPERBER, J. L. INVESTIGATIONS OF HEXAGONAL BORON NITRIDE: BULK CRYSTALS AND ATOMICALLY-THIN TWO DIMENSIONAL LAYERS. (Kansas State University, 2016).
19. Boylan, J. Carbon - Graphite Materials. *Mater. World* **4**, 1–8 (1996).
20. Chopra, N. G. & Zettl, A. Measurement of the elastic modulus of a multi-wall boron nitride nanotube. **105**, 297–300 (1998).
21. Yu, M., Files, B. S., Arepalli, S. & Ruoff, R. S. Tensile Loading of Ropes of Single Wall Carbon Nanotubes and their Mechanical Properties. **1**, 24–27 (2000).
22. Jiang, J. W., Wang, J. S. & Li, B. Young's modulus of graphene: A molecular dynamics study. *Phys. Rev. B - Condens. Matter Mater. Phys.* **80**, 15–18 (2009).

23. Belkerk, B. E. *et al.* Thermal conductivity of vertically aligned boron nitride nanotubes. *Appl. Phys. Express* **9**, (2016).

24. Han, Z. & Fina, A. Progress in Polymer Science Thermal conductivity of carbon nanotubes and their polymer nanocomposites : A review. *Prog. Polym. Sci.* **36**, 914–944 (2011).

25. Balandin, A. A. *et al.* Superior thermal conductivity of single-layer graphene. *Nano Lett.* **8**, 902–907 (2008).

26. Patel, P. *et al.* Mechanism of thermal decomposition of poly (ether ether ketone) (PEEK) from a review of decomposition studies. *Polymer Degradation and Stability* vol. 95 (2010).

27. Farivar, F., Yap, P. L., Karunagaran, R. U. & Losic, D. Thermogravimetric Analysis (TGA) of Graphene Materials: Effect of Particle Size of Graphene, Graphene Oxide and Graphite on Thermal Parameters. *J. Carbon Res.* **7**, 41 (2021).

28. Kostoglou, N. *et al.* Boron Nitride Nanotubes Versus Carbon Nanotubes : A Thermal Stability and Oxidation Behavior Study. *Nanomaterials* **10**, 2435 (2020).

29. Kostoglou, N., Polychronopoulou, K. & Rebholz, C. Thermal and chemical stability of hexagonal boron nitride (h-BN) nanoplatelets. *Vacuum* **112**, 42–45 (2015).

30. Gleiman, S., Chen, C., Datye, A. & Phillips, J. LA-UR-01-4327 Melting and spheroidization of hexagonal boron nitride in a microwave-powered , atmospheric pressure nitrogen plasma Chun-Ku Chen , University of New Mexico , Department of Chemical and Nuclear Abhaya Datye , University of New Mexico , Cente. *Energy* **836**,.

31. Yamamoto, M., Einstein, T. L., Fuhrer, M. S. & Cullen, W. G. Charge Inhomogeneity Determines Oxidative Reactivity of Graphene on Substrates. *ACS Nano* **6**, 8335–8341 (2012).

32. Stafford, B. Top 7 Topics for Materials Science Research in 2020. *Matmatch* https://matmatch.com/resources/blog/top-seven-topics-for-materials-science-research-in-2020/ (2020).

33. Liu, Z., Tabakman, S., Welsher, K. & Dai, H. Carbon Nanotubes in Biology and Medicine : In vitro and in vivo Detection , Imaging and Drug Delivery. *Nano Res.* **2**, 85–120 (2009).

34. Ouyang, M. I. N., Huang, J. & Lieber, C. M. Fundamental Electronic Properties and Applications of Single-Walled Carbon Nanotubes. *Acc. Chem. Res.* **35**, 1018–1025 (2002).

35. Guo, G. Y., Chu, K. C. & Wang, D. Linear and nonlinear optical properties of carbon nanotubes from first-principles calculations. *Phys. Rev. B* **69**, 205416 (2004).

36. Thostenson, E. T., Ren, Z. & Chou, T. Advances in the science and technology of carbon nanotubes and their composites : a review. *Compos. Sci. Technol.* **61**, 1899–1912 (2001).

37. Saint-Gobain. Tres BN Consmetic Powders. https://www.bn.saint-gobain.com/products/powders/cosmetic-powders.

38. Fredrickson, J. E. & Redanz, W. H. Boron Nitride for Aerospace Applications. *Mater. Sci. Res.* 245–260 (2012) doi:10.1007/978-1-4684-7450-3_14.

39. Xia, Q., Zhang, Z., Liu, Y. & Leng, J. Buckypaper and its composites for aeronautic applications. *Compos. Part B Eng.* **199**, 108231 (2020).

40. Strack, G. *et al.* Bioelectrocatalytic generation of directly readable code: Harnessing cathodic current for long-term information relay. *Chem. Commun.* **47**, 7662–7664 (2011).

41. Papa, H., Gaillard, M., Gonzalez, L. & Chatterjee, J. Fabrication of functionalized carbon nanotube buckypaper electrodes for application in glucose biosensors. *Biosensors* **4**, 449–

460 (2014).

42. Halámková, L. *et al.* Implanted biofuel cell operating in a living snail. *J. Am. Chem. Soc.* **134**, 5040–5043 (2012).

43. Gross, A. J., Holzinger, M. & Cosnier, S. Buckypaper bioelectrodes: Emerging materials for implantable and wearable biofuel cells. *Energy Environ. Sci.* **11**, 1670–1687 (2018).

44. Huang, W. *et al.* Electrophoretic deposited boron nitride nanosheets-containing chitosan-based coating on Mg alloy for better corrosion resistance , biocompatibility and antibacterial properties. *Colloids Surfaces A Physicochem. Eng. Asp.* **638**, 128303 (2022).

45. Raza, M. A., Nadeem, A. & Muhammad, T. I. Corrosion Study of Boron Nitride Nanosheets Deposited on Copper Metal by Electrophoretic Deposition. *TMS 2019 148th Annu. Meet. Exhib. Suppl. Proc.* pp 681–685 (2019) doi:10.1007/978-3-030-05861-6_66.

46. Terao, T. *et al.* Alignment of boron nitride nanotubes in polymeric composite films for thermal conductivity improvement. *J. Phys. Chem. C* **114**, 4340–4344 (2010).

47. Xiao, A. W. *et al.* Electrophoretic Fabrication of Robust Carbon Nanotube 'buckyfilms' for Flexible Electronics. *ACS Appl. Nano Mater.* **2**, 5190–5199 (2019).

48. Cho, J. *et al.* Characterisation of carbon nanotube films deposited by electrophoretic deposition. **7**, 0–9 (2008).

49. Girifalco, L. A., Hodak, M. & Lee, R. S. Carbon nanotubes, buckyballs, ropes, and a universal graphitic potential. *Phys. Rev. B - Condens. Matter Mater. Phys.* **62**, 13104–13110 (2000).

50. HANSEN, C. M. The Three Dimensional Solubility Parameter and Solvent Diffusion Coefficient Doctoral Dissertation. (University of Copenhagen, 1967).

51. Qu, J., Li, Q., Luo, C., Cheng, J. & Hou, X. Characterization of flake boron nitride prepared from the low temperature combustion synthesized precursor and its application for dye adsorption. *Coatings* vol. 8 at https://doi.org/10.3390/coatings8060214 (2018).

52. Hansen, C. M. & Smith, A. L. Using Hansen solubility parameters to correlate solubility of C60 fullerene in organic solvents and in polymers. *Carbon N. Y.* **42**, 1591–1597 (2004).

53. Nazarov, A. S. *et al.* Functionalization and Dispersion of Hexagonal Boron Nitride (h-BN) Nanosheets Treated with Inorganic Reagents. *Asian Chem. Editor. Soc.* **7**, 554–560 (2012).

54. Tian, X. *et al.* Shear-Assisted Production of Few-Layer Boron Nitride Nanosheets by Supercritical CO2 Exfoliation and Its Use for Thermally Conductive Epoxy Composites. *Sci. Rep.* **7**, (2017).

55. Coleman, J. N. *et al.* Two-Dimensional Nanosheets Produced by Liquid Exfoliation of Layered Materials. *Science (80-.).* **331**, 568–572 (2011).

56. Cheng, Q., Debnath, S., Gregan, E. & Byrne, H. J. Ultrasound-Assisted SWNTs Dispersion : Effects of Sonication Parameters and Solvent Properties. *J. Phys. Chem. C* **114**, 8821–8827 (2010).

57. Dumée, L., Sears, K., Schütz, J., Finn, N. & Duke, M. Influence of the Sonication Temperature on the Debundling Kinetics of Carbon Nanotubes in Propan-2-ol. *Nanomaterials* **3**, 70–85 (2013).

58. Lu, K. L. *et al.* Mechanical damage of carbon nanotubes by ultrasound. *Carbon N. Y.* **34**, 814–816 (1996).

59. Lee, C. H., Zhang, D. & Yap, Y. K. Functionalization, Dispersion, and Cutting of Boron NitrideNanotubes in Water. *J. Phys. Chem. C* **116**, 1798–1804 (2012).

60. Baig, Z., Mamat, O., Mustapha, M., Mumtaz, A. & Munir, K. S. Investigation of tip sonication effects on structural

quality of graphene nanoplatelets (GNPs) for superior solvent dispersion. *Ultrason. - Sonochemistry* **45**, 133–149 (2018).

61. TIAN, Z. *et al.* Crystalline boron nitride nanosheets by sonication-assisted hydrothermal exfoliation. *J. Adv. Ceram.* **8**, 72–78 (2019).

62. Yang, D.-Q., Rochette, J.-F. & Sacher, E. Functionalization of Multiwalled Carbon Nanotubes by Mild Aqueous Sonication. *J. Phys. Chem. B* **109**, 7788–7794 (2005).

63. Lin, Y. *et al.* Aqueous dispersions of few-layered and monolayered hexagonal boron nitride nanosheets from sonication-assisted hydrolysis: Critical role of water. *J. Phys. Chem. C* **115**, 2679–2685 (2011).

64. Huang, Y. Y. & Terentjev, E. M. Dispersion of carbon nanotubes: Mixing, sonication, stabilization, and composite properties. *Polymers (Basel).* **4**, 275–295 (2012).

65. Islam, M. F., Rojas, E., Bergey, D. M., Johnson, A. T. & Yodh, A. G. High weight fraction surfactant solubilization of single-wall carbon nanotubes in water. *Nano Lett.* **3**, 269–273 (2003).

66. Kun, Y. *et al.* Sonication-assisted dispersion of carbon nanotubes in aqueous solutions of the anionic surfactant SDBS : The role of sonication energy. *Chinese Sci. Bull.* **58**, 2082–2090 (2013).

67. Matatyaho, A. *et al.* Understanding the Exfoliation and Dispersion of Hexagonal Boron Nitride Nanosheets by Surfactants: Implications for Antibacterial and Thermally Resistant Coatingś . *ACS Appl. Nano Mater.* **4**, 142–151 (2021).

68. Terao, T. *et al.* Thermal conductivity improvement of polymer films by catechin-modified boron nitride nanotubes. *J. Phys. Chem. C* **113**, 13605–13609 (2009).

69. Zhi, C. *et al.* Perfectly Dissolved Boron Nitride Nanotubes Due to Polymer Wrapping. 15996–15997 (2005) doi:10.1021/ja053917c.

70. Rausch, J., Zhuang, R. & Ma, E. Surfactant Assisted Processing of Carbon Nanotube / Polypropylene Composites : Impact of Surfactants on the Matrix Polymer. *J. Appl. Ploymer Sci.* **117**, 2583–2590 (2010).

71. Petit, P., Mathis, C., Journet, C. & Bernier, P. Tuning and monitoring the electronic structure of carbon nanotubes. *Chem. Phys. Lett.* **305**, 370–374 (1999).

72. Clancy, A. J., White, E. R., Tay, H. H., Yau, H. C. & Shaffer, M. S. P. Systematic comparison of conventional and reductive single-walled carbon nanotube puri fi cations. *Carbon N. Y.* **108**, 423–432 (2016).

73. Pénicaud, A., Poulin, P., Derré, A., Anglaret, E. & Petit, P. Spontaneous dissolution of a single-wall carbon nanotube salt. *J. Am. Chem. Soc.* **127**, 8–9 (2005).

74. Voiry, D., Drummond, C. & Pénicaud, A. Portrait of carbon nanotube salts as soluble polyelectrolytes. *Soft Matter* **7**, 7998–8001 (2011).

75. Clancy, A. J., Melbourne, J. & Shaffer, M. S. P. A one-step route to solubilised, purified or functionalised single-walled carbon nanotubes. *J. Mater. Chem. A* **3**, 16708–16715 (2015).

76. Connelly, N. G. & Geiger, W. E. Chemical redox agents for organometallic chemistry. *Chem. Rev.* **96**, 877–910 (1996).

77. Izutsu, K. Redox Properties of Solvents and Potential Windows. in *Electrochemistry in Nonaqueous Solutions* 103–106 (John Wiley & Sons, 2009).

78. Cui, Z., Oyer, A. J., Glover, A. J., Schniepp, H. C. & Adamson, D. H. Large Scale Thermal Exfoliation and Functionalization of Boron Nitride. 2352–2355 (2014) doi:10.1002/smll.201303236.

79. Li, C., Wang, D., Liang, T. & Wang, X.

Oxidation of multiwalled carbon nanotubes by air : benefits for electric double layer capacitors. *Powder Technol.* **142**, 175–179 (2004).

80. Sainsbury, T. *et al.* Oxygen Radical Functionalization of Boron Nitride Nanosheets. (2012) doi:10.1021/ja3080665.

81. Zhi, C. Y. *et al.* Chemically activated boron nitride nanotubes. *Chem. - An Asian J.* **4**, 1536–1540 (2009).

82. Roscaa, I. D., Watari, F., Uo, M. & Akasaka, T. Oxidation of multiwalled carbon nanotubes by nitric acid. *Carbon N. Y.* **43**, 3124–3131 (2005).

83. Ciofani, G. *et al.* Journal of Colloid and Interface Science A simple approach to covalent functionalization of boron nitride nanotubes. *J. Colloid Interface Sci.* **374**, 308–314 (2012).

84. Liao, Y. *et al.* Oxidative Etching of Hexagonal Boron Nitride Toward Nanosheets with Defined Edges and Holes. *Sci. Rep.* **5**, (2015).

85. Santangelo, S., Messina, G., Faggio, G., Abdul Rahim, S. H. & Milone, C. Effect of sulphuric-nitric acid mixture composition on surface chemistry and structural evolution of liquid-phase oxidised carbon nanotubes. *J. Raman Spectrosc.* **43**, 1432–1442 (2012).

86. Osorio, A. G., Silveira, I. C. L., Bueno, V. L. & Bergmann, C. P. H 2 SO 4 /HNO 3 /HCl-Functionalization and its effect on dispersion of carbon nanotubes in aqueous media. *Appl. Surf. Sci.* **255**, 2485–2489 (2008).

87. Datsyuk, V. *et al.* Chemical oxidation of multiwalled carbon nanotubes. *Carbon N. Y.* **6**, 2–9 (2008).

88. Arya, S. P. S. PREPARATION, PROPERTIES AND APPLICATIONS OF BORON NITRIDE THIN FILMS. *Thin Solid Films* **157**, 267–282 (1988).

89. Clancy, A. J. *et al.* Charged Carbon Nanomaterials: Redox Chemistries of Fullerenes, Carbon Nanotubes, and Graphenes. *Chem. Rev.* **118**, 7363–7408 (2018).

90. Hof, F., Bosch, S., Eigler, S., Hauke, F. & Hirsch, A. New basic insight into reductive functionalization sequences of single walled carbon nanotubes (SWCNTs). *J. Am. Chem. Soc.* **135**, 18385–18395 (2013).

91. Stephenson, J. J., Sadana, A. K., Higginbotham, A. L. & Tour, J. M. Highly functionalized and soluble multiwalled carbon nanotubes by reductive alkylation and arylation: The billups reaction. *Chem. Mater.* **18**, 4658–4661 (2006).

92. Mukherjee, A. *et al.* Attachment of nitrogen and oxygen centered radicals to single-walled carbon nanotube salts. *Chem. Mater.* **20**, 7339–7343 (2008).

93. Knirsch, K. C. *et al.* Topology-Driven Reductive Silylation of Synthetic Carbon Allotropes. *J. Am. Chem. Soc.* **138**, 15642–15647 (2016).

94. Voiry, D. & Roubeau, O. Stoichiometric control of single walled carbon nanotubes functionalization. *J. Mater. Chem.* **20**, 4385–4391 (2010).

95. Schmidt, G., Gallon, S., Esnouf, S., Bourgoin, J. P. & Chenevier, P. Mechanism of the coupling of diazonium to single-walled carbon nanotubes and its consequences. *Chem. - A Eur. J.* **15**, 2101–2110 (2009).

96. Garst, J. F., Barbas, J. T. & Barton, F. E. Radical Mechanism of Alkylation of Sodium Naphthalenide. *J. Am. Chem. Soc.* **90**, 7159–7160 (1968).

97. Nanotubes, N. *et al.* Covalent Functionalization of Boron Nitride Nanotubes via Reduction Chemistry. 12573–12582 (2015) doi:10.1021/acsnano.5b06523.

98. Khan, Z. U., Kausar, A., Ullah, H., Badshah, A. & Khan, W. U. A review of graphene oxide, graphene buckypaper, and polymer/graphene composites:

Properties and fabrication techniques. *J. Plast. Film Sheeting* **32**, 336–379 (2016).

99. Baughman, R. H., Zakhidov, A. A. & Heer, W. A. De. Carbon Nanotubes — the Route Toward Applications. *Sci. Compass Rev.* **297**, 787–793 (2002).

100. Baughman, R. H. *et al.* Carbon Nanotube Actuators. *Science (80-.).* **284**, 1340–1345 (1999).

101. Rinzler, A. G. *et al.* Large-scale purification of single-wall carbon nanotubes: Process, product, and characterization. *Appl. Phys. A Mater. Sci. Process.* **67**, 29–37 (1998).

102. Mattevi, B. C. *et al.* Evolution of Electrical , Chemical , and Structural Properties of Transparent and Conducting Chemically Derived Graphene Thin Films. *Adv. Funct. Mater.* **19**, 2577–2583 (2009).

103. Zhu, W. *et al.* Preparation of buckypaper supported Pt catalyst for PEMFC using a supercritical fluid method. *Electrochem. Solid-State Lett.* **14**, 81–84 (2011).

104. Du, C., Heldbrant, D. & Pan, N. Preparation and preliminary property study of carbonnanotubes films by electrophoretic deposition. *Mater. Lett.* **57**, 434–438 (2002).

105. Zhang, X., Sreekumar, T. V., Liu, T. & Kumar, S. Properties and structure of nitric acid oxidized single wall carbon nanotube films. *J. Phys. Chem. B* **108**, 16435–16440 (2004).

106. Mazinani, A. *et al.* Comparative antibacterial activity of 2D materials coated on porous-titania. *J. Mater. Chem. B* **9**, 6412–6424 (2021).

107. Schindler, A., Brill, J., Fruehauf, N., Novak, J. P. & Yaniv, Z. Solution-deposited carbon nanotube layers for flexible display applications. *Phys. E Low-Dimensional Syst. Nanostructures* **37**, 119–123 (2007).

108. Ou, E. *et al.* Macroscopic, Free-Standing Ag-Reduced, Graphene Oxide Janus Films Prepared by Evaporation-Induced Self-Assembly. *Chem. – A Eur. J.* **17**, 8789–8793 (2011).

109. Duggal, R., Hussain, F. & Pasquali, M. Self-assembly of single-walled carbon nanotubes into a sheet by drop drying. *Adv. Mater.* **18**, 29–34 (2006).

110. Xie, C. *et al.* Flexible S@C-CNTs cathodes with robust mechanical strength via blade-coating for lithium-sulfur batteries. *J. Colloid Interface Sci.* **592**, 448–454 (2021).

111. Parija, B. & Panigrahi, S. Fundamental understanding and modeling of spin coating process : A review. *Indian J. Phys.* **83**, 493–502 (2009).

112. Baddour, C. E. & Briens, C. Carbon Nanotube Synthesis : A Review. *Int. J. Chem. React. Eng.* **3**, (2005).

113. Nessim, G. D. Properties , synthesis , and growth mechanisms of carbon nanotubes with special focus on thermal chemical vapor deposition. *Nanoscale* **2**, 1306–1323 (2010).

114. Kim, J. H., Pham, T. V., Hwang, J. H., Kim, C. S. & Kim, M. J. Boron nitride nanotubes : synthesis and applications. *Nano Converg.* **5**, (2018).

115. Bao, J. *et al.* Synthesis and Applications of Two-Dimensional Hexagonal Boron Nitride in Electronics Manufacturing. *Electron. Mater. Lett.* **12**, 1–16 (2016).

116. Wang, D., Song, P., Liu, C., Wu, W. & Fan, S. Highly oriented carbon nanotube papers made of aligned carbon nanotubes. *Nanotechnology* **19**, (2008).

117. Fan, S. *et al.* Self-Oriented Regular Arrays of Carbon Nanotubes and Their Field Emission Properties. *Science (80-.).* **283**, 512–515 (1999).

118. Li, L. H. & Chen, Y. Superhydrophobic Properties of Nonaligned Boron Nitride Nanotube Films. *Langmuir* **26**, 5135–5140 (2010).

119. Atiq, M. R. U., Chen, Q., Braem, A., Shaffer, M. S. P. & Boccaccini, A. R.

Electrophoretic deposition of carbon nanotubes : recent progress and remaining challenges. *Int. Mater. Rev.* **66**, 533–562 (2021).

120. Boccaccini, A. R. *et al.* Electrophoretic deposition of carbon nanotubes. *Carbon N. Y.* **44**, 3149–3160 (2006).

121. Hanaor, D. *et al.* Anodic aqueous electrophoretic deposition of titanium dioxide using carboxylic acids as dispersing agents. *J. Eur. Ceram. Soc.* **31**, 1041–1047 (2011).

122. Hamaker, H. C. FORMATION OF A DEPOSIT BY ELECTRO-PHORESIS. *Trans. Faraday Soc.* 279–287 (1939).

123. Verwey, E. J. W. & Hamaker, H. C. THE ROLE OF THE FORCES BETWEEN THE PARTICLES IN ELECTRODEPOSITION AND OTHER PHENOMENA . *Trans. Faraday Soc.* (1939).

124. Koelmans, H. SUSPENSIONS IN NON-AQUEOUS MEDIA. *Philips Res. Reports* **10**, 161–193 (1955).

125. Geçgin, M., Bakan, F. & Ay, N. Electrophoretic deposition of hydroxyapatite-hexagonal boron nitride composite coatings on Ti substrate. *Mater. Sci. Eng. C* **79**, 343–353 (2017).

126. Holter, J. JEOL JSM-840F. *DCCEM* https://www-em.materials.ox.ac.uk/jeol-jsm-840f (1992).

127. Holter, J. Zeiss Merlin - Analytical. *DCCEM* https://www-em.materials.ox.ac.uk/zeiss-merlin-analytical.

128. Ted Pella Inc. Cressingto 208HR Specification. *Cressington* https://www.cressington.com/spec_208hr.html.

129. Photon energies of principal K-, L-, and M-shell emission lines. *X-Ray Data Booklet Table 1-2.* at http://xdb.lbl.gov/Section1/Table_1-2.pdf.

130. OxfordInstruments. X-Max Silicon Drift Detector Range Brochure. at http://cellbiology.umcg.nl/wp-content/uploads/2018/07/Brochure-Xmax150-Oxford-Instr.pdf (2013).

131. Sachdev, H. Influence of impurities on the morphology and Raman spectra of cubic boron nitride. *Diam. Relat. Mater.* **12**, 1275–1286 (2003).

132. Arenal, R. *et al.* Raman spectroscopy of single-wall boron nitride nanotubes. *Nano Lett.* **6**, 1812–1816 (2006).

133. Wirtz, L., Lazzeri, M., Mauri, F. & Rubio, A. Raman spectra of BN nanotubes: Ab initio and bond-polarizability model calculations. *Phys. Rev. B - Condens. Matter Mater. Phys.* **71**, 2–5 (2005).

134. Boron, H. Normal modes in hBN. **146**, (1966).

135. Jung, J. H. *et al.* Defect engineering route to boron nitride quantum dots and edge-hydroxylated functionalization for bio-imaging. *RSC Adv.* **6**, 73939–73946 (2016).

136. Lee, H. *et al.* Dual Functionalization of Hexagonal Boron Nitride Nanosheets Using Pyrene-Tethered Poly(4-vinylpyridine) for Stable Dispersion and Facile Device Incorporation. *ACS Appl. Nano Mater.* **3**, 7633–7642 (2020).

137. Gorbachev, R. V. *et al.* Hunting for monolayer boron nitride: Optical and raman signatures. *Small* **7**, 465–468 (2011).

138. Dresselhaus, M. S., Dresselhaus, G., Saito, R. & Jorio, A. Raman spectroscopy of carbon nanotubes. *Phys. Resports* **409**, 47–99 (2005).

139. Cuesta, A., Dhamelincourt, P., Laureyns, J., Martinez-Alonso, A. & Tascon, J. M. D. Raman Microprobe Studies on Carbon Materials. *Carbon N. Y.* **32**, 1523–1532 (1994).

140. Ferrari, A. C. Raman spectroscopy of graphene and graphite : Disorder , electron – phonon coupling , doping and nonadiabatic effects. **143**, 47–57 (2007).

141. Bokobza, L. & Zhang, J. Raman spectroscopic characterization of multiwall carbon nanotubes and of composites. *eXPRESS Polym. Lett.* **6**, 601–608 (2012).

142. Hof, F., Bosch, S., Englert, J. M., Hauke, F. & Hirsch, A. Statistical Raman Spectroscopy : A Method for the Characterization of Covalently Functionalized Single-Walled Carbon Nanotubes. *Angew. CHemie* 11727–11730 (2012) doi:10.1002/anie.201204791.

143. Al-Ajlan, S. A. Measurements of thermal properties of insulation materials by using transient plane source technique. *Appl. Therm. Eng.* **26**, 2184–2191 (2006).

144. Paynter, R. XPS Theory Notes. 19–20.

145. Okpalugo, T. I. T., Papakonstantinou, P., Murphy, H., McLaughlin, J. & Brown, N. M. D. High resolution XPS characterization of chemical functionalised MWCNTs and SWCNTs. *Carbon N. Y.* **43**, 153–161 (2005).

146. Varga, M. *et al.* Diamond / carbon nanotube composites : Raman , FTIR and XPS spectroscopic studies. *Carbon N. Y.* **111**, 54–61 (2017).

147. Lee, S.-W., Lee, B.-J. & Oda, T. XPS Investigation and Field Emission Property of the Ar Plasma Processed Carbon Nanotube Films. *Trans. Electr. Electron. Mater.* **9**, 52–56 (2008).

148. Soin, N., Roy, S. S., Karlsson, L. & McLaughlin, J. A. Sputter deposition of highly dispersed platinum nanoparticles on carbon nanotube arrays for fuel cell electrode material. *Diam. Relat. Mater.* **19**, 595–598 (2010).

149. Velamakanni, A. *et al.* Site-specific deposition of au nanoparticles in cnt films by chemical bonding. *ACS Nano* **4**, 4962 (2010).

150. Thamaraiselvan, C., Lerman, S., Weinfeld-Cohen, K. & Dosoretz, C. G. Characterization of a support-free carbon nanotube-microporous membrane for water and wastewater filtration. *Sep. Purif. Technol.* **202**, 1–8 (2018).

151. Chen, X., Wang, X. & Feng, D. A review on C1s XPS-spectra for some kinds of carbon materials. *Fullerenes, Nanotub. Carbon Nanostructures* **28:12**, 1048-1058, (2020).

152. Blume, R. *et al.* Characterizing Graphitic Carbon with X-ray Photoelectron Spectroscopy: A Step-by-Step Approach. *ChemCatChem* vol. 7 2871–2881 at https://doi.org/10.1002/cctc.201500344 (2015).

153. DESIMON, E., CASELLA, G. ., CATALDI, T. R. I. & MALITESTA, C. A comparison of some asymmetrical line shapes for xps data analysis. *J. Electron Spectros. Relat. Phenomena* **49**, 247–261 (1989).

154. Qu, J., Li, Q., Luo, C., Cheng, J. & Hou, X. Characterization of flake boron nitride prepared from the low temperature combustion synthesized precursor and its application for dye adsorption. *Coatings* **8**, (2018).

155. Guimon, C. *et al.* XPS study of BN thin films deposited by CVD on SiC plane substrates. *Surf. Interface Anal.* **16**, 440–445 (1990).

156. Trehan, R., Lifshitz, Y. & Rabalais, J. W. Auger and x-ray electron spectroscopy studies of h BN, c BN, and N + 2 ion irradiation of boron and boron nitride . *J. Vac. Sci. Technol. A Vacuum, Surfaces, Film.* **8**, 4026–4032 (1990).

157. Sudeep, P. M. *et al.* Functionalized boron nitride porous solids. *RSC Adv.* **5**, (2015).

158. Angizi, S., Shayeganfar, F., Azar, M. H. & Simchi, A. Surface/edge functionalized boron nitride quantum dots: Spectroscopic fingerprint of bandgap modification by chemical functionalization. *Ceram. Int.* **46**, 978–985 (2020).

159. Wang, G. *et al.* Interlayer Coupling Behaviors of Boron Doped Multilayer

Graphene. *J. Phys. Chem. C* **121**, 26034–26043 (2017).

160. Il'inchik, E. A., Volkov, V. V. & Mazalov, L. N. X-ray photoelectron spectroscopy of boron compounds. *J. Struct. Chem.* **46**, 523–534 (2005).

161. Achour, H. *et al.* Plasma surface functionalization of boron nitride nano-sheets. *Diam. Relat. Mater.* **77**, 110–115 (2017).

162. Zhang, D., Davalle, D. M., O'Brien, W. L. & McIlroy, D. N. The chemical composition of as-grown and surface treated amorphous boron carbon thin films by means of NEXAFS and XPS. *Surf. Sci.* **461**, 16–22 (2000).

163. Kolel-Veetil, M. K. *et al.* Substitution of silicon within the rhombohedral boron carbide (B4C) crystal lattice through high-energy ball-milling. *J. Mater. Chem. C* **3**, 11705–11716 (2015).

164. SUMIYA, H., UESAKA, S. & SATOH, S. Mechanical properties of high purity polycrystalline cBN synthesized by direct conversion sintering method. *J. Mater. Sci.* **35**, 1181–1186 (2000).

165. Pang, L. S. K., Saxby, J. & Chatfield, P. S. Thermogravimetric Analysis of Carbon Nanotubes and Nanoparticles. *J. Phys. Chem.* **97**, 6941–6942 (1993).

166. Titus, E. *et al.* Chemically Functionalized Carbon Nanotubes and Their Characterization Using Thermogravimetric Analysis , Fourier Transform Infrared , and Raman Spectroscopy. *JMEPEG* **15**, 182–186 (2006).

167. Mansfield, E., Kar, A. & Hooker, S. A. Applications of TGA in Quality Control of SWCNTs. *Anal Bioanal Chem* **396**, 1071–1077 (2010).

168. Bom, D. *et al.* Thermogravimetric Analysis of the Oxidation of Multiwalled Carbon Nanotubes: Evidence for the Role of Defect Sites in Carbon Nanotube Chemistry. *Nano Lett.* **2**, 615–619 (2002).

169. Iman Faridmehr, Mohd Hanim Osman, Azlan Bin Adnan, Ali Farokhi Nejad, Reza Hodjati, M. A. Correlation between Engineering Stress-Strain and True Stress-Strain Curve. *Am. J. Civ. Eng. Archit.* **2**, 53–59 (2014).

170. Sbai, K., Rahmani, A., Chadli, H., Colloı, L. & Nanomate, V. Infrared Spectroscopy of Single-Walled Carbon Nanotubes. *J. Phys. Chem.* **110**, 12388–12393 (2006).

171. Kuhlmann, U. *et al.* Infrared active phonons in single-walled carbon nanotubes. *Chem. Phys. Lett.* **294**, 237–240 (1998).

172. Ovejero, G., Sotelo, J. L., Romero, M. D., Rodrı, A. & Ocan, M. A. Multiwalled Carbon Nanotubes for Liquid-Phase Oxidation . Functionalization , Characterization , and Catalytic Activity. *Ind. Eng. Chem. Res.* **45**, 2206–2212 (2006).

173. Zhang, Y. F., Tang, Y. H., Lee, C. S., Bello, I. & Lee, S. T. Nanocrystalline C – BN synthesized by mechanical alloying. **8**, 610–613 (1999).

174. Bhimanapati, G. R., Kozuch, D. & Robinson, J. A. Large-scale synthesis and functionalization of hexagonal boron nitride nanosheets. *Nanoscale* **6**, 11671–11675 (2014).

175. Xia, Z. P. & Li, Z. Q. Structural evolution of hexagonal BN and cubic BN during ball milling. *J. Alloys Compd.* **436**, 170–173 (2007).

176. Evans, D. A. *et al.* Determination of the optical band-gap energy of cubic and hexagonal boron nitride using luminescence excitation. *Condens. Matter* **20**, (2008).

177. Holder, C. F. & Schaak, R. E. Tutorial on Powder X - ray Diff raction for Characterizing Nanoscale Materials. *ACS Nano* **13**, 7359–7365 (2019).

178. Cao, A., Xu, C., Liang, J., Wu, D. & Wei, B. X-ray diffraction characterization on the alignment degree of carbon nanotubes.

Chem. Phys. Lett. **344**, 13–17 (2001).

179. Wazir, A. H. & Kundi, I. W. Synthesis of Graphene Nano Sheets by the Rapid Reduction of Electrochemically Exfoliated Graphene Oxide Induced by Microwaves. *J.Chem.Soc.Pak* **38**, 11–16 (2016).

180. Pham, G. T. *et al.* Mechanical and electrical properties of polycarbonate nanotube buckypaper composite sheets. *Nanotechnology* **19**, (2008).

181. Nguyen, N. *et al.* High-Performance and Lightweight Thermal Management Devices by 3D Printing and Assembly of Continuous Carbon Nanotube Sheets. *ACS Appl. Mater. Interfaces* **10**, 27171–27177 (2018).

182. Zhang, H. *et al.* Recent advances in nanostructured carbon for sodium-ion batteries. *J. Mater. Chem. A* **8**, 1604–1630 (2020).

183. Tao, F. *et al.* Carbon nanotube-based nanomaterials for high-performance sodium-ion batteries: Recent advances and perspectives. *J. Alloys Compd.* **873**, 159742 (2021).

184. B.G. Demczyka, Y.M. Wanga, J. Cumingsa, M. Hetmana, W. Hana, A. Zettla, R. O. R. Direct mechanical measurement of the tensile strength and elasticmodulus of multiwalled carbon nanotubes. *Mater. Sci. Eng. A* **334**, 173–178 (2002).

185. Dresselhaus, M. S., Dresselhaus, G., Charlier, J. C. & Hernández, E. Electronic, thermal and mechanical properties of carbon nanotubes. *Philos. Trans. R. Soc. A Math. Phys. Eng. Sci.* **362**, 2065–2098 (2004).

186. Wang, Z., Liang, Z., Wang, B., Zhang, C. & Kramer, L. Processing and property investigation of single-walled carbon nanotube (SWNT) buckypaper/epoxy resin matrix nanocomposites. *Compos. Part A Appl. Sci. Manuf.* **35**, 1225–1232 (2004).

187. Online, V. A., Clancy, A. J. & Melbourne, J. A one-step route to solbilised, purified or functionalised single-walled carbon nanotubes. 16708–16715 (2015) doi:10.1039/c5ta03561a.

188. Besra, L. & Liu, M. A review on fundamentals and applications of electrophoretic deposition (EPD). *Prog. Mater. Sci.* **52**, 1–61 (2007).

189. De Marco, M. *et al.* Cross-linked single-walled carbon nanotube aerogel electrodes via reductive coupling chemistry. *J. Mater. Chem. A* **4**, (2016).

190. Rodriguez-Salinas, J. *et al.* Enhancing Electrical and Thermal Properties of Al6061 Parts by Electrophoresis Deposition of Multi-Walled Carbon Nanotubes. *Coatings* **10**, 656 (2020).

191. Park, J. G. *et al.* Effects of surfactants and alignment on the physical properties of single-walled carbon nanotube buckypaper. *Journal of Applied Physics* vol. 106 at https://doi.org/10.1063/1.3255901 (2009).

192. Bekyarova, E. *et al.* Electronic Properties of Single-Walled Carbon Nanotube Networks. 5990–5995 (2005).

193. Kim, T. *et al.* Inkjet-printed stretchable single-walled carbon nanotube electrodes with excellent mechanical properties. *Applied Physics Letters* vol. 104 at https://doi.org/10.1063/1.4868633 (2014).

194. Ansón-Casaos, A., González-Domínguez, J. M., Terrado, E. & Martínez, M. T. Surfactant-free assembling of functionalized single-walled carbon nanotube buckypapers. *Carbon N. Y.* **48**, 1480–1488 (2010).

195. Bilu, L., Fanqi, W., Hui, G., Ming, Z. & Chongwu, Z. Chirality Controlled Synthesis and applications of single walled carbon nanotubes.pdf. *ACS Nano* **11**, 31–53 (2017).

196. Thamaraiselvan, C., Lerman, S., Weinfeld-Cohen, K. & Dosoretz, C. G.

Characterization of a support-free carbon nanotube-microporous membrane for water and wastewater fi ltration. *Sep. Purif. Technol.* **202**, 1–8 (2018).

197. Phys, A., Chen, X., Zhang, L. & Park, C. Mechanical strength of boron nitride nanotube-polymer interfaces. *Appl. Phys. Lett.* **253105**, (2015).

198. Jia, Y., Sauti, G. & Park, C. Thermal properties of polymer - derived ceramic reinforced with boron nitride nanotubes. *J. Am. Ceram. Soc.* 7584–7593 (2019) doi:10.1111/jace.16670.

199. Walsh, F. *et al.* Transistor Package ' s Boron Nitride Film Microstructure and Roughness : Effect of EPD Suspensions ' pH and Related papers Transistor Package ' s Boron Nitride Film Microstructure and Roughness : Effect of EPD Suspensions ' pH and Binder. *J. Telecommun. Electron. Comput. Eng.* **8**, 99–104 (2016).

200. Mapleback, B. J. *et al.* Development of Stable Boron Nitride Nanotube and Hexagonal Boron Nitride Dispersions for Electrophoretic Deposition. *Langmuir* 3425–3438 (2020) doi:10.1021/acs.langmuir.0c00018.

201. TuballTM. Tuball/Graphene Nanotubes Product Sheet. https://tuball.com/additives/tuball.

202. BNNT(LLC). BNNT Refined PuffBall Specifications. www.bnnt.com/nanotubes/refined-puffball (2022).

203. Kim, J. H. *et al.* Dual growth mode of boron nitride nanotubes in high temperature pressure laser ablation. *Sci. Rep.* **9**, 1–10 (2019).

204. McGurty, D. *et al. Two-Step Aerosol Assisted Synthesis of Structurally Uniform B(X)C(Y)N(Z) Nanotubes: Tuning Properties via Co-Doping*. (2022).

205. Shin, H. *et al.* Covalent Functionalization of Boron Nitride Nanotubes via Reduction Chemistry. *ACS Nano* **9**, 12573–12582 (2015).

206. Wang, M., Cheng, J., Li, M. & He, F. Raman spectra of sodalimesilicate glass doped with rare earth. *Physica B: Condensed Matter* vol. 406 3865–3869 at https://doi.org/10.1016/j.physb.2011.07.014 (2011).

207. O'Sullivan, E., Grobert, N. & Swart, M. *Atomic Insights into the Processes of B,C, and N on Cu(111)*. (2022).

208. De, F., HE, F., Junlin, X. & Lihu, X. Calibration of Binding Energy Positions with CIs for XPS Results. *J. Wuhan Univ. Technol.* **35**, 711–718 (2020).

209. EurofinsScientrific. XPS Chemical Bond Infomation. *EAG Laboritories* https://www.eag.com/resources/appnotes/xps-provides-chemical-bond-information/ (2015).

210. Huber, C. *et al.* The multistep decomposition of boric acid. *Energy Sci. Eng.* 1650–1666 (2020) doi:10.1002/ese3.622.

211. Kim, K. S. *et al.* Scalable manufacturing of boron nitride nanotubes and their assemblies : a review. *Semicond. Sci. Technol.* **32**, 013003 (2016).

212. Absolute & Reports. *GLOBAL BORON NITRIDE NANOTUBES (BNNT) MARKET RESEARCH REPORT 2022*. (2022) doi:QYR-21606043.

213. Market_Research_Future. *Hexagonal Boron Nitride Market By Type (Tubes, Rods, Plates, Gaskets, Crucibles, Sheets and Others), By Application (Electrical Insulation, Lubrication Industrial, Coatings & Mold Release, Cosmetics, Composites, Thermal Spray and Others) and - Forecast ti*. (2018).

214. Fang, H., Bai, S. & Wong, C. P. "White graphene" – hexagonal boron nitride based polymeric composites and their application in thermal management. *Compos. Commun.* **2**, 19–24 (2016).

215. Raman, C. & Meneghetti, P. Boron nitride finds new applications in thermoplastic

Compounds. *Plast. Addit. Compd.* **10**, 26–30 (2008).

216. Liu, J., Li, W., Guo, Y., Zhang, H. & Zhang, Z. Improved thermal conductivity of thermoplastic polyurethane via aligned boron nitride platelets assisted by 3D printing. *Compos. Part A* **120**, 140–146 (2019).

217. Lin, Z. *et al.* Magnetic Alignment of Hexagonal Boron Nitride Platelets in PolymerMatrix: Toward High Performance Anisotropic Polymer Compositesfor Electronic Encapsulation. *ACS Appl. Mater. Interfaces* **5**, 7633–7640 (2013).

218. Davesne, A.-L. *et al.* Hexagonal Boron Nitride Platelet-Based Nanocoating for Fire Protection. *ACS Appl. Nano Mater.* **2**, 5450–5459 (2019).

219. 3M(TM). *Boron Nitride Cooling Filler Platelets Product Infomation*. (2022).

220. Savaram, K. *et al.* Synergy of oxygen and a piranha solution for eco-friendly production of highly conductive graphene dispersions. *Green Chem* **17**, 869–881 (2015).

221. Hui, W. C. Secret of formulating a selective etching or cleaning solution for boron nitride (BN) thin film. in *Proc.SPIE* vol. 5276 143–153 (2004).

222. Shurvell, H. F. & Faniran, J. A. Infrared spectra of triphenylboron and triphenylborate. *Can. J. Chem.* **46**, 2081–2087 (1968).

223. ChemicalBook. Boron Oxide CAS DataBase List. https://www.chemicalbook.com/ChemicalProductProperty_EN_CB1264526.htm (2022).

224. Backes, C. *et al.* Equipartition of Energy Defines the Size-Thickness Relationship in Liquid-Exfoliated Nanosheets. *ACS Nano* (2019) doi:10.1021/acsnano.9b02234.

225. Liao, Y. *et al.* Chemical Sharpening, Shortening, and Unzipping of Boron Nitride Nanotubes. *Adv. Funct. Mater.* **24**, 4497–4506 (2014).

226. Xue, Y. *et al.* Densely Interconnected Porous BN Frameworks for Multifunctional and Isotropically Thermoconductive Polymer Composites. *Adv. Funct. Mater.* **28**, 1801205 (2018).

227. Zhigadlo, N. D. Crystal growth of hexagonal boron nitride (hBN) from Mg – B – N solvent system under high pressure. *J. Cryst. Growth* **402**, 308–311 (2014).

228. Paton, K. R. *et al.* Scalable production of large quantities of defect-free few-layer graphene by shear exfoliation in liquids. *Nat. Mater.* **13**, 624–630 (2014).

229. Chen, X., Dobson, J. F. & Raston, C. L. Vortex fluidic exfoliation of graphite and boron nitride. *Chem. Commun.* **48**, 3703–3705 (2012).

230. Holzwarth, U. & Gibson, N. The Scherrer equation versus the 'Debye-Scherrer equation'. *Nat. Nanotechnol.* **6**, 534 (2011).

231. Sharma, R., Chadha, N. & Saini, P. Determination of defect density , crystallite size and number of graphene layers in graphene analogues using X-ray diffraction and Raman spectroscopy. **55**, 625–629 (2017).

232. Cai, M., Thorpe, D., Adamsonb, D. H. & Schniepp, H. C. Methods of graphite exfoliation. *J. Mater. CHemsitry* **22**, 24992–25002 (2012).

233. Hernandez, Y. *et al.* High-yield production of graphene by liquid-phase exfoliation of graphite. *Nat. Nanotechnol.* **3**, 563–568 (2008).

234. Hamilton, C. E., Lomeda, J. R., Sun, Z., Tour, J. M. & Barron, A. R. High-Yield Organic Dispersions of Unfunctionalized Graphene. *Nano Lett.* **9**, 3460–3462 (2009).

235. Bourlinos, A. B., Georgakilas, V., Zboril, R., Steriotis, A. & Stubos, A. K. Liquid-Phase Exfoliation of Graphite Towards Solubilized Graphenes. *Small* **5**, 1841–

1845 (2009).

236. Khan, U., Neill, A. O., Lotya, M., De, S. & Coleman, J. N. High-Concentration Solvent Exfoliation of Graphene. *Small* **6**, 864–871 (2010).

237. Ng, K. L. *et al.* Direct evidence of exfoliation efficiency and graphene dispersibility of green solvents towards sustainable graphene production. *ChemRxiv* 1–8 (2022).

238. Benedict, L. X. *et al.* Microscopic determination of the interlayer binding energy in graphite. *Chem. Phys. Lett.* **286**, 490–496 (1998).

239. Spanu, L., Sorella, S. & Galli, G. Nature and Strength of Interlayer Binding in Graphite. *Phys. Rev. Lett.* **103**, 1–4 (2009).

240. Marom, N. *et al.* Stacking and registry effects in layered materials: The case of hexagonal boron nitride. *Phys. Rev. Lett.* **105**, 1–4 (2010).

241. Damm, C., Körner, J. & Peukert, W. Delamination of hexagonal boron nitride in a stirred media mill. *J. Nanoparticle Res.* **15**, 1–12 (2013).

242. Newey-Keane, L. & Carrington, S. Controlling the Stability of Medicinal Suspensions. *Am. Pharm. Rev.* (2016).

243. Gao, W., Zhao, Y. & Yin, H. Lateral size selection of liquid exfoliated hexagonal boron nitride nanosheets. *RSC Adv.* 5976–5983 (2018) doi:10.1039/c7ra12872j.

244. Constantinescu, G., Kuc, A. & Heine, T. Stacking in Bulk and Bilayer Hexagonal Boron Nitride. *Phys. Rev. Lett.* **111**, 036104 (2013).

245. Yamamoto, H. Hansen Solubility Parameters (HSP) Application Notes. *Pirika* https://www.pirika.com/NewHP/PirikaE2/Sphere-Dbl.html (2010).

246. Hansen, C. Hansen Solubility Paraeters: The HSP Sphere. https://www.hansen-solubility.com/HSP-science/sphere.php (2022).

247. Abbott, S. Solubility Science Principles & Practice. Hansen Solubility Parameters at (2021).

248. Kim, D. H., Yun, Y. S. & Jin, H. J. Difference of dispersion behavior between graphene oxide and oxidized carbon nanotubes in polar organic solvents. *Curr. Appl. Phys.* **12**, 637–642 (2012).

249. Bergin, S. D. *et al.* Multicomponent Solubility Parameters for Single-Walled Carbon Nanotube-Solvent Mixtures. *ACSNano* **3**, 2340–2350 (2009).

250. Tiano, A. L. *et al.* Thermodynamic approach to boron nitride nanotube solubility and dispersion. *Nanoscale* **8**, 4348–4359 (2016).

251. Torres Castillo, C. S., Bruel, C. & Tavares, J. R. Chemical affinity and dispersibility of boron nitride nanotubes. *Nanoscale Adv.* **2**, 2497–2506 (2020).

252. Cheng, F. C. Insulation Thickness Determination of Polymeric Power Cables. *IEEE Trans. Dielectr. Electr. Insul.* **1**, 624–629 (1994).

253. Laturia, A. & Put, M. L. Van De. Dielectric properties of hexagonal boron nitride and transition metal dichalcogenides : from monolayer to bulk. *npj 2D Mater. Appl.* **6**, (2018).

254. Oldervoll, F. High Electric Stress and Insulation Challenges in Integrated Microelectronic Circuits. *IEEE Electr. Insul. Mag.* **18**, 16–20 (2002).

255. Grillon, F., Fayeulle, D. & Jeandin, M. Quantitative image analysis of electrophoretic coatings. *J. Mater. Sci. Lett.* **11**, 272–275 (1992).

256. Arkhipova, E. A. *et al.* Structural evolution of nitrogen-doped carbon nanotubes : From synthesis and oxidation to thermal defunctionalization. *Carbon N. Y.* **125**, 20–31 (2017).

257. Sawant, S. V, Patwardhan, A. W., Joshi, J. B. & Dasgupta, K. Boron doped carbon nanotubes : Synthesis , characterization and emerging applications – A review. *Chem. Eng. J.* **427**, 131616 (2022).

258. Ayala, P., Arenal, R., Ru, M., Rubio, A. & Pichler, T. The doping of carbon nanotubes with nitrogen and their potential applications. *Carbon N. Y.* **48**, 575–586 (2009).

259. Zhi, C., Bando, Y., Tang, C., Kuwahara, H. & Golberg, D. Large-Scale Fabrication of Boron Nitride Nanosheets and Their Utilization in Polymeric Composites with Improved Thermal and Mechanical Properties. *Adv. Mater.* **21**, 2889–2893 (2009).

260. Postole, G. *et al.* Boron nitride : A high potential support for combustion catalysts. *Thermochim. Acta* **434**, 150–157 (2005).

261. Kimura, Y., Kubo, Y. & Hayashi, N. HIGH-PERFORMANCE BORON-NITRIDE FIBERS FROM POLY (BORAZINE) PRECERAMICS. **51**, 173–179 (1994).

262. Qiu, Y. *et al.* Large-Scale Production of Aligned Long Boron Nitride Nanofibers by Multijet / Multicollector Electrospinning. 11228–11234 (2009).

263. Lin, J. *et al.* Ultrafine porous boron nitride nanofibers synthesized via a freeze-drying and pyrolysis process and their adsorption properties. *RSC Adv.* **6**, 1253–1259 (2016).

264. Bernard, S., Chassagneux, F., Berthet, M. P., Cornu, D. & Miele, P. Crystallinity, crystalline quality, and microstructural ordering in boron nitride fibers. *J. Am. Ceram. Soc.* **88**, 1607–1614 (2005).

265. Wu, C. *et al.* Molecular-scale understanding on the structure evolution from melamine diborate supramolecule to boron nitride fi bers. *Ceram. Int.* **46**, 1083–1090 (2020).

266. Fang, H., Bai, S. L. & Wong, C. P. Thermal, mechanical and dielectric properties of flexible BN foam and BN nanosheets reinforced polymer composites for electronic packaging application. *Compos. Part A Appl. Sci. Manuf.* **100**, 71–80 (2017).

267. AnaPath. AnaPath ELECTRON MICROSCOPY. https://anapath.ch/electron-microscopy-2/ (2023).

268. Mahajan, A., Kingon, A., Kukovecz, Á., Konya, Z. & Vilarinho, P. M. Studies on the thermal decomposition of multiwall carbon nanotubes under different atmospheres. *Mater. Lett.* **90**, 165–168 (2013).

11 APPENDIX

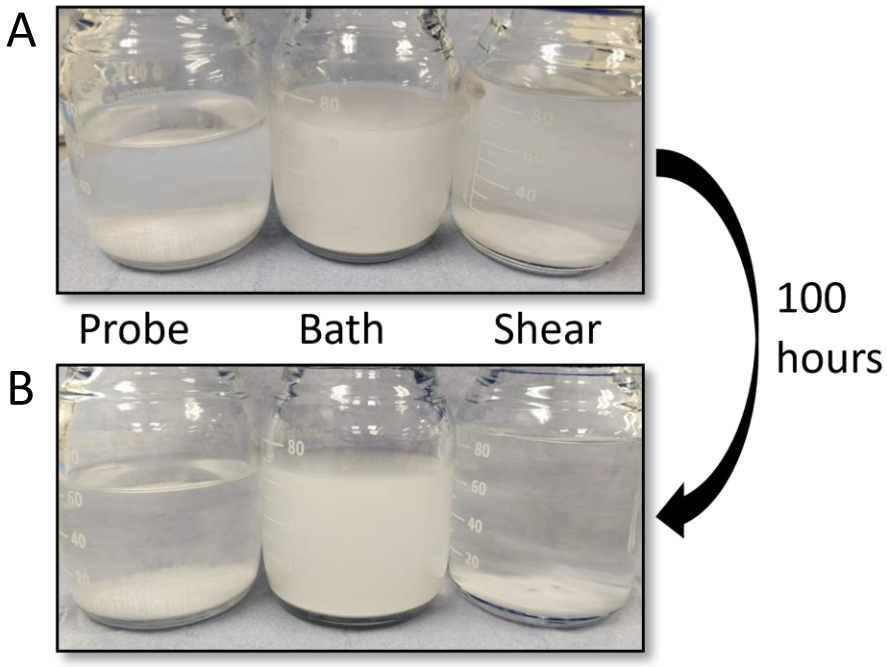


Figure 11.1. Qualitative images of the exfoliated BNP solutions immediately after testing by UV-Vis [A] for concentration and 100 hours (4 days) after this [B] showing little change in the Probe and Bath sonicated samples but the near complete sedimentation of the shear mixed sample.

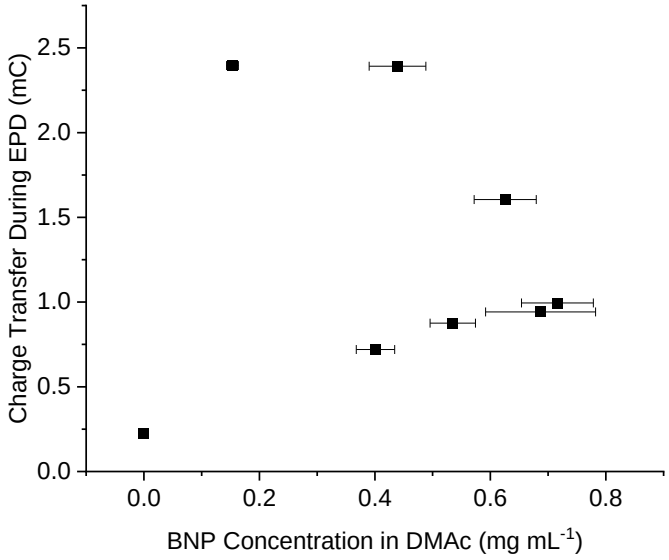


Figure 11.2. Graph showing the relationship between the total charge transfer (calculated from the current/time curves) and the concentration of the starting dispersions for the EPD of DMAc suspended 'oxidised' BNP samples. As can be seen there is no linear trend as would be expected.

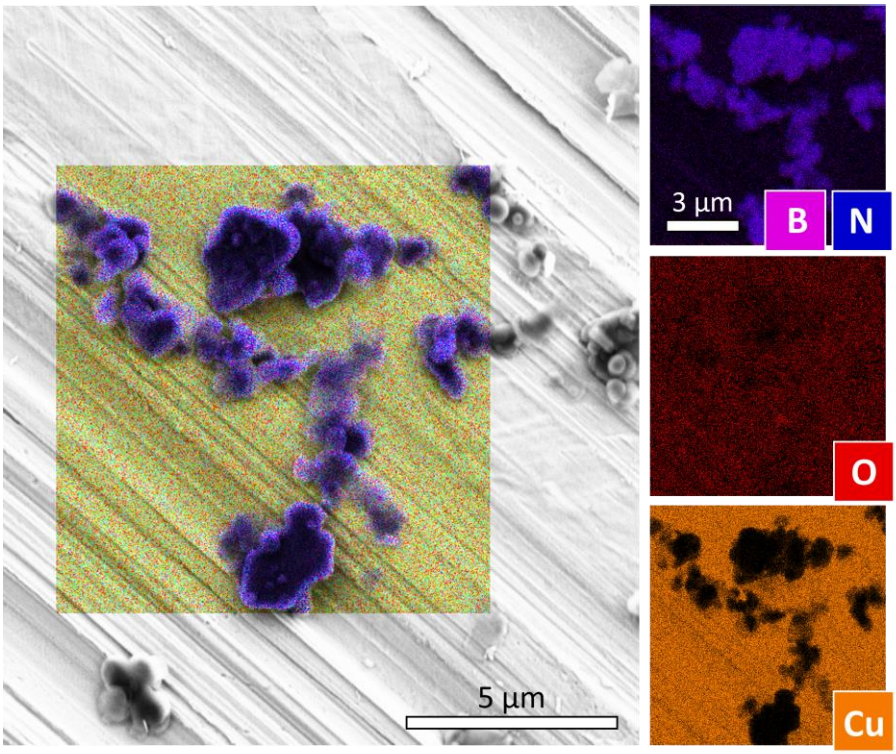


Figure 11.3. Additional EDS atomic map of 003 BNP starting material that has been deposited by EPD onto Cu foil. The oxygen map (red) clearly shows small, localised areas of O density similar to the exfoliated and acid sonicated sample displayed in Figure 7.9

“If you trust in yourself…

and believe in your dreams…

and follow your star…

You'll still get beaten by people who spent their time working

hard and learning things and weren't so lazy.”

— Terry Pratchett

The Wee Free Men